

SPIN ORIENTATIONS AND SPIN-ORBIT TORQUE IN MAGNETIC  
NANOSTRUCTURES

by

Vedat Karakaş

M.Sc., Physics, Marmara University, 2012,

B.S., Integrated MS & BS Program in Physics, Ondokuz Mayıs University, 2008

Submitted to the Institute for Graduate Studies in  
Science and Engineering in partial fulfillment of  
the requirements for the degree of  
Doctor of Philosophy

Graduate Program in Physics

Boğaziçi University

2019

## ACKNOWLEDGEMENTS

First off all, I would like to thank my thesis supervisor Prof. Özhan Özatay for giving me a chance to gain an ability to observe and interpret physics problems in his laboratory. He has always been nice to me, patiently instructing and expressing endless support. He taught me how to be a good scientist in physics. He always approached to me as a friend through my hard PhD time. Especially, I would like to thank him for sharing his apartment for one year during my visitor PhD student time in Argonne National Laboratory.

I would like to thank Dr. Ayşe Gökce Özbay who thought me how to solve an experimental problem and not to lose concentration in any condition. She helped me with valuable guidance for every step of this study. I acknowledge her for helpful discussions and behaving like a family member. I feel honored to work with her husband Dr. Arif Özbay. Thanks to Buspin group member we shared a lot of difficult and joyful times together. They have always been helpful and kind to me.

I would like to specially thank to Hakan Erkol, I always feel lucky to meet him, for giving me illuminating advise in difficult conditions and behaving like my elder brother without any hesitation. I thank to Nasire Uluc, Defne Yılmaz for sharing my happiness and sadness during PhD period. They are always kind and helpful to me.

Special thanks to Sevde Nur Arpacı, she was a MS student and we had 4 years overlap time with her. We shared plenty of joyful time. This long friendship has been a great treasure to me and has benefited me both inside and outside the lab. Undoubtedly, I could not have finished my experiments and thesis without her precious help.

I would like to thank Gülen Aktas Greenwood, Mehmet Burcin Ünlü, Hakan Erkol, Arif Ozbay and İlhan Yavuz for serving as my committee members in my thesis defense. I appreciated many valuable comments and some constructive criticisms from them on my thesis.

Most particularly I would like to express my gratitude to Dr. Axel Hoffman for hosting me in Argonne National Laboratory for one year and I want to thank Dr. Yılmaz Simsek, Dr. Hilal Saglam, Dr. Yi Li, Dr. Ralu Nana Silva Divan and Dr. Sergi Lendinez for their help, guidance during Argonne National Laboratory days.

I want to thank on the spot, Prof. Giovanni Finnochio and his group members Paola Tiberto, Silvia Tacchi, Riccardo Tomasello, Vito Puliafito whose support and guidance made part of my thesis work possible.

I would like to thank TUBITAK (Grant no: 113F378), TUBITAK (Grant No: 114F318), TUBITAK (Grant No: 118F116), Bogazici University Research funding (Grant No:12420D) for supporting me and TUBITAK 2214/A (2016 / 2) Grant for funding of the "THE EFFECT OF SPIN TORQUE ON ANTIFERROMAGNETIC ORDERING" titled work.

Last but not the least, I would like to thank my family, Hasan, Emine, Veyis, Birgül, Sefa, Selma and Saba for their endless support and not letting me alone in any moment of my life.

## ABSTRACT

# SPIN ORIENTATIONS AND SPIN-ORBIT TORQUE IN MAGNETIC NANOSTRUCTURES

In this thesis three different spintronic devices and their static behaviours are studied under external magnetic field or applied current. We started to work on the static properties of magnetic antivortices, formed in a special geometry called astroid, and achieved stable antivortex nucleation, annihilation and manipulation. We also observed the response of antivortex to the external magnetic field.

Another study was the observation of magnetic radial vortices in the presence of interfacial Dzyaloshinskii-Moriya interaction (i-DMI) in Pt/CoFeB/Ti nanopillar multilayers. By tuning the magnetic anisotropy via interface engineering and postproduction treatments, we achieved to stabilize a variety of magnetic configurations such as Néel skyrmions, horseshoes and radial vortices at room temperature and under zero bias field.

Lastly, we have focused on the observation of self-torque of (100) oriented IrMn<sub>3</sub> antiferromagnet. We observed the exchange field shift with respect to applied current. Additionally, we studied the effect of spin orbit torque by measuring DC current dependence of Hall bar resistance. The efficiency of different types of heavy metals, which have different spin Hall angles, was studied to compare their resistance variation of the device.

## ÖZET

# MANYETİK NANOYAPILARDA SPİN YÖNELİMLERİ VE SPİN YÖRÜNGE TORKU

Bu tezde üç farklı spintronik aygıtın statik özellikleri, uygulanan dış manyetik alan ya da akım atması altında incelendi. Astroid olarak isimlendirilen geometride oluşan manyetik antivorteksin statik özelliklerini incelemek ile işe başladık. Kararlı antivorteksi dış manyetik alanla oluşturmayı ve yok etmeyi başardık. Ayrıca antivorteksin dış manyetik alana verdiği tepkiyi inceledik.

Bir diğer çalışmamızda, Pt/CoFeB/Ti çok katmanlı nano-sütunlarda arayüzey Dzyaloshinskii-Moriya etkileşimi (i-DMI) sayesinde oluşan manyetik radyal vorteksi gözlemledik. Çok katmanlı filmin manyetik anizotropisinin, üretim aşamalarında maruz kaldığı koşulların yardımı ile değiştirilebilmesi sonucunda kararlı Néel skyrmion, atnalı ve radyal vorteks gibi manyetik konfigürasyonları oda koşullarında sıfır dış manyetik alan altında gözlemledik.

Son olarak özellikle (100) kristal yöneline sahip  $\text{IrMn}_3$  antiferromagnetinin öz-torkunun gözlemlenmesine odaklandık. Değiş-tokuş alanının, uygulanan dış akım atmaları ile orantılı şekilde kaymasını gözlemledik. Ayrıca Hall bar geometrisine sahip aygıtın, spin orbital torku etkisinden kaynaklı DC akıma karşı direncindeki değişimini çalıştık. Farklı spin Hall açılı ağır metaller kullanarak verimliliklerini kıyasladık.

## TABLE OF CONTENTS

ACKNOWLEDGEMENTS . . . . .	iii
ABSTRACT . . . . .	v
ÖZET . . . . .	vi
LIST OF FIGURES . . . . .	x
LIST OF TABLES . . . . .	xxvi
LIST OF SYMBOLS . . . . .	xxvii
LIST OF ACRONYMS/ABBREVIATIONS . . . . .	xxviii
1. INTRODUCTION . . . . .	1
1.1. Magnetization Dynamics LLG Equation . . . . .	2
1.2. Micromagnetic Structure and DMI . . . . .	4
1.3. Magnetization Dynamics Driven by Spin Torque . . . . .	7
1.4. Antiferromagnets . . . . .	11
2. MATERIAL CHARACTERIZATION . . . . .	15
2.1. Thin Film Deposition . . . . .	15
2.1.1. Deposition Rate Calibration . . . . .	15
2.1.2. Ion Milling Rate Calibration . . . . .	22
2.2. Electrical Characterization . . . . .	23
2.3. Magnetic Characterization with Vibrating Sample Magnetometer and SQUID . . . . .	30
2.4. Structural Characterization with X-ray Diffraction and X-Ray Photo Electron Spectroscopy . . . . .	38
2.4.1. Auger Effect . . . . .	40
2.4.2. Inelastic Mean Free Path . . . . .	41
2.4.3. The Spectroscope . . . . .	41
2.4.4. Calibration of Insulating Specimens . . . . .	42
2.4.5. Charging Effect . . . . .	42
2.5. Measuring Morphology with Atomic Force Microscopy . . . . .	43
2.5.1. Surface Roughness Measurement . . . . .	45
2.6. Magnetic Imaging with Magnetic Force Microscopy . . . . .	46

3. FABRICATION OF NANOPILLAR, THREE TERMINAL AND HALL BAR DEVICES . . . . .	53
3.1. Preparation of wafers . . . . .	53
3.1.1. Wafer cleaving with a dicer . . . . .	54
3.1.2. Wafer cleaving with a scribe . . . . .	57
3.1.3. Spin coating . . . . .	58
3.2. Photolithography . . . . .	60
3.3. Electron Beam Lithography . . . . .	62
3.3.1. Wafer chip production . . . . .	64
3.4. Nanopillar Device . . . . .	66
3.4.1. E-beam evaporation . . . . .	69
3.5. Hall Bar Device . . . . .	71
4. MAGNETIC ANTIVORTEX . . . . .	77
4.1. Anisotropic Magnetoresistance . . . . .	78
4.2. Experiments . . . . .	81
4.2.1. Characterization of Permalloy Thin Films . . . . .	81
4.2.2. Determination of EBL resists and parameters . . . . .	82
4.2.3. Magnetic force microscopy measurements . . . . .	86
4.3. Results . . . . .	86
5. EVOLUTION OF MAGNETIC STATES FROM NÉEL SKYRMIONS TO RADIAL VORTICES . . . . .	93
5.1. Nucleation of Magnetic Configurations . . . . .	93
5.2. Manipulation of Radial Vortex via Magnetic Field . . . . .	95
6. ELECTRORESISTANCE AND EXCHANGE BIAS MANIPULATION BY CURRENT IN ANTIFERROMAGNETS . . . . .	112
6.1. Magnetic Characterization of (100) Oriented IrMn <sub>3</sub> Thin Film . . . . .	112
6.2. Structural Characterization of (100) Oriented IrMn <sub>3</sub> Thin Film . . . . .	113
6.3. Exchange Bias Manipulation by Spin Orbit Torque . . . . .	117
6.4. Electroresistance in Antiferromagnet . . . . .	124
7. CONCLUSION . . . . .	135
REFERENCES . . . . .	139

APPENDIX A: 3 Terminal Device . . . . . 149

## LIST OF FIGURES

Figure 1.1.	Spin orientation in magnetic materials . . . . .	1
Figure 1.2.	Schematic drawing of the Magnetization dynamics driven by the Landau-Liftshitz equation(precession term) [1] . . . . .	2
Figure 1.3.	Schematic drawing of the Magnetization dynamics driven by the Landau-Liftshitz-Gilbert equation(precession, damping terms) [1] .	4
Figure 1.4.	Astroid geometry . . . . .	5
Figure 1.5.	Magnetic Force Microscopy image of an antivortex located at the center of the astroid shaped nanomagnet . . . . .	6
Figure 1.6.	Micromagnetic simulations of a) Néel skyrmion, b) horseshoe and c) radial vortex . . . . .	6
Figure 1.7.	Schematic drawing of the Magnetization dynamics driven by the Landau-Lifshitz-Gilbert-Slonczewski equation(precession, damping and spin torque terms) [1] . . . . .	8
Figure 1.8.	Schematic representation of anti-damping and field-like torques. a) In the case of anti-damping torque, absorption of the transverse part of the spin current rotates M towards the direction of m, and b) in field-like torque, M precesses about the exchange field created by m . . . . .	10
Figure 1.9.	Spin valve Structure . . . . .	11

Figure 1.10.	Typical temperature dependence of magnetic susceptibility for a) ferromagnets or ferrimagnets and b) antiferromagnets . . . . .	12
Figure 1.11.	a,b) STT on AFM through spin polarized current from FM layer c,d) SOT on AFM through pure spin current from normal metal [2].	13
Figure 2.1.	Calibration grating design drawing with Layout Editor software .	16
Figure 2.2.	Steps of calibration grating sample production a) Precleaning of Si substrate, vibration inside first acetone and then isopropanol, ends with N <sub>2</sub> blow dry. b) Resist coating with spin coater. After the coating of appropriate resists, the substrate is either c) exposed in a mask aligner under a photomask or d) directly exposed in a laser writer with UV light. Both options are followed by e) developing the resist by soaking it in a specific chemical and sample is ready for f) material deposition by magnetron sputtering, lastly g) Lift-off with acetone and cleaning any residue by vibrating inside isopropanol and blow drying with nitrogen gas. With this, substrate has only the calibration grating patterns left, ready for thickness measurement with profilometer . . . . .	17
Figure 2.3.	The calibration grating design, all dimensions given in micrometers. a) the part of an array, b) single pattern . . . . .	18
Figure 2.4.	Equipment for calibration process a) Bruker DektakXT Stylus Profiler b) Microtech Laser Writer LW405 . . . . .	18

Figure 2.5.	a) Spin coater in a filtered room of the clean room. Resist drops are applied to the center of the substrate while it is either spinning at low speed or not spinning at all. The substrate is then rotated at high speed to spread the resist by centrifugal force, and as a result it is coated. b) Microscope image of a calibration grating sample after we found the right parameters and successful developing. . . . .	19
Figure 2.6.	Vision64 software for DektakXT Stylus Profiler which is equipped with a microscope. We choose a random set of calibration gratings from top, bottom and middle of the sample, we measure the section from the middle of the pattern . . . . .	20
Figure 2.7.	Measurement of a section with cursors after the levelling the data. The thickness is read with respect to the adjacent plateaus. . . . .	21
Figure 2.8.	Optical microscopy image of contact pads over bow tie pattern before deposition . . . . .	24
Figure 2.9.	Sample mounted onto the resistivity option puck with GE varnish, before it is wirebonded to the corresponding channels such as 2V+, 2V . . . . .	25
Figure 2.10.	The calculation variables given on a schematic trapezoid . . . . .	25
Figure 2.11.	Bow tie resistivity measurement sample of Ta after it is wire bonded to PPMS puck and connected to the rest of the circuit . . . . .	27
Figure 2.12.	Resistivity versus temperature graph for a) 4 samples of 100 nm Ti, 15 nm ion milled before contact deposition b) 3 samples of 100 nm Ti, 3 nm ion milled before contact deposition . . . . .	28

Figure 2.13. Resistivity versus temperature graph for 4 samples of 50 nm Cu . . . . .	28
Figure 2.14. Resistivity versus temperature graph for 3 samples of 50 nm IrMn . . . . .	29
Figure 2.15. Resistivity versus temperature graph for 2 samples of 100 nm Ta . . . . .	29
Figure 2.16. Moment versus field procedure for VSM measurement on DynaCool MultiVU software by Quantum Design . . . . .	31
Figure 2.17. PPMS SQUID sequence for magnetization versus magnetic field (hysteresis) measurement . . . . .	32
Figure 2.18. Effect of HF on a) coercivity and b) exchange bias field . . . . .	34
Figure 2.19. Hysteresis loops, magnetization vs magnetic field graphs for a,b,c) HF spun samples and d,e,f) not HF spun samples given for both FC and ZFC conditions at a,d) 8 K, b,e) 50 K and c,f) 100 K. . . . .	35
Figure 2.20. Hysteresis loops, magnetization vs magnetic field graphs for a-d) HF spun samples and e,h) not HF spun samples given for both FC and ZFC conditions at a,e) 150 K, b,f) 200 K, c,g) 250 K and d,h) 300 K . . . . .	36
Figure 2.21. Magnetization vs Magnetic Field graph for HF spinned sample at all temperatures with a) FC and b) ZFC . . . . .	37
Figure 2.22. Temperature dependence of a) coercivity and b) exchange bias field and the shift for HF spun samples with ZFC and FC for all tem- peratures . . . . .	37

Figure 2.23. Photoemission process of atoms. A visual representation of Equation 2.7. . . . .	39
Figure 2.24. Energy diagram of photoemission process from 2s and 2p orbitals .	40
Figure 2.25. Bruker Dimension Edge Atomic Force Microscopy [3] . . . . .	43
Figure 2.26. Atomic force microscopy diagram . . . . .	44
Figure 2.27. Atomic force microscopy surface roughness measurement of silicon dioxide thin film coated on silicon substrate. Surface RMS roughness is 0.73 nm . . . . .	45
Figure 2.28. Attractive and repulsive interactions [4] . . . . .	47
Figure 2.29. Scanning electron microscopy image of a magnetic tip [4] . . . . .	48
Figure 2.30. Schematic drawing and AFM measurement of tip-sample convolution artifact . . . . .	49
Figure 2.31. MFM images taken with a clean (on the left) and dirty (on the right) tip [5]. . . . .	49
Figure 2.32. MFM images taken with a new (on the left) and broken (on the right) tip [6]. . . . .	50
Figure 2.33. MFM image of laser interference artifact [6]. . . . .	50
Figure 2.34. MFM image of flying tip artifact [6]. . . . .	51

Figure 2.35.	MFM image of radial vortices a) height sensor and b) tapping phase scan. . . . .	52
Figure 3.1.	Fabrication of silicon ingot with Czochralski method which later on will be sliced with chemical mechanical saw and polished to make wafers. a) Melting of polysilicon and doping, b) introduction of the seed crystal, c) beginning of the crystal growth, d) crystal pulling, e) formed crystal with a residue of melted silicon . . . . .	54
Figure 3.2.	DAD-320 Dicing Saw by Disco . . . . .	55
Figure 3.3.	Dicer keyboard . . . . .	55
Figure 3.4.	Wafer chip mounted on UV sensitive tape, ready to be diced . . .	56
Figure 3.5.	Precision Diamond Scriber model SV-129 by ATV Tech . . . . .	57
Figure 3.6.	Spin coater keyboard . . . . .	58
Figure 3.7.	Midas Mask Aligner in the yellow room of SUNUM clean room . .	60
Figure 3.8.	A typical lift-off process. a) Clean substrate, b) resist coated substrate, c) developed resist after exposure, d) material deposited on top of the resist and the pattern, e) remaining resist dissolving in acetone, f) patterned substrate . . . . .	62
Figure 3.9.	A typical etching process, the steps between c and d differ depending on the pattern that needs to be produced. a) Clean substrate, b) full film deposited substrate, c) resist coated on top of the film, d) developed resist after exposure, e) material etched, f) remaining resist dissolving in acetone, g) patterned substrate . . . . .	63

Figure 3.10.	Layout Editor drawing of the 5" mask with grids . . . . .	65
Figure 3.11.	Nanopillar process diagram . . . . .	67
Figure 3.12.	TORR International e-beam & thermal evaporator . . . . .	69
Figure 3.13.	Main switch of the e-beam evaporator . . . . .	70
Figure 3.14.	E-beam evaporator a) pocket and b) sample holder . . . . .	70
Figure 3.15.	Hall bar design, drawn in Layout Editor, all dimensions in micrometers . . . . .	71
Figure 3.16.	Hall bar contact designs a) first type: simple and dense wirebonder only contact pads, b) second type: contains everything in the first design and the probe pads for Hall voltage measurement, c) third type: everything in the first design and the probe pads for 4-probe electroresistance measurement, all dimensions in micrometers . . . . .	72
Figure 3.17.	Hall bar regular chip design with dimensions of 2x2 cm <sup>2</sup> , four 1x1 cm <sup>2</sup> parts, each part containing 24 samples, drawn in Layout Editor. Alignment marks at the corners of every 1x1 piece, A and C labels are there to enable determination of the chip orientation . . . . .	73
Figure 3.18.	PPMS Electrical Transport Option sequence for temperature versus resistance measurement from 10 K to 350 K . . . . .	74
Figure 3.19.	a) Technical drawing of the part for modification of PPMS puck (dimensions given in millimeters) and b) in-plane chip carrier holder mounted on PPMS puck . . . . .	75

Figure 3.20.	Wirebonding equipment a) schematics of the wirebonder stage and 8-pin gold plated CERDIP (Ceramic Dual Inline Packages) chip carrier, b) chip carrier mounted on wirebonder stage with our custom made aluminum stepping stage and c) Hall bar electrodes wirebonded to chip carrier gold pads under the microscope . . . . .	76
Figure 4.1.	Micromagnetic simulations of a) AC demagnetized state, b) -10 mT magnetic applied field at $135^\circ$ . Local magnetic moments are mapped by blue and red arrows [7]. . . . .	77
Figure 4.2.	Experimental setup for the anisotropic magnetoresistance measurements. a) Schematic drawing of the probe station design, b) sample and probes mounted onto the manufactured station of GMW electromagnet. . . . .	79
Figure 4.3.	Circuitry of the AC measurement setup . . . . .	79
Figure 4.4.	Energy Dispersive X-Ray Spectroscopy measurement performed on 20 nm $\text{Ni}_{81}\text{Fe}_{19}$ thin film and the calculated percentages of resulting elements. . . . .	81
Figure 4.5.	Vibrating Sample Magnetometer measurement of 20 nm $\text{Ni}_{81}\text{Fe}_{19}$ thin film, a) magnetic hysteresis at room temperature and b) saturation magnetization vs temperature measured at 1 T external field . . . . .	82
Figure 4.6.	Dimensions of the astroid shaped nanomagnet design . . . . .	83

Figure 4.7.	Fabrication of astroid shaped nanomagnets, a) cleaning Si substrate in acetone and isopropanol, b) spincoating EBL resist, c) e-beam exposure and development, d) deposition of permalloy by magnetron sputtering, and e) lift-off . . . . .	84
Figure 4.8.	Atomic force microscopy images of astroid shaped nanomagnets, EBL dose test with a) $400 \mu\text{C}/\text{cm}^2$ , b) $500 \mu\text{C}/\text{cm}^2$ , c) $600 \mu\text{C}/\text{cm}^2$ and d) $650 \mu\text{C}/\text{cm}^2$ exposure doses. . . . .	84
Figure 4.9.	Scanning electron microscopy (SEM) images of $2 \times 2 \mu\text{m}^2$ Py astroid devices. a) Measured dimensions of a fabricated astroid device and b) astroid devices with lift off problems. . . . .	85
Figure 4.10.	Atomic force microscopy images of fabricated astroid samples a) without contacts and b) with contacts. . . . .	86
Figure 4.11.	MFM images of astroid devices after application of a) AC demagnetization, b) 1 T out of plane magnetic field, c-d) 10 mT in plane magnetic field applied in the specified directions. . . . .	87
Figure 4.12.	Layout Editor drawing for the astroid photomask, including contact pads compatible with both RF probes and wirebonding for our electrical measurements. . . . .	87
Figure 4.13.	AMR measurement of 30 nm thick astroid device. Positive field values correspond to the applied field parallel to the current direction, and negative field values correspond to field applied antiparallel to the current. Red and green data points are for decreasing and increasing in plane parallel field, respectively. . . . .	88
Figure 4.14.	Dimensions of the reduced astroid design on Layout Editor drawing	89

Figure 4.15. Scanning electron microscopy image of the new designed geometry and the contact pads . . . . .	89
Figure 4.16. Resistance vs perpendicular magnetic field measurements taken at a) 10 K, b) 50 K, c) 200 K and d) 300 K . . . . .	91
Figure 4.17. Resistance vs parallel magnetic field measurements taken at a) 10 K, b) 50 K, c) 200 K and d) 300 K . . . . .	92
Figure 5.1. a) 60 repeat continuous film, sample 60C, b) 15 repeat partially patterned, sample 15PP-A c) 15 repeat fully patterned, sample 15FP-AI. . . . .	96
Figure 5.2. BLS measurements of the full film samples . . . . .	97

Figure 5.3. In-plane external field VSM, XRD , MFM and SEM measurements. a) Room temperature VSM measurements with in-plane external magnetic field for samples 15C (red dash-dotted line), 15C-AI (brown-red solid line) and 60C (purple dashed line). The inset shows the zoomed in version for sample 15C-AI, the only one showing hysteresis. The arrows indicate the field scan direction. b) XRD data for samples 15C-AI (orange solid line) and 60C (red dashed line) are shown along with Si/SiO<sub>2</sub> substrate data as background (blue solid line). The crystal orientations corresponding to the diffraction peaks are identified as being due to Pt [8] and Ti that gets progressively oxidized to TiO thin films suggesting a strong <111> texture. For reference JCPDS card data of TiO is included<sup>20</sup>. c-d) MFM images of sample 15C-AI after saturation with 1 T in-plane field, (c) at remanence, (d) under 20 mT in-plane field applied along the direction indicated by the arrow. e-g) Scanning Electron Microscopy (SEM) images of nano disk with various diameters, e) 300 nm f) 500 nm and g) 1200 nm. . . . . 100

Figure 5.4. Room temperature VSM measurements with out-of-plane external magnetic field for samples 15C-AI (brown-red solid line) and 60C (purple solid line). The inset shows the zoomed in version for sample 15C-AI, showing the hard axis loop . . . . . 101

Figure 5.5. Custom-made in plane magnetic field stage for in situ magnetic field application during MFM measurements, a) schematic drawing and b) machined stage and screw. . . . . 101

- Figure 5.6. MFM images of a set of three 300 nm diameter disks from sample type 15FP-AI. The measurement was done after the field conditioning (-4 T out-of-plane field following an AC demagnetization process with a maximum 1 T in-plane field). MFM images taken under a) zero field, b) -13 mT, c) zero field after the application of -25 mT and d) 13 mT in-plane field . . . . . 102
- Figure 5.7. MFM images of a single array of 300 nm diameter disks sample type 15FP-AI . . . . . 103
- Figure 5.8. MFM images of disk arrays for 15PP-A (a-b) and 15FP-AI (c-d) samples taken under no external field after in-plane AC demagnetization with 1 T maximum field and application of 3 T perpendicular-to-plane field. MFM images belong to arrays of disks with diameters a) 500 nm, c) 300 nm, b) and d) 1200 nm . . . . . 104
- Figure 5.9. MFM images of sample 60C after in-plane AC demagnetization with a maximum field of 1 T a) with no external field b) under 35 mT external perpendicular to plane magnetic field in the indicated direction. . . . . 105
- Figure 5.10. Micromagnetic simulation results obtained by using the experimental parameters indicate radially a) outward b) inward radial vortices. 106

- Figure 5.11. MFM images of 300 nm diameter disks sample type 15FP-AI under different conditions. a-b) 3 T out-of-plane field and c) -4 T out-of-plane field, both following an AC demagnetization process with a maximum 1 T in-plane field. The response to the external field is highlighted such that an upward or downward motion is indicated by triangles, appearance of the dots in disks after field application is denoted by a – sign. c) Motion under different in-plane magnetic fields. Relative displacement versus applied in-plane field . . . . . 107
- Figure 5.12. Overlaid XPS spectra of continuous Ti films, deposited at a) 20°C and b) 60°C. Dotted and bold lines correspond to Ti 2p peaks of metallic titanium and titanium monoxide, respectively. . . . . 110
- Figure 6.1. Coercivity(red), Exchange bias (blue) vs IrMn<sub>3</sub> thickness at 10 K . 113
- Figure 6.2. Magnetization vs field measurements at a) 10 K and b) 200 K for 1 nm IrMn<sub>3</sub> . . . . . 114
- Figure 6.3. Magnetization vs field measurements at a) 10 K and b) 200 K for 1.5 nm IrMn<sub>3</sub> . . . . . 114
- Figure 6.4. Magnetization vs field measurements at a) 10 K, b) 200 K and c) 300 K for 2 nm IrMn<sub>3</sub> . . . . . 115
- Figure 6.5. Magnetization vs field measurements at a) 10 K, b) 200 K and c) 300 K for 3 nm IrMn<sub>3</sub> . . . . . 116
- Figure 6.6. X-Ray diffraction measurement of MgO/IrMn<sub>3</sub>(3 nm)/Pt(2 nm)/Ti (3 nm) . . . . . 118

Figure 6.7.	X-Ray photoelectron spectroscopy of MgO/IrMn <sub>3</sub> (3 nm)/Pt(2 nm)/Ti(3 nm) . . . . .	118
Figure 6.8.	Transmission electron microscopy (TEM) of MgO/IrMn <sub>3</sub> (3 nm)/Au(200 nm) . . . . .	119
Figure 6.9.	Resistance vs Magnetic Field for 1 mA (black), 2 mA (red), 3 mA (green), 5 mA (blue) applied current for the sample MgO/IrMn <sub>3</sub> (3 nm)/Py(2 nm)/Ti(2 nm). . . . .	120
Figure 6.10.	Exchange bias field vs current (parallel current direction o the field cooling direction (black), perpendicular current direction to the field cooling direction (red) of MgO/IrMn <sub>3</sub> (3nm)/Py(2 nm)/Ti(2nm)	121
Figure 6.11.	Resistance vs Current of MgO/IrMn <sub>3</sub> (3nm)/Py(2 nm)/Ti(2nm) . . . . .	122
Figure 6.12.	Resistance vs Temperature of MgO/IrMn <sub>3</sub> (3nm)/Py(2 nm)/Ti(2nm)	123
Figure 6.13.	Resistance vs Temperature of Si/SiO <sub>2</sub> /Ti(5Å)/Pt(10 nm)/IrMn <sub>3</sub> (3 nm)/Ti(3 nm) . . . . .	125
Figure 6.14.	Resistance vs Temperature of Si/SiO <sub>2</sub> /Ti(5Å)/Pt(2 nm)/IrMn <sub>3</sub> (3 nm)/Ti(3 nm) . . . . .	126
Figure 6.15.	Resistance vs Temperature of MgO/IrMn <sub>3</sub> (3nm)Pt(2 nm)/Ti(3 nm)	127
Figure 6.16.	Resistance vs Temperature of MgO/IrMn <sub>3</sub> (3 nm)/W(2 nm)/Ti(3 nm) . . . . .	128
Figure 6.17.	Field cooling ( $H_C$ ) and applied current ( $I_{DC}$ ) directions, 1 T external field applied in one of the above three directions. . . . .	128

- Figure 6.18. R vs  $I_{DC}$  measurements for Si/SiO<sub>2</sub>/Ti (5 Å)/Pt (10 nm)/IrMn<sub>3</sub> (3 nm)/Ti (3 nm) at 10 K with zero external field. (Green curve shows parallel field cooling, red curve belongs to perpendicular field cooling.) . . . . . 129
- Figure 6.19. R vs  $I_{DC}$  for a) positive and b) negative current measurements for Si/SiO<sub>2</sub>/Ti(5Å)/Pt (2nm)/IrMn<sub>3</sub> (3 nm)/Ti (3 nm) at 10 K with zero external field. (Green, red and blue curves show parallel, perpendicular and out of plane field cooling directions respectively.) 130
- Figure 6.20. R vs  $I_{DC}$  for positive current measurements for MgO/IrMn<sub>3</sub> (3 nm)/Pt (2 nm)/Ti (3 nm) at 10 K with zero external field. (Green, red and blue curves show parallel, perpendicular and out of plane field cooling directions respectively for a) 1 T, b) 3 T and c) 7 T field cooling magnetic field value.) . . . . . 131
- Figure 6.21. R vs  $I_{DC}$  for negative current measurements for MgO/IrMn<sub>3</sub>(3 nm)/Pt(2nm)/Ti(3nm) at 10 K with zero external field. (Green, red and blue curves show parallel, perpendicular and out of plane field cooling directions respectively for a) 1 T, b) 3 T and c) 7 T field cooling magnetic field value.) . . . . . 132
- Figure 6.22. R vs  $I_{DC}$  (positive left, negative current right) measurements for MgO/IrMn<sub>3</sub>(3nm)/W(2 nm)/Ti(3 nm) at 10 K with zero external field. black and red curves show parallel, perpendicular and out of plane field cooling directions respectively, for 1 T field cooling magnetic value.) . . . . . 133

Figure 6.23. R vs $I_{DC}$ ( positive left, negative current right ) measurements for MgO/5x[IrMn <sub>3</sub> (3nm)/W(2 nm)]/Ti(3 nm) at 10 K with zero external field. (Green, red and blue curves show parallel, perpendicular field cooling directions respectively, for 1 T field cooling magnetic value.) . . . . .	134
Figure A.1. Schematic drawing of three terminal device . . . . .	150
Figure A.2. Layout Editor drawing of three terminal device design . . . . .	151
Figure A.3. Optical microscopy images of the three terminal device after the developing omnicoat/PMMA/HSQ resist combination, a) magnified 5 times, b) magnified 20 times. . . . .	152
Figure A.4. Optical microscopy image of the sample after Au deposition and lift off . . . . .	153
Figure A.5. Optical microscopy images after isolating the device, a) magnified 20 times, b) magnified 50 times. . . . .	153
Figure A.6. Optical microscopy image after defining 30x30 $\mu\text{m}$ device area . . . . .	154
Figure A.7. Optical microscopy image after MgO deposition and lift off . . . . .	155
Figure A.8. The final state of the three terminal device . . . . .	155

## LIST OF TABLES

Table 2.1.	Typical Deposition rates of materials for different power values . . .	22
Table 2.2.	Typical Mill rates of materials for standard ion mill parameters of system . . . . .	23
Table 2.3.	Resistivity values of materials at room temperature . . . . .	30
Table 4.1.	EBL parameters for the first set of astroid devices . . . . .	85
Table 5.1.	Production parameters and measurement techniques for individual samples . . . . .	96
Table 5.2.	Percentage values of oxidation states of titanium in thin films deposited at 20°C and 60°C. Residual amounts of Ti(III) and Ti(IV) states are not listed here. . . . .	103
Table A.1.	Deposition rates of the three terminal device materials . . . . .	150
Table A.2.	Ion milling rates of the three terminal device materials . . . . .	151

## LIST OF SYMBOLS

$D$	Interfacial Dzyaloshinskii-Moriya interaction strength
$E_b$	Binding energy of the excited photoelectron
$E_k$	Kinetic energy
$H_a$	Anisotropy field
$H_{app}$	External applied magnetic field
$H_d$	Demagnetization field
$H_{eff}$	Effective magnetic field
$H_{ex}$	Exchange field
$h$	Planck's constant
$M$	Magnetization
$M_s$	Saturation magnetization
$r$	Distance between particles
$T_N$	Néel temperature
$Z$	Atomic number
$\alpha_G$	Gilbert damping parameter
$\gamma$	Gyromagnetic ratio
$\delta$	Resistance change
$\nu$	Photon frequency
$\tau_{AD}$	Antidamping torque
$\tau_{FL}$	Field-like torque
$\tau_{STT}$	Spin-transfer torque
$\Phi$	Work function
$\chi$	Magnetic susceptibility

**LIST OF ACRONYMS/ABBREVIATIONS**

AES	Auger Electron Spectroscopy
AFM	Antiferromagnet
AMR	Anisotropic Magnetoresistance
CMOS	Complementary Metal Oxide Semiconductor
DC	Direct Current
DMI	Dzyaloshinskii-Moriya Interaction
DMS	Dilute Magnetic Semiconductors
EDX	Energy-dispersive X-ray Spectroscopy
ESCA	Electron Spectroscopy for Chemical Analysis
FC	Field Cooling
FMR	Ferromagnetic Resonance
FM	Ferromagnetic Material
GMR	Giant Magnetoresistance
HM	Heavy Metal
i-DMI	Interfacial Dzyaloshinskii-Moriya Interaction
IMFP	Inelastic Mean Free Path
JCPDS	Joint Committee on Powder Diffraction Standards
LL	Landau-Lifshitz
LLG	Landau-Lifshitz-Gilbert
LLGS	Landau-Lifshitz-Gilbert-Slonczewski
MFM	Magnetic Force Microscopy
MTJ	Magnetic Tunnel Junction
NIST	National Institute of Standards and Technology
NM	Normal Metal
PPMS	Physical Property Measurement System
RF	Radio Frequency
SEM	Scanning Electron Microscopy
SHE	Spin Hall Effect

SOC	Spin Orbit Coupling
SOT	Spin Orbit Torque
SQUID	Superconducting Quantum Interference Device
STT	Spin Transfer Torque
TAMR	Tunneling Anisotropic Magnetoresistance
TEM	Transmission Electron Microscopy
TMR	Tunneling Magnetoresistance
VSM	Vibrating Sample Magnetometer
XPS	X-ray Photoelectron spectroscopy
ZFC	Zero Field Cooling

# 1. INTRODUCTION

Magnetism has a long history dating back to ancient times. It had many applications in the past and still has great potential for future technology [9]. Magnetic materials can be classified as diamagnets, paramagnets, ferromagnets, ferrimagnets and antiferromagnets as whose spin configurations are as shown in Figure 1.1. Magnetism plays a significant role in spectacular physical phenomena in which spins of electrons may exhibit unique characteristic behaviour with external magnetic field.

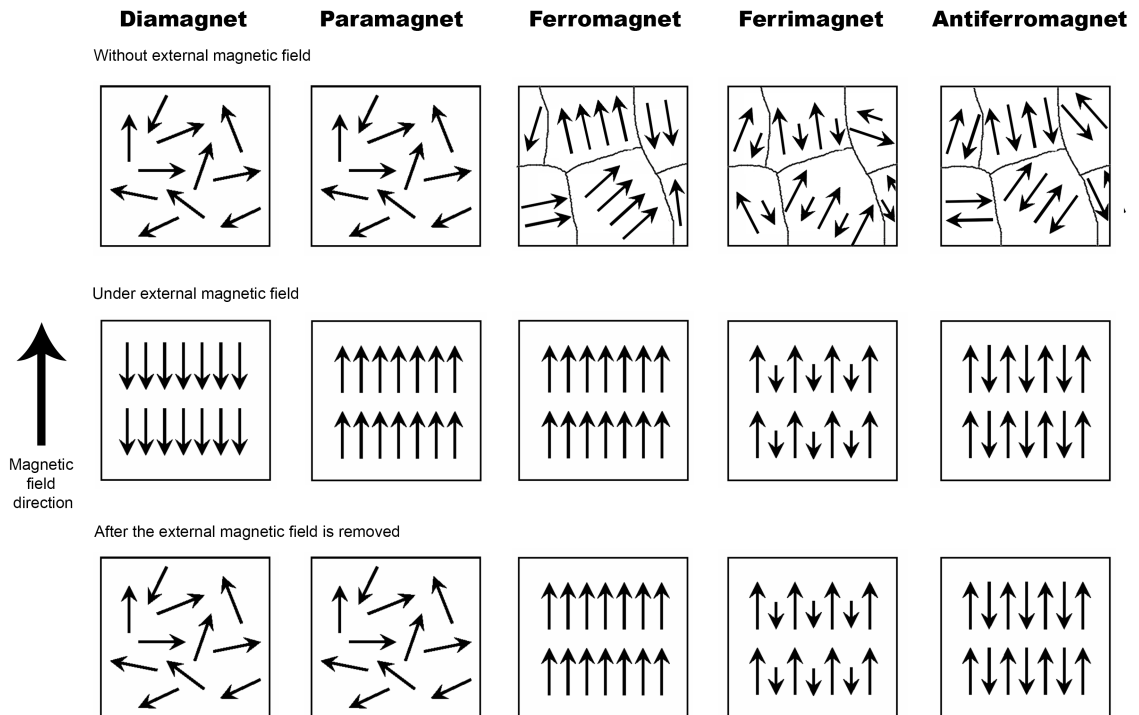


Figure 1.1. Spin orientation in magnetic materials

Origin of magnetism stems from orbital and spin angular moment of their mutual interactions. Heisenberg shown that Pauli exclusion principle is responsible for ferromagnetism in 1929 [10]. Ferromagnetic materials (FM) can display unusual behavior under applied external magnetic field or current which motivated their study over half a century. They are considered to be technologically essential materials for their potential spintronic applications such as magnetic sensor, detector and memory due to their nonvolatility and easy manipulation [11].

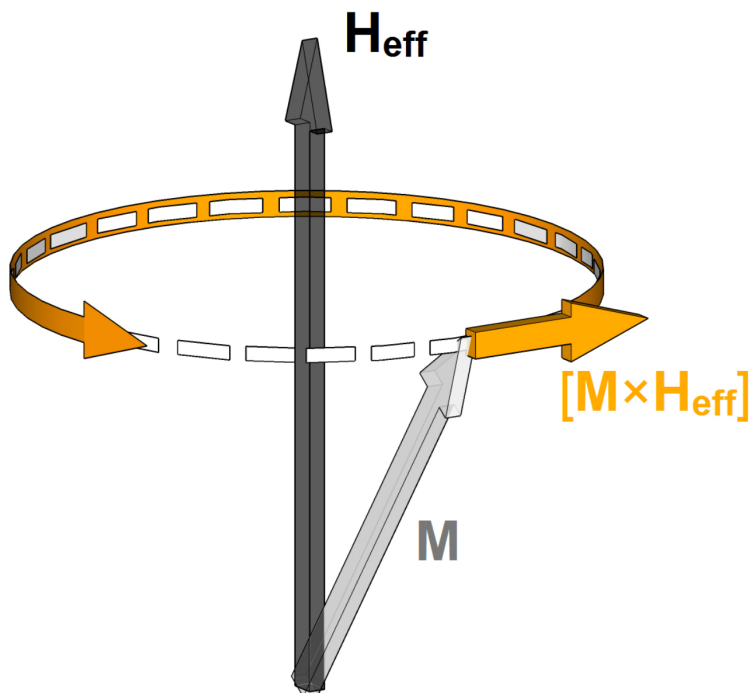


Figure 1.2. Schematic drawing of the Magnetization dynamics driven by the Landau-Lifshitz equation (precession term) [1]

### 1.1. Magnetization Dynamics LLG Equation

Today's data storage technology is far from satisfying the current requirements in terms of data storage capacity, scalability, write and read speeds etc. Therefore lots of research groups are still trying to build new data technologies with benefits such as less power consumption, high durability and compatibility with current complementary metal oxide semiconductor (CMOS) technology. For the spintronic applications, understanding spin dynamics is an essential ingredient. Traditional electronic applications utilize electronic properties of the electron, however spintronic based devices also utilize spin properties of the electron. With less consumption of power, spin information can be transferred from one point to another with or without charge transfer. Landau and Lifshitz proposed an equation to explain magnetization precession in 1935. Magnetization switching dynamics provide means for writing and reading the information in magnetic memory based applications [12]. Equation of motion for dynamics of

spin can be represented by the following Landau-Lifshitz (LL) equation:

$$\frac{d\vec{M}}{dt} = -\gamma(\vec{M} \times \vec{H}_{\text{eff}}) \quad (1.1)$$

where  $M$  is the magnetization (the magnetic moment per volume),  $\gamma$  is the gyromagnetic ratio and  $H_{\text{eff}}$  is the effective magnetic field which takes into account anisotropy ( $H_a$ ), demagnetization ( $H_d$ ), exchange ( $H_{ex}$ ) and external applied field ( $H_{app}$ ):

$$\vec{H}_{\text{eff}} = \vec{H}_a + \vec{H}_d + \vec{H}_{ex} + \vec{H}_{app}. \quad (1.2)$$

Landau-Lifshitz model assumed that total magnetic moment is related to the total angular momentum. Furthermore it experiences the net torque resulting in precessional motion [9]. As a result the magnetization vector precesses around the effective magnetic field as shown in Figure 1.2. But in reality magnetization precession magnitude gradually decreases with time and LL equation was modified by Gilbert in order to account for damping. When Gilbert damping parameter is introduced, magnetization vector follows the trajectory shown in Figure 1.3.

The LLG equation becomes:

$$\frac{d\vec{M}}{dt} = -|\gamma|\vec{M} \times \vec{H}_{\text{eff}} + \frac{\alpha_G}{M_s} \left( \vec{M} \times \frac{d\vec{M}}{dt} \right) \quad (1.3)$$

where  $\alpha_G$  is the Gilbert damping parameter and  $M_s$  is the saturation magnetization.

From experimental point of view one of the common techniques to study magnetization dynamics is ferromagnetic resonance (FMR). FMR can be defined as the collective dynamics of spins in ferromagnets where the magnitude of the spin wave amplitude is infinitely large under external magnetic field. Resonance occurs when the frequency of the external ac field matches with the precession frequency of magneti-

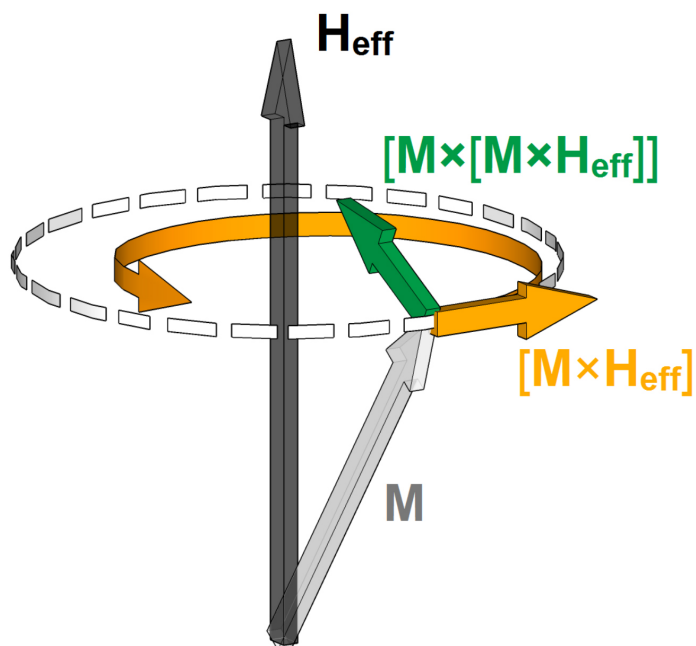


Figure 1.3. Schematic drawing of the Magnetization dynamics driven by the Landau-Liftshitz-Gilbert equation (precession, damping terms) [1]

zation in the ferromagnet [9]. This was first observed experimentally by Griffiths in 1946 [13].

## 1.2. Micromagnetic Structure and DMI

Magnetic configuration is affected by size, thickness and shape of thin films leading to different energy terms and material properties. This property enables manufacturing spintronic devices like magnetic memory elements, nano-RF-oscillators, detectors and magnetic sensors. They are soft magnetic materials which have weak magnetocrystalline anisotropy energy and therefore allow various configurations of magnetic microstructures when fabricated into small dimensions like a couple of microns or smaller (nano-magnets).

One such magnetization configuration called antivortex that has a core with out of plane polarization around which the magnetization curls away from the core. Such states have been shown to exist in larger films together with vortices (like in cross-tie

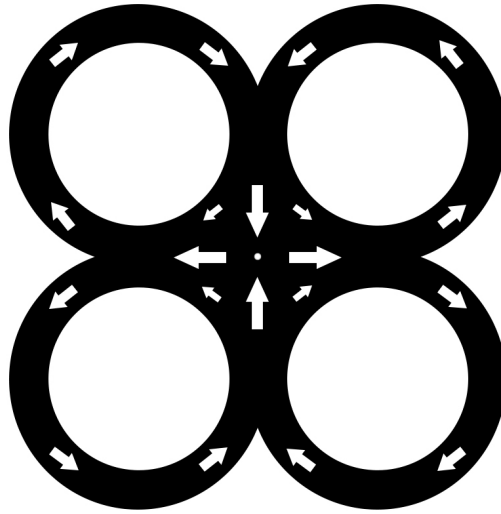


Figure 1.4. Astroid geometry

walls) but have been hard to isolate unlike vortices [14–16]. Antivortices form stray fields and therefore are difficult to stabilize. Several geometries, such as astroid shown in Figure 1.4, have been suggested to lead the flux lines so that an antivortex can be stabilized at the center of the film [7, 15, 16]. In Figure 1.5, magnetic force microscopy (MFM) image of an antivortex is shown at the center of an astroid, a double 8-like geometry which allows closure of magnetization lines and favors the formation of an antivortex at its center [7, 16]. Stabilizing the antivortex depends not only on the geometry but also on the production and post-production conditions [7, 15] and is a challenging task.

In this thesis, the first study was regarding the stability of antivortices at the center of patterned nanomagnets. The characteristics of antivortex formation are studied through micromagnetic simulations and after determining a suitable geometry, nanomagnets were manufactured using DC magnetron sputtering and lithography techniques.

Exchange interaction together with anisotropy in magnetic materials results in collinear spin alignments whereas with broken inversion symmetry, strong spin–orbit coupling at the interfaces of heavy metal (HM) and FM layers, the Dzyaloshinskii–Moriya interaction stabilizes helical magnetic order such as magnetic skyrmions, particle-like

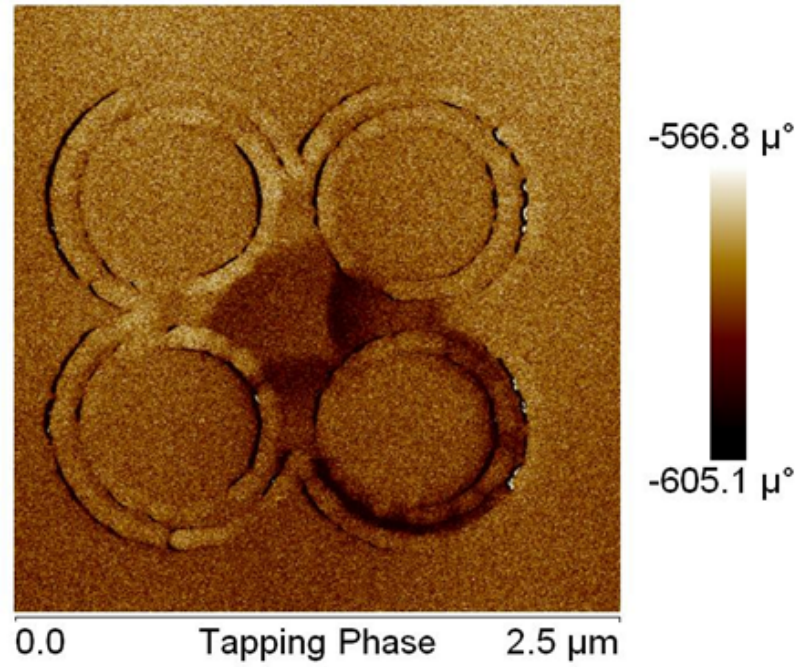


Figure 1.5. Magnetic Force Microscopy image of an antivortex located at the center of the astroid shaped nanomagnet

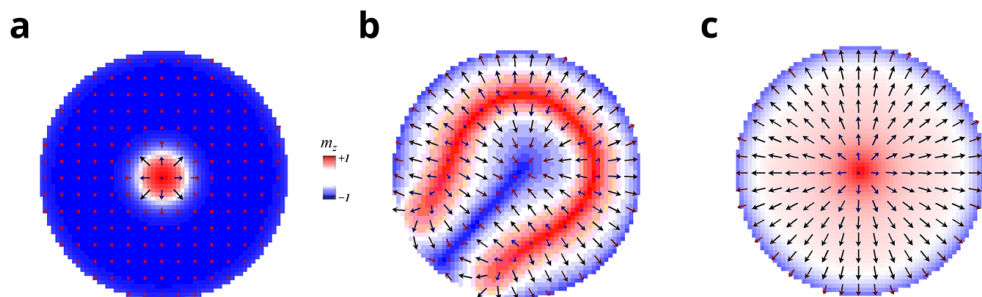


Figure 1.6. Micromagnetic simulations of a) Néel skyrmion, b) horseshoe and c) radial vortex

chiral spin textures that are topologically isolated and can be manipulated with relatively low current densities [17].

Bulk DMI arises as a result of lack of inversion symmetry in chiral magnets, whereas the interfacial DMI (i-DMI) stems from the interaction between ferromagnetic atoms and strong spin-orbit coupling (SOC) atoms of an adjacent heavy metal [18,19]. I-DMI strength is parameterized by a constant  $D$  and can be incorporated into the effective field in Landau-Lifshitz-Gilbert (LLG) equation competing with other energy terms such as exchange, anisotropy and magneto-static energies. The resulting micromagnetic configuration in systems with i-DMI can lead to a range of interesting canted spin orientations such as Néel skyrmions [20,21], horseshoes [21,22], spider-web domains and radial vortices [21,23]. These spin structures are demonstrated by simulations in Figure 1.6 and experimentally observed in 60 and 15 repeat multilayers of Pt(5)/Co<sub>20</sub>Fe<sub>60</sub>B<sub>20</sub>(1)/Ti(1) partially and fully patterned nanopillar disks (all thicknesses in nm). The disk diameter, i-DMI strength  $D$  and magnetic anisotropy play the prominent role in determining the resulting magnetic configuration.

As a second objective this project focuses on the effects of DMI at the surface of the nanomagnet by depositing a strong spin-orbit coupling heavy metal like Pt, W or Ta underneath the magnet. Effects are studied via direct observation of skyrmions at the surface. Understanding and therefore controlling the micromagnetic configurations in nanomagnets is a challenging task however it opens a window of opportunities in functional nanodevices. I aimed to shed light on the formation and functionality of nanomagnets having antivortices and skyrmions.

### 1.3. Magnetization Dynamics Driven by Spin Torque

In order to understand the dynamics of magnetic materials, in the presence of an electrical current we need to work with the final version of magnetization dynamics equation called Landau-Lifshitz-Gilbert-Slonczewski(LLGS) equation, schematically shown in Figure 1.7. The initial equation of Landau and Lifshitz predicted the precession motion of the magnetic moment under the effective magnetic field. The equation

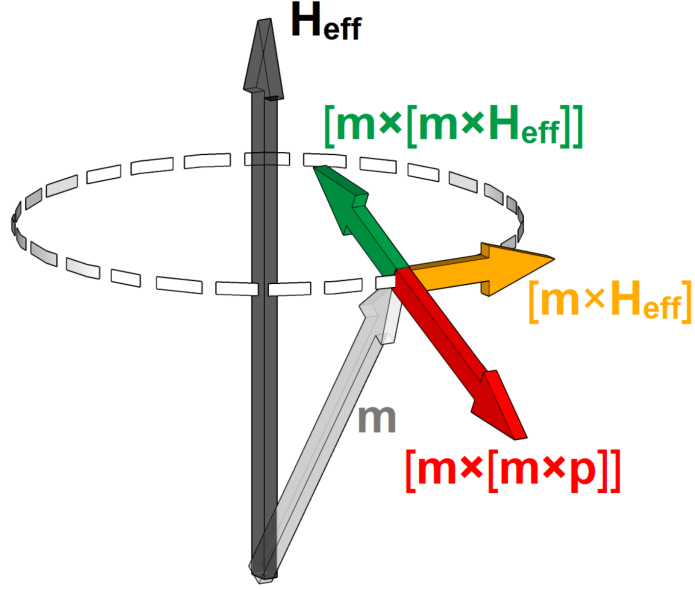


Figure 1.7. Schematic drawing of the Magnetization dynamics driven by the Landau-Lifshitz-Gilbert-Slonczewski equation (precession, damping and spin torque terms) [1]

was modified by Gilbert who added the term describing the damping, and finally the effect of the spin polarized current was added with the spin-transfer torque (STT) term by Slonczewski and Berger independently [24,25].

LLGS equation can be written in the following simplified form where  $\tau_{STT}$  is the term representing the spin-transfer torque.

$$\frac{d\vec{M}}{dt} = -\gamma \left( \vec{M} \times \vec{H}_{\text{eff}} \right) + \frac{\alpha_G}{M_s} \left( \vec{M} \times \frac{d\vec{M}}{dt} \right) + \vec{\tau}_{STT} \quad (1.4)$$

Spin-transfer torque has two contributions which can be defined as  $\tau_{FL}$  field-like and  $\tau_{DL}$  anti-damping torque:

$$\vec{\tau}_{STT} = \vec{\tau}_{FL} + \vec{\tau}_{AD} \quad (1.5)$$

$$\begin{aligned}\vec{\tau}_{FL} &= \vec{m} \times \vec{p} = \frac{d\vec{m}}{dt} \\ \vec{\tau}_{DL} &= \vec{m} \times (\vec{m} \times \vec{p}) = \frac{d\vec{m}}{dt}\end{aligned}\tag{1.6}$$

Whichever will dominate is determined by the spin-carrier lifetime of the material, whether the spin has enough time to precess around the local magnetic moments or not. If we have low spin-carrier lifetime, there is no or very little time for precession, resulting in the field-like torque,  $\vec{\tau}_{FL}$ , where spin polarization of the delocalized electrons acts as an effective field on the localized moments. If we have high spin-carrier lifetime, there is significant precession resulting in anti-damping torque,  $\vec{\tau}_{DL}$ , where the angular momentum of the polarized electron spin is transferred to and exerts a torque on the local magnetic magnetization [2]. Field-like STT can only cause precession of local magnetic moments whereas anti-damping STT might cause switching/flip of local moments or high frequency oscillation of magnetic moments. The direction of the spin polarization can be written in the following form.

$$\vec{p} = \vec{J}_e \times \vec{J}_s\tag{1.7}$$

Unlike the case with spin valves where the electrons are polarized through the fixed layer, this results in pure spin current which is expected to be more efficient, meaning less power consumption. The spin carrier lifetime is a material dependent parameter, but generally we observe anti-damping torque as dominant and field-like torque gives a small correction.

The physical phenomena which are the primary sources of action in our experiments are spin-orbit coupling (SOC), spin Hall effect (SHE) and spin-orbit torque (SOT). Spin-orbit coupling is a quantum mechanical effect due to the interaction between the electron's spin and the electromagnetic field generated by the electron's orbital motion. It allows us to manipulate the spin without the aid of a magnetic field, and it is especially strong in heavy metals as its strength goes by the forth power of atomic number,  $Z^4$ , which can be derived by a simplistic perturbation theory. SHE

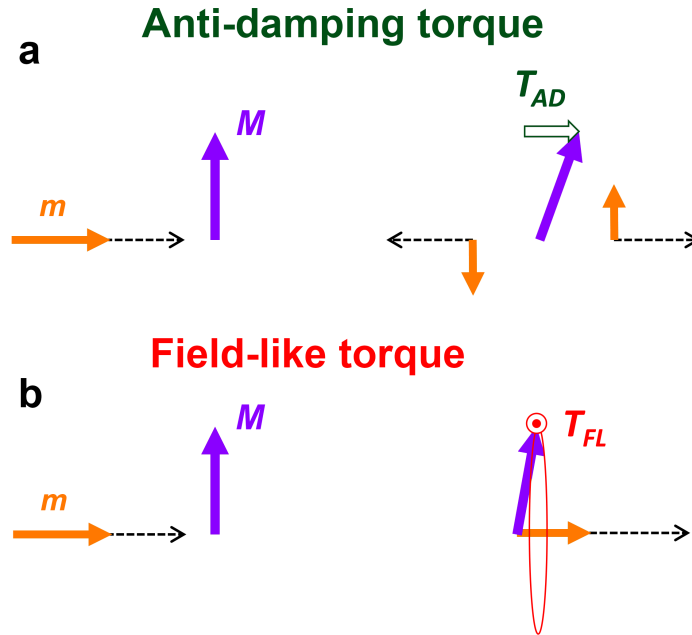


Figure 1.8. Schematic representation of anti-damping and field-like torques. a) In the case of anti-damping torque, absorption of the transverse part of the spin current rotates  $M$  towards the direction of  $m$ , and b) in field-like torque,  $M$  precesses about the exchange field created by  $m$

was predicted by two Russian physicists M.I. Dyakonov and V.I. Perel in 1971 [26]. It is analogous to classical Hall effect. However in this case an electric current generates a transverse spin current which leads to accumulation of spins of opposite signs. Just like STT in spin polarized charge current, such pure spin current can be utilized to manipulate magnetization via spin orbit torque. SHE is caused by high SOC and occurs without an external magnetic field.

Exciting vortex dynamics is possible via a spin polarized direct current (DC). This can be achieved by using a spin-valve structure as shown in Figure 1.9 in which a dc current injected through the first ferromagnet (permalloy,  $\text{Ni}_{81}\text{Fe}_{19}$ , in this case) becomes spin polarized depending on the direction of magnetization in the layer. This current then exerts a torque on the magnetization of the second layer [27]. Vortex dynamics triggered this way is not only due to the torque, but also due to magnetostatic interactions between the layers [28]. Vortex nucleation can be induced via a nanocontact in similar multilayer structures. In such a device spin polarized current

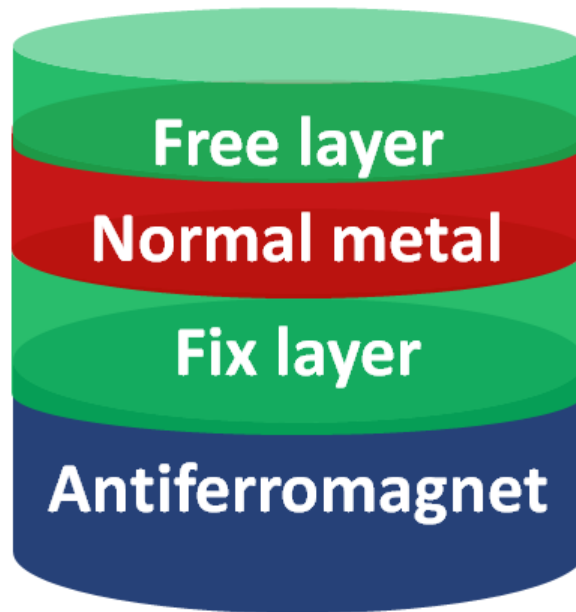


Figure 1.9. Spin valve Structure

is injected through nanocontact region(s) between the magnetic layer and the metallic layer above it instead of the whole area [27, 29, 30]. The application of a DC current through the device nucleates vortices near the nanocontact and excites high frequency oscillations of the vortex core [27].

#### 1.4. Antiferromagnets

Another class of materials potentially interesting for spintronics are antiferromagnets which have spontaneous magnetization of two sublattices with opposite directions below a critical temperature called Néel temperature,  $T_N$ . As a result, they have no net magnetization and act like paramagnets in the sense that their susceptibility is positive but very low, and it increases with temperature below Néel temperature and above Néel temperature they have a phase transition to paramagnetism [31].

Recently there has been a renewed interest in AFMs for potential use in spintronic devices. In the famous Nobel lecture by Néel, AFMs are called therotically interesting but useless. Indeed AFMs found limited application in magnetism up until now. They have been used to harden ferromagnetic layer, forming the fixed layer in spin valves by the interaction called exchange bias which was discovered by Meiklejohn and Bean in

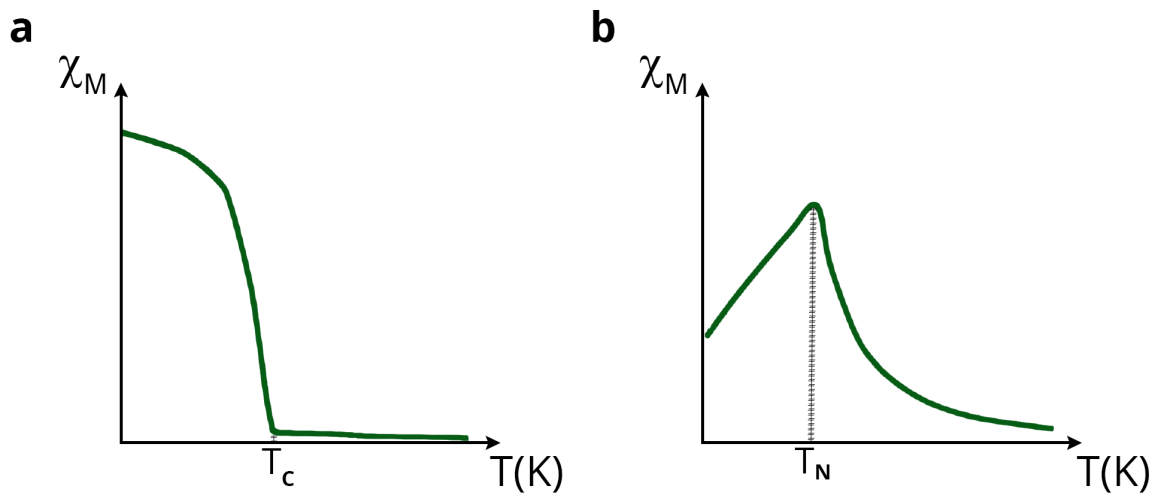


Figure 1.10. Typical temperature dependence of magnetic susceptibility for a) ferromagnets or ferrimagnets and b) antiferromagnets

General Electric Laboratories in 1956 [32]. In order to use AFMs spintronic devices, we need to be able to read and write. Just like FM spintronic devices, antiferromagnetic spintronic devices need giant magnetoresistance (GMR) or tunneling magnetoresistance (TMR) like effects to read and spin torque effects to write.

Unfortunately, STT originating from spin polarized current cannot be used to write AFM memory as it can be seen in Figure 2.26 with a calculation of torque directions in a FM/AFM bilayer system. The spin polarized current only flips the magnetization of AFM moments from parallel to perpendicular configuration once and they cannot be switched back by changing the current direction in either case of anti-damping or field-like torque being dominant. This is where the SOT originating from SHE comes into the story.

In addition to possible spintronic applications, there are other significant advantages of antiferromagnets over current ferromagnet based technology such as AFM's insensitivity to external magnetic perturbations thanks to their low susceptibility; and their potential for high density storage. This is possible due to their zero net magnetization which prevents any stray fields, there is no magnetic cross-talk between neighboring bits. AFMs also provide magnetic cloaking which means stored informa-

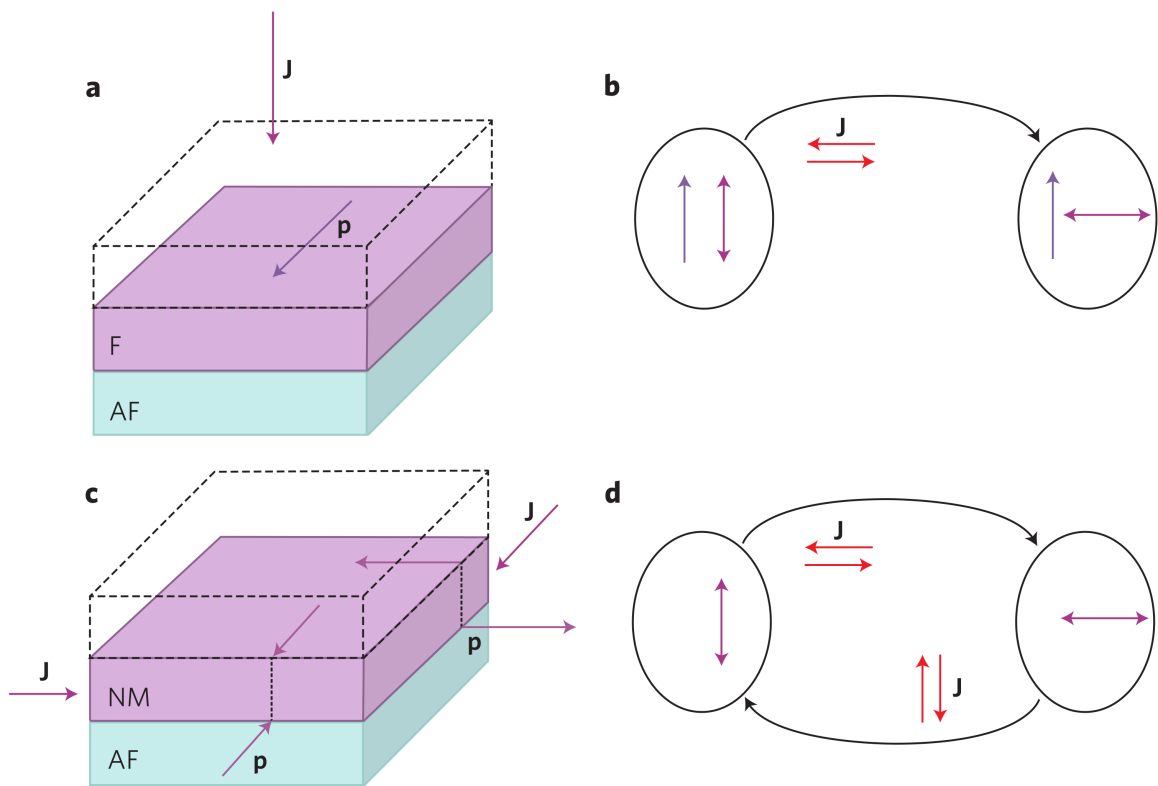


Figure 1.11. a,b) STT on AFM through spin polarized current from FM layer c,d) SOT on AFM through pure spin current from normal metal [2].

tion is invisible to magnetic probes and insensitive to common magnetic fields. AFMs have super radiation hardness allowing them to be used for space memory applications. It is theoretically predicted that they have equivalent responses/effects of GMR, STT, spin pumping, etc. Enabling the possibility of their usage as magnetic tunnel junction (MTJ) and spin valve devices.

AFMs could also provide intrinsic high frequency, on the order of terahertz, dynamics, which would enable the manipulation of motion of the charges on the femtosecond timescale, ultrafast control of the spin degree of freedom. THz dynamics also implies higher quality factor meaning sharp oscillations and less damping resulting in a lower rate of energy loss.

Characterization of the materials which we are going to use to fabricate the aforementioned devices is explained in Chapter 2. Different methods for patterning the thin films and manufacturing different types of devices are given in detail in Chapter 3. The study on the magnetic antivortices is given in Chapter 4. Several magnetic configurations from radial vortices to Néel skyrmions are thoroughly illustrated in Chapter 5. Lastly, the work on the antiferromagnets, especially (100) oriented  $\text{IrMn}_3$ , is described in Chapter 6. All in all, this thesis provides a perspective for future investigations on spintronics and antiferromagnetic spintronic.

## 2. MATERIAL CHARACTERIZATION

### 2.1. Thin Film Deposition

#### 2.1.1. Deposition Rate Calibration

We choose to lay the groundwork to experiments by characterizing the materials we use. In order to have precise control over the thicknesses of the materials, we devised a systematical procedure for the calibration of thin films. For this, we started by designing the specific samples called calibration grating. The purpose with this design is to directly measure the thickness of thin films so that we can produce devices in the exact thicknesses needed. Also the uniformity of the thin film has to be checked, so an array of approximately a hundred patterns used for calibration. As a result, calibration grating design is basically an array of the same pattern consisting of steps with different widths indicating how the deposition works with different features. The design of the samples are drawn on the software, Layout Editor shown Figure 2.1, that is generally used to create the input for the final lithography instrument that will write the pattern to the substrate.

After the design, the production process, shown in Figure 2.2 is followed. The design feature size is in micrometers, shown in Figure 2.3, photolithography precision suffices for calibration procedure. Lithography technique can be conducted by two ways either using a photomask along with a mask aligner or laser writer. A photomask is a fused quartz plate with chrome film on top allowing light to shine through in a defined pattern. It has 1:1 dimensions of the original design but it can be exactly the same or mirror image of the design according to the type of process, direct lithography or image reversal, respectively. Direct photolithography process, also called positive lithography, involves single exposure to the sample with the photomask and a single bake (pre-bake); the parts that come off when developed will be the places that had been exposed, open areas on the mask. On the other hand, for image reversal, also called negative lithography, there will be two exposures and two bakes (pre- and post-

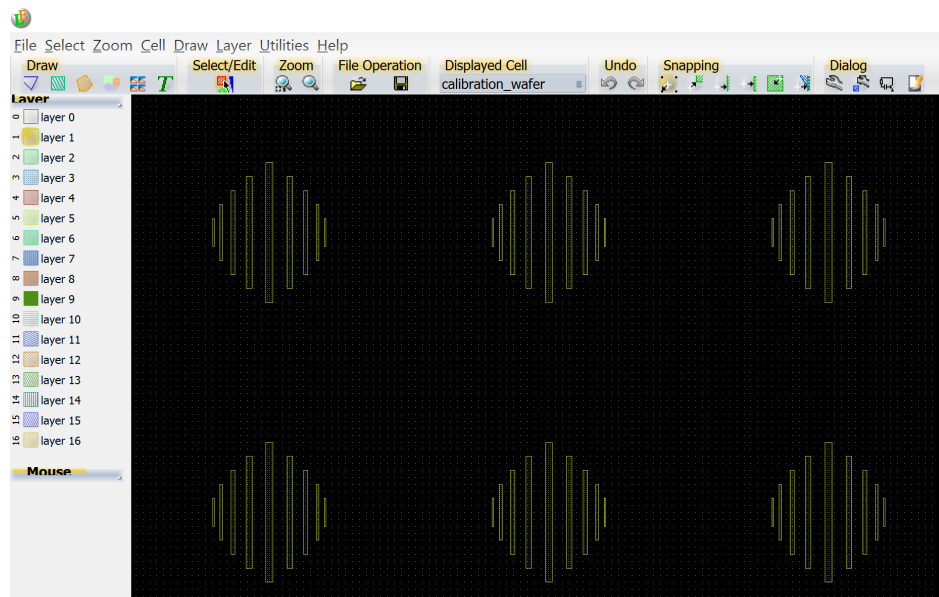


Figure 2.1. Calibration grating design drawing with Layout Editor software

bake). First one will be with the mask and the second exposure will be a flood exposure without a mask. As a result, the places that will come off will be the unexposed parts (chrome parts on the mask). Image reversal is a commonly used process and preferred to direct lithography as it provides sharper features.

The photomask provides as the base for pattern generation and it will be used in a mask aligner, under UV light in the photolithography step to write the patterns to the substrates. Another way is to use a laser writer shown in Figure 2.4b and directly write the pattern to the substrate. The resist coating, by spin coater shown in Figure 2.5a, and exposure procedures are the key points for pattern generation. After exposing and developing, shown in Figure 2.5b, the sample is ready for deposition.

As an example of direct photolithography process, AZ5214E photoresist is coated at 4000 rpm for 45 seconds and baked at 105 °C for 1 minute. The sample is exposed under mask for 4.5 seconds. After the exposure, developing the sample is followed by soaking it in AZ 726 MIF Developer for 35 seconds. DI water is used as a stopper for chemical reaction. In case of a patterning process with the laser writer, Shipley S1813 positive photoresist is used under 3000 rpm for 45 seconds and baked at 115 °C for 1 minute and then exposed. It is developed for 45 seconds in CD 26 and water is used.

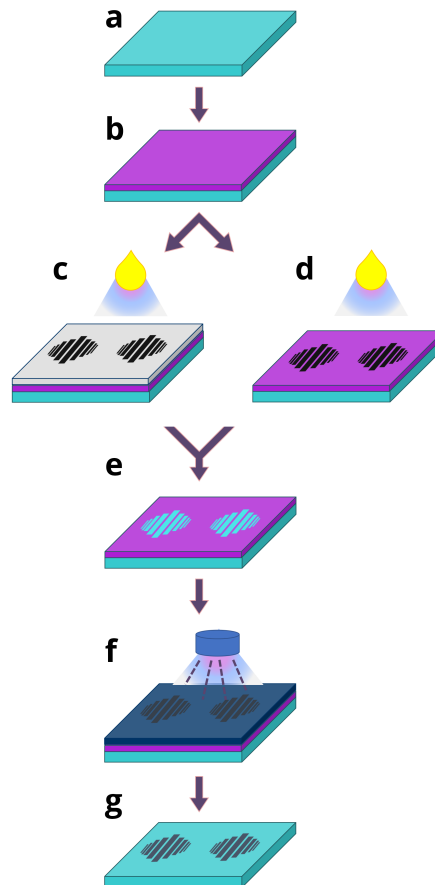


Figure 2.2. Steps of calibration grating sample production a) Precleaning of Si substrate, vibration inside first acetone and then isopropanol, ends with  $N_2$  blow dry. b) Resist coating with spin coater. After the coating of appropriate resists, the substrate is either c) exposed in a mask aligner under a photomask or d) directly exposed in a laser writer with UV light. Both options are followed by e) developing the resist by soaking it in a specific chemical and sample is ready for f) material deposition by magnetron sputtering, lastly g) Lift-off with acetone and cleaning any residue by vibrating inside isopropanol and blow drying with nitrogen gas. With this, substrate has only the calibration grating patterns left, ready for thickness measurement with profilometer

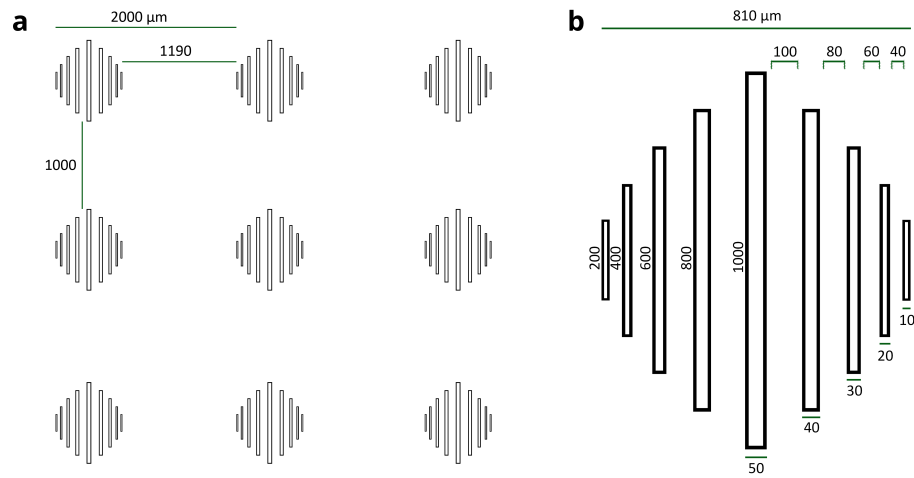


Figure 2.3. The calibration grating design, all dimensions given in micrometers. a) the part of an array, b) single pattern

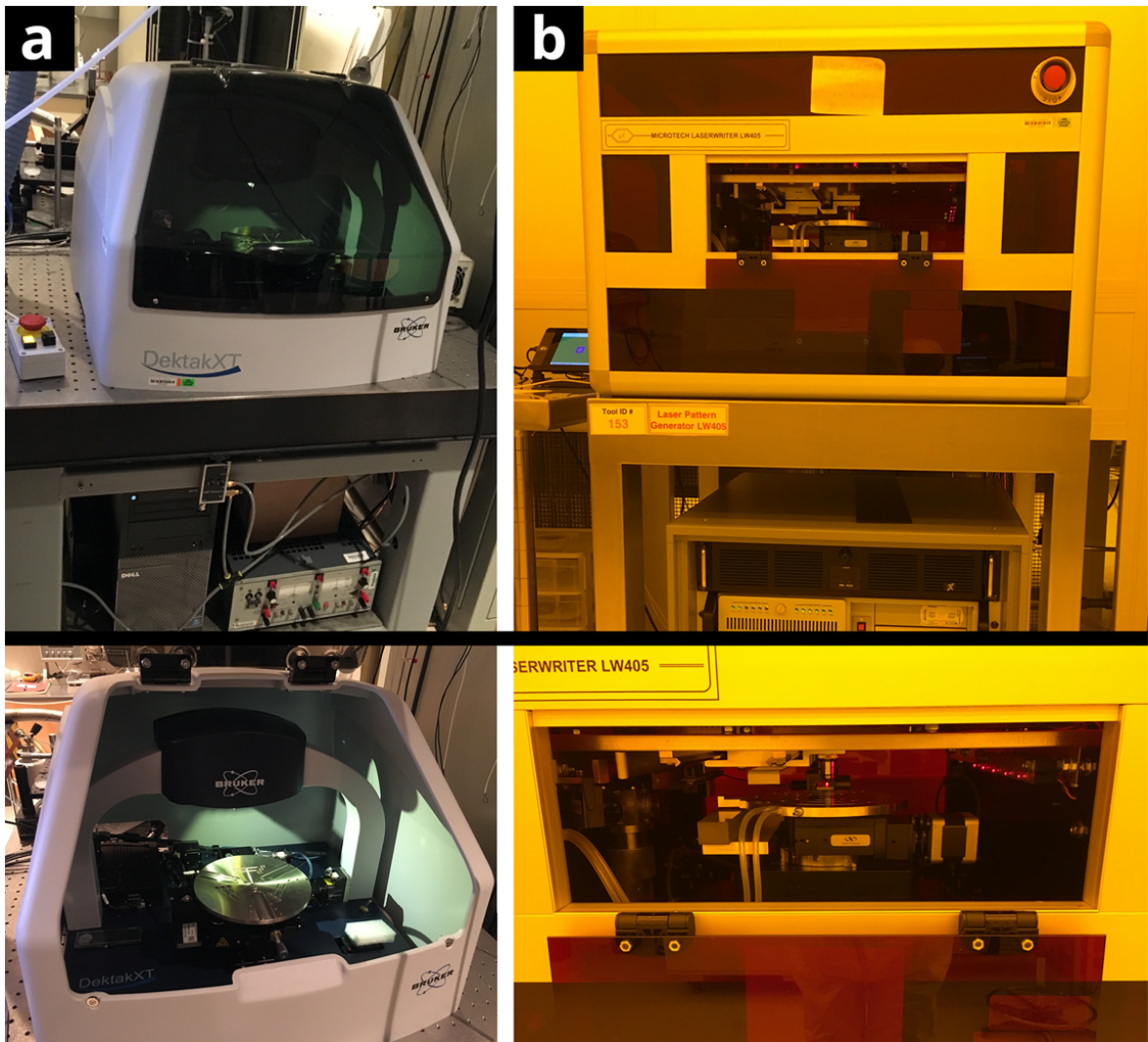


Figure 2.4. Equipment for calibration process a) Bruker DektakXT Stylus Profiler b) Microtech Laser Writer LW405

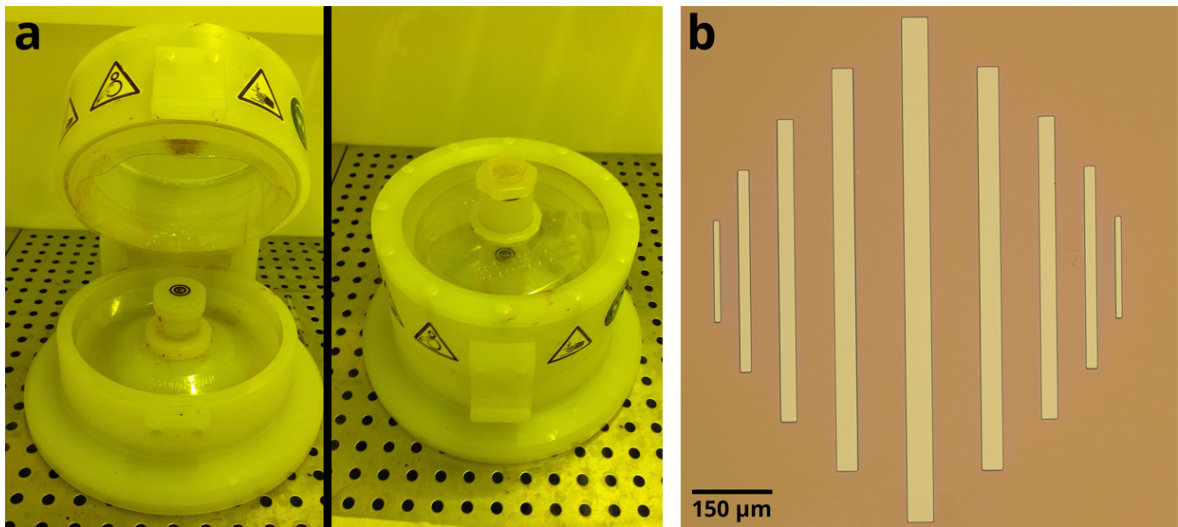


Figure 2.5. a) Spin coater in a filtered room of the clean room. Resist drops are applied to the center of the substrate while it is either spinning at low speed or not spinning at all. The substrate is then rotated at high speed to spread the resist by centrifugal force, and as a result it is coated. b) Microscope image of a calibration grating sample after we found the right parameters and successful developing.

Following the determination of proper exposure and spin coating, we proceed with the material deposition. Materials are deposited in AJA Sputtering system in Ar environment. Sputtering is a deposition process where particles are ejected from a solid material called target, due to bombardment of the target by energetic gas ions, in a vacuum chamber. This is possible with the generation of plasma state on top of the target material with the aid of DC voltage applied (AC voltage for insulators, RF sputtering) through the material. Ejected particles are deposited onto whole inner surface of the chamber and substrate.

The opposite of the sputter deposition process is the ion milling process where accelerated ions hit the surface of the substrate, hence etching away the material. Ion milling can be used as a way of cleaning the substrate surface or for patterning with different techniques as the etch rate differs from material to material like sputtering rates.

The optimal operation condition for the sputtering system is 2 mTorr Ar pressure,

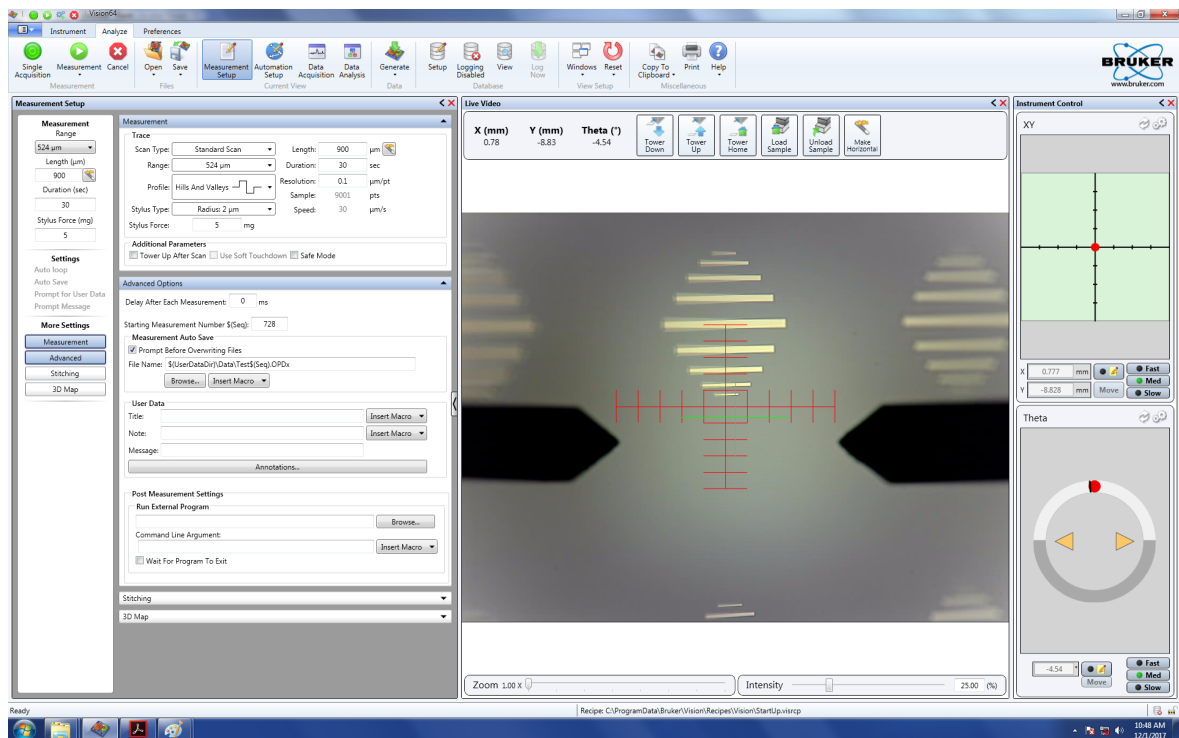


Figure 2.6. Vision64 software for DektakXT Stylus Profiler which is equipped with a microscope. We choose a random set of calibration gratings from top, bottom and middle of the sample, we measure the section from the middle of the pattern

$5 \times 10^{-8}$  Torr base pressure and 5 sccm gas flow rate. For the contact layer, Au is used. Conditioning is carried out for 5 minutes as the natural oxide layer on top of metals also influences the deposition rate and uniformity of thin film. Conditioning is done in the following way: before sputtering process power should be turned on, igniting the plasma, without opening the shutter for the required duration.

After deposition calibration, the sample is taken out from the vacuum chamber of system and put in acetone for the lift-off process. At this point sample is vibrated in ultrasonic bath with acetone and isopropanol respectively. If there is any resist residue after lift off process, oxygen plasma which etches organic materials can be used. As an alternative method for removing residue is to ion mill just before deposition inside vacuum chamber.

Thickness measurement for calibration grating is done by profilometer, shown in Figure 2.4a, an instrument to measure a surface's profile. It measures profile by moving

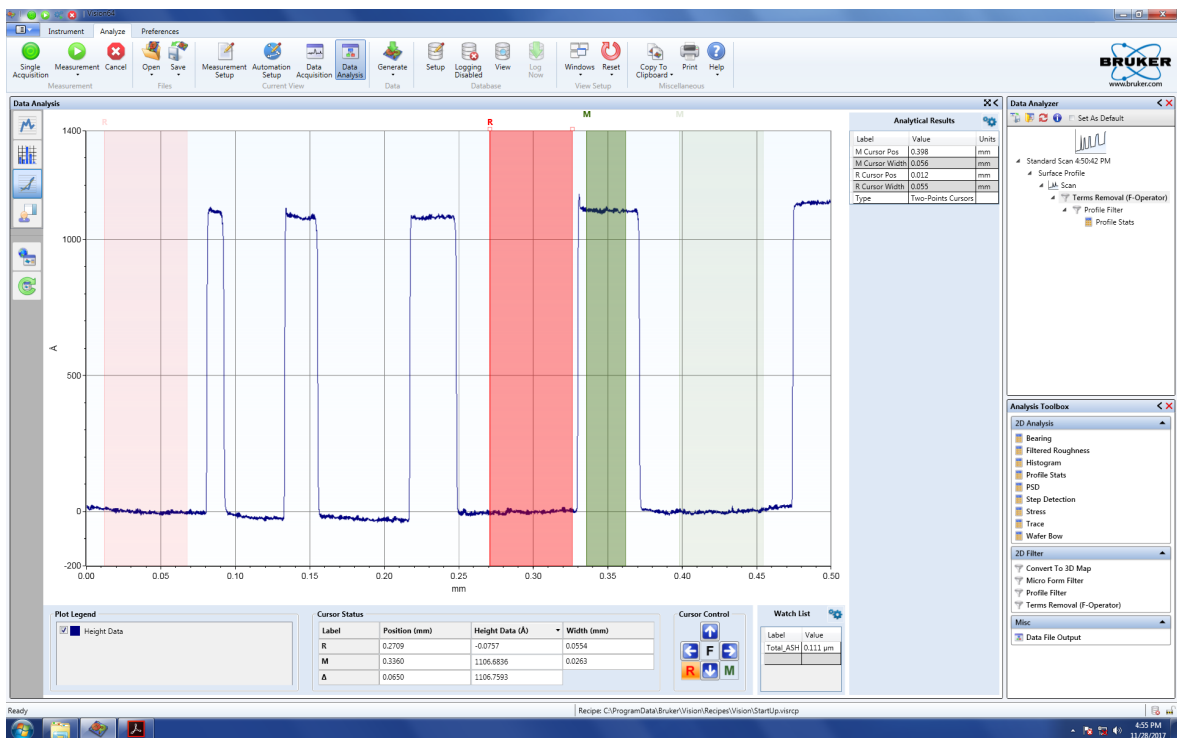


Figure 2.7. Measurement of a section with cursors after the levelling the data. The thickness is read with respect to the adjacent plateaus.

a stylus across the surface while making contact with it. The sample is placed onto chuck. The equipment is connected to a computer and Vision64 software is installed for DektakXT Stylus Profiler with an embedded microscope shown in Figure 2.6. Adjustment may be needed for the position of the sample to align the steps so that they will be perpendicular to the stylus scanning direction. Random set of calibration gratings from top, bottom and middle of the sample are scanned to figure out the uniformity of the film. The force applied by the stylus onto the surface and the speed with which it scans through the designated length according to the material may be adjusted to get accurate measurement result. As an example of profilometer is shown in Figure 2.7.

For thickness calibration AJA sputter system is used with typical power setting for sputter deposition about 100 Watts DC power sources. All sputtering processes are done with 5 sccm Ar flow rate and at 2 mTorr Ar pressure. The resulting deposition rates are given in the following Table 2.1.

Table 2.1. Typical Deposition rates of materials for different power values

Target	Pressure (mTorr)	Power (Watt)	Sputter Rate (Å/sec)
Ti	2	100	$0.343 \pm 0.01$
Ta	2	100	$0.703 \pm 0.01$
Ta	2	40	$0.251 \pm 0.01$
Pt	2	100	$1.074 \pm 0.01$
Au	2	80	$1.907 \pm 0.01$
Cu	2	50	$0.795 \pm 0.01$
Cu	2	20	$0.312 \pm 0.01$
IrMn	2	100	$1.004 \pm 0.01$
IrMn	2	50	$0.414 \pm 0.01$

### 2.1.2. Ion Milling Rate Calibration

For the calibration of ion mill rates, the following procedure is carried out. While sputtering the material for deposition calibration, we put another wafer full of calibration gratings beside the original one (or use a big wafer and cut the half of it after the deposition). After we are done with the calibration of deposition rates of all materials, we know the thickness of the material on the other wafer. We use this already deposited calibration gratings for ion mill calibration. We put it back into vacuum chamber and mill for a while according to an approximate rate. Then we take it out and again measure in the profilometer to determine how much of material was milled by measuring the new thickness and subtracting it from the first one. one should be note that the wafer ion mill calibration will still have photoresist on it, but the resist is very thick, on the order of 1 micrometer, so it does not affect the result even if some of it gets milled down. Most of the resist is still left which can be removed it with lift-off as in the case of the deposition calibration.

After deposition rates, ion milling rates of all materials are calibrated with typical milling parameters; 300 V beam voltage, 60 V accelerator voltage, 12 mA beam current at 2 mTorr Ar pressure. Silicone grease is used between wafers and sample stage for

Table 2.2. Typical Mill rates of materials for standard ion mill parameters of system

Target	Pressure (mTorr)	Beam Voltage (V)	Accelerator Voltage (V)	Beam Current (mA)	Ion Milling Etch Rate (A/sec)
Ti	2	300	60	12	$0.358 \pm 0.01$
Ta	2	300	60	12	$0.323 \pm 0.01$
Pt	2	300	60	12	$0.510 \pm 0.01$
Au	2	300	60	12	$0.524 \pm 0.01$
Cu	2	300	60	12	$0.351 \pm 0.03$
IrMn	2	300	60	12	$0.305 \pm 0.01$

better heat conduction and the milling is operated with shutter 30 open/ 30 closed seconds to prevent the resist from getting hard baked. After the sample is taken out of the chamber, the unpolished backside of the wafers is wiped with isopropanol to remove silicon grease. This is done so that thin film does not get contaminated with grease during lift off procedure. The resulting mill rates are given in the following Table 2.2.

## 2.2. Electrical Characterization

For experiments and simulations of devices, the electrical properties of materials should be characterized. Required procedure involves two lithography and two sputtering steps which consist of overlapping patterns with alignment marks, first bow tie and second the contact pads. The bow tie design is essentially a thin wire between two contact area as shown in Figure 2.8.

After sputtering the material the sample taken out for lift-off (vibrate the sample in acetone overnight and vibrate isopropanol and dry with nitrogen gas). then second aligned lithography is done for gold contact leads by aligned (Midas mask aligner) photolithography, by overlapping the matching patterns on each side of the sample. After the coarse alignment is done, we check the alignment marks around each bow tie pattern. Subsequently, we put the sample back into vacuum chamber 150 nm Au

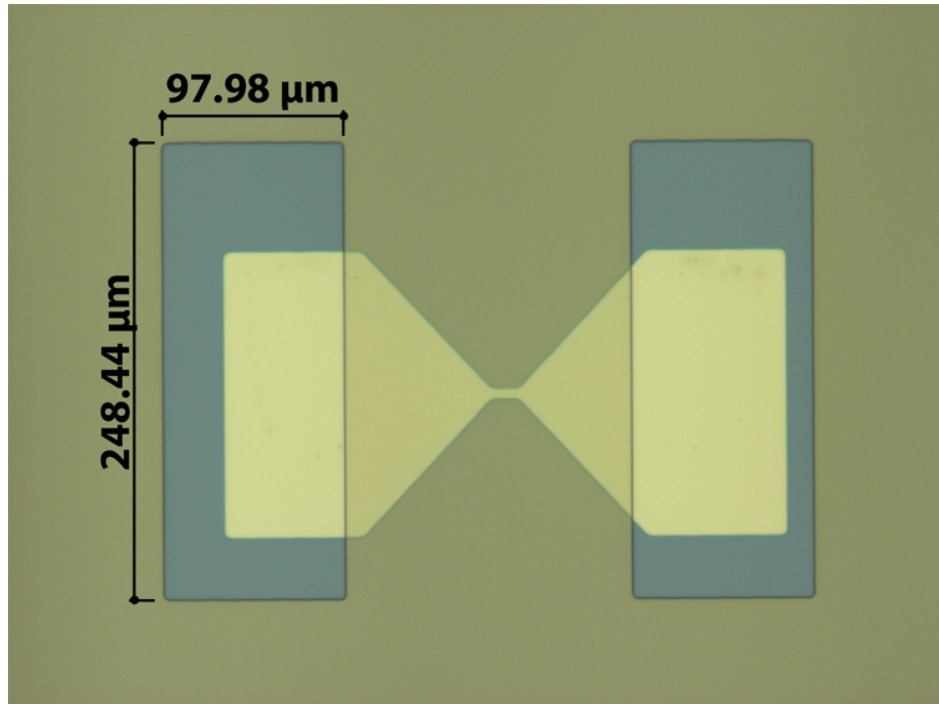


Figure 2.8. Optical microscopy image of contact pads over bow tie pattern before deposition

is sputtered for the contact pads and sample production is concluded after the second lift-off process.

Wafer piece is glued to resistivity option puck shown, in Figure 2.9, with GE varnish (a specific adhesive chemical commonly used in vacuum on a range of very high and very low temperatures; thinned with ethanol and toluene during application, takes at least a day to dry). The sample is connected to Physical Property Measurement System (PPMS) through LEMO cable connector. Sample is placed inside PPMS and the resistance measurement is done. Obtained data is analyzed; we calculate the resistivity of material after deriving the required formula with respect to the geometry shown in Figure 2.10 of samples.

Our sample is not an ordinary cylindrical wire, we cannot use the ordinary equation used for Ohm's law. So, we will use an integration implemented version of Pouillet's law. We start with ordinary resistance equation and derive the ones for our geometry

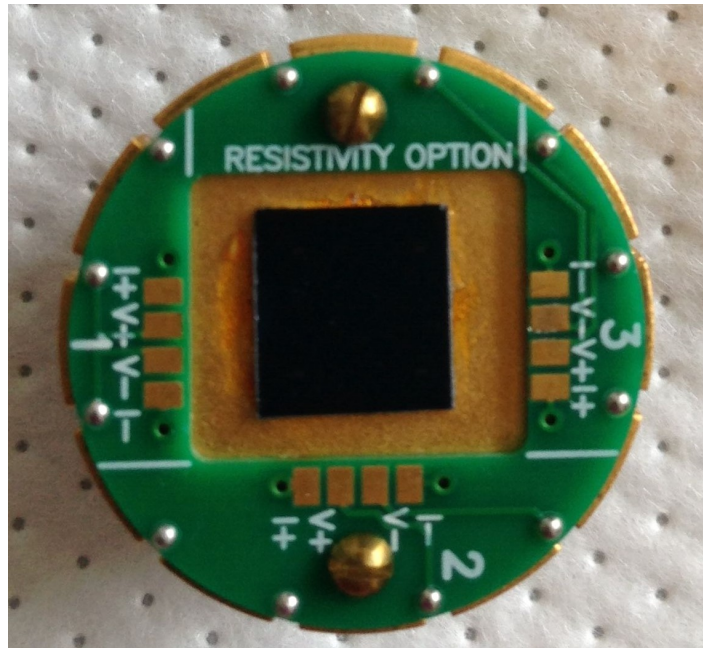


Figure 2.9. Sample mounted onto the resistivity option puck with GE varnish, before it is wirebonded to the corresponding channels such as 2V+, 2V-

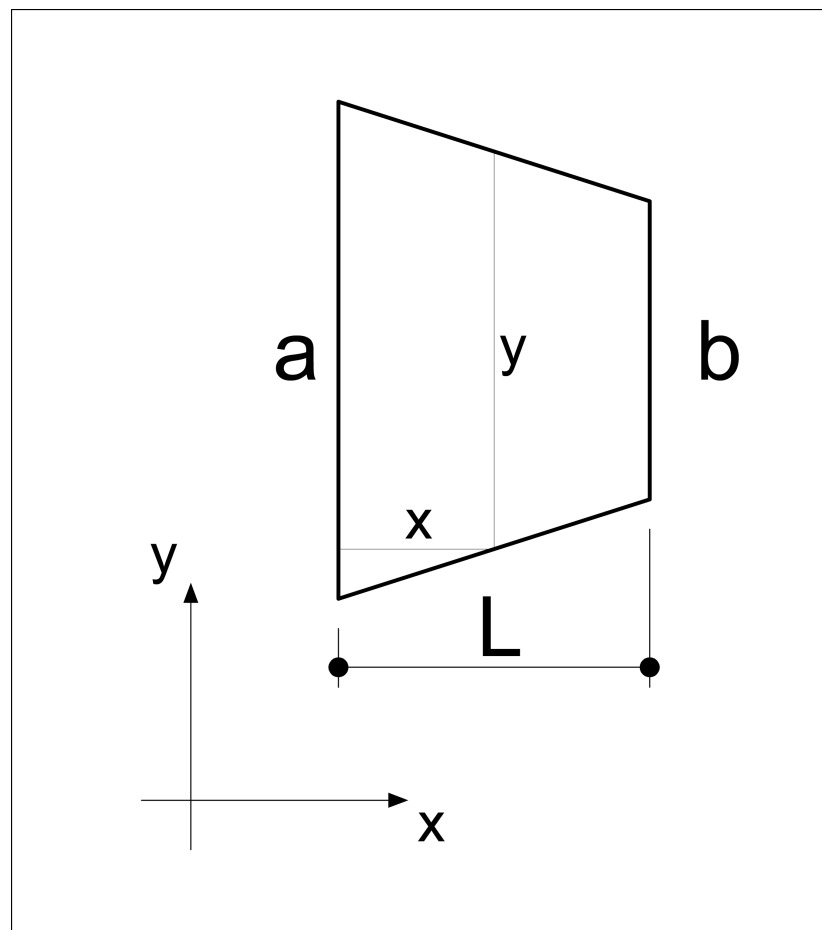


Figure 2.10. The calculation variables given on a schematic trapezoid

which involves trapezoid and rectangles. Ordinary Pouillet's law,

$$R = \rho \frac{l}{A} \quad (2.1)$$

modified to integration becomes

$$R = \rho \int \frac{dx}{A} \quad (2.2)$$

where  $A$  is the cross-sectional area of our thin film. In this case, it is thickness  $t$  multiplied with width  $y$ . Hence, the resistance for the trapezoid shape becomes,

$$R = \rho \int \frac{dx}{y \cdot t} \quad (2.3)$$

where  $y = \frac{a-b}{L}x + b$  due to similarity. Using this relation, the resistance of a trapezoid shaped wire is calculated with the following integration.

$$R = \frac{\rho}{t} \int_{x=0}^{x=L} \frac{dx}{\frac{a-b}{L}x + b} \quad (2.4)$$

And as a result, we get:

$$R = \frac{\rho}{t} \frac{L}{(a-b)} \ln \left( \frac{a}{b} \right) \quad (2.5)$$

After we derived the equation of resistivity for trapezoid, we used the following equation for the rectangle parts.

$$R = \rho \cdot \frac{\ell}{A} = \rho \cdot \frac{\ell}{y \cdot t} \quad (2.6)$$

We are done with derivation part and using the microscope images, an example shown in Figure 2.11, we divide the sample geometry into rectangles and trapezoids in order to proceed with the resistivity calculation. For this, we took precise x100 microscope images and measured the dimensions with Leica microscope software.

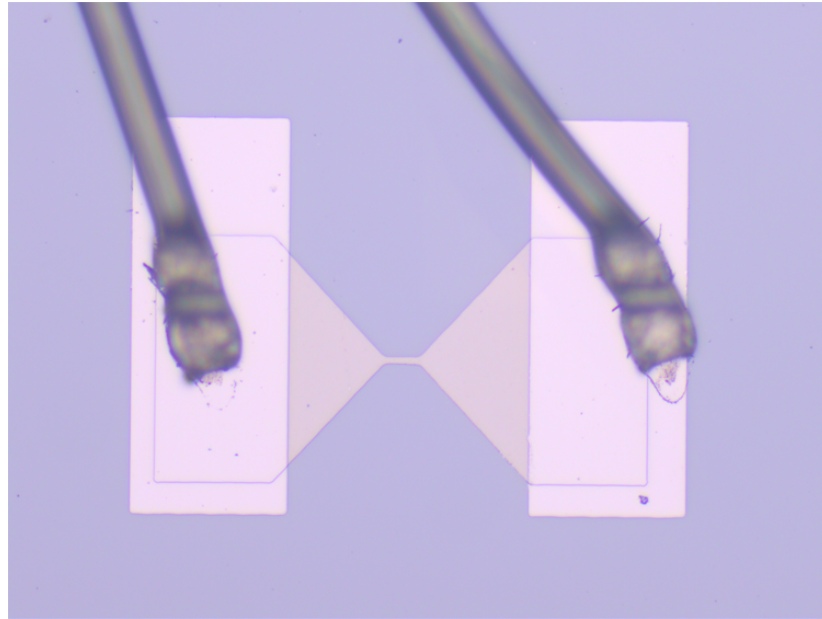


Figure 2.11. Bow tie resistivity measurement sample of Ta after it is wire bonded to PPMS puck and connected to the rest of the circuit

I-V measurements are conducted at temperatures varied in the range of 10 K and 300 K by Electrical Transport Option of PPMS (Physical Property Measurement System) by Quantum Design. We calculated the geometric constants to extract the resistivity values for each sample with the aid of microscope images. Finally, we determined the resistivities and plotted the resistivity versus temperature graphs shown in Figure 2.12, 2.13, 2.14, 2.15 for Ti, Cu, IrMn, Ta materials respectively.

Ion mill thickness is the amount we mill after the second lithography before the deposition of contact Pt, this was done in order to observe the effect of milling to the quality of interface. As can be seen in Figure 2.12 for the case Ti.

The average resistivity values at room temperature for all materials except Au and Pt are given in the following Table 2.3.

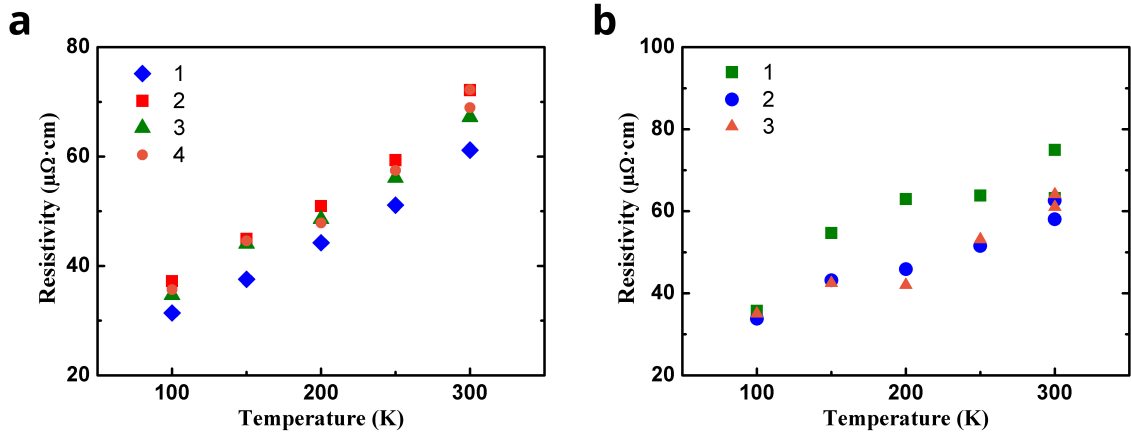


Figure 2.12. Resistivity versus temperature graph for a) 4 samples of 100 nm Ti, 15 nm ion milled before contact deposition b) 3 samples of 100 nm Ti, 3 nm ion milled before contact deposition

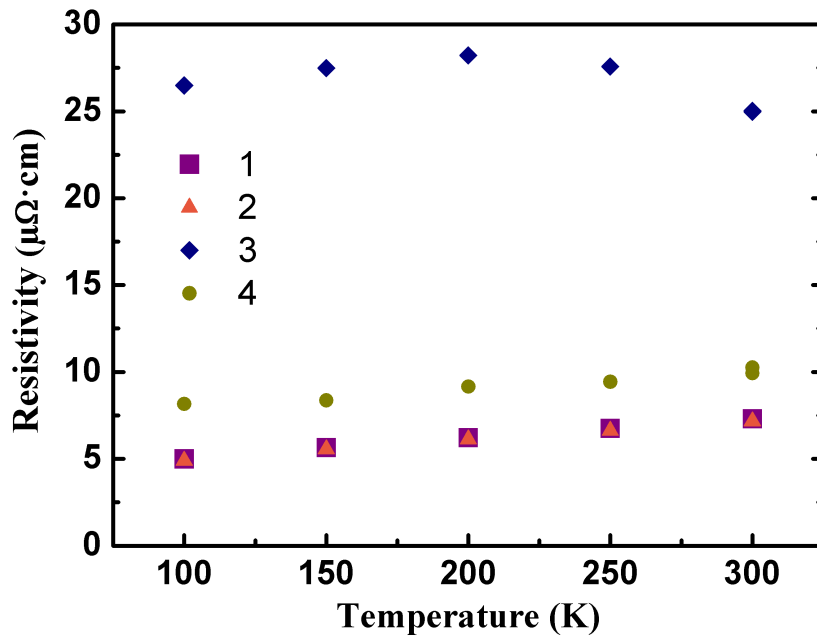


Figure 2.13. Resistivity versus temperature graph for 4 samples of 50 nm Cu

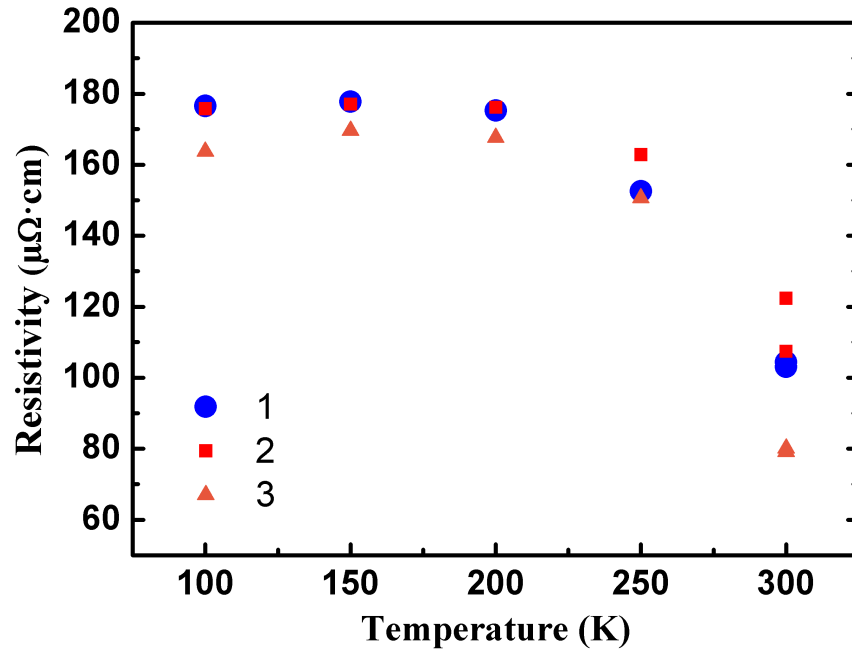


Figure 2.14. Resistivity versus temperature graph for 3 samples of 50 nm IrMn

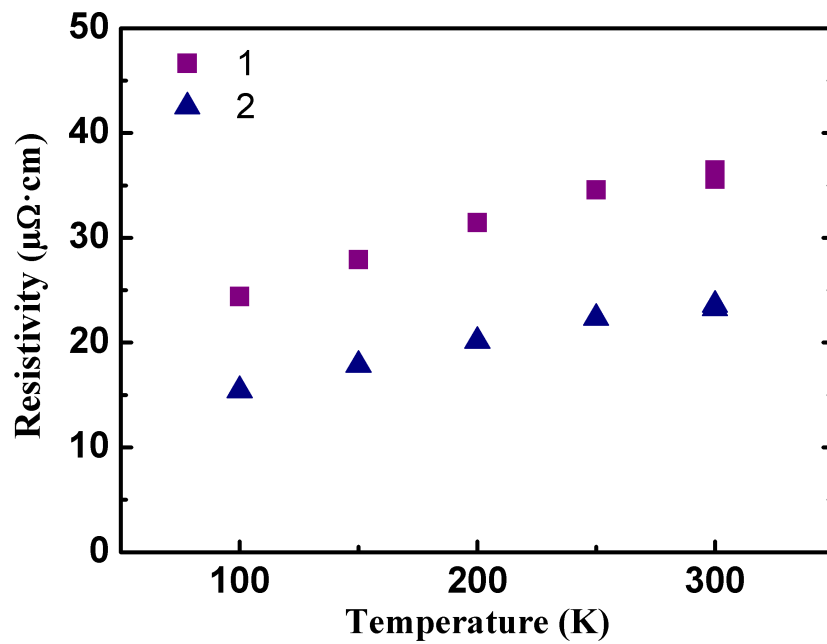


Figure 2.15. Resistivity versus temperature graph for 2 samples of 100 nm Ta

Table 2.3. Resistivity values of materials at room temperature

Material	Sample Thickness (nm)	Ion Mill Depth (nm)	Resistivity @RT
Cu	2	15	$12.4 \pm 0.1$
Ta	2	15	$30.0 \pm 0.1$
Ti1	2	15	$67.4 \pm 0.1$
Ti2	2	3	$60.8 \pm 0.1$
IrMn	2	15	$96.6 \pm 0.1$

### 2.3. Magnetic Characterization with Vibrating Sample Magnetometer and SQUID

After the thickness calibration of our materials and the determination of electrical properties, we moved on to the magnetic characterization of our materials such as IrMn. We want to detect Néel temperature of IrMn, the temperature at which IrMn goes through phase transition and becomes a paramagnet. Since antiferromagnets have no net magnetic moment, the presence of a ferromagnetic layer is necessary to identify the magnetic properties of antiferromagnets. IrMn was reported to have good combination of exchange fields, corrosive resistance and temperature stability when coupled with NiFe [33].

PPMS Vibrating Sample Magnetometer (VSM) Option and SQUID (Superconducting Quantum Interference Device) magnetometer were used for magnetic moment versus magnetic field measurements, software panel shown in Figure 2.16, and the correspondent magnetization of the material was found by dividing the magnetic moments with thin film dimensions, giving us the hysteresis loop of magnetic material.

For the characterization, IrMn/NiFe thin films were fabricated instead of solely IrMn thin films. Exchange Bias is the shift in magnetic field axis in the hysteresis loop. It occurs when an FM-AFM interface is cooled through the Néel temperature in presence of an external magnetic field. The cooling process should start from a temperature above Néel temperature and below Curie temperature. Curie temperature

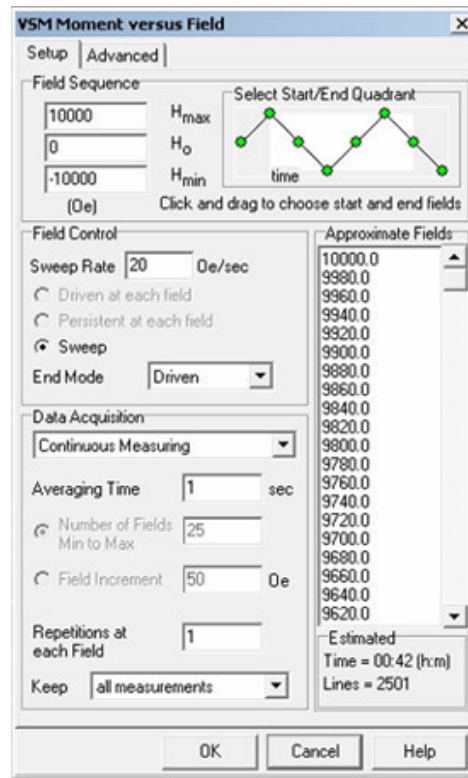


Figure 2.16. Moment versus field procedure for VSM measurement on DynaCool MultiVU software by Quantum Design

of ferromagnetic material must be larger than Néel temperature. Hysteresis loop of FM-AFM system generally shifts in the opposite direction of the external magnetic field after the field cooling process. The magnitude of the exchange bias field is equal to the average of the values of magnetic field which hysteresis loop intersects with magnetic field axis [34]. The blocking temperature is the temperature at which the exchange bias field goes to zero. Blocking temperature can be lower than Néel temperature or can be around Néel temperature. Blocking temperature can be different from domain to domain. This means that we can only talk about an average blocking temperature for an antiferromagnetic material.

After the fabrication of the samples, Vibrating Sample Magnetometer (VSM) measurements were done on PPMS. VSM systems are used to measure the magnetic properties of materials as a function of magnetic field, temperature, and time. The magnetic field is generated by an electromagnet. Temperature control is accomplished through cryostat. When sample is placed inside the chamber and special VSM coil

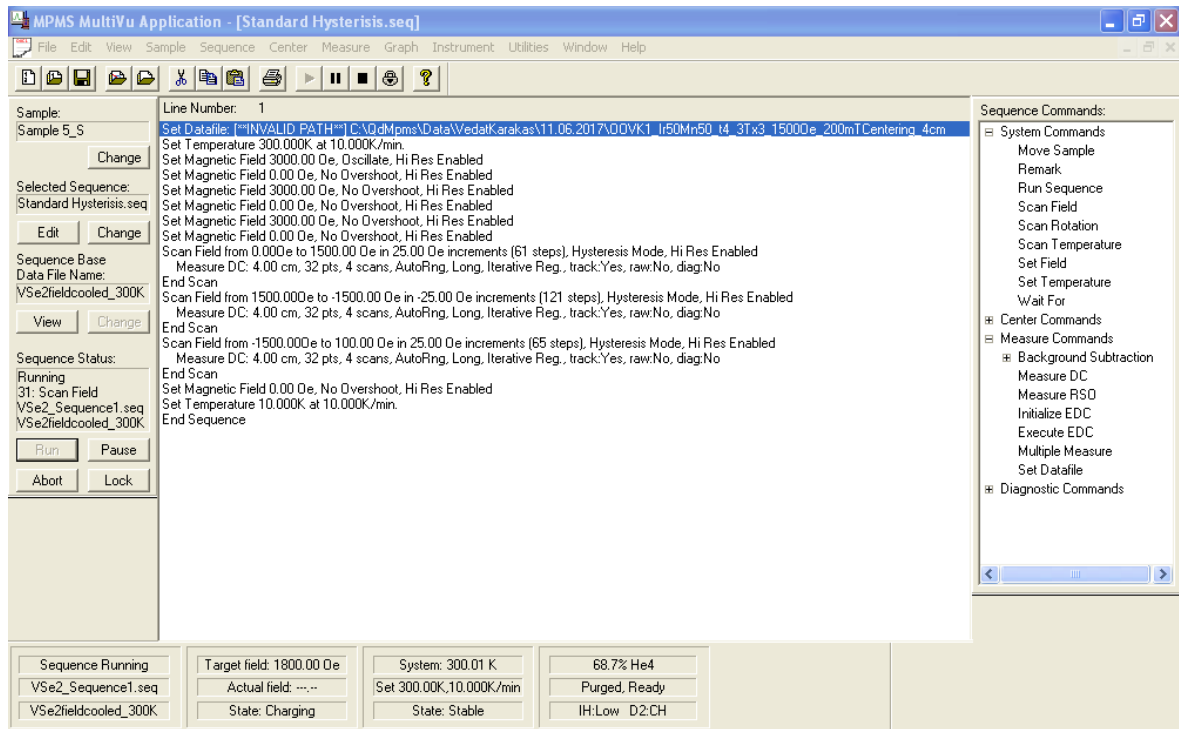


Figure 2.17. PPMS SQUID sequence for magnetization versus magnetic field (hysteresis) measurement

set; a uniform magnetic field is applied meanwhile the sample undergoes vibration, i.e. sinusoidal motion. The magnetic flux through the coil changes as a result of induced magnetic moment of the sample and induces a voltage to the coils that is proportional to the magnetic moment of the sample. In our system, we can change magnetic field from 10 T to -10 T and temperature from 1.3 K to 400 K. The sequence shown in Figure 2.17 is used for PPMS SQUID measurements.

Since antiferromagnetic materials do not have net magnetic moment we use an indirect method such as demonstration of exchange bias. In order to confirm the antiferromagnetic property of IrMn, we used thin film stacks of Si/SiOx(300nm)/Pt(5nm)/NiFe(3nm)/Cu(5nm) where (100) p-type silicon substrate is used and thickness  $t$  of IrMn is varied.

To obtain the exchange bias effect, IrMn should be grown on a  $\langle 111 \rangle$  oriented surface. The silicon wafers which are used in experiments were  $\langle 111 \rangle$  oriented. Silicon can be easily oxidized, and oxidized silicon loses its orientation and become amorphous. To have  $\langle 111 \rangle$  orientation for IrMn, one needs to get rid of oxidized surface of the

silicon wafer. For this purpose, we have used RF bias techniques for sputtering and HF spin (spinning the Si wafer at high rpms and pouring 18% Hydrofluoric acid solution onto wafer for 15 seconds, after that the surface is washed with ethanol) in a spin coater on silicon wafers. 7.5 nm thickness of IrMn is needed in order to provide large exchange. It has been observed that exchange bias field is inversely proportional to the thickness of the FM. However, if the FM layer is too thin, some discontinuities occur on the interface therefore this relationship does not hold anymore. In case of the AFM thickness; if it is over 20 nm, exchange bias field will be independent of AFM thickness.

The relatively higher blocking temperature of IrMn provides temperature stability to it. However, thickness of the IrMn affects its blocking temperature. For thickness above than 20 nm, the blocking temperature is in the range of 200-250°C [35]. Below this thickness, the blocking temperature decreases with decreasing thickness and is found about 130°C for 7.5 nm thickness [35]. For our measurements, we have chosen the IrMn thickness to be 50 nm.

The silicon wafers are cleaned with RF substrate bias prior to deposition. Deposition is done under 500 Oe longitudinal magnetic field at 300 K and 3 mTorr Ar pressure with 5 sccm Ar gas flow. 1, 1.5, 2, 3, 4, 5, 10, 15, 25 and 50 nm thick IrMn films are used for each configuration. 10 W and 30 W powers are used for ultrathin and thicker sample thicknesses respectively.

We have investigated how coercivity and exchange bias depends on temperature, how HF spin process effects exchange bias and coercivity, training effect and the effect of annealing in higher temperatures. HF Spin cleaning process is done to observe any effect on the exchange bias and coercivity of the sample. We had a control sample which we did not apply HF spin. There were also two sets of measurements; the one measured after field cooling (FC) and the one with zero field cooling (ZFC). For zero field cooling, we cooled the samples from 300 K to 4 K without any magnetic field; and we cooled the samples under 1 Tesla external magnetic field for field cooling. Then we measured their magnetization in different temperatures: 8 K, 50 K, 100 K, 150 K, 200 K, 250 K, 300 K. Figure 2.19 and Figure 2.20 shows the magnetization vs. magnetic

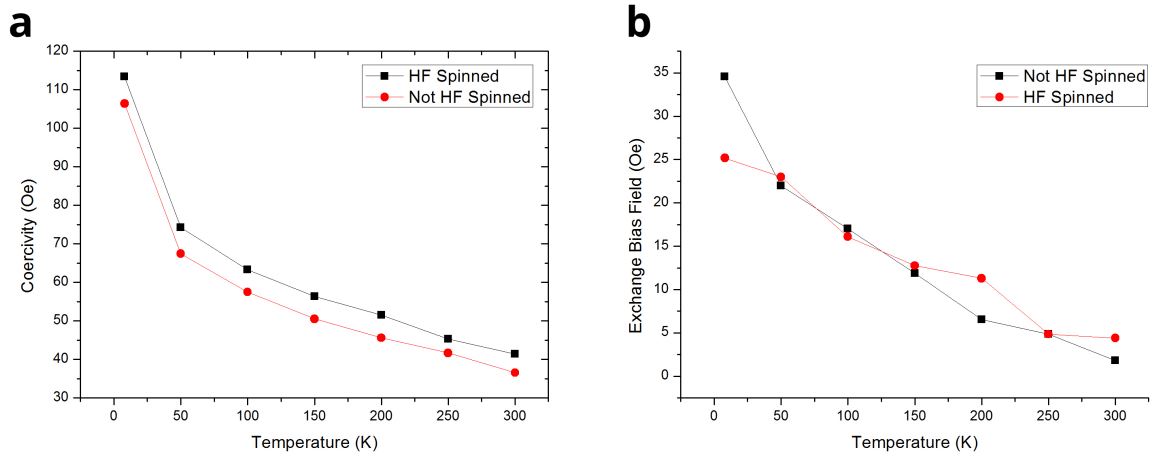


Figure 2.18. Effect of HF on a) coercivity and b) exchange bias field

field graphs of HF-spun and not-HF-spun samples for each temperature and each of the graphs contains both FC and ZFC. The resulting data were plotted, coercivities and exchange bias fields for these samples in different temperatures are given in Figure 2.18.

It is seen from the graphs that coercivity is higher in the sample with HF spin for each temperature and there is no remarkable amount of change in exchange bias magnitude whether it is HF spun or not.

We can see that coercivity increases with decreasing temperature. We plotted coercivity values for ZFC and FC for different temperatures in the same graph in order to see how coercivity was affected from field cooling process, shown in Figure 2.21. It can be seen from the graph that coercivity increased with field cooling process. Figure 2.22 also shows that the shift in exchange bias field is larger in lower temperatures.

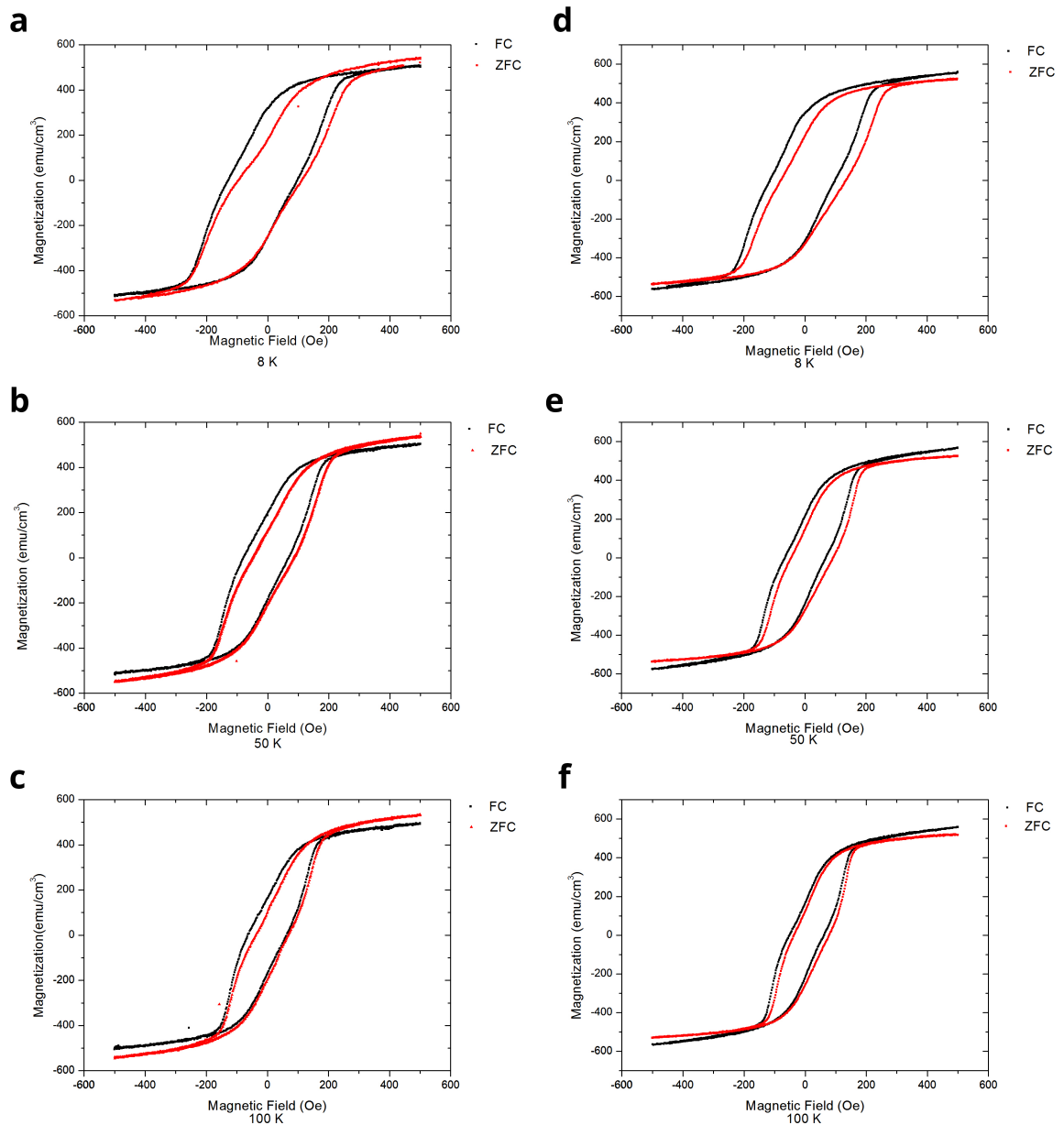


Figure 2.19. Hysteresis loops, magnetization vs magnetic field graphs for a,b,c) HF spun samples and d,e,f) not HF spun samples given for both FC and ZFC conditions at a,d) 8 K, b,e) 50 K and c,f) 100 K.

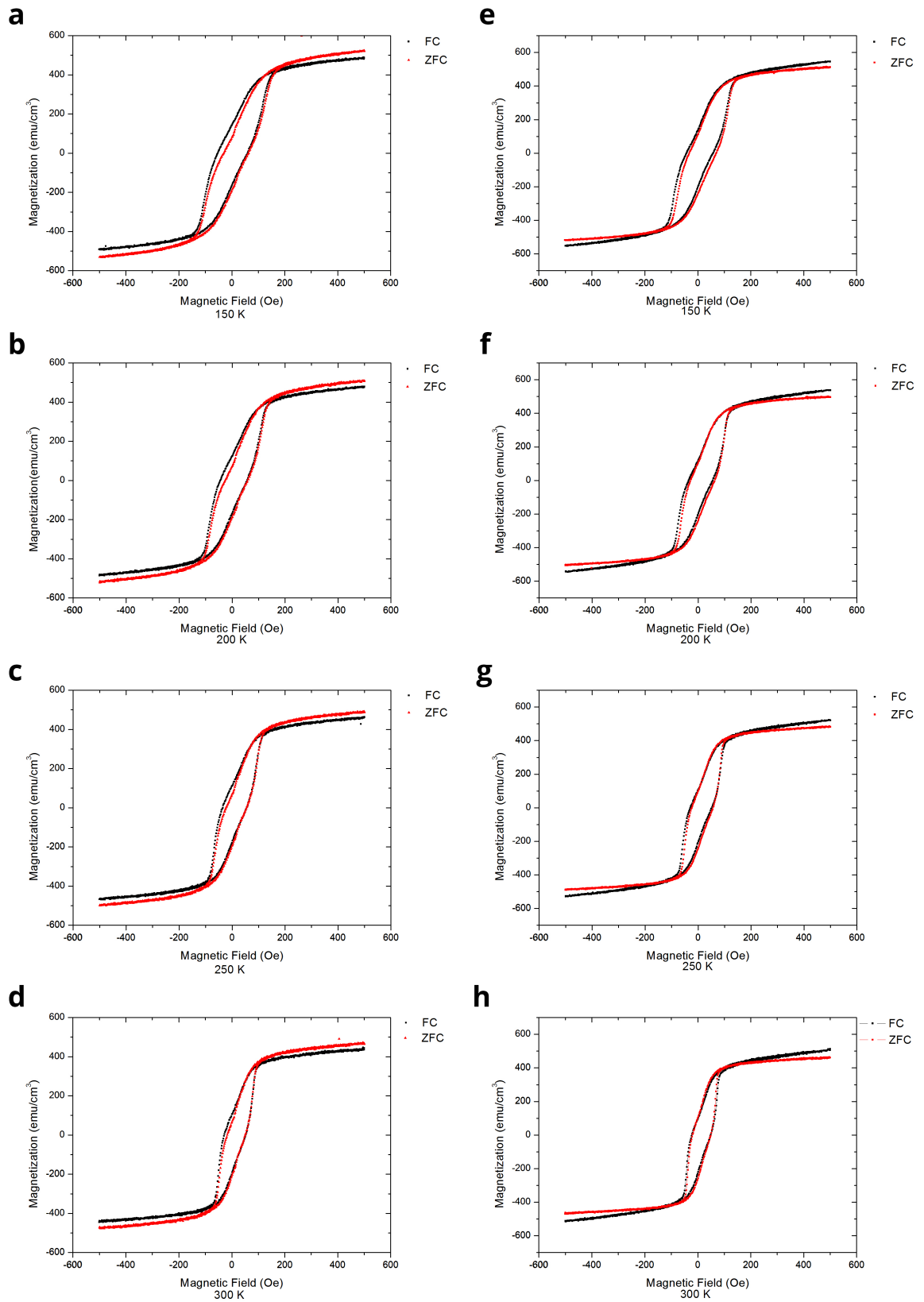


Figure 2.20. Hysteresis loops, magnetization vs magnetic field graphs for a-d) HF spun samples and e,h) not HF spun samples given for both FC and ZFC conditions at a,e) 150 K, b,f) 200 K, c,g) 250 K and d,h) 300 K

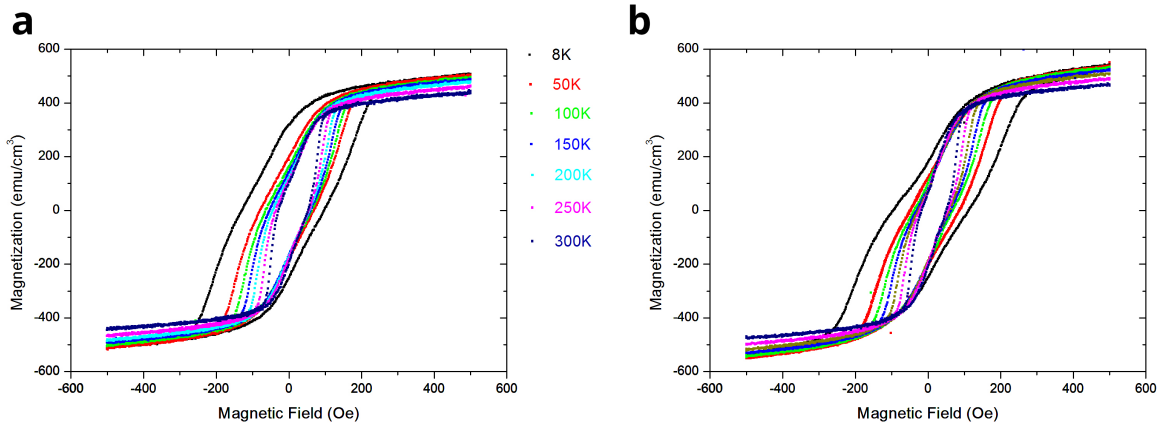


Figure 2.21. Magnetization vs Magnetic Field graph for HF spinned sample at all temperatures with a) FC and b) ZFC

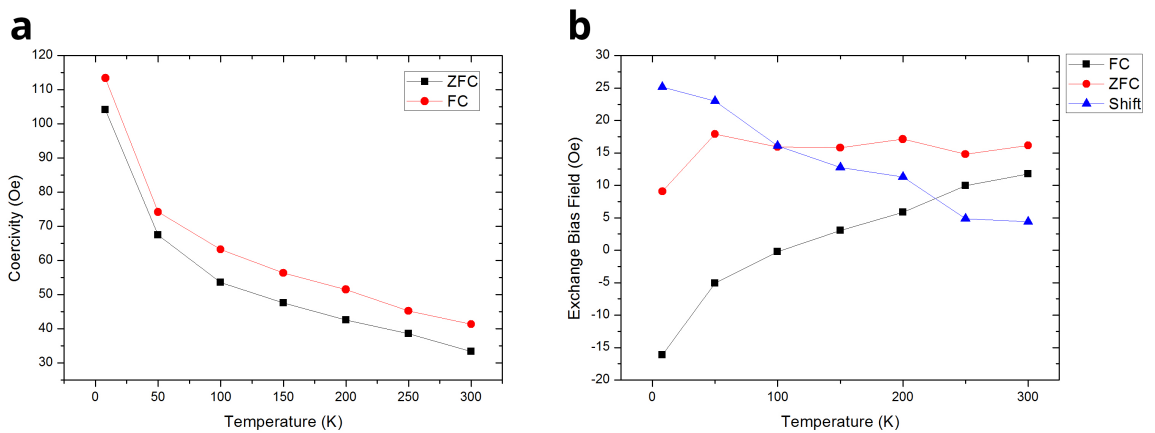


Figure 2.22. Temperature dependence of a) coercivity and b) exchange bias field and the shift for HF spun samples with ZFC and FC for all temperatures

## 2.4. Structural Characterization with X-ray Diffraction and X-Ray Photo Electron Spectroscopy

A large number of techniques are available for physical and chemical material analyses. In all of those techniques the sample is excited with electrons, photons or ions and ejected electrons, photons or ions are measured [36].

X-ray photoelectron spectroscopy (XPS) and Electron spectroscopy for chemical analysis (ESCA) are techniques for analyzing the surface chemistry of a material which can measure the elemental composition, empirical formula, chemical state and electronic state of the elements within a specimen [37]. XPS technique makes use of photoelectric effect, first discovered by Hertz in 1887 and outlined by Einstein in 1905, by exciting the sample surface with energetic photons and analysing emitted photoelectrons.

The analyser measures the kinetic energy of the emitted photoelectrons. Binding energy is extracted using the following equation:

$$E_b = h\nu - E_k - \Phi \quad (2.7)$$

$E_b$  is the binding energy of the excited photoelectron,  $h\nu$  is the energy the photon that excites the photoelectron  $E_k$  is the kinetic energy of the photoelectron and  $\Phi$  is the work function of the specimen from which the photoelectron is excited.

X-ray radiation of Al  $K_\alpha$  of 1486.7 eV or Mg  $K_\alpha$  of 1253.6 eV is most commonly used as the monochromatic light sources in XPS. Binding energy of its electrons is a characteristic of an element, so the analysis of the binding energies of photoelectrons yields the atomic content of a specimen.

Though Equation 2.7 seems to be straightforward, there are two inherent experimental problems which make it difficult to make an accurate measurement of  $E_b$  [38].

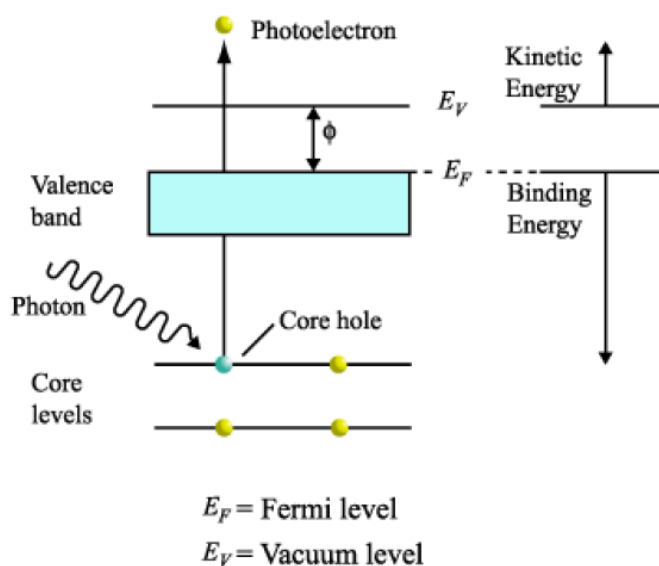


Figure 2.23. Photoemission process of atoms. A visual representation of Equation 2.7.

First, work function  $\Phi$  of a specimen often depends on factors such as crystallinity which makes it a hard task to determine the accurate value of it.

Second, a photoelectron must overcome the work function of spectrometer ( $\Phi'$ ) in order to be detected.  $\Phi'$  is most likely different than the work function of the specimen. Moreover, the binding energies measured by a spectrometer ( $E'_b$ ) are measured relative to that spectrometer's Fermi level which in general is not the same as  $E_b$ . Thus, binding energies measured are dependent on the spectrometer.

One can eliminate the latter obstacle by making a good electrical connection between the sample and the spectrometer to equalize their Fermi levels. And the work function of the spectrometer ( $\Phi'$ ) can be extracted by examining a specimen with a known binding energy. This process is called *calibration*. It requires an extra effort to calibrate the XPS spectra of insulating specimen.

In XPS technique, a low resolution survey scan is sufficient for elemental identification. However, a study of chemical states requires a deconvolution analysis on high resolution scans by fitting synthetic peaks to elemental peaks. Usually, element identification from survey scan spectrum is an easy job as elemental peaks are sepa-

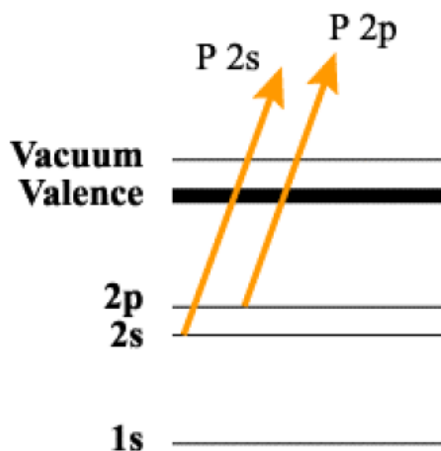


Figure 2.24. Energy diagram of photoemission process from 2s and 2p orbitals

rated on binding energy axis well enough to leave no ambiguity. In contrast, synthetic peak fitting is always laborious as it involves not only logical algorithm but also human interpretation that comes along with human error. Most of the time, there are infinitely many ways to make "good" synthetic peak fits, yet almost one in infinity of those possibilities represent a physically meaningful case. This is the main reason why compound peak locations given by different references in NIST (National Institute of Standards and Technology) database [39] are diverse. Nevertheless, accepting a peak location approximately close to the previously report values and performing the same peak deconvolution procedure for all measurements enhances the credibility of the result.

#### 2.4.1. Auger Effect

When a core level electron is liberated from the atom, an electron from outer levels fills its place releasing a photon. This photon can excite another electron from outer levels resulting in an Auger electron emission. The escape depth of low-energy Auger electrons is on the order of a nanometer only [36]. Auger effect can be observed in XPS spectra with broader peaks when compared to the peaks of photoemission process. Kinetic energies of Auger electrons are unique for every element and useful for the identification of the elemental structure of a specimen. Auger electron spectroscopy (AES) makes use of Auger effect for material analysis. AES and XPS are similar as

both techniques measure low energy electrons that originate from the sample surface only. Yet, in AES sample surface is excited by electrons [36].

#### **2.4.2. Inelastic Mean Free Path**

The distance that electrons can travel without suffering inelastic collisions in a specimen is called *inelastic mean free path* (IMFP) which is on the order of a few nanometres. That is, the photoelectrons and Auger electrons liberated from deep enough regions of the sample can not make it to the detector without being inelastically scattered. Therefore, XPS can only measure the elemental or chemical composition of a specimen at the surface. Those inelastically scattered photoelectrons lose kinetic energy at arbitrary extents and contribute to the background of XPS spectra. That is why an XPS spectrum has step like background where each step starts with a photoelectron peak and extends towards the increasing binding energy (decreasing kinetic energy) direction.

#### **2.4.3. The Spectroscope**

The spectroscope consists of two subsystems that are in an ultra high vacuum environment. The first contains the X-ray source and the sample on which the photoemission process occur. The second one encloses the electron energy analyser and the detector [38].

An electron gun accelerates electrons towards an aluminium anode. Those accelerated electrons excite Al atoms resulting in an X-ray emission from Al target. This emission spectrum consists of some peaks on a background radiation which is called bremsstrahlung background. Bremsstrahlung background consists of continuous X-ray radiation due to the emissions from decelerating electrons that enter the Al target. Sharp peaks on this background are called characteristic X-ray with energies unique to the target material. A quartz monochromator selects only Al  $K_{\alpha}$  line and filters the rest of the spectrum. Then using a lens this radiation is focused on the specimen.

#### 2.4.4. Calibration of Insulating Specimens

For an insulating specimen the Fermi level is not well defined, so it is not convenient to measure binding energy relative to the Fermi level. In such cases, XPS spectra must be calibrated with respect to a peak of well known binding energy in order to conduct a proper XPS analysis. Fortunately, all specimen that are exposed to the atmospheric environment carry a surface contamination of carbon element which constitutes a reference for calibration. In calibration process C 1s peak is constrained to have 285 eV binding energy, which is the experimentally acknowledged value.

#### 2.4.5. Charging Effect

When an electron (a negative charge) is liberated, a neutral sample gains positive charge. If the sample is conducting, a good electrical connection to XPS instruments ground supplies electrons to neutralize the sample again. This not the case for insulating samples where the negative charges required to neutralize the sample can not be supplied and a positive charge build up occurs. As a result, electrons that move away from the sample after the photoemission process are attracted to the sample. So they lose kinetic energy. Equation 2.7 dictates if  $E_K$  is decreasing,  $E_b$  must increase. Therefore, in XPS spectra photoemission peaks are shifted towards increasing binding energy direction. Those peaks are also widened. This makes identification of those peaks difficult and deconvolution analysis unreliable.

To tackle this issue, an XPS instrument must contain a flood gun which deluges the insulating sample surface with low energy (0 - 20 eV) electrons. If the power of flood gun is set too low it can not supply enough charge to neutralize the sample. On the other hand, if the power is set too high it can overcharge the sample by causing negative charging. Flood gun should be optimized to properly neutralize the sample [38].

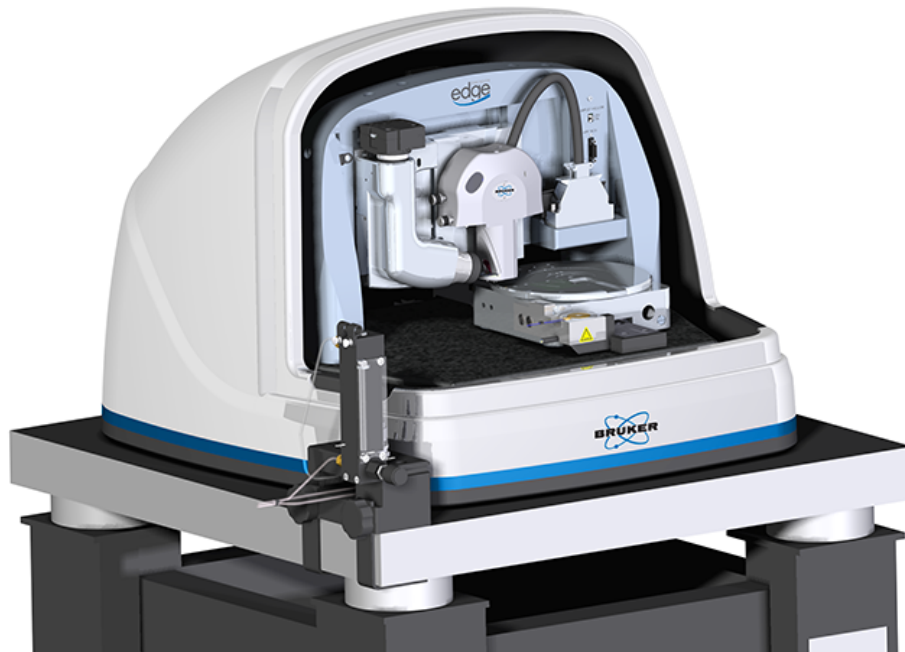


Figure 2.25. Bruker Dimension Edge Atomic Force Microscopy [3]

## 2.5. Measuring Morphology with Atomic Force Microscopy

Scanning probe microscopy (SPM) is a collection of techniques which use a sharp nano scale tip on a cantilever to scan the sample. The interaction of the tip with the surface is measured. This interaction can be physical distance (sensed by the tunnelling current between the tip and the surface in the scanning tunnelling microscopy, STM) or magnetic, capacitive, chemical or many other interactions [36].

The atomic force microscope which has nanometer scale resolution, is a favorite metrology tool in microfabrication. In the atomic force microscopy technique, the force in question can be mechanical contact force, Van der Waals force, electrostatic or magnetic forces between the tip and the surface atoms at very short distances.

Van der Waals interactions arise due to a temporary redistribution of electrons in the atoms and molecules. This results in the occasional formation of dipoles, Due to the formation of dipoles, the two molecules experience a mutual attraction, which is referred to as a van der Waals interaction. Forces can be explained by van der Waals

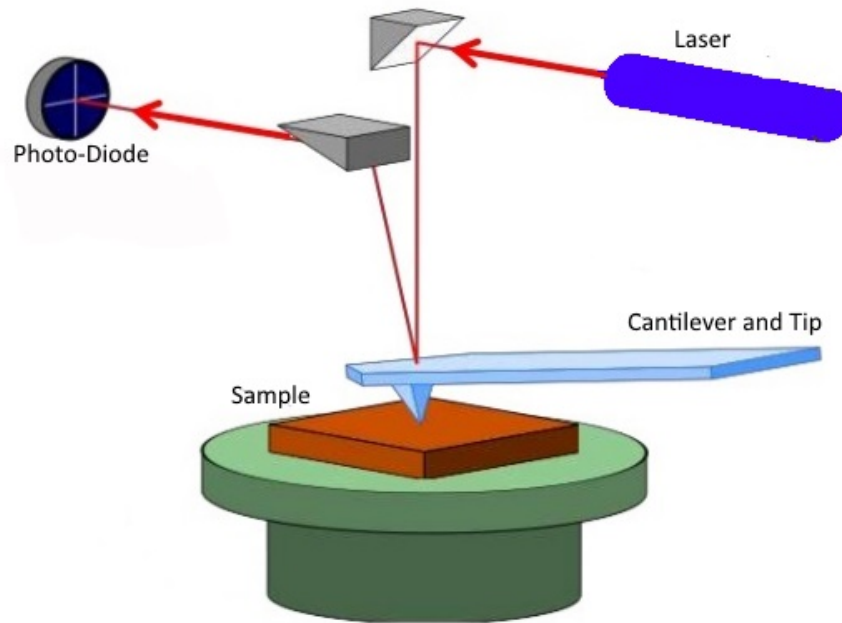


Figure 2.26. Atomic force microscopy diagram

forces, approximated by Lennard-Jones potential [40]:

$$U_{LD}(r) = U_0 \left\{ -2 \left( \frac{r_0}{r} \right)^6 + \left( \frac{r_0}{r} \right)^{12} \right\} \quad (2.8)$$

where  $U_0$  is the depth of the potential well,  $r_0$  is the finite distance at which the inter-particle potential is zero,  $r$  is the distance between the particles.

Working principle of atomic force microscopy, schematically shown in Figure 2.26, is as follows: laser spot reflects from cantilever to the photo diode, when cantilever faces with the a bump or well laser deflects and this deflection after turning to the signal image can be obtained. Many materials can be used for tips (e.g. silicon, silicon nitride etc.) on silicon cantilevers. Atomic force microscope setup includes optical instruments to measure the deflection of the tip due to either repulsive or attractive forces with a precision as good as 0.01 nm.

Bruker Dimension Edge [3] was used as the imaging tool (See Figure 2.25). Atomic force microscopy module is placed on top of a vibration isolation table. First, an appropriate atomic force microscopy tip (TESPA tips in this case) is placed on the

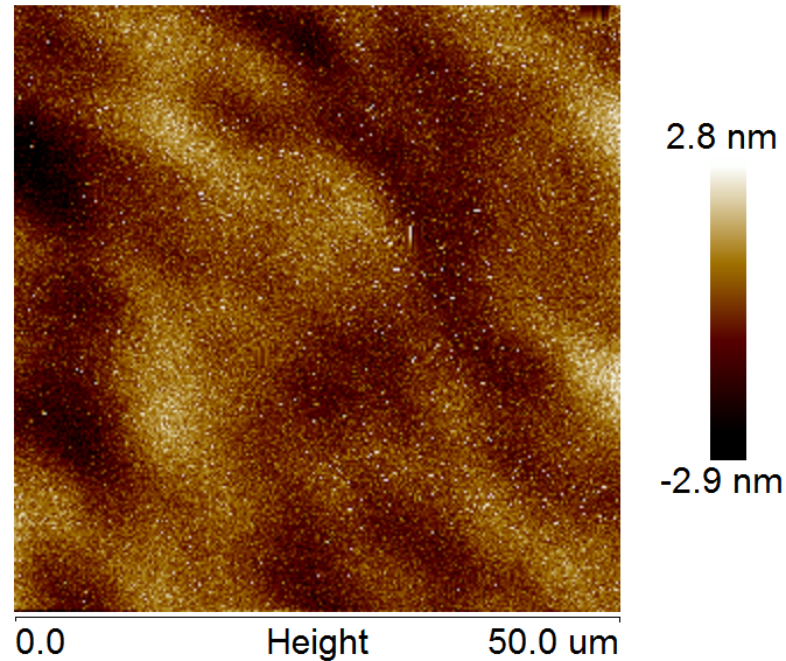


Figure 2.27. Atomic force microscopy surface roughness measurement of silicon dioxide thin film coated on silicon substrate. Surface RMS roughness is 0.73 nm

cantilever holder and attached to it with a clip. This cantilever holder is mounted on the head of atomic force microscopy scanning module so that the tip faces towards the sample stage. Second, proper laser adjustments are made and the sample is placed onto the stage. Then, phase tuning adjustments are made, operated with the computer software. At last, the tip is engaged to the surface to take measurements. The detailed operation procedures can be found in the computer as a text file named "AFM quick guide".

### 2.5.1. Surface Roughness Measurement

One of the most common uses of atomic force microscopy is surface roughness measurement. For example, surface roughness of silicon dioxide thin film is measured using "Roughness" function of NanoScope Analysis software which is commonly used to analyse atomic force microscopy data. In addition to the silicon dioxide surface, polished silicon wafer's surface roughness is measured, shown in Figure 2.27. Surface root mean square (RMS) roughness is measured to be 0.73 nm for silicon dioxide thin film and 1.12 nm for silicon substrate. Expectedly, silicon dioxide coating decreased

surface roughness by smoothing defects such as grain boundaries.

## 2.6. Magnetic Imaging with Magnnetic Force Microscopy

Magnetic force microscopy (MFM) can be defined as a modified style of the atomic force microscope. Basically working principle depends a magnetic probe, which is close to a surface of the sample and sense the magnetic stray fields. Magnetic interaction determines by means of motion of the tip along with the z direction when it scans through the sample. MFM was introduced after the discovery of the atomic force microscopy [41], and became one of the most common techniques providing high resolution images at room temperature.

The force occurring between the tip and sample can be defined as follows:

$$F \sim (m_{tip} \cdot \nabla) H_{sample} \quad (2.9)$$

where  $H_{sample}$  is the stray field originating from the magnetic sample and  $m_{tip}$  is the magnetic moment.

MFM operation principle is based on Hooke's Law:

$$F_z = -k\Delta z \quad (2.10)$$

$$\delta F / \partial z = F'_z \quad (2.11)$$

where k (typical values  $\sim 0.01-0.1\text{N/m}$ ) is the spring constant of the cantilever,  $\Delta z$  is the displacement of cantilever from the equilibrium position,  $F_z$  is the force applied by MFM acting on the cantilever and  $F'_z$  is the force gradient. The cantilever starts to

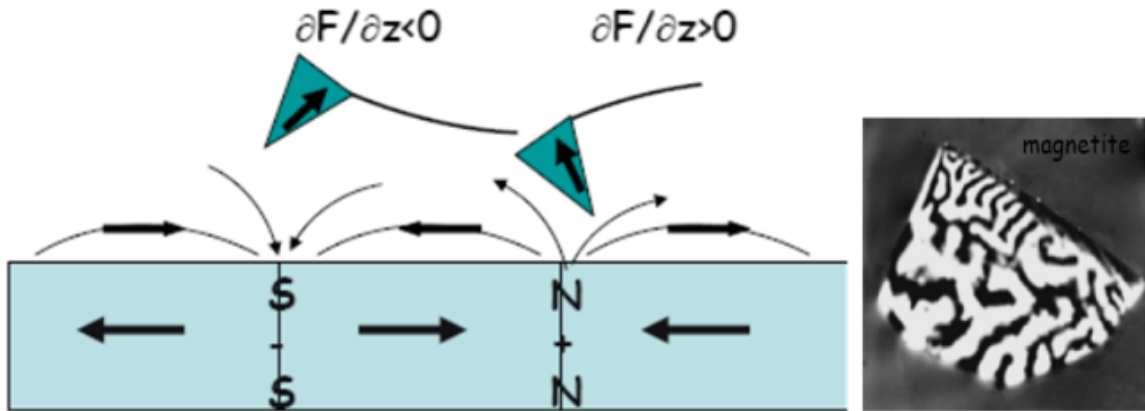


Figure 2.28. Attractive and repulsive interactions [4]

oscillate as if it has a modified spring constant,  $k_{eff}$ :

$$k_{eff} = k - F'_z. \quad (2.12)$$

Magnetic force acting on the flexible cantilever results in a shift in the resonant frequency,  $\omega_0$ :

$$\begin{aligned} \omega'_0 &= \omega_0 [1 - F'_z/2k]^{\frac{1}{2}} \\ \Delta\omega_0 &= \omega'_0 - \omega_0 \approx -\frac{\omega_0}{2k} F'_z, \Delta\omega_0 \ll \omega_0 \end{aligned} \quad (2.13)$$

In the case of an attractive interaction ( $dF/dz > 0$ ), negative phase shift corresponds to dark image contrast whereas in the existence of repulsive interaction ( $dF/dz < 0$ ), positive phase shift introduces bright image contrast, shown in Figure 2.28. The difference between atomic force microscopy and MFM is the usage of a magnetic tip (atomic force microscopy tip covered by a layer of ferromagnetic material with specific magnetization) and noncontact mode (lift mode). Basically, MFM measurement introduces two scans. First scan is a tapping mode scan sensing the surface topography by van der Waals interactions. In second scan, lift mode is enabled where van der Waals interactions are negligible, long-range magnetic and electrostatic forces are dominant. Two types, low moment and high moment, magnetic tips are available for this measurement. They have an end radii around 25-80 nm, shown in Figure 2.29,

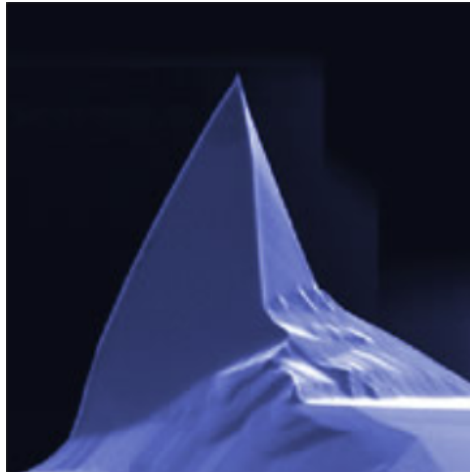


Figure 2.29. Scanning electron microscopy image of a magnetic tip [4]

and MFM resolution is limited by the size of the magnetic volume at tip apex and radii.

For MFM measurement, another limitation is the coercivity of the tip when the stray fields from the sample are high, or the tip coercivity is small, the sample can remagnetize the tip:

$$B_{\text{sample}} > \mu_0 H_c^{\text{tip}} \quad (2.14)$$

High tip coercivity,  $H_c$ , tip prevents surface-induced remagnetization.

The advantages of MFM are high spatial resolution, operating under ambient conditions, measuring bulk samples, allowing in-field and low-temperature (not routinely practiced) measurements whereas the possibility of influencing the sample with the magnetic tip is one of the disadvantages of this technique.

During measurements, we can face with tip defects that occurs due to the interaction of the tip with the sample, and scanner artifacts due to the peculiarities of the piezoelectric scanner. For example, tip-sample convolution (shown in Figure 2.30, is an inherent feature of MFM and it can never be fully removed.

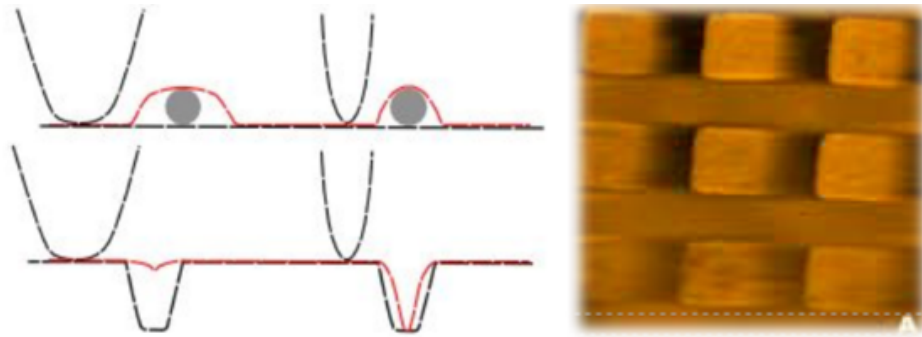


Figure 2.30. Schematic drawing and AFM measurement of tip-sample convolution artifact

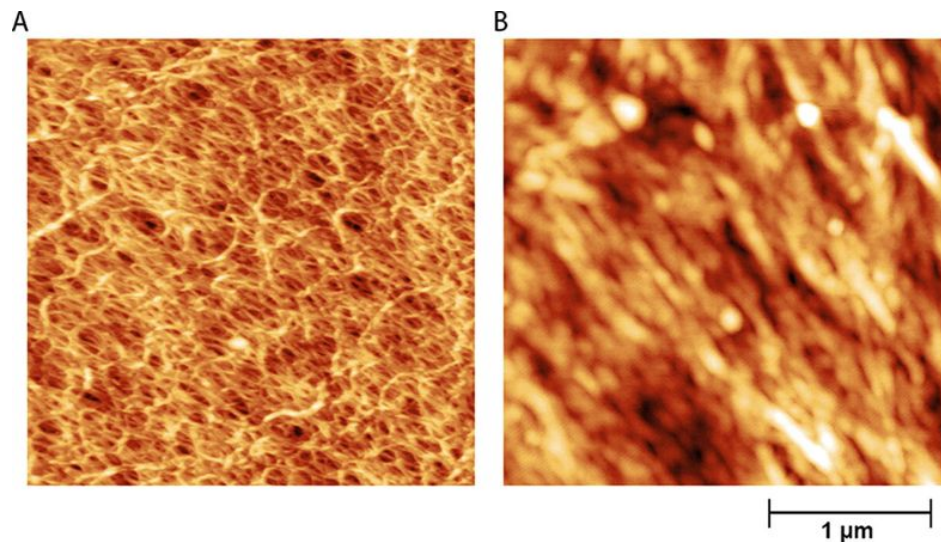


Figure 2.31. MFM images taken with a clean (on the left) and dirty (on the right) tip [5].

Another artifact occurs due to the scanning by dirty or contaminated tips shown in Figure 2.31.

When the tip is broken, "double tip" artifact may show up. An illustration of a double tip artifact is shown in Figure 2.32.

Laser misalignment results in an interference artifact which is seen as broad "stripes" in MFM images, shown in Figure 2.33.

One of the most common artifacts we face during MFM measurements is flying tip artifact which means the tip is not properly scanning the surface, shown in Figure

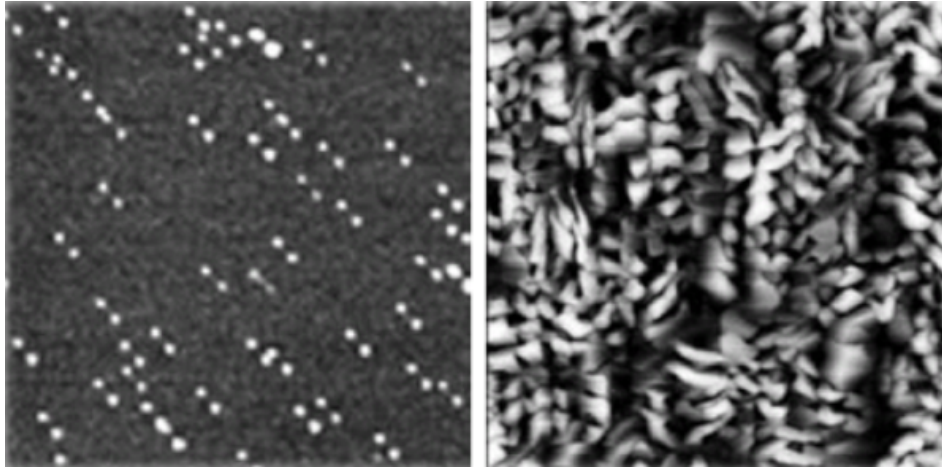


Figure 2.32. MFM images taken with a new (on the left) and broken (on the right) tip [6].

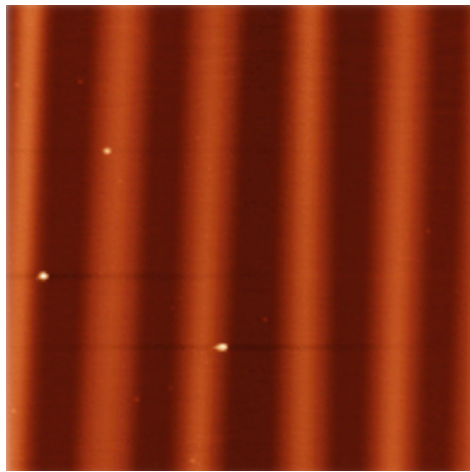


Figure 2.33. MFM image of laser interference artifact [6].

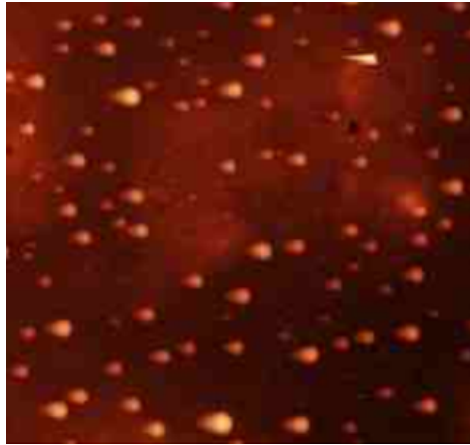


Figure 2.34. MFM image of flying tip artifact [6].

2.34.

For this technique, we generally use the following parameters for Bruker MESP Low Moment tip:

- Laser Sum: 1.722 V
- Set Point: 1.2 V
- Tuning Frequency: 69.450 kHz
- Proportional P: 0.920
- Integral I: 0.330
- Derivative D: 0
- Lift height: 60 nm

However these parameters depend on the magnetic properties of the sample. For example, 80 nm lift height may be not sufficient to detect the magnetic signal of the sample and we may need to decrease the distance between the tip and sample surface.

We show some applications of the MFM technique where the formation and manipulation of magnetic configurations such as anti-vortex, Neel skyrmion, horse-shoe, radial vortex (shown in Figure 2.35) and Skyrmion lattice have been observed in patterned nanomagnets under external field.

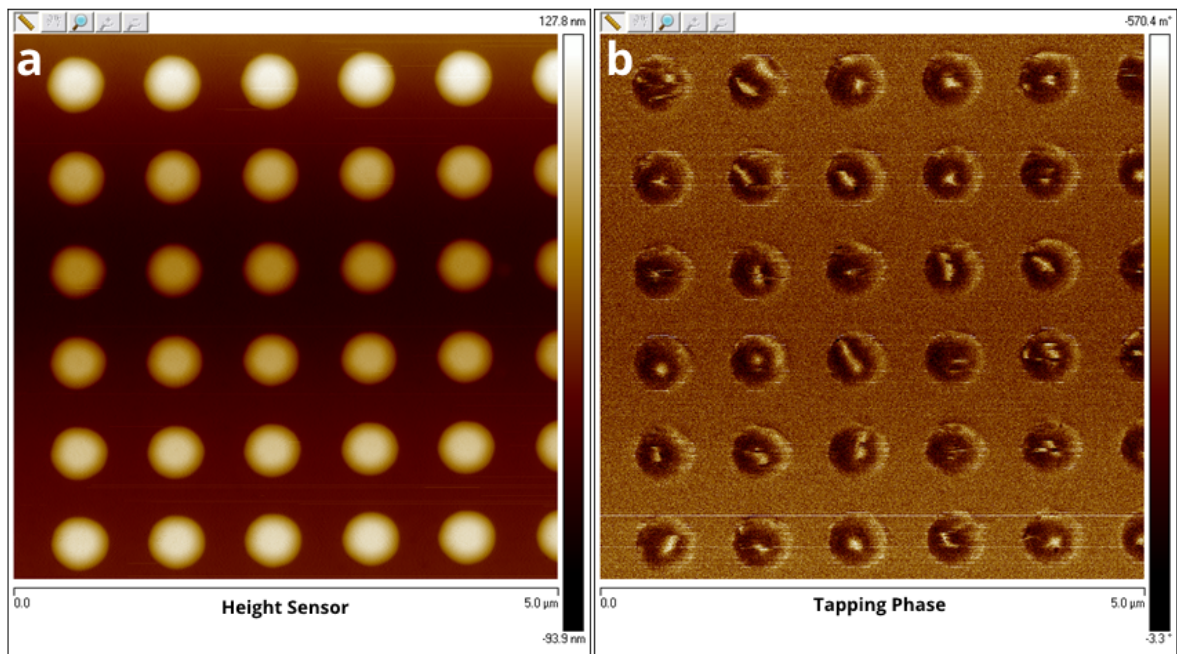


Figure 2.35. MFM image of radial vortices a) height sensor and b) tapping phase scan.

### 3. FABRICATION OF NANOPILLAR, THREE TERMINAL AND HALL BAR DEVICES

Device production processes consist of multiple lithography and deposition steps. Depending on the device geometry, several techniques including evaporation, sputtering, ion milling, plasma etching, etc. may be required. Material deposition can be done by means of DC sputtering, chemical vapor deposition (CVD), plasma enhanced chemical vapor deposition (PECVD), molecular beam epitaxy (MBE), etc. In this chapter, the production procedures for three types of devices, that were necessary for our investigations, are elaborately described.

#### 3.1. Preparation of wafers

A wafer serves as the substrate for microelectronic devices to be built in and undergoes many fabrication process steps such as doping (ion implantation), etching, material deposition, lithographic patterning, etc. Finally, the individual chips are separated (dicing) and packaged.

Wafers are pure single crystal materials which can be obtained with elaborate processes such as Czochralski method [42] shown in Figure 3.1. Impurity atoms can be added to the molten intrinsic material in precise amounts in order to dope the crystal, thus changing it into n-type or p-type extrinsic semiconductor.

Silicon wafers are most commonly used in experiments as the cheapest option. Usually four inch wafers with a thickness of  $525 \mu\text{m}$  are used in our experiments. Cleaving the wafer can be accomplished with various different equipments such as diamond scribes, wafer cleaving pliers, dicing saws, etc. The easy axis for the wafer to be cut easily occurs only in a few well-defined directions, depending on the crystal orientation of the wafer such as (100) or (111). Scribing the wafer along cleavage planes allows it to be easily diced into individual chips.

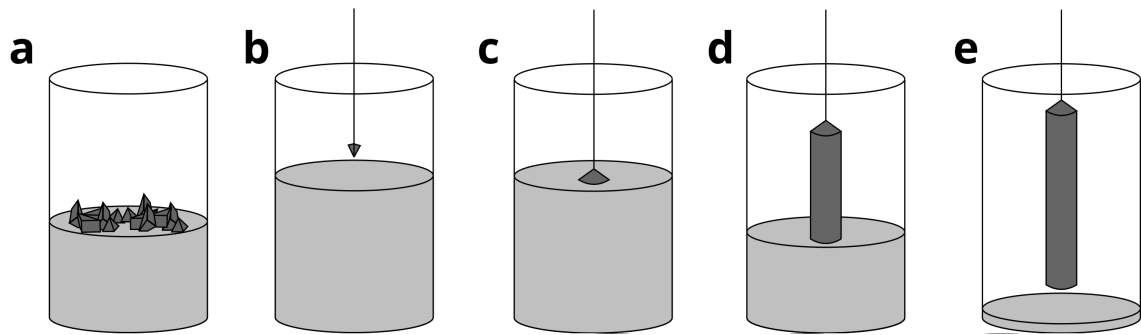


Figure 3.1. Fabrication of silicon ingot with Czochralski method which later on will be sliced with chemical mechanical saw and polished to make wafers. a) Melting of polysilicon and doping, b) introduction of the seed crystal, c) beginning of the crystal growth, d) crystal pulling, e) formed crystal with a residue of melted silicon

### 3.1.1. Wafer cleaving with a dicer

During dicing, wafers are typically mounted on dicing tape which has a sticky backing that holds the wafer on a thin sheet metal frame. Dicing tape has different properties depending on the dicing application. UV curable tapes are used for smaller sizes and non-UV dicing tape for larger chip sizes. We use DAD-320 Dicing Saw by Disco which has a 6" chuck shown in Figure 3.2 , multiple blade options, 1.5kW spindle.

#### Operation Steps of Dicer

- (i) Turn on DAD-320 Dicing Saw
  - (a) Turn on the cooling water by a quarter,
  - (b) Turn on the high pressure air,
  - (c) Press ON on the device keyboard, shown in Figure 3.3,
  - (d) Release emergency button,
  - (e) Turn on the key switch,
  - (f) Press SYS INIT to initialize the system,
  - (g) Check the blade type.
- (ii) Mount the sample to UV sensitive dicing tape
- (iii) Remove the cover of the machine and place the wafer to the middle of the chuck.



Figure 3.2. DAD-320 Dicing Saw by Disco

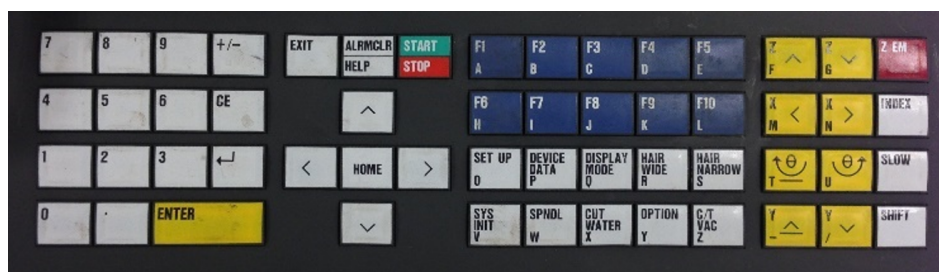


Figure 3.3. Dicer keyboard



Figure 3.4. Wafer chip mounted on UV sensitive tape, ready to be diced

- (iv) Press C/T VAC button and turn on the vacuum.
- (v) When initialization is completed select recipe then press “F1” to continue.
- (vi) Press F1 and check parameter of the recipe.
  - Choose Recipe Device No. 111
  - Work thickness: 525 um
  - Tape: 110 um
  - Blade height: 2500 um
  - Horizontal distance it cuts – 105 mm (max. 150mm)
  - Feed Speed: 10.00 mm/s
  - Blade thickness: 80 um
- (vii) Press F7 to select Semi Auto mode and check the parameters.
  - Kerf width is 40-400 um.
  - Period: 20 mm
  - Alignment escape amount: 20.000 mm
- (viii) Adjust focus.
- (ix) Align the first line by using “X” “Y” and “ $\Theta$ ” buttons.
- (x) When the alignment is done enter the number of lines and select the direction of repetition by pressing F5 or F10.

- (xi) Press **START** to run the dicing process when everything is ready.
- (xii) When dicing is finished press “**C/T VAC**” to get the sample.
- (xiii) Press “**SPNDL**” to stop blade rotating.
- (xiv) **EXIT** command till we reach main menu.
- (xv) Turn off by turning the keyswitch.
- (xvi) Lower the pressure to 50 PSI.
- (xvii) Turn off the water.
- (xviii) Unmount the tape after finishing the dicing.

### 3.1.2. Wafer cleaving with a scriber

We use Precision Diamond Scriber model SV-129 by ATV Tech which is a stage with a diamond tip scriber, rotating vacuum chuck for maximum 200 mm wafer, microscope, digital gauge (electronic ruler) and fine angle adjustment screws to manually cut the wafer.

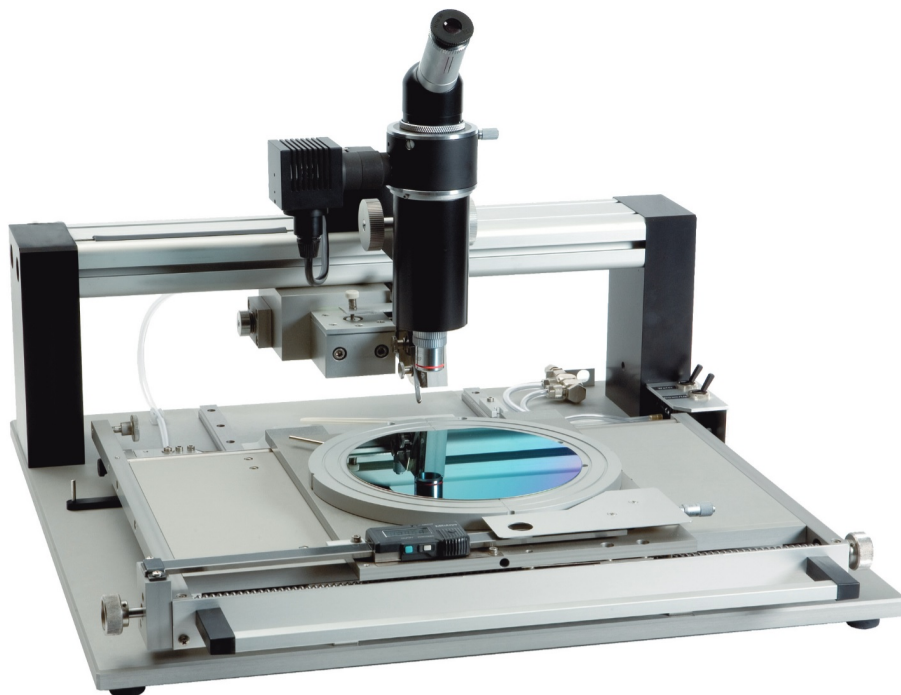


Figure 3.5. Precision Diamond Scriber model SV-129 by ATV Tech

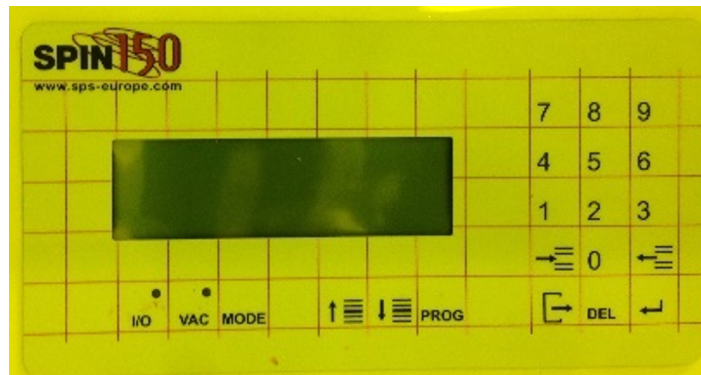


Figure 3.6. Spin coater keyboard

#### Operation steps

- (i) Before starting, make sure that the microscope is aligned with the scriber tip.
- (ii) Place the sample on the sample holder and turn on the vacuum.
- (iii) Adjust the alignment of the sample with angle screws and checking with the microscope.
- (iv) Check alignment marks by pulling the sample stage back and forth.
- (v) Align and lower the tip of the scriber.
- (vi) Pull the drawer outwards and cut the wafer.
- (vii) The electronic ruler is synchronized with the movement of the scriber tip.
- (viii) In order to cut the wafer perpendicular to the direction, turn the sample holder exactly  $90^\circ$  with handles by snapping it to the slot hence we will not need to align the sample again.

#### 3.1.3. Spin coating

Spin coating is a procedure used to deposit uniform thin films to wafer. Resist is a thin organic polymer which undergoes chemical changes when exposed to UV or e-beam. The wafer is immersed into acetone and isopropanol respectively and dried with nitrogen blow before the process starts. The wafer is placed on the spin coater chuck and an appropriate amount of resist is applied on the center of the wafer, which is either spinning at low speed or not spinning at all and then rotated at high speed in order to spread the coating material by centrifugal force.

## Operation Steps of Spin Coater

- (i) Set the temperature of the hot plate.
  - Baking temperature for EBL: 170°C (5 minutes)
  - Baking temperature for Photolithography: for photoresist AZ5214
    - \* Direct lithography: 105°C (1 minute)
    - \* Image Reversal: First bake (prebake) 90°C for 2 minutes, second bake (postbake) 115°C for 2 minutes.
- (ii) Turn on water over the sink for circulation.
- (iii) Open the spinner:
  - Turn the spinner power on by rotating the switch clockwise.
  - Press any key on the keyboard, shown in Figure 3.6, following the instructions on the panel.
  - Test the lid switch following the instructions.
  - Panel should say, Test is OK and then press any key on the keyboard. It is ready to use and program according to chosen recipe.
- (iv) Replace the protective liner with a new one if it is too dirty.
- (v) Enter the values. We can program process in a few steps or in a single step. For example, for photolithography we use a program which has a single step:
  - 4000 rpm
  - 45 seconds
  - 500 rpm/sec

VAC: \* means vacuum is ON it should be checked for every step.
- (vi) Place the sample to the middle of the chuck with tweezer, turn on vacuum.
- (vii) Put 1 ml resist per inch.
- (viii) Take the resist with appropriate disposable pipette.
  - Plastic for photoresist
  - Glass for EBL resist
- (ix) If there are any bubbles in the pipette, pour them to liner and then pour the resist onto the sample.
- (x) Close the lid tightly.
- (xi) Pressing I/O starts the process.

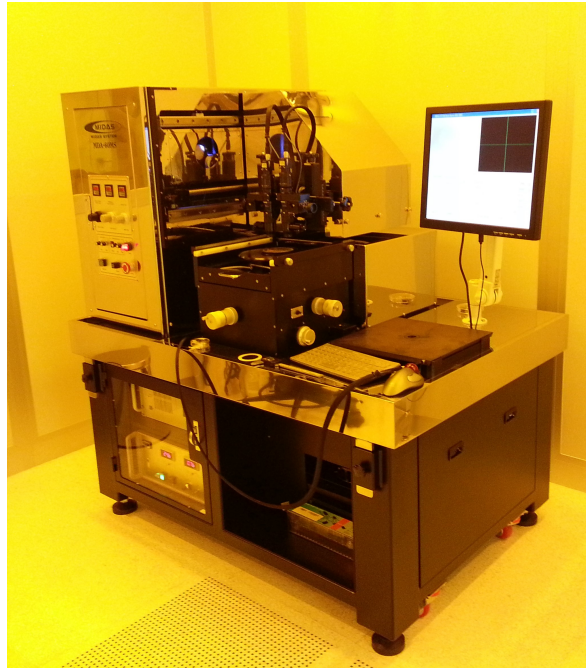


Figure 3.7. Midas Mask Aligner in the yellow room of SUNUM clean room

(xii) After spincoating the sample, prebake it to drive off excess resist solvent.

### 3.2. Photolithography

The technique of engraving patterns, geometric shapes forming the devices, on a resist coated wafer with ultra violet (UV) light or electron beam exposure is called lithography. The feature size of the device geometry determines which type of lithography is going to be performed. Photolithography (optical lithography or UV lithography) and electron beam lithography (e-beam lithography, EBL) are used for microfabrication and nanofabrication, respectively.

Photolithography is the process of writing the pattern on the photoresist with UV light exposure. We use contact photolithography which usually makes use of photomasks with approximately 5 micrometer precision. For multilayer processes we have alignment marks on the sample and the mask. We can choose the contact type according to design. There are four different types of contact: vacuum contact, hard contact, soft contact and proximity. While having the best resolution, vacuum contact requires the use of an O-ring which contaminates the mask irreversibly. Whereas proximity is

safer, mask damage is reduced to minimum. With soft and hard contact, mask and the wafer are brought into contact. They have better resolution than in proximity exposure.

In our processes, AZ5214E image reversal photoresist by MicroChemicals is generally used. The samples are spincoated 1 ml resist per inch for 45 seconds with rotation of 4000 rpm. The baking and exposure differ according to which type of lithography we are aiming to do. Direct lithography, called positive lithography, which involves single exposure to the sample with the photomask. We use MDA-60MS Mask Aligner 4" by Midas, shown in Figure 3.7. The parameters we use are the following:

- Mask thickness: 2.34 mm
- Sample thickness: 527  $\mu\text{m}$
- PR thickness: 1  $\mu\text{m}$  (photoresist thickness)
- Align Gap: 30  $\mu\text{m}$
- Power: 23.66 (Lamp power constant)

The steps for direct lithography we practice on the samples will be the following:

- coat the sample with photoresist AZ5214E with the standard parameters,
- bake the coated sample in 105°C for 1 minute,
- expose the sample for 4,5 seconds with the mask,
- develop the sample with AZ 726 MIF Developer for around 35 seconds, stop when the patterns look clearly,
- stop the developing process by soaking sample into DI water for around 1 minute.

For image reversal, also called negative lithography, there will be two exposures. First one will be the exposure with the mask. After postbaking the sample, the sample will be exposed without a mask (flood exposure). The steps are the following:

- coat the sample with AZ5214E,
- bake the sample at 90°C for 2 minutes,

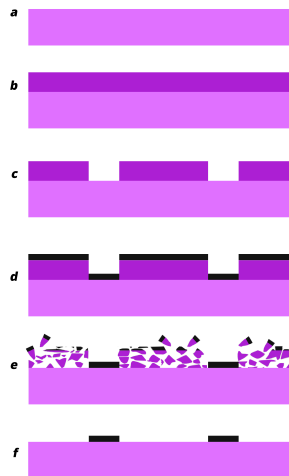


Figure 3.8. A typical lift-off process. a) Clean substrate, b) resist coated substrate, c) developed resist after exposure, d) material deposited on top of the resist and the pattern, e) remaining resist dissolving in acetone, f) patterned substrate

- expose the sample for 2.5 seconds with the mask,
- bake the sample at  $115^{\circ}\text{C}$  for 2 minutes,
- flood expose the sample for 12 seconds,
- develop the sample with AZ 726 MIF Developer for around 35 seconds, stop when the patterns look clearly,
- stop the developing process by soaking sample into DI water for around 1 minute.

According to the type of photolithography process (positive or negative), exposed or unexposed parts of the resist will dissolve. As a result, the pattern on the resist will be ready for either lift-off or etching processes, shown in Figure 3.8 and Figure 3.9, respectively. For the lift-off process, the material is deposited onto the patterned wafer. An example of a lift-off process is given in Figure 2.2.

### 3.3. Electron Beam Lithography

Electron beam lithography performs the same action as the photolithography with greater precision ( $\sim 5$  nm) due to focused beam of electrons. The beam exposure changes the solubility of the resist. The exposure occurs completely automated and

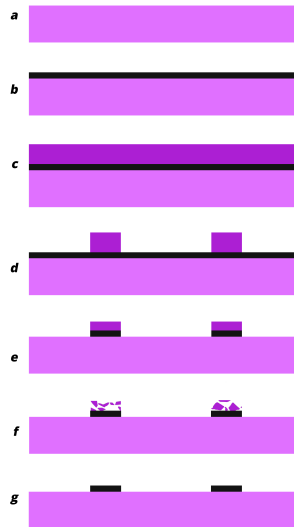


Figure 3.9. A typical etching process, the steps between c and d differ depending on the pattern that needs to be produced. a) Clean substrate, b) full film deposited substrate, c) resist coated on top of the film, d) developed resist after exposure, e) material etched, f) remaining resist dissolving in acetone, g) patterned substrate

software based, and no masks are used. It is an excessively slow process for mass production which is the reason photolithography is mostly still in use for microdevice making. The working principle of EBL can be very simply formalized in the following manner [43]:

$$D \cdot A = T \cdot I \quad (3.1)$$

where  $T$  is the exposure time in seconds,  $I$  is the beam current in nano amperes,  $D$  is the dose in coulombs per centimeter square,  $C/cm^2$  and  $A$  is the area exposed in centimeter square,  $cm^2$ .

The resolution is limited not by the electron beam size but the secondary electron effect in the resist due to high energy collisions. There is the proximity effect correction, PEC, operated by the software for small isolated features of the pattern. It mainly adjusts the beam dose taking into account the scattering of the beam. Otherwise the sharpness and the high resolution of the pattern around the edges would be lost.

The spin coating recipe for EBL resist (PMMA):

- Set the hotplate on 170°C.
- Process is programmed on spin coater software in 3 steps.
  - First one is at 4000 rpm for 4 seconds,
  - Second step is at 5000 rpm for 50 seconds,
  - for the last step it decelerates at 0 rpm for 3 seconds. This is done in order to obtain a uniform coating.
- Take out the sample, put on the hotplate and start the timer,
- Sample is baked for 5 minutes at 170°C. The same procedure is repeated for additional layers of resist.

The developing procedure for the EBL resist after the exposure:

- Prepare 3 beakers and 2 timers. The developing time, the time sample spends in each solvent is very critical.
- Soak the sample into 25% MIBK 75% ISO for 1 minute, this part functions as high resolution and low sensitivity developing.
- Second, soak it into 50% MIBK 50% ISO for 5 seconds which functions as low resolution and high sensitivity developing,
- Transfer it to ISO and rinse it for 1 minute.

### 3.3.1. Wafer chip production

For most of processes, the first step is to have 2x2 cm<sup>2</sup> square wafer chips. For EBL, the maximum chip size is 2x2 cm<sup>2</sup> due to the sample holder of Vistec EBPG5000plusES, the e-beam lithography equipment.

In order to produce 2x2 cm<sup>2</sup> square wafer chips precisely, we made a 5" photomask with a grid of squares, shown in Figure 3.10, to apply onto 4" wafers. We manufactured the mask with EBL with the following parameters:

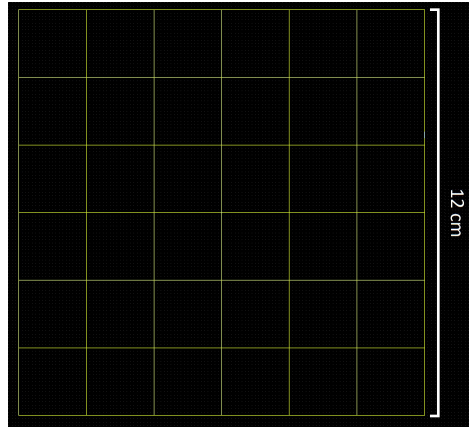


Figure 3.10. Layout Editor drawing of the 5" mask with grids

- Beam current: 120 nA
- Dose: 800  $\mu\text{A}$
- No PEC because the mask does not require high precision, the smallest feature is 100  $\mu\text{m}$ .

The chrome masks come precoated and after exposure we develop the mask with following solvents:

- Developer I: 93% MEK, 7% Anisole. Soak the mask in this for 1 minute and 20 seconds.
- Soak the mask in 50% MIBK, 50% ISO for 10 seconds.
- Soak in ISO for a few minutes, ISO is the stopper of the developing process for EBL.
- Dry the mask with nitrogen blow gun.

This was done to develop the resist on the chrome coated mask. In order to complete the mask production process, we need to apply etch. For this purpose, we use Chrome ETCH N°1, we soak the mask in this for 2 minutes in the ultrasonic bath. While etching process occurs, bubbles form. To dispel these bubbles, we dip the mask to DI water and put it back into the etch. After etching is done, place the mask in DI water while preparing for piranha cleaning which is the last step for mask production.

Piranha cleaning is a sensitive process involving acid usage. Before starting piranha cleaning, wear eye protection, acid gloves over usual gloves and additional acid resistive apron over usual gown. Piranha solution we prepared consists of 25% hydrogen peroxide (35%  $\text{H}_2\text{O}_2$ ) and 75% sulfuric acid (95-98%  $\text{H}_2\text{SO}_4$ ). The treatment should be done with glass (Pyrex glassware), stainless steel and PTFE(Teflon) tools or containers as the solution reacts violently with organic materials such as plastics and the solution should not be put in direct contact with isopropanol or acetone.

The mask is put inside the solution for 5 minutes. A hotplate may be used at  $100^\circ\text{C}$  in order to have a stronger reaction. Later it is placed in another container filled with DI water, taken out and sprayed DI water with the gun, put in acetone and isopropanol to clean off any solution residue, and lastly blown dry with nitrogen gun.

We spincoat 4" wafer with AZ5214E photoresist and apply photolithography. After we get the grid of chips pattern on the 4" wafer, we cleave the wafer with a dicer or scribe with the guidance of the grids. Because we apply photoresist which is very thick on the wafer, it protects the wafer in the process and keep them clean till we use them but we need to thoroughly clean the chips before we start the process.

### 3.4. Nanopillar Device

In order to investigate certain micromagnetic structures such as radial vortex, in chapter 5, nanopillar devices were produced. Before the production of the nanopillars, the materials which were going to be used were determined, their deposition and ion mill rates were calibrated. After the magnetic characterization of the different repeats of full film Pt/ $\text{Co}_{20}\text{Fe}_{60}\text{B}_{20}$ /Ti stack, we began the nano pillar process by the following steps:

- (i) thin film deposition of full film Pt/ $\text{Co}_{20}\text{Fe}_{60}\text{B}_{20}$ /Ti stack,
- (ii) e-beam evaporation of carbon on top of the full film,
- (iii) e-beam lithography of nanopillar pattern,
- (iv)  $\text{O}_2$  plasma etch to remove resist residue on the pattern,

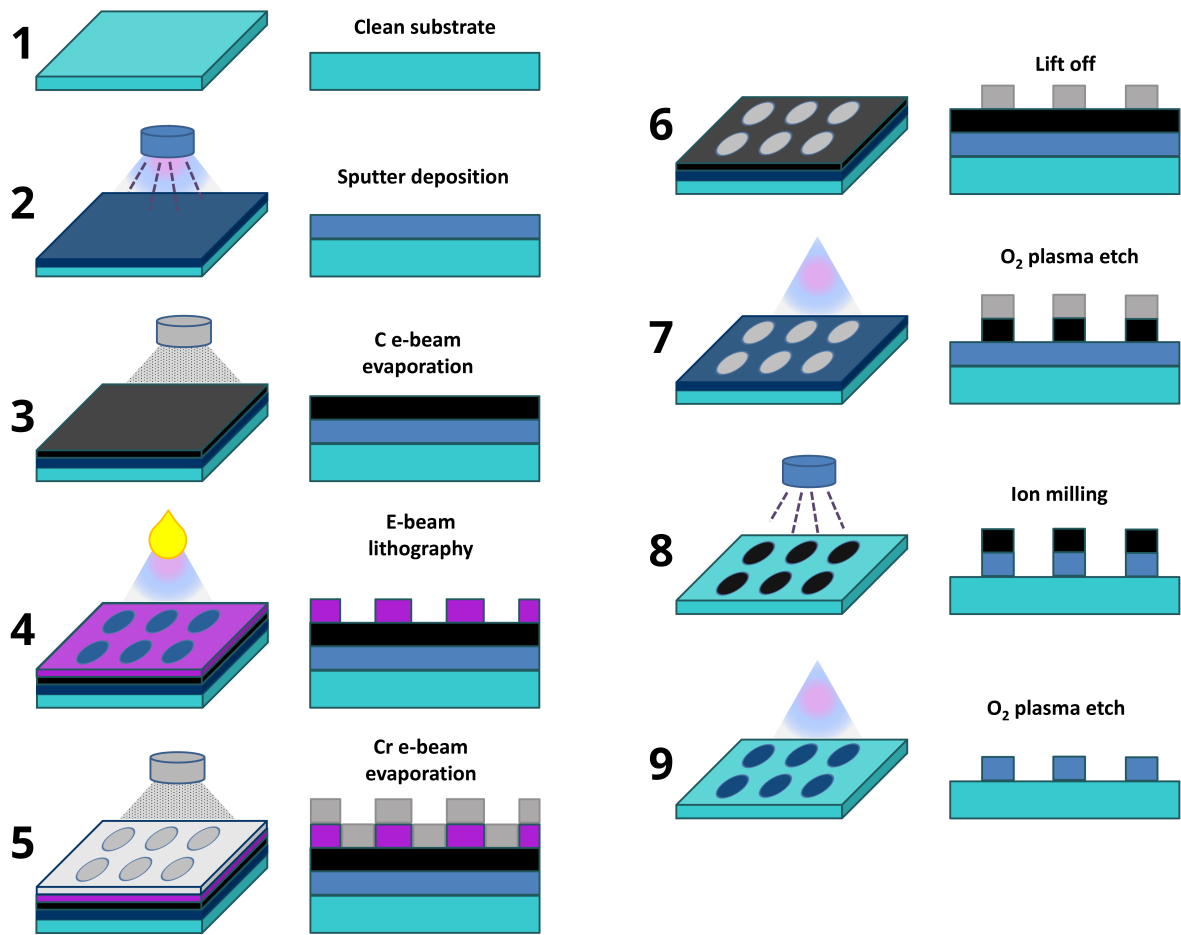


Figure 3.11. Nanopillar process diagram

- (v) e-beam evaporation of chromium,
- (vi) lift-off,
- (vii) second O<sub>2</sub> plasma etch,
- (viii) ion milling,
- (ix) final O<sub>2</sub> plasma etch.

The deposition and ion mill rates of all materials; Co<sub>20</sub>Fe<sub>60</sub>B<sub>20</sub>, Pt, Ti, are determined. The repeated stack is deposited with a programmed sequence by the software of AJA magnetron sputtering system at 2 mTorr Ar pressure.

After the thin film deposition, the sample is C coated with e-beam evaporation. Carbon is a relatively tough material for evaporation because it needs adjustment of the applied current to reach stable evaporation rate due to the its instant rate increment

during evaporation. However we found the rate was to be 0.2 Å/s, our target carbon thickness for this process was 50 nm. The deposition was performed at  $10^{-5}$  Torr pressure, the current was adjusted throughout the deposition in order to keep the rate steady. As evaporation material, we used 1/8" x 12" carbon rods cut into 0.5 cm long pieces. We mounted our samples on a 4" dummy wafer. Our parameters for carbon evaporation were as follows: 150% tooling factor, 2.25 g/cm<sup>3</sup> density, 3.26 Z factor.

Two different e-beam resists, C2 495 and C 950, are used for the patterning of nanopillars. They give 130 nm and 100 nm thicknesses, respectively. First C2 495 is spin coated at 5000 rpm for 50 sec, then the sample is baked at 170°C for 5 minutes. Subsequently, C2 950 is coated with the same parameters and baked at 170°C for another 5 minutes. After coating the resists, next step is to exposing the sample to e-beam for patterning and developing. For developing process, three different solutions are prepared: first one containing 25% MIBK developer and 75% isopropanol, second one containing 50% MIBK and 50% isopropanol, third one is 100% isopropanol which functions as the stopper. In order to develop, the sample is soaked into the first solution for 1 minutes, then taken out quickly and soaked into the second solution for 30 seconds, finally taken out and soaked into the stopper which is isopropanol.

After developing process, O<sub>2</sub> plasma is applied for 3 seconds at 10°C with 5 Å/s rate to make sure that there is no resist residue before Cr coating. Next, the sample is coated 6 nm Cr with e-beam evaporation with the following parameters: 117% tooling factor, 7.21 g/cm<sup>3</sup> density and 0.31 Z factor. Cr evaporation rate was found to be 0.3 Å/s. For the lift off process, Cr coated sample is soaked in acetone for 2 days and later sonicated in acetone and isopropanol separately at 50% power for 4 seconds. The sample is exposed to O<sub>2</sub> plasma at 10°C to get rid of 50 nm C layer.

After O<sub>2</sub> plasma etch, we have 56 nm thick pillars of C (50 nm) and Cr (6 nm) on top of the magnetic full thin film stack, as shown in step 7 of Figure 3.11. Etch rates of C and Cr are smaller than metallic stack (Pt/Co<sub>20</sub>Fe<sub>60</sub>B<sub>20</sub>/Ti) so that we could get 110 nm nanopillar structure at the end of the milling operation.



Figure 3.12. TORR International e-beam & thermal evaporator

Finally, in order to remove remaining C layer on the nanopillar,  $O_2$  plasma etch was used for 90 seconds.

#### 3.4.1. E-beam evaporation

Electron beam evaporation technique is used for carbon and chromium deposition steps. The specific system, TORR e-beam & thermal evaporator shown in Figure 3.12, used during the nanopillar production is operated by the following steps:

- (i) Turn on the chiller of the system.
- (ii) Turn on the system from main switch shown in Figure 3.13.
- (iii) Open the chamber door handles and open the chamber door.
- (iv) After opening the main chamber, check the appropriate boat/crucible (shown in Figure 3.14a), place the required boat/crucible and enough material.
- (v) Select appropriate pocket for the crucible by pressing the “pocket indexer” button. Press the button “one at a time” so the pocket rotation do not end up at



Figure 3.13. Main switch of the e-beam evaporator

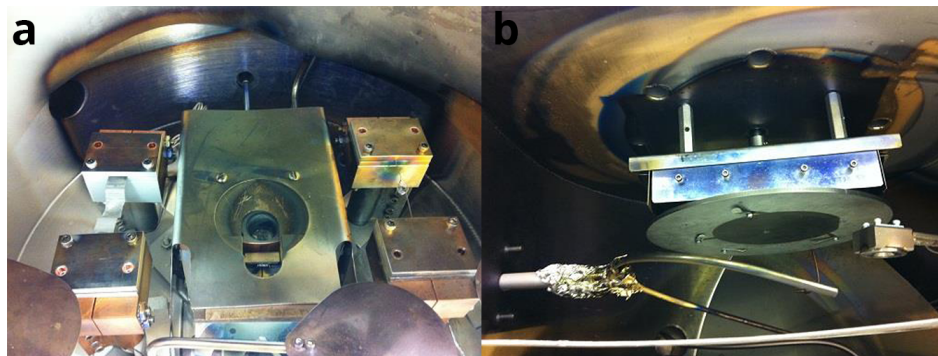


Figure 3.14. E-beam evaporator a) pocket and b) sample holder

half rotation.

- (vi) Take the sample holder, shown in Figure 3.14b, out by rotating it clockwise and using screws on it, use vacuum tape and stick the samples onto the sample holder.
- (vii) After placing the wafer into the system, start the vacuuming sequence by turning on the vacuum switch.
- (viii) For appropriate vacuum level we should wait until  $\sim 8 \times 10^{-6}$  Torr. Vacuuming to that level takes generally 45 to 60 minutes. Pressure can be read from pressure gauge.
- (ix) After reaching to desired vacuum level, set the thickness monitor. Press “program” button and turn the knob for selecting the film number, if it has been already set and press “next” button till the end of the menu and press “program” button again to exit the menu.
- (x) Turn on the “e-beam shutter”.
- (xi) Turn on the main power on the high voltage power supply, press “FIL ON” and wait 3-5 minutes for warming and press “HV ON”.

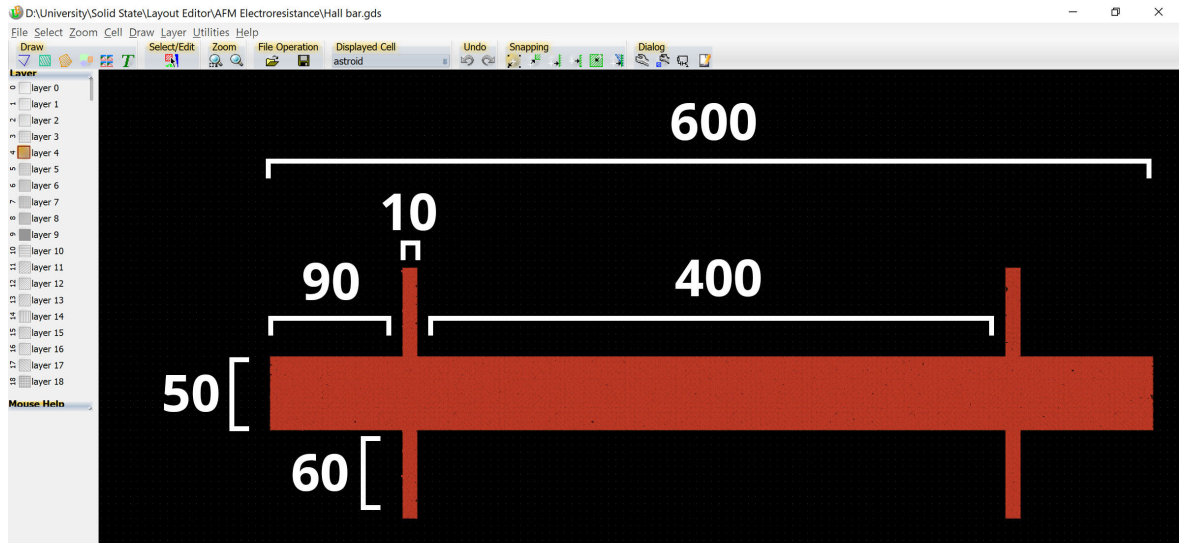


Figure 3.15. Hall bar design, drawn in Layout Editor, all dimensions in micrometers

- (xii) Increase the current with the current knob until we see some rate on thickness monitor.
- (xiii) After reaching the desired thickness, turn off in this order:
  - (a) Turn the Shutter off
  - (b) Turn the current knob off slowly
  - (c) "HV" off/reset
  - (d) Filament "FIL OFF"
  - (e) Turn off the main power for e-beam high voltage source.
- (xiv) When the deposition is finished, turn off the vacuum switch and wait 15 minutes for turbo pump to slow down.
- (xv) When pressure level is reached to  $8 \times 10^{-3}$  Torr level, turn on the "VENT" switch.
- (xvi) Open the chamber, take the samples out, put the sample holder back in, close the chamber, close the system from the main switch, turn off the chiller.

### 3.5. Hall Bar Device

We started by designing Hall bar device, chapter 6, and the contact area that will come on top. The dimensions of a typical Hall bar are known in literature. We chose the area of magnetic material without the contact area to be around  $400 \times 50 \mu\text{m}$ . We preferred to have as wide contact area as possible and extended the length of

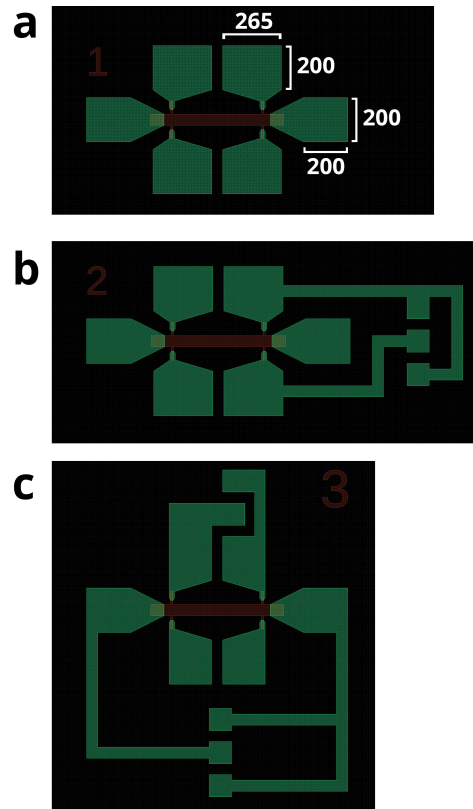


Figure 3.16. Hall bar contact designs a) first type: simple and dense wirebonder only contact pads, b) second type: contains everything in the first design and the probe pads for Hall voltage measurement, c) third type: everything in the first design and the probe pads for 4-probe electroresistance measurement, all dimensions in micrometers

the bar by  $100\mu\text{m}$  at each end where large electrodes will emerge. Main current will be passing through these electrodes. We also need the other contact points to measure the response of the material to the current such as ordinary Hall effect and spin Hall effect. In this study, we focus on electroresistance, the change in the resistance of the material with changing current but, we would also like to be able to do other standard experiments performed on Hall bars with our design.

We use  $2\times 2\text{ cm}^2$  wafer chips Figure 3.17 because, this is the maximum size we can put in e-beam lithography stage and GMW electromagnet stage. We divide the square chip in four  $1\times 1\text{ cm}^2$  parts. There are two photolithography steps for the production of these samples. First one is for the deposition of the magnetic material, shown in red in the drawings, for stripes, sample numbers, cross alignment marks and the chip

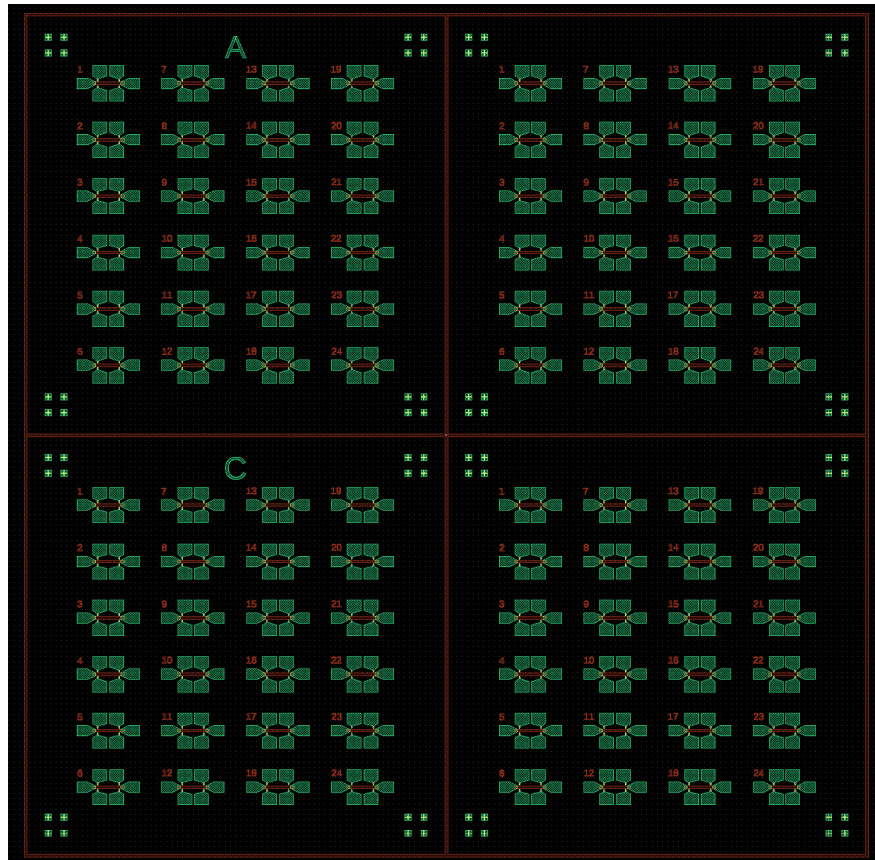


Figure 3.17. Hall bar regular chip design with dimensions of  $2 \times 2 \text{ cm}^2$ , four  $1 \times 1 \text{ cm}^2$  parts, each part containing 24 samples, drawn in Layout Editor. Alignment marks at the corners of every  $1 \times 1$  piece, A and C labels are there to enable determination of the chip orientation

frame. In the second step, we deposit contact material for electrodes. Au is deposited for the electrodes, shown in green in the drawings. For electroresistance experiments we designed three types of electrodes for different applications. The initial design has wide contact pads suitable only for wirebonding, dimensions shown in Figure 3.16a. First design has the highest density with 24 samples in each quarter,  $1 \times 1 \text{ cm}^2$  pieces. We also designed the other two types for room temperature applications with the use of RF probe.

Second design Figure 3.16b has RF Probe pads with dimensions of  $100 \times 100 \mu\text{m}$  for ordinary Hall effect measurements such as Hall voltage and Hall resistance in addition to the wirebonding contact pads. Each quarter can contain 18 samples with this type. Lastly the third design Figure 3.16c has RF Probe pads for electroresistance

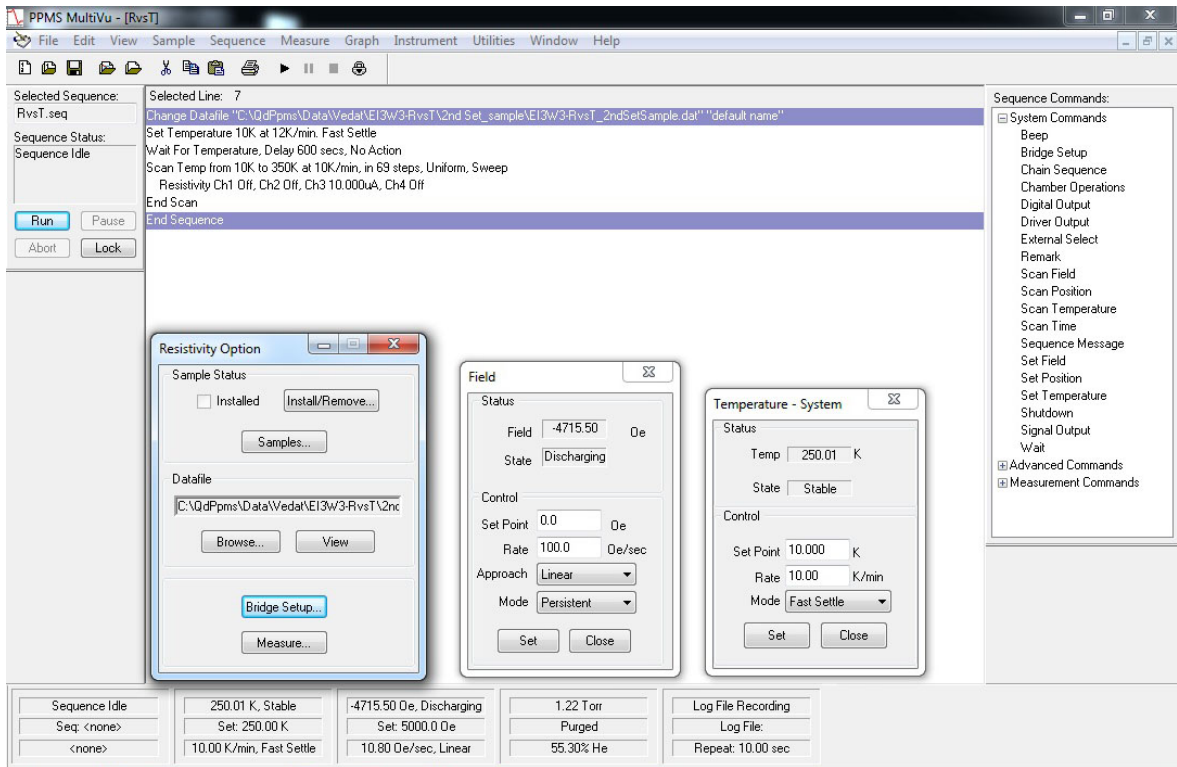


Figure 3.18. PPMS Electrical Transport Option sequence for temperature versus resistance measurement from 10 K to 350 K

measurements, 2-probe and 4-probe. This large design allows only 9 samples per each quarter. The distance between pads are arranged in a way to prevent shortage but to maximize the contact area in order to decrease the contact resistance and provide space for multiple wirebonding trials. On the other hand, there was not much freedom on probe pad design as the distance between each arm is fixed.

With two lithography and two deposition steps, the samples were developed and ready for the experiments. PPMS is used for field cooling, resistance ( $R$ ) vs current ( $I$ ),  $R$  vs temperature ( $T$ ), magnetization ( $M$ ) vs magnetic field ( $H$ ) measurements. An example sequence is shown in Figure 3.18.

The samples are divided into small parts by dicer to fit them into chip carriers. These small pieces are then glued to the 8-pin chip carriers with GE varnish. In order to apply magnetic field in different directions inside PPMS, a regular electrical transport puck was transformed to an in-plane chip carrier holder, shown in Figure 3.19b.

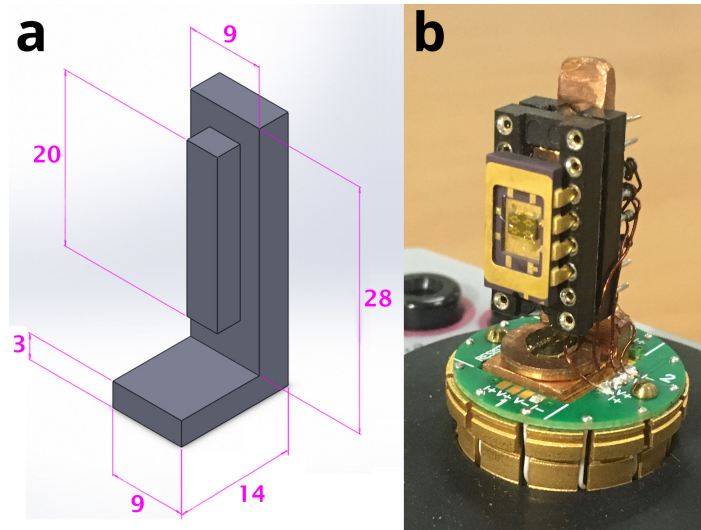


Figure 3.19. a) Technical drawing of the part for modification of PPMS puck (dimensions given in millimeters) and b) in-plane chip carrier holder mounted on PPMS puck

In detail, in-plane sample holder was milled out of bronze, schematic drawing shown in Figure 3.19a, mounted onto PPMS puck with a screw and, a 16-pin IC socket was glued to the bronze piece with GE varnish, shown in Figure 3.19b. This sample holder was designed to hold an 8-pin chip carrier and, the connections between 8 of the IC socket pins and the gold pads on the puck corresponding LEMO channel connections were made by soldering very thin copper magnet wire. We used lead-free solder to improve the conductivity of our connection and, we used least flux possible to avoid any shorting between very small and in close proximity channels. While using thin magnet wire, we removed the insulating layer from the tips of the wire with a razor blade and etched the remaining insulating material with the hot soldering tip.

After the samples are glued to the chip carriers, the last step before we start the measurements is the wirebonding. The electrodes are connected to the pads on the chip carriers with wirebonder as shown in Figure 3.20c. An aluminum piece, schematic drawing shown in Figure 2.11a, was machined to enable operation of the wirebonder on chip carriers. The aluminum stage also functions as a shorting bridge, as shown in Figure 3.20b, to protect the samples from static electric during wirebonding process.

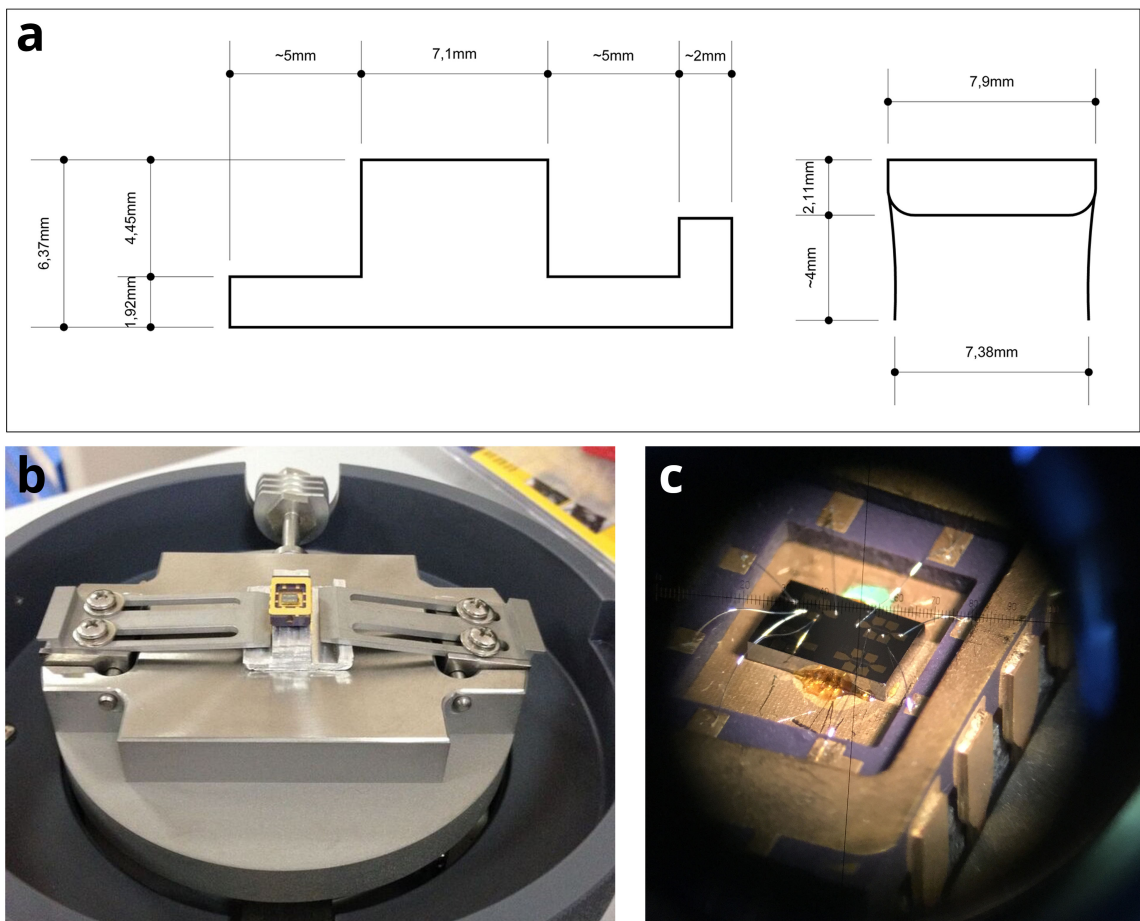


Figure 3.20. Wirebonding equipment a) schematics of the wirebonder stage and 8-pin gold plated CERDIP (Ceramic Dual Inline Packages) chip carrier, b) chip carrier mounted on wirebonder stage with our custom made aluminum stepping stage and c) Hall bar electrodes wirebonded to chip carrier gold pads under the microscope

## 4. MAGNETIC ANTIVORTEX

In order to observe and investigate the stability of magnetic antivortices, micromagnetic configurations that have not been intensively explored, we work with permalloy ( $\text{Ni}_{81}\text{Fe}_{19}$ ) nanomagnets. We used a special geometric shape called astroid that can allow antivortex nucleation, predicted by micromagnetic simulations [7]. According to this theoretical study, nucleation and annihilation of stable antivortex conditions were determined. AC demag state and -10 mT external magnetic field applied state where stable antivortex forms at the crossing point (red and blue arrows) were shown in Figure ??.

We fabricated nanomagnets with e-beam lithography and aimed to observe the magnetic configurations under magnetic force microscopy. Several contact designs have been tried and different electrical setups have been constructed for room temperature and low temperature measurements under magnetic magnetic field.

Magnetic imaging with MFM and anisotropic magnetoresistance measurements proved that nucleation and observation of antivortex micromagnetic configuration in astroid shaped nanomagnets were successfully achieved. Manipulation of antivortex motion by interaction with applied magnetic field was also accomplished.

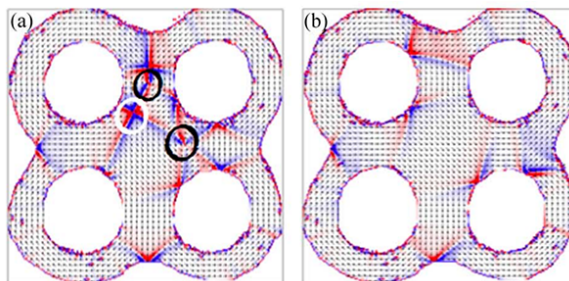


Figure 4.1. Micromagnetic simulations of a) AC demagnetized state, b) -10 mT magnetic applied field at  $135^\circ$ . Local magnetic moments are mapped by blue and red arrows [7].

### 4.1. Anisotropic Magnetoresistance

Magnetoresistance is the inclination of magnetic materials (most commonly ferromagnets) to have a change in their electrical resistance under a magnetic field [1]. Anisotropic Magnetoresistance (AMR) is the change in the resistance of the material according to the applied magnetic field. AMR was first discovered by William Thomson, also known as Lord Kelvin. The observation of an increase in the resistance when a large magnetic field is applied parallel to the conduction current and a decrease in the resistance when applied field is perpendicular to the current in iron and then the more significant change, especially with longitudinal magnetization, in nickel were reported [44].

The change in resistivity of a ferromagnetic material due to AMR can be defined with the following Equation [45],

$$\rho(\varphi) = \rho_{\perp} + (\rho_{//} - \rho_{\perp}) \cos^2 \varphi = \rho_{\perp} + \Delta\rho \cos^2 \varphi \quad (4.1)$$

where  $\varphi$  is the angle between the magnetization direction and current direction flowing through material,  $\rho$  is the longitudinal resistivity of the material,  $\rho_{\perp}$  is the resistivity of the material when magnetization and current are perpendicular to each other, and  $\rho_{//}$  is the resistivity of the material when they are parallel. Additionally,  $\Delta\rho$  can be defined as the difference between parallel and perpendicular resistivities.

In this study we focused on astroid shaped patterned nanomagnet made up of 35 nm  $\text{Ni}_{19}\text{Fe}_{81}$  (Py), soft ferromagnet, because Py is a special material that has almost 5% of anisotropic magnetoresistance (AMR) ratio. To nucleate antivortex spin alignment at the center of the device geometry AC demagnetization process was done with a 1 T out of plane magnetic saturation. We used the lock-in technique to conduct the AMR measurement. The sample was connected to a lock-in amplifier, a resistance box, a DC power supply and our custom made circuit box that contains Wheatstone bridge to obtain AMR signal.

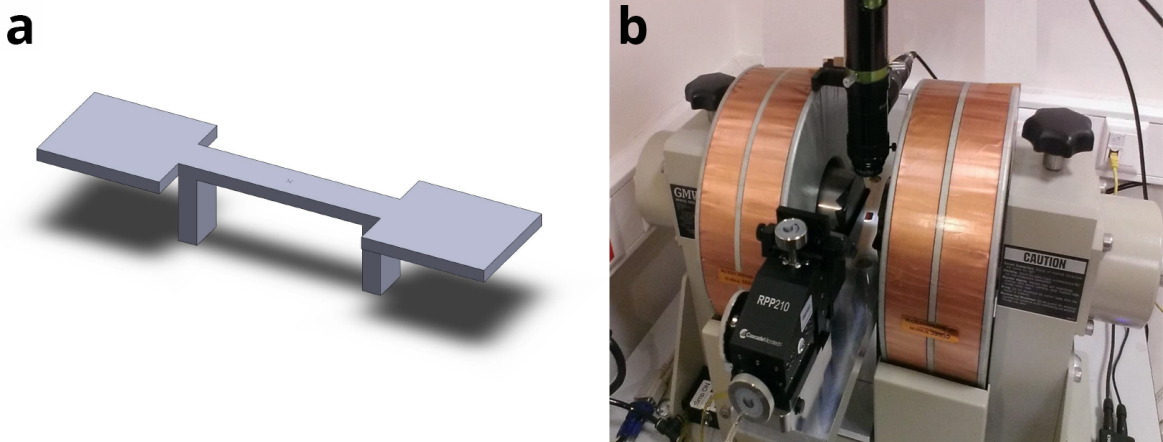


Figure 4.2. Experimental setup for the anisotropic magnetoresistance measurements.

- a) Schematic drawing of the probe station design, b) sample and probes mounted onto the manufactured station of GMW electromagnet.

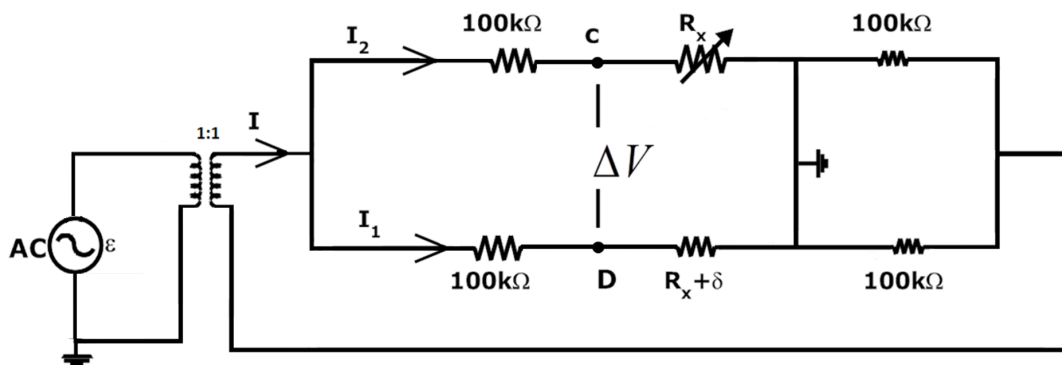


Figure 4.3. Circuitry of the AC measurement setup

Measurements were done at room temperature using the GMW electromagnet shown in Figure 4.2b. In order to incorporate RF Z probes onto our electromagnet, a custom-made sample stage was machined.

A Wheatstone bridge was used to detect the AMR signal and mathematical calculation was done through applying Kirchhoff's Rules in each loop, the electrical circuit schematic is demonstrated in Figure 4.3.

We read the output voltage  $V_{out}$  by balancing the base resistance,  $R_{sample}$ , with the decade resistance box. Resistance variation of the sample,  $\delta$ , with respect to the angle between the applied current and magnetization directions was read via  $V_{out}$ . Derivation of the  $V_{out}$  formula in terms of  $R_{sample} = R_x + \delta$  and  $R_{box} = R_x$  for electrical measurement setup is given below.

$$\begin{aligned}
I &= \frac{\epsilon}{R_{eq}} = \frac{\epsilon}{100k\Omega} \\
I &= I_1 + I_2 \\
I_2 &= I - I_1 \\
I_2 (100k\Omega + R_x + \delta) - I_1 (100k\Omega + R_x) &= 0 \\
I_2 (100k\Omega + R_x + \delta) &= I_1 (100k\Omega + R_x) \\
(I - I_1) (100k\Omega + R_x + \delta) &= I_1 (100k\Omega + R_x) \\
I (100k\Omega + R_x + \delta) &= I_1 (200k\Omega + 2R_x + \delta) \\
I_1 &= \frac{I (100k\Omega + R_x + \delta)}{(200k\Omega + 2R_x + \delta)} \\
I_2 &= \frac{I (100k\Omega + R_x)}{(200k\Omega + 2R_x + \delta)} \tag{4.2} \\
\Delta V &= V_D - V_C \\
\Delta V &= \frac{\epsilon}{100k\Omega} \frac{(100k\Omega + R_x)}{(200k\Omega + 2R_x + \delta)} (R_x + \delta) - \frac{\epsilon}{100k\Omega} \frac{(100k\Omega + R_x + \delta) R_x}{(200k\Omega + 2R_x + \delta)} \\
\Delta V &= \frac{\epsilon}{100k\Omega} \frac{\epsilon}{(200k\Omega + 2R_x + \delta)} \\
&\quad \times ((100k\Omega + R_x) (R_x + \delta) - (100k\Omega + R_x + \delta) R_x) \\
\Delta V &= \frac{\epsilon}{100k\Omega} \frac{1}{(200k\Omega + 2R_x + \delta)} (100k\Omega \delta) \\
\Delta V (200k\Omega + 2R_x + \delta) &= \epsilon(\delta) \\
\Delta V (200k\Omega + 2R_x) &= (\epsilon - \Delta V)\delta \\
\frac{\Delta V (200k\Omega + 2R_x)}{(\epsilon - \Delta V)} &= \delta
\end{aligned}$$

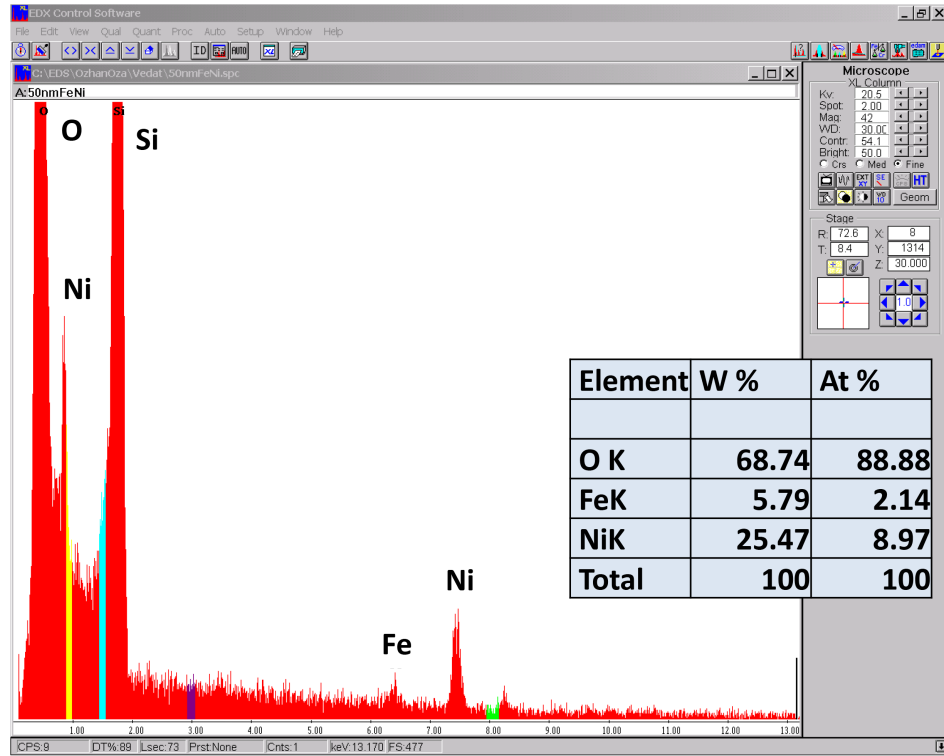


Figure 4.4. Energy Dispersive X-Ray Spectroscopy measurement performed on 20 nm  $\text{Ni}_{81}\text{Fe}_{19}$  thin film and the calculated percentages of resulting elements.

## 4.2. Experiments

### 4.2.1. Characterization of Permalloy Thin Films

Before the antivortex measurements, we needed to characterize the physical and magnetic properties of ferromagnetic  $\text{Ni}_{81}\text{Fe}_{19}$  (Py) thin films. We calibrated deposition rate of Py in 2 mTorr Ar pressure, at 100 W supplied by a DC power source, to fabricate the magnetic thin film in optimal conditions. After the calibration, the magnetic films were characterized chemically by Energy Dispersive X-Ray Spectroscopy (EDX) and magnetically by Vibrating Sample Magnetometer (VSM). In EDX measurement done on 20 nm  $\text{Ni}_{81}\text{Fe}_{19}$  thin film, Ni, Fe, Si, O peaks can be seen in Figure 4.4. Detected Si and O are due to the fact that thin film has been grown on Si substrate. Another reason for the detected O is that the thin film prepared for EDX measurement did not have an oxidation passivation layer. Calculating Ni/Fe ratio from EDX measurement, we find  $8.97/2.14=4.2$  which is very close to our target ratio  $81/19=4.3$ .

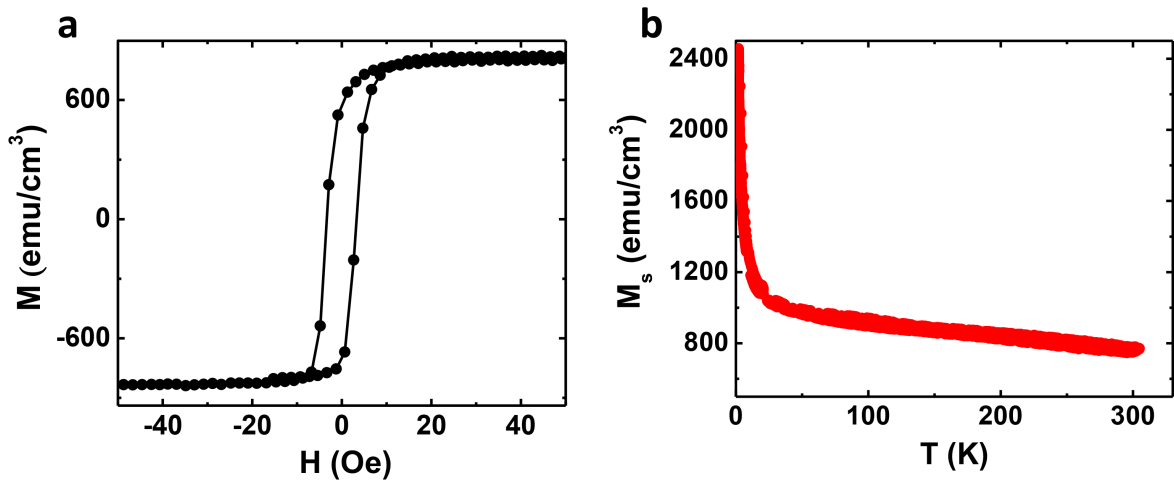


Figure 4.5. Vibrating Sample Magnetometer measurement of 20 nm  $\text{Ni}_{81}\text{Fe}_{19}$  thin film, a) magnetic hysteresis at room temperature and b) saturation magnetization vs temperature measured at 1 T external field

As shown in Figure 4.5, our thin film has ferromagnetic properties with  $800 \text{ emu/cm}^3$  saturation magnetization and 3.5 Oe coercive field at room temperature. We also observed that saturation magnetization increases with decreasing temperature up to  $2400 \text{ emu/cm}^3$  at 2 K.

#### 4.2.2. Determination of EBL resists and parameters

Following the optimization of magnetic thin film fabrication, we proceeded with patterning astroid shaped nanomagnet. Dimensions of the astroid design are given in Figure 4.6 on Layout Editor drawing. These dimensions were determined via simulations [7] and proved to produce antivortices [16]. As this geometry contains nanometer sized features, its patterning can only be achieved by electron beam lithography. Fabrication steps of astroid shaped nanomagnets are given in Figure 4.7. The process starts with a cleaning Si substrate and followed by spin coating EBL resist.

The first set of samples we produced had no contacts. They were fabricated only to observe the magnetic structure inside astroid shape under magnetic force microscopy. After MFM measurements, we worked on different contact ideas. The first scheme we tried was using a pattern design that will contain the astroid geometry and the contacts

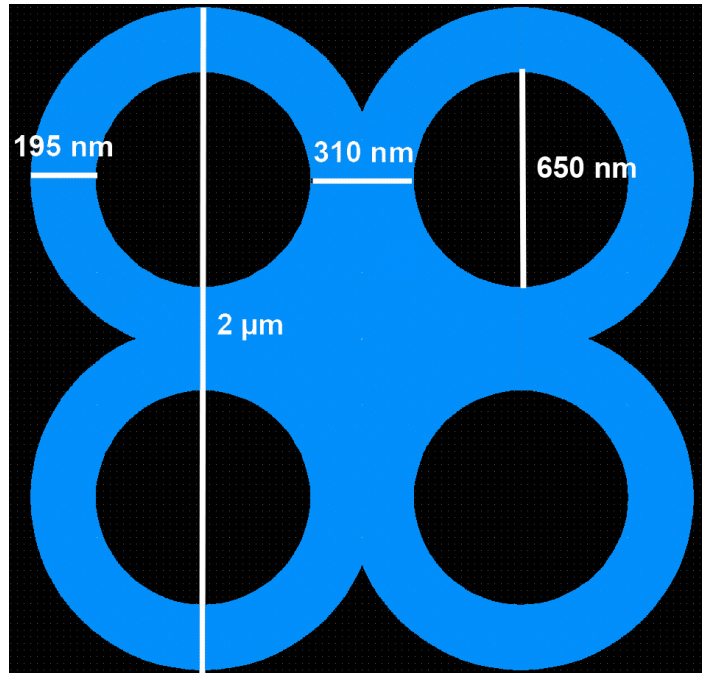


Figure 4.6. Dimensions of the astroid shaped nanomagnet design

together. This would enable us to have the device and the contact area with a single electron beam lithography step. We were successful with patterning of an isolated astroid geometry, but we needed to perform additional tests in order to determine appropriate EBL parameters for this scheme. The result of our EBL exposure dose test is shown in Figure 4.8. Later this contact scheme was abandoned, but the findings from this dose test proved to be useful.

With the exposure dose test, we determined the optimal parameters for astroid fabrication shown in Table 4.1. Fine features include nanometer sized astroid devices and alignment marks whereas coarse features include the wafer chip frame, coarse alignment marks and device numbers. The maximum chip size we could use with EBL sample holder was limited to  $2 \times 2 \text{ cm}^2$  square, we divide this square chip into  $1 \times 1 \text{ cm}^2$  squares by including frames to our lithography pattern.

In addition to adjusting EBL parameters, we also tried different EBL resist combination that will provide the necessary features for our device. We used a single layer resist, PMMA C2 495 at 5000 rpm for 50 seconds which is supposed to result in 130 nm thickness. On another sample, we coated our chip with PMMA C2 495 first, 130

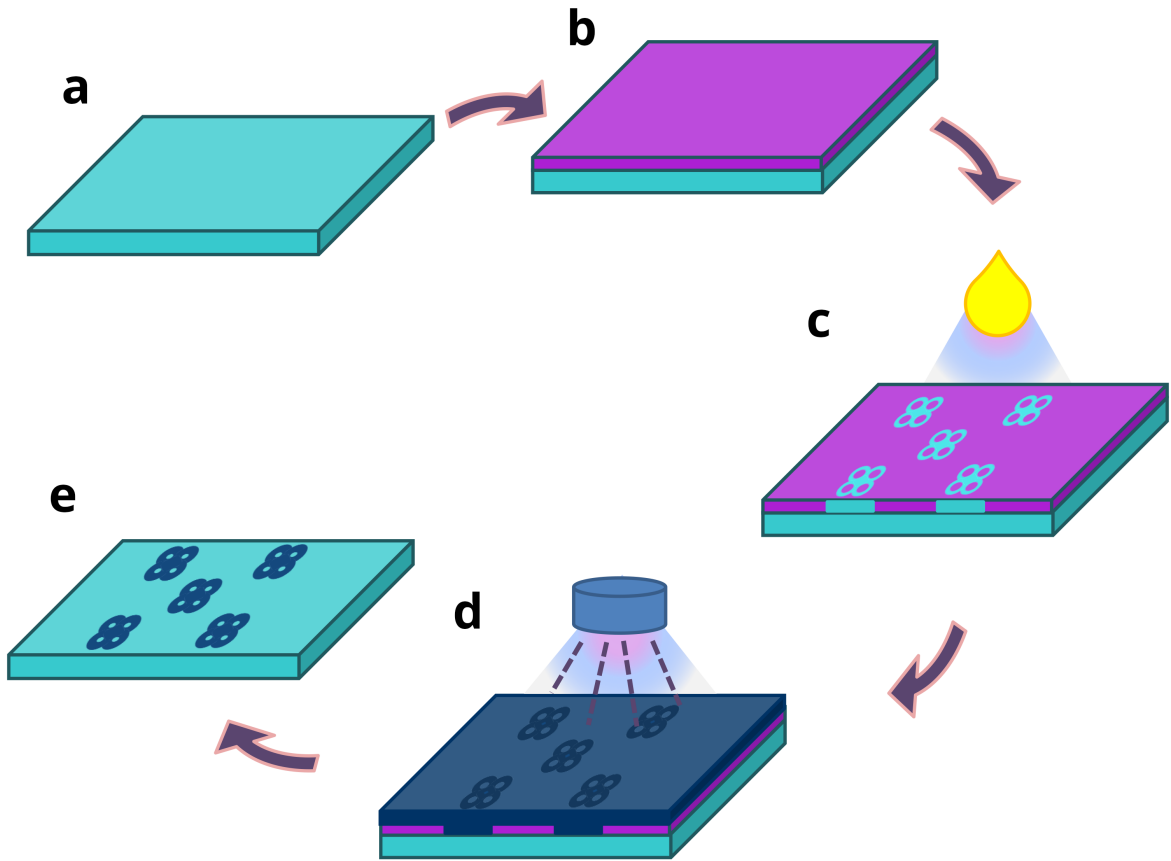


Figure 4.7. Fabrication of astroid shaped nanomagnets, a) cleaning Si substrate in acetone and isopropanol, b) spincoating EBL resist, c) e-beam exposure and development, d) deposition of permalloy by magnetron sputtering, and e) lift-off

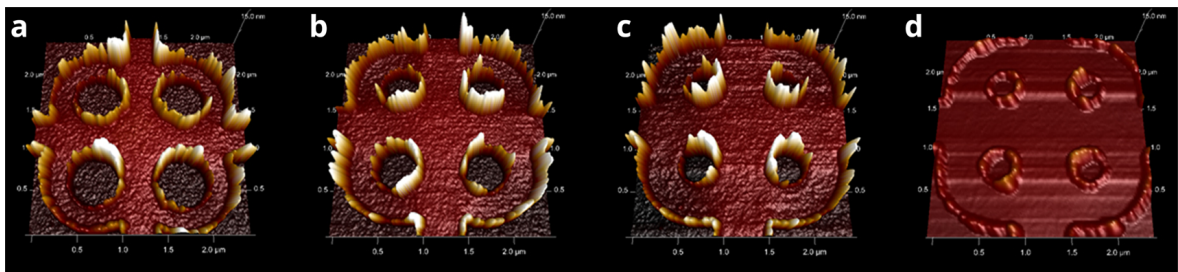


Figure 4.8. Atomic force microscopy images of astroid shaped nanomagnets, EBL dose test with a)  $400 \mu\text{C}/\text{cm}^2$ , b)  $500 \mu\text{C}/\text{cm}^2$ , c)  $600 \mu\text{C}/\text{cm}^2$  and d)  $650 \mu\text{C}/\text{cm}^2$  exposure doses.

Table 4.1. EBL parameters for the first set of astroid devices

Features	Fine	Coarse
Beam Current	300 pA	80 nA
Beam Dose	400 $\mu\text{C}/\text{cm}^2$	600 $\mu\text{C}/\text{cm}^2$
Resolution	2 nm	25 nm

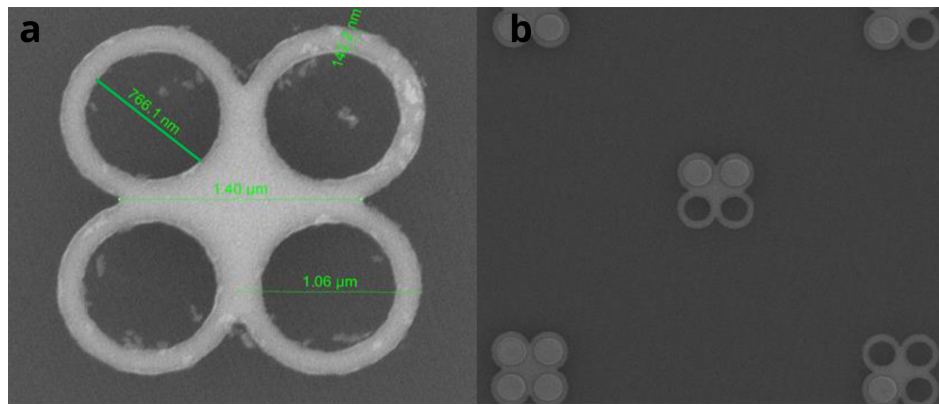


Figure 4.9. Scanning electron microscopy (SEM) images of  $2 \times 2 \mu\text{m}^2$  Py astroid devices. a) Measured dimensions of a fabricated astroid device and b) astroid devices with lift off problems.

nm, and for the second layer we coated PMMA C2 950 with 100 nm thickness. For additive process, we need high undercut profile. We decided to use PMMA C2 495 for the first layer and PMMA A2 950, 100 nm, for the second layer.

Permalloy deposition on our astroid patterns is performed with DC magnetron sputtering at 2 mTorr Ar pressure. The first samples consisted of 1 nm Ti, 30 nm Py, 5 nm Ta. 1 nm Ti is seed layer and 5 nm Ta capping layer in order to protect permalloy from getting oxidized. Although the fabrication was successful with these samples, the magnetic signal was hindered by thick Ta layer which we decided to thin down to 1 nm.

Images taken with scanning electron microscopy and atomic force microscopy of fabricated astroid nanomagnets are given in Figure 4.9 and Figure 4.10, respectively.

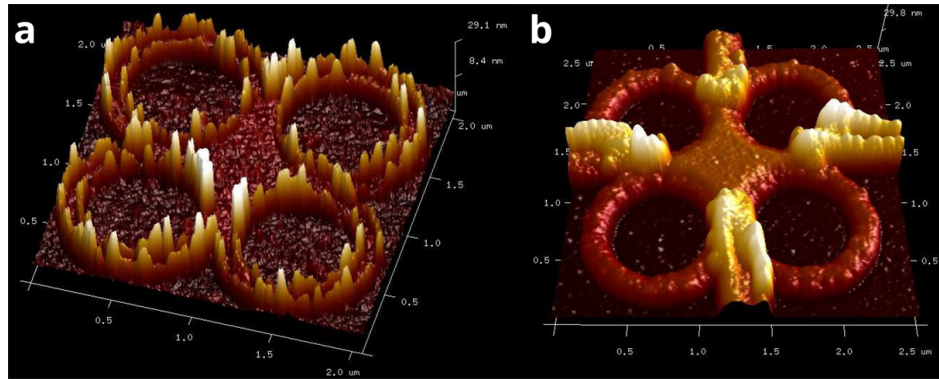


Figure 4.10. Atomic force microscopy images of fabricated astroid samples a) without contacts and b) with contacts.

### 4.2.3. Magnetic force microscopy measurements

Patterned Py astroid devices went through conditioning with an electromagnet before the magnetic force microscopy measurements. In order to have a reproducible starting point, all samples went through in plane AC demagnetization starting from 1.6 T with 50 mT steps, and then 1 T out of plane saturation magnetic field. After this conditioning, the samples were removed from the presence of external magnetic field, scanned by MFM and antivortex-vortex pairs were consistently observed in all of them.

In Figure 4.11, successful nucleation of antivortex and its manipulation with external field were observed. In order to move the antivortex, the sample was applied 10 mT in plane magnetic field by the electromagnet, taken out of applied field and then observed under MFM. The movement of the antivortex core after in plane magnetic field application occurs as predicted by Ragusa et.al [7].

## 4.3. Results

Anisotropic magnetoresistance measurements require us to connect the astroid devices to our electrical circuit. A design which would allow us to do 2-probe and 4-probe measurements was needed, hence we manufactured a photomask that will not only form a circuit but also provide contact pads compatible with both Cascade Z

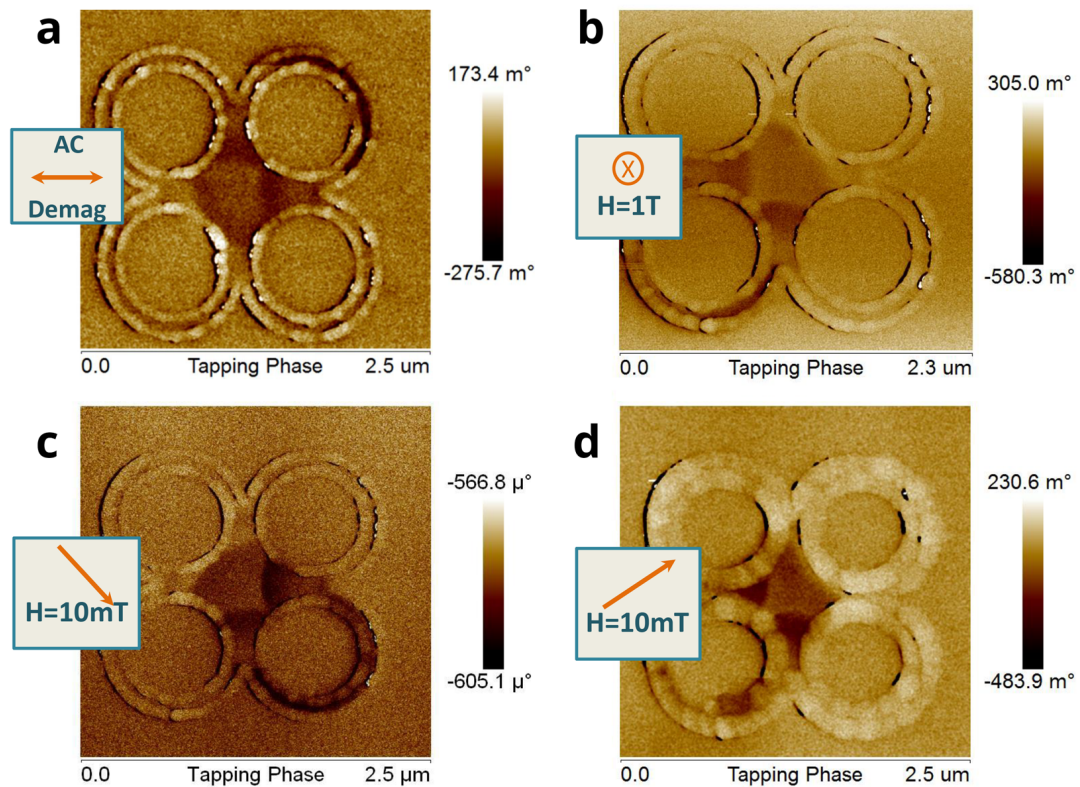


Figure 4.11. MFM images of astroid devices after application of a) AC demagnetization, b) 1 T out of plane magnetic field, c-d) 10 mT in plane magnetic field applied in the specified directions.

probes and wirebonding. This photomask, shown in Figure 4.12, incorporated alignment marks matching the ones patterned along with astroid devices in EBL step. This contact design also supported current application in directions parallel and perpendicular to magnetic field without moving the sample.

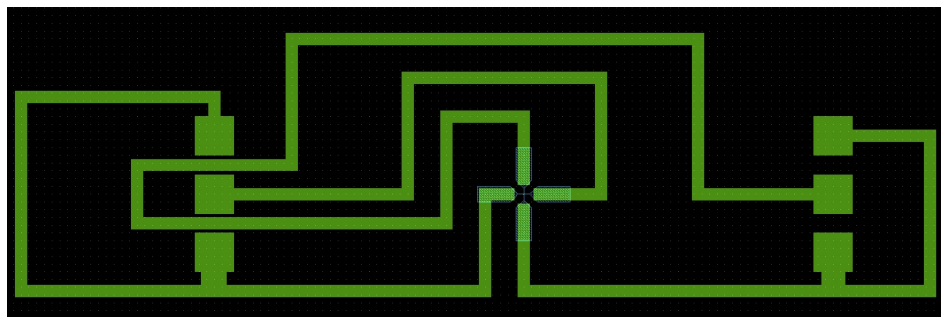


Figure 4.12. Layout Editor drawing for the astroid photomask, including contact pads compatible with both RF probes and wirebonding for our electrical measurements.

The samples mentioned above had high resistance, around 900 ohms, which pre-

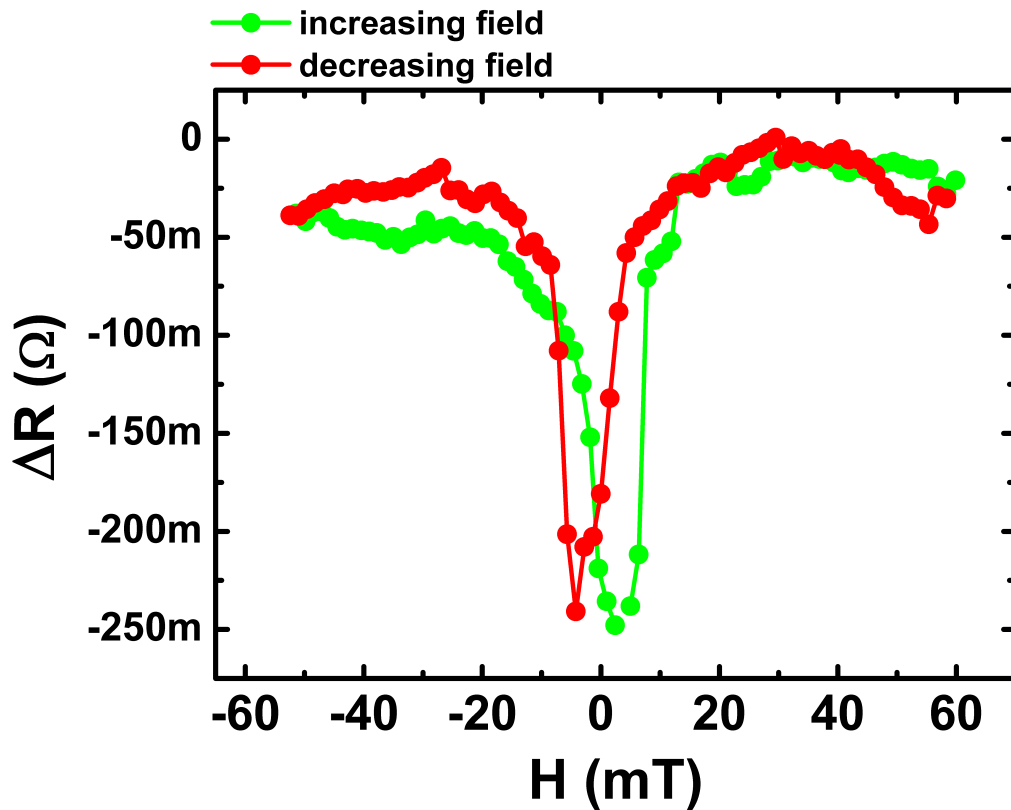


Figure 4.13. AMR measurement of 30 nm thick astroid device. Positive field values correspond to the applied field parallel to the current direction, and negative field values correspond to field applied antiparallel to the current. Red and green data points are for decreasing and increasing in plane parallel field, respectively.

vented us from obtaining a detectable AMR signal. AMR data taken with these samples is shown in Figure 4.13. Additionally, due to high resistance of the samples we could not apply more than 3 mA DC current as the samples were blowing up due to Joule heating. To eliminate the heating problem we decided to change device and contact geometry. To make sure that the signal we receive from the device is coming from only the antivortex, we removed the top and bottom current paths.

New designed geometry, shown in Figure 4.14, was a reduced version of the initial geometry and contact pads, shown in Figure 4.15, were wider than the previous one to get rid of blowing of the contact leads.

Astroid devices were patterned by e-beam lithography. Si/SiO<sub>x</sub> wafer chip was

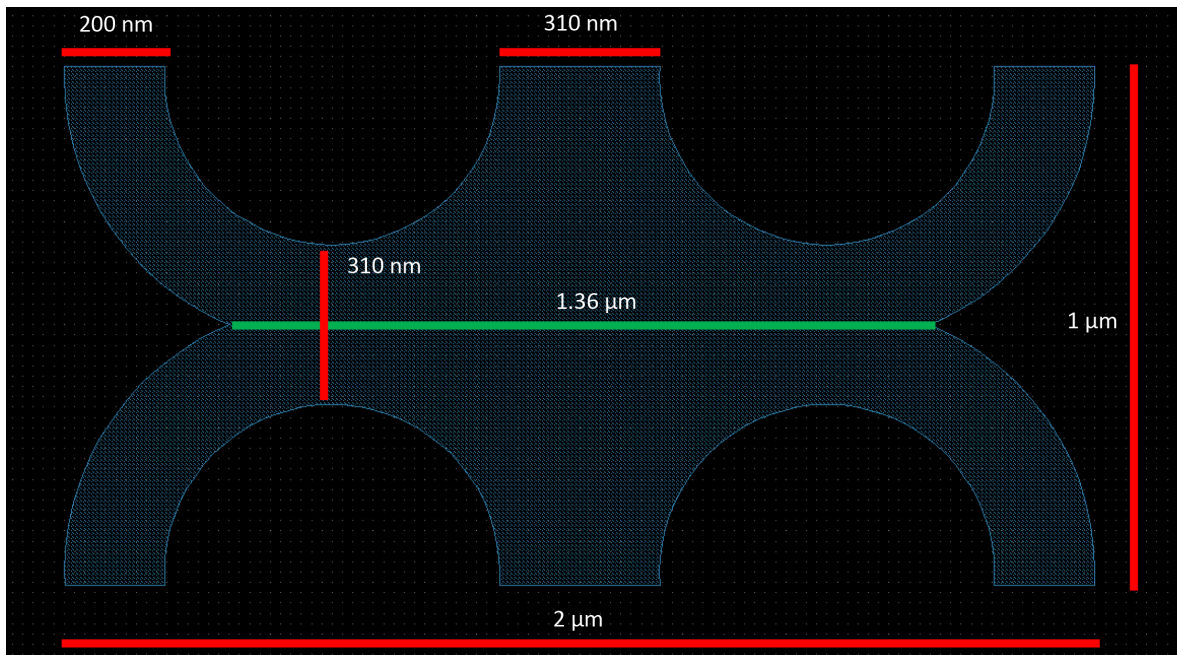


Figure 4.14. Dimensions of the reduced astroid design on Layout Editor drawing

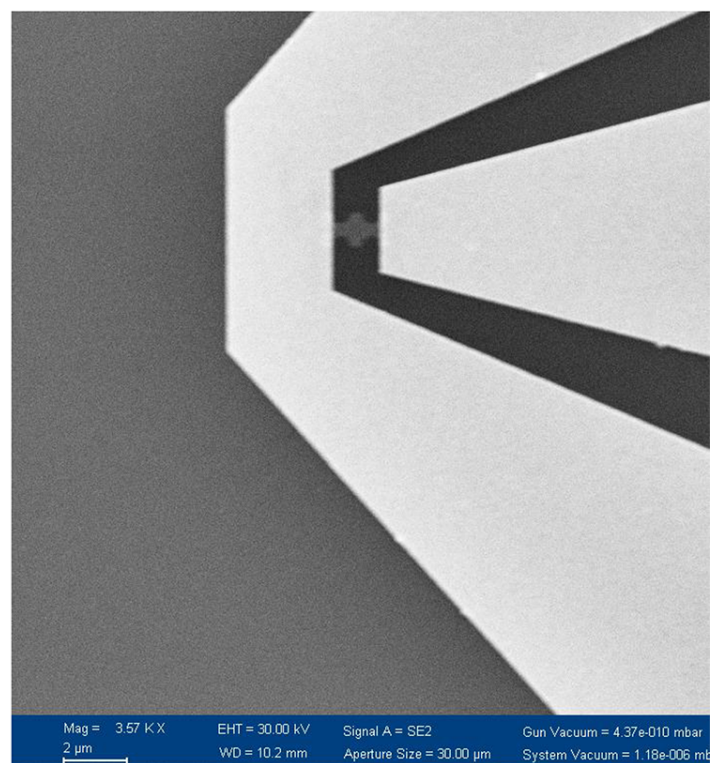


Figure 4.15. Scanning electron microscopy image of the new designed geometry and the contact pads

first coated with PMGI SF6 at 4000 rpm for 45 seconds and baked at 230°C for 6 minutes. Then it was coated with 1:1 ZEP 520/Anisole mixture at 4000 rpm for 45 seconds and baked at 180°C for 3 minutes. The resist coated sample was exposed to 80  $\mu\text{C}/\text{cm}^2$  dose, 30 kV, 10 nm step size and 25.42 pA beam current. Then the sample was developed in two steps. First, it is soaked in ZED 50 for 2 minutes then the stopper isopropanol. Second, it is soaked in A101 for 2 minutes and stopper DI water. After reduced astroid pattern was developed, 5 nm Ti and 35 nm  $\text{Ni}_{20}\text{Fe}_{80}$  were deposited by e-beam evaporation. Lift off was performed by leaving the sample in PG Remover overnight.

Resistance vs field (Oe) measurements were taken to determine under what conditions the antivortex was nucleated and annihilated. The measurements were conducted under 10  $\mu\text{A}$  DC applied current with +1000, -1000 Oe sweeping field with respect to parallel or perpendicular to applied current directions as a function of temperature, ranging from 10 K to 300 K. Device resistance was around 53  $\Omega$  level at room temperature.

we have seen stable antivortex at zero field in parallel case. When the applied current was flown to parallel to the field direction, antivortex nucleation and annihilation were detected as shown in Figure 4.17 which is consistent with previous result shown in Figure 4.13. When the current was flown to perpendicular to the field direction, there were some steps as shown in Figure 4.16 that may stem from defects or there can be nucleated antivortex or vortex-antivortex pairs. Simulations are in progress by our Italian collaborators to clarify the measurement.

All in all, we successfully fabricated stable antivortex in nanoshape geometry. Also, the nucleation and annihilation conditions of antivortex were explained both theoretically and experimentally.

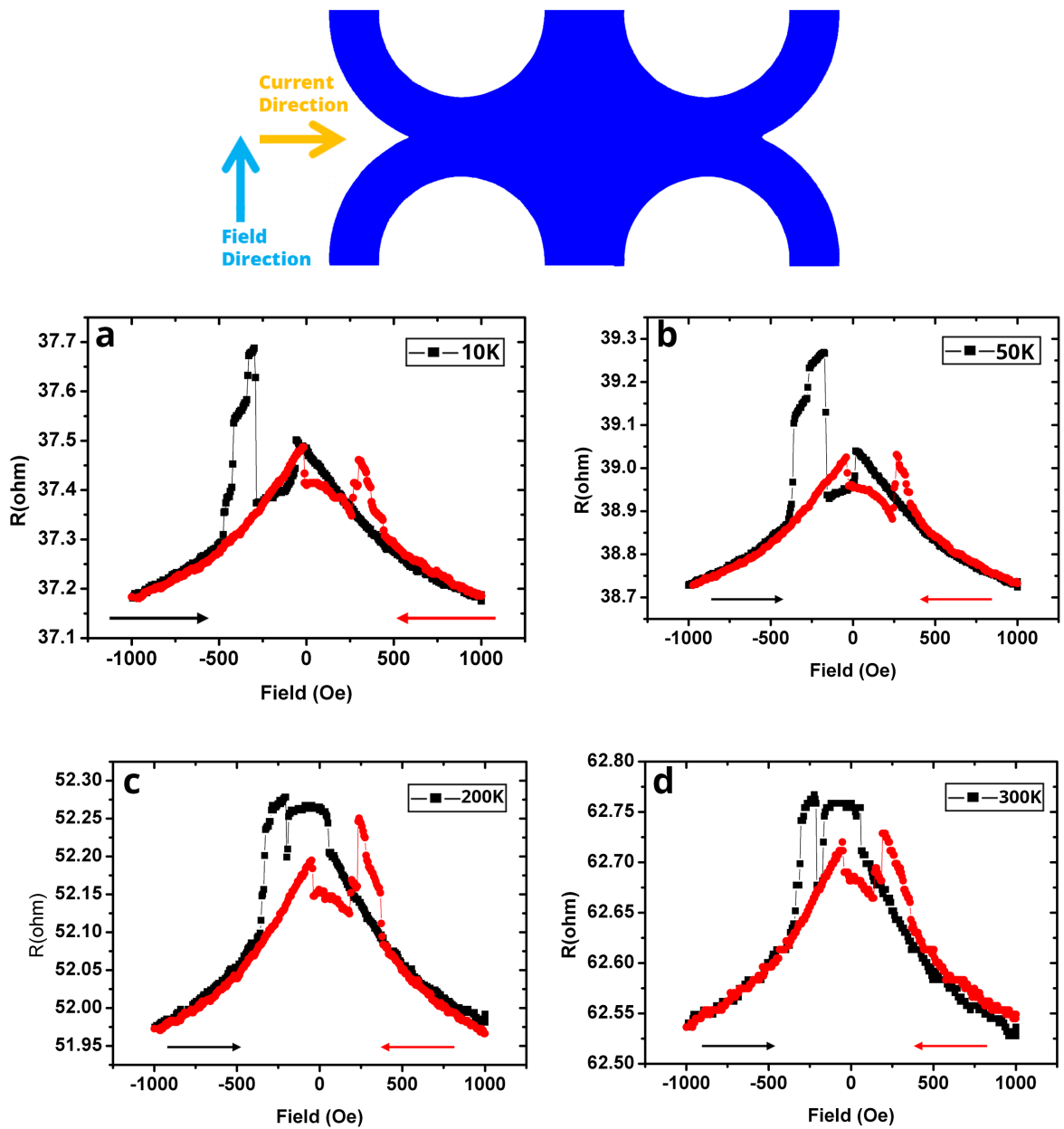


Figure 4.16. Resistance vs perpendicular magnetic field measurements taken at a) 10 K, b) 50 K, c) 200 K and d) 300 K

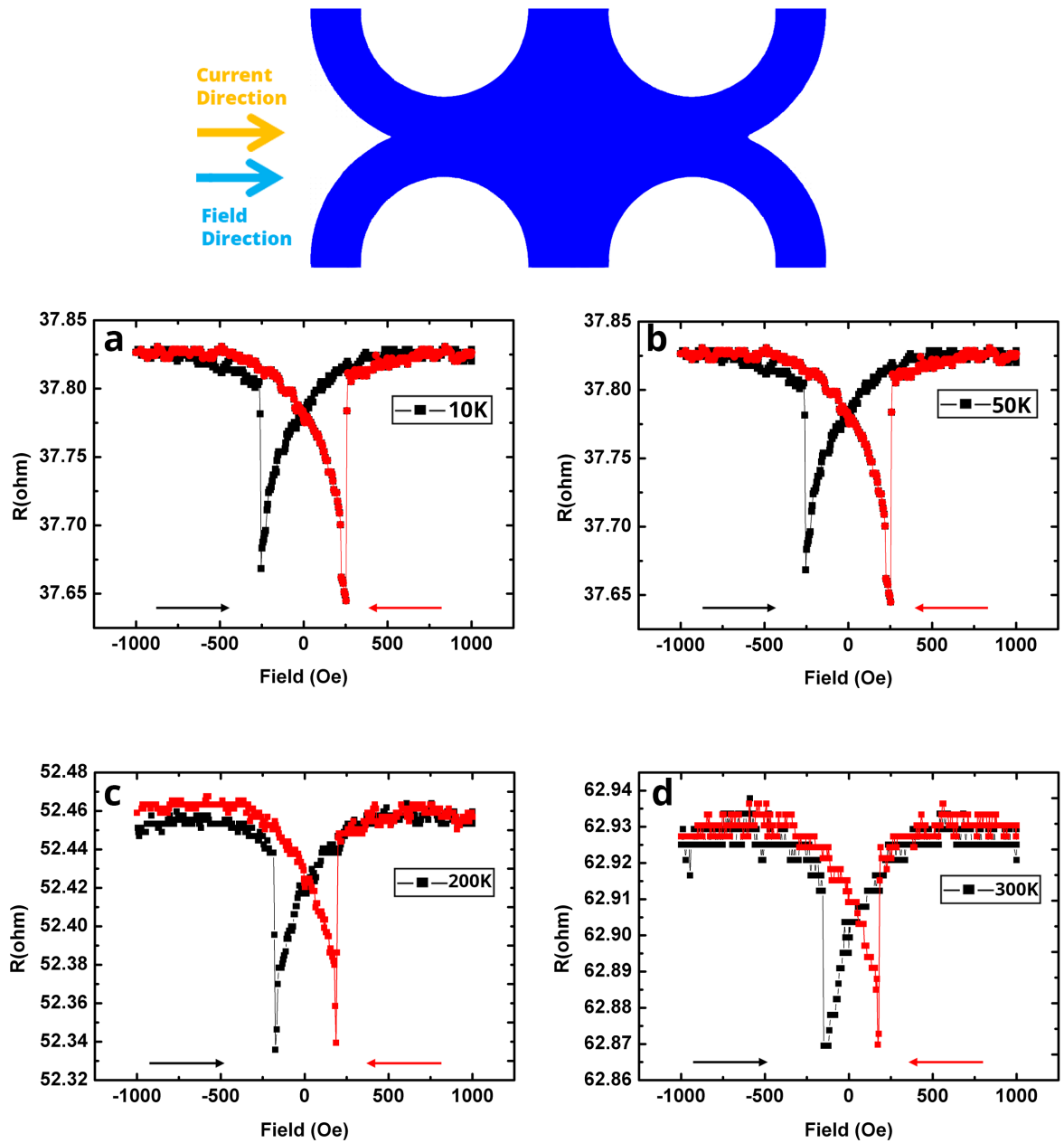


Figure 4.17. Resistance vs parallel magnetic field measurements taken at a) 10 K, b) 50 K, c) 200 K and d) 300 K

## 5. EVOLUTION OF MAGNETIC STATES FROM NÉEL SKYRMIONS TO RADIAL VORTICES

Recently discovered exotic magnetic configurations, namely magnetic solitons appearing in the presence of bulk or interfacial Dzyaloshinskii-Moriya Interaction (i-DMI), have excited scientists to explore their potential applications in emerging spintronic technologies such as race-track magnetic memory, spin logic, radio frequency nano-oscillators and sensors. Such studies are motivated by their foreseeable advantages over conventional micro-magnetic structures due to their small size, topological stability and easy spin-torque driven manipulation with much lower threshold current densities giving way to improved storage capacity, and faster operation with efficient use of energy. We show that in the presence of i-DMI in Pt/CoFeB/Ti multilayers by tuning the magnetic anisotropy (both in-plane and perpendicular-to-plane) via interface engineering and postproduction treatments, we can stabilize a variety of magnetic configurations such as Néel skyrmions, horseshoes and most importantly for the first time, the recently predicted isolated radial vortices at room temperature and under zero bias field. Especially, the radial vortex state with its absolute convergence to or divergence from a single point can potentially offer exciting new applications such as particle trapping/detrapping in addition to magnetoresistive memories with efficient switching, where the radial vortex state can act as a source of spin-polarized current with radial polarization.

### 5.1. Nucleation of Magnetic Configurations

Magnetic skyrmions are spin configurations with a topology that has perpendicular to plane magnetization components at the core and the edges with opposite directions [46, 47]. They can be Bloch or Néel type depending on the chirality of the transition region between the core and the edges, being circular or radial, respectively [23]. Unique properties of skyrmions such as their intrinsically small size, topological stability and efficient manipulation with much lower threshold current den-

sities compared to conventional micromagnetic structures have recently attracted the attention of researchers to look for ways of utilizing them in technological applications. Envisioned skyrmionic devices [46,47] are expected to possess the benefits of combining storage, logic operations and microwave functionalities at the same level with efficient use of energy [48,49].

Skyrmions appear due to Dzyaloshinskii-Moriya Interaction in the bulk of chiral magnets (Bulk DMI), at the interface of heavy metal/ferromagnet thin film stacks (interfacial DMI) [50–52] or in perpendicular magnetic anisotropy materials as a result of long range dipolar interactions [53,54] in the presence of DMI. Bulk DMI arises as a result of lack of inversion symmetry in chiral magnets, whereas the interfacial DMI (i-DMI) stems from the interaction between ferromagnetic atoms and strong spin-orbit coupling (SOC) atoms of an adjacent heavy metal [18,19,55]. I-DMI strength is parameterized by a constant  $D$  and can be incorporated into the Landau-Lifshitz-Gilbert (LLG) equation competing with other energy terms such as exchange, anisotropy and magneto-static energies. The resulting micromagnetic configuration in systems with i-DMI can lead to a range of interesting canted spin orientations such as Néel skyrmions [20], horseshoes [22], spider-web domains and radial vortices [23].

We demonstrate an evolution of these spin structures in 60 and 15 repeat Pt(5)/Co<sub>20</sub>Fe<sub>60</sub>B<sub>20</sub>(1)/Ti(1) multilayers (all thicknesses in nm), partially and fully patterned into nanopillar disks, respectively. The disk diameter, i-DMI strength  $D$  and magnetic anisotropy play the prominent role in determining the resulting magnetic configuration. An advantage of using repeated magnetic multilayer stacks is the enhancement of the magnetic signal and the interface quality with increasing number of repeats. Most importantly, we were able to tune the magnetic anisotropy by adjusting the number of repeats in the thin film stack as well as performing a set of post-production treatments such as ion irradiation during milling and annealing, in order to be able to stabilize both radial vortices and Néel skyrmions at room temperature. In fact, we were able to detect these solitons via Magnetic Force Microscopy (MFM) with an in situ parallel to the thin film surface plane magnetic field application capability. This technique serves as a quick, straightforward and cost effective method unlike conventional skyrmion

imaging techniques such as Lorentz Transmission Electron Microscopy [19], Scanning Tunneling Microscopy [50] or Small Angle Neutron Scattering [55] at the cost of a reduced spatial resolution limited by the magnetic tip diameter (on the order of 50 nm in our case).

Heavy-Metal/Ferromagnet/Spacer-Metal multilayer stack with variable number of repeats  $n$ , patterned into a nanostructure provides a unique workbench for the study of various micromagnetic structures nucleated within both in-plane and perpendicular-to-plane anisotropies in the presence of i-DMI. The ability to investigate exotic magnetic states with i-DMI and in-plane anisotropy allowed us to discover for the first time the nucleation of recently predicted radial vortices that are stable under zero bias field and at room temperature. These radial vortices can potentially offer novel applications such as particle trapping/detrapping by applying a magnetic field with radial symmetry in addition to non-uniform magnetization magnetoresistive memory where radial vortex chirality is fixed for one layer and free to switch for the other, providing full read out signal. The radial vortex can also act as a source of spin-polarized current with radial polarization for spin-torque memory and microwave nano-oscillator devices.

## 5.2. Manipulation of Radial Vortex via Magnetic Field

The experimental studies were performed on  $[\text{Pt}(5)/\text{Co}_{20}\text{Fe}_{60}\text{B}_{20}(1)/\text{Ti}(1)]_n$  multilayers (all thicknesses in nm) with number of repeats  $n$  being 1, 10, 15, and 60. Material stack, including a 5 nm Ti adhesion layer and a 5 nm Pt capping layer, was grown on Si/SiO<sub>2</sub>(500 nm) substrate via DC magnetron sputtering in 2 mTorr Ar pressure starting from a base pressure of  $\sim 10^{-9}$  Torr.

Sample naming convention: Abbreviations: C for continuous, A for annealed, I for ion-irradiated during milling, PP for partially patterned, FP for fully patterned Table 5.1 uses the sample label convention where the number of repeats in multilayer stack is 1, 10, 15 or 60, C stands for continuous films as shown in Figure 5.1a. Post production treatment A stands for annealed at 170°C for 45 minutes and I for ion-irradiation during milling with 300 V beam voltage, 60 V Accelerator voltage, 12 mA Beam current for

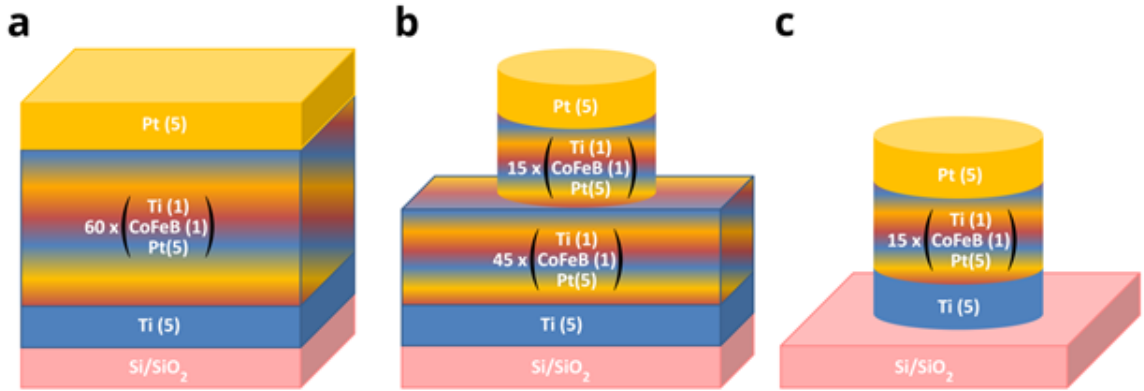


Figure 5.1. a) 60 repeat continuous film, sample 60C, b) 15 repeat partially patterned, sample 15PP-A c) 15 repeat fully patterned, sample 15FP-AI.

Table 5.1. Production parameters and measurement techniques for individual samples

Name	# of Repeats	Measurement Technique	Continuous Film	Partially Patterned	Completely Patterned	Post-production Treatment		
						None (As deposited)	Annealed	Ion-irradiated
1C	1	BLS	X			X		
10C	10	BLS	X			X		
15C	15	VSM	X			X		
60C	15	VSM, XRD and MFM	X				X	X
15C-AI	60	VSM and XRD	X			X		
15PP-A	45 extend. 15 pattern.	MFM (nanodisk)		X			X	
15FP-AI	15 pattern.	MFM (nanodisk)			X		X	X

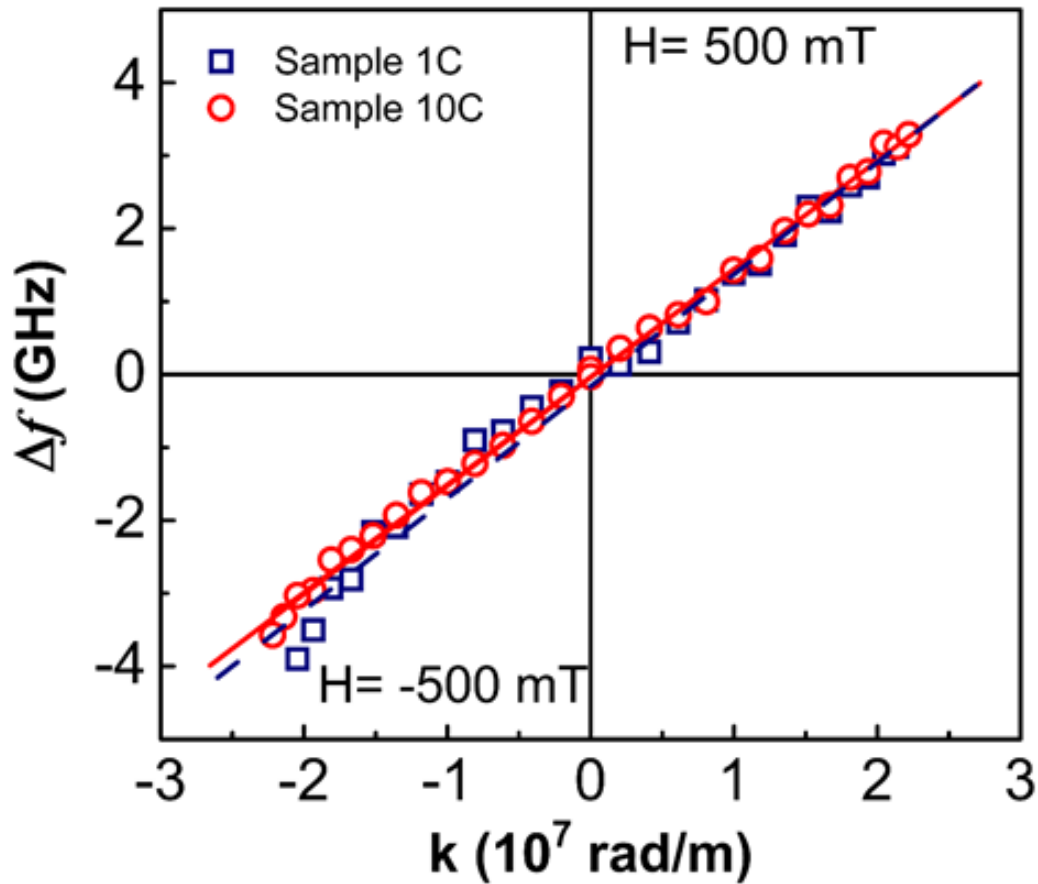


Figure 5.2. BLS measurements of the full film samples

2 hours. The sample 15PP-A consists of 45 repeat continuous film underneath the 15 repeat nano disks as shown in Figure 5.1b and the sample 15FP-AI, obtained by ion mill etching of 45 repeats of sample 15PP-A, is completely patterned into 15 repeat nano disks as shown in Figure 5.1c. The measurement techniques are Brillouin Light Scattering (BLS), Vibrating Sample Magnetometer (VSM), X-ray diffraction (XRD) and Magnetic Force Microscopy (MFM).

Red circle for 10 repeat (10C) sample and blue square for single repeat sample (1C). Frequency difference, between Stokes and anti-Stokes peaks is plotted against wave vector  $k$  for 500 mT bias field applied parallel to the film plane;  $k$  values are inverted for negative bias field -500 mT. Line fits to the data of samples 10C and 1C are shown by a red line and a blue dashed line, respectively.

Brillouin Light Scattering (BLS) has been exploited to evaluate the i-DMI strength  $D$  originating at the interface of Pt/CoFeB for a single repeat, 1C, and 10 repeat stack, 10C. In ultrathin films, the presence of i-DMI induces a noticeable frequency asymmetry between oppositely propagating Damon-Eshbach (DE) modes, which increases as a function of the wave vector  $k$  following the relation [56]:

$$\Delta f = f_{DMI}(k) - f_{DMI}(-k) = \frac{2\gamma D}{\pi M_s} k \quad (5.1)$$

where  $\gamma$  is the gyromagnetic ratio [57], and  $M_s$  is the saturation magnetization of the magnetic layer. Using BLS the frequency asymmetry caused by i-DMI can be quantified by measuring the frequency difference,  $\Delta f$ , between Stokes and anti-Stokes peaks corresponding to spin waves propagating in opposite directions. Figure 5.2 shows  $\Delta f$  measured (points) as a function of wave vector  $k$  for both samples, applying a bias field of +500 mT and -500 mT. The strength of i-DMI has been determined by a linear fit of the experimental data, using Equation 5.1. The  $D$  values were found to be  $1.49 \pm 0.05$  mJ/m<sup>2</sup> and  $1.45 \pm 0.02$  mJ/m<sup>2</sup>, for single repeat (1C) and 10 repeat stack (10C) samples, respectively. It is known that the  $D$  value, for a fixed CoFeB thickness of 2 nm, saturates [56] at 0.45 mJ/m<sup>2</sup> for Pt thicknesses greater than 2 nm whereas for a CoFeB thickness of 0.8 nm,  $D$  increases [57] to  $1.0 \pm 0.1$  mJ/m<sup>2</sup>. In our samples characterized by a CoFeB thickness of 1 nm and a Pt thickness of 5 nm (greater than the saturation thickness of 2 nm), we found  $D$  values of 1.4 - 1.5 mJ/m<sup>2</sup>, which are larger than the previously reported [57] value of  $1.0 \pm 0.1$  mJ/m<sup>2</sup>. These higher  $D$  values can be ascribed to the slightly different Co/Fe ratio of 20/60 as compared to 40/40 in refs. [8, 58] and different deposition conditions. Remarkably, we found that for [Pt(5)/Co<sub>20</sub>Fe<sub>60</sub>B<sub>20</sub>(1)/Ti(1)]<sub>n</sub> stacks where  $n > 1$ , the presence of a non-heavy metal Ti interlayer 1 nm thick, successfully avoids degradation [51, 58] of i-DMI strength due to symmetric contribution of bottom and top Pt electrodes. The fact that  $D$  saturates as a function of number of repeats (approximately the same  $D$  values for sample 1C and sample 10C) implies that Ti interlayer tends to delete the spin-orbit coupling from the top Pt. Figure 5.3a shows room temperature, in-plane field Vibrating Sample Magnetometer (VSM) measurements of 15 and 60 repeats of the full

film stack [Pt(5)/Co<sub>20</sub>Fe<sub>60</sub>B<sub>20</sub>(1)/Ti(1)]<sub>n</sub> (as deposited samples 15C, 60C and with the post-deposition treatment of annealing at 170°C for 45 minutes and ion-irradiation during milling for 2 hours for sample 15C-AI). The post deposition treatments were done to clarify the role of nano patterning of resist bake and ion mill etch procedures on the resulting device performance.

The first trend evident in Figure 5.3a is the reduction of magnetization, at an applied field of 500 mT, from 60 kA/m for sample 15C to 31 kA/m for sample 60C as a result of the increase in number of repeats. The linear M-H curve suggests an in-plane hard axis, i.e. an out-of-plane anisotropy which gets stronger as the number of repeats increase. We estimated a perpendicular anisotropy constant  $K=2.1 \times 10^4$  J/m<sup>3</sup> for sample 60C and  $K=1.3 \times 10^4$  J/m<sup>3</sup> for sample 15C, whereas we found that postproduction treatment of annealing and ion irradiation during milling switched the easy axis direction towards in-plane for sample 15C-AI with in-plane anisotropy constant  $K=1 \times 10^4$  J/m<sup>3</sup>. Furthermore, the magnetization at 500 mT for sample 15C-AI increased to 141 kA/m as compared to 15C and 60C. The inset of Figure 5.3a shows a zoomed in version of the data for sample 15C-AI. Unlike the other two samples 15C and 60C, sample 15C-AI displays a clear hysteresis with 1 mT coercive field. For completeness, the corresponding out of plane M-H curves were plotted in Figure 5.4.

In order to gain more insights into the behavior of sample 15C-AI with weak in-plane anisotropy, we investigated the magnetic configuration under Magnetic Force Microscopy (MFM) with a custom-made magnetic stage, shown in Figure 5.5, that has in-plane field application capability, after saturation with 1 T in-plane field. Figure 5.3c and Figure 5.3d show the MFM images of the remnant state and in the presence of 20 mT in-plane field, respectively. The effect of increasing the in-plane magnetic field from 0 to 20 mT was the growth of average size of the dark domains from 122 nm to 135 nm in figure 5.6.

Furthermore, domain walls were observed to move incrementally as a function of increasing field consistent with low field behavior seen in the VSM measurement Figure 5.3a inset. We attribute this gradual change in the domain sizes and accompanying

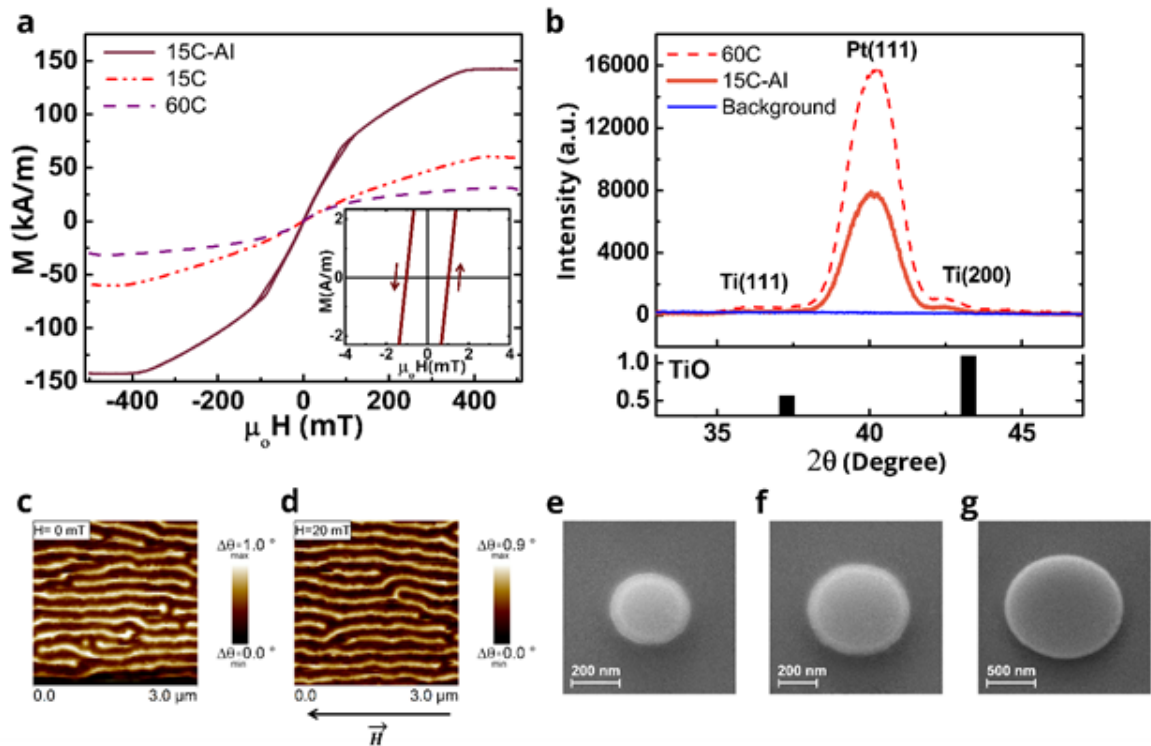


Figure 5.3. In-plane external field VSM, XRD , MFM and SEM measurements. a) Room temperature VSM measurements with in-plane external magnetic field for samples 15C (red dash-dotted line), 15C-AI (brown-red solid line) and 60C (purple dashed line). The inset shows the zoomed in version for sample 15C-AI, the only one showing hysteresis. The arrows indicate the field scan direction. b) XRD data for samples 15C-AI (orange solid line) and 60C (red dashed line) are shown along with Si/SiO<sub>2</sub> substrate data as background (blue solid line). The crystal orientations corresponding to the diffraction peaks are identified as being due to Pt [8] and Ti that gets progressively oxidized to TiO thin films suggesting a strong  $\langle 111 \rangle$  texture. For reference JCPDS card data of TiO is included. c-d) MFM images of sample 15C-AI after saturation with 1 T in-plane field, (c) at remanence, (d) under 20 mT in-plane field applied along the direction indicated by the arrow. e-g) Scanning Electron Microscopy (SEM) images of nano disk with various diameters, e) 300 nm f) 500 nm and g) 1200 nm.

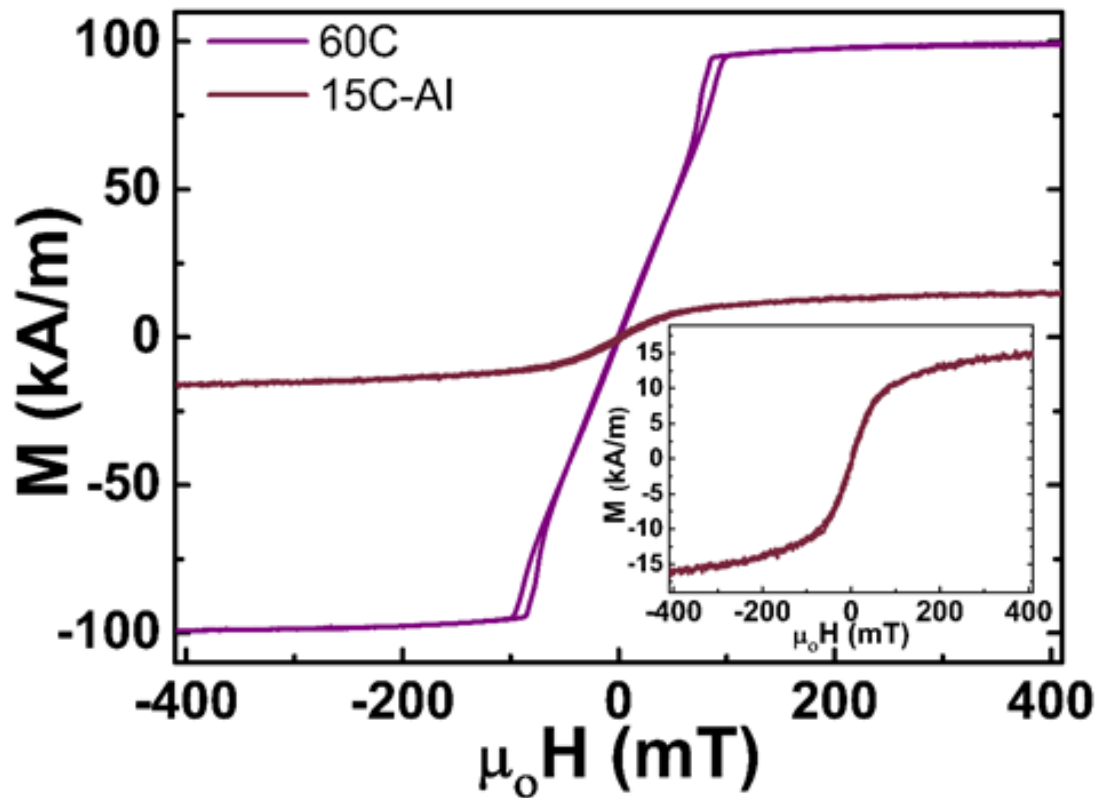


Figure 5.4. Room temperature VSM measurements with out-of-plane external magnetic field for samples 15C-AI (brown-red solid line) and 60C (purple solid line). The inset shows the zoomed in version for sample 15C-AI, showing the hard axis loop

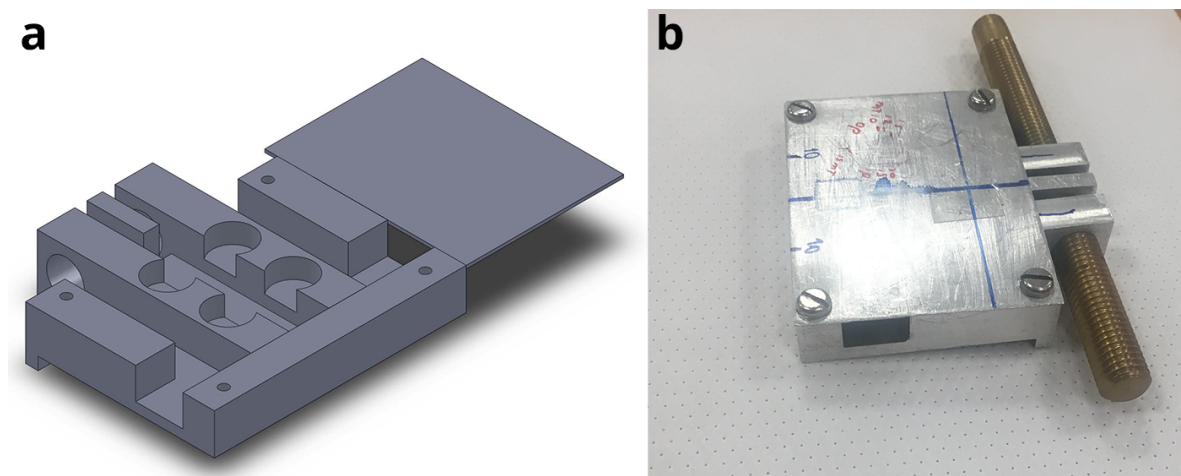


Figure 5.5. Custom-made in plane magnetic field stage for in situ magnetic field application during MFM measurements, a) schematic drawing and b) machined stage and screw.

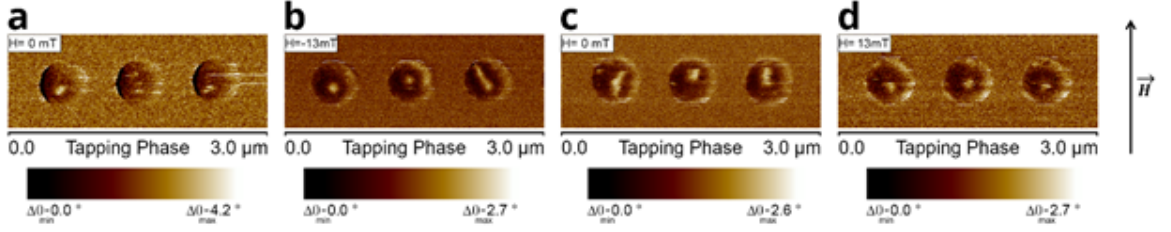


Figure 5.6. MFM images of a set of three 300 nm diameter disks from sample type 15FP-AI. The measurement was done after the field conditioning (-4 T out-of-plane field following an AC demagnetization process with a maximum 1 T in-plane field). MFM images taken under a) zero field, b) -13 mT, c) zero field after the application of -25 mT and d) 13 mT in-plane field

incremental domain wall motion to the presence of defects acting as pinning centers. Most importantly, the formation of the stripe domains confirm that the post-production treatment causes a reduction of the out-of-plane magnetic anisotropy and consequently the rotation of the easy axis from the perpendicular direction towards the surface plane.

To understand the role of number of repeats and post-production treatments on the anisotropy direction, X-ray diffraction (XRD) measurements with Cu  $K_\alpha$  radiation were performed on 60C and 15C-AI samples. The results are shown in Figure 5.3b which also displays the Si/SiO<sub>2</sub> substrate background data. Thin film crystal orientations were identified by the corresponding  $2\theta$  values of each individual peak. Highest intensity peaks of both 15C-AI and 60C occurred at  $40.15^\circ$  which indicate preferred Pt  $\langle 111 \rangle$  crystal orientation [8] while the peaks appearing at  $42.3^\circ$  and  $36.1^\circ$  were identified as Ti $\langle 200 \rangle$  and Ti $\langle 111 \rangle$  peaks. Pt  $\langle 111 \rangle$  peak intensity was doubled for 60C as compared to 15C-AI. We observed the presence of TiO peaks in accordance with Joint Committee on Powder Diffraction Standards (JCPDS) card data [59]. This behavior can be understood considering the fact that the substrate temperature gradually increases from  $20^\circ\text{C}$  to  $60^\circ\text{C}$  in the course of 4 hourlong deposition of the multilayer stack promoting further oxidation of Ti interlayers in Figure 5.7 and Table 5.2, which indicates that the ratio of TiO to Ti increases with number of repeats. From literature [60], lattice constants of Ti, TiO and Pt can be found as  $4.68 \text{ \AA}$ ,  $4.18 \text{ \AA}$  and  $3.92 \text{ \AA}$ , respectively, corresponding to a decreasing lattice mismatch from 16% to 6%

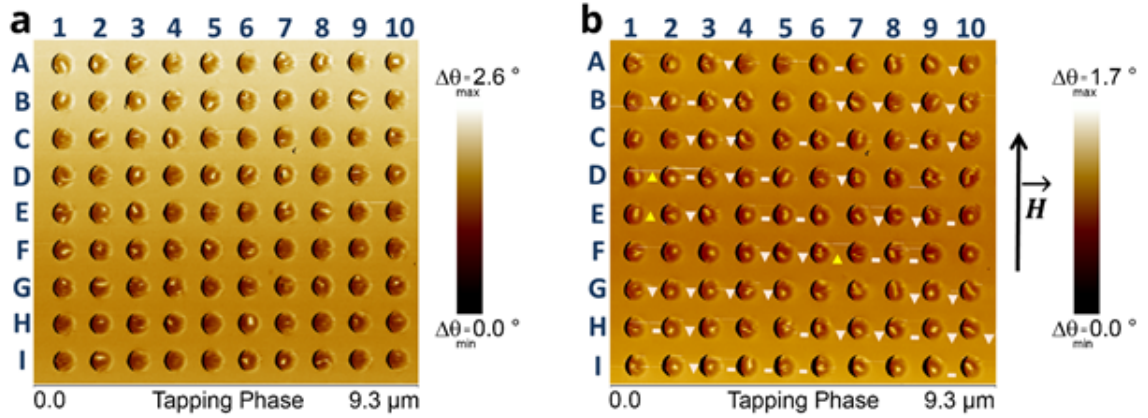


Figure 5.7. MFM images of a single array of 300 nm diameter disks sample type 15FP-AI

Table 5.2. Percentage values of oxidation states of titanium in thin films deposited at 20°C and 60°C. Residual amounts of Ti(III) and Ti(IV) states are not listed here.

	Ti – Metallic (atomic percent)	TiO (atomic percent)
Deposited at 20° C	59.97	34.51
Deposited at 60° C	49.22	41.77

with increasing oxygen content. The decreasing lattice strain favors strong Pt  $\langle 111 \rangle$  orientation and the perpendicular magnetic anisotropy (PMA) induced by this crystal structure in sample 60C whereas the increasing magneto-elastic energy due to larger lattice strain alleviates PMA in sample 15C–AI. This also explains why the PMA of sample 15C is much weaker than sample 60C. Enhancement of the quality of CoFeB/Pt interface and Ti/Pt interface results in modification of anisotropy as evidenced by the evolution of spectrum of possible micromagnetic configurations [23], shown in Figure 5.8 and Figure 5.11.

Following the BLS measurements of i-DMI strength, magnetic characterization with VSM and structural characterization with XRD, top down method involving electron beam lithography and ion mill etching were utilized to pattern the films into nano disks with diameters ranging from 100 to 1200 nm. Figure 5.3 e-g show SEM images

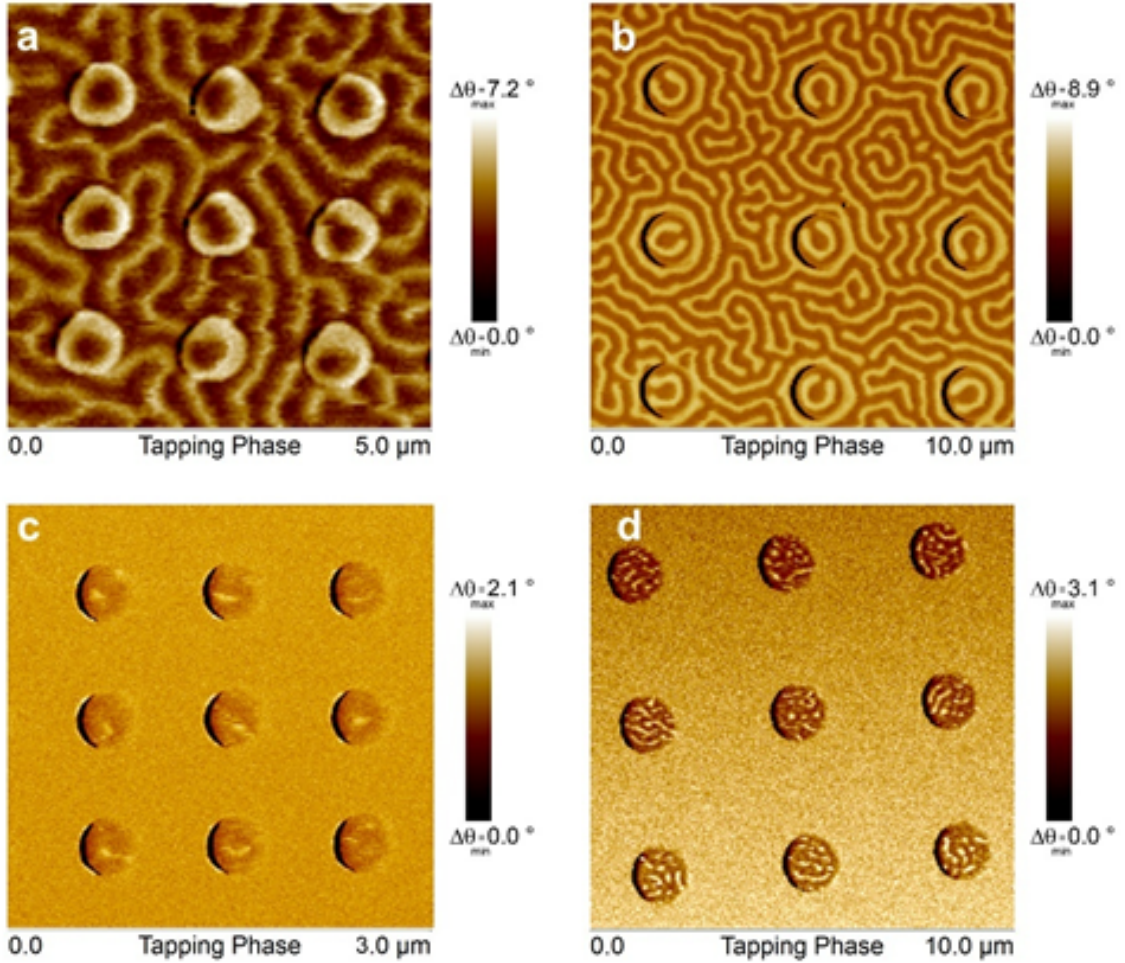


Figure 5.8. MFM images of disk arrays for 15PP-A (a-b) and 15FP-AI (c-d) samples taken under no external field after in-plane AC demagnetization with 1 T maximum field and application of 3 T perpendicular-to-plane field. MFM images belong to arrays of disks with diameters a) 500 nm, c) 300 nm, b) and d) 1200 nm

of 300, 500 and 1200 nm diameter nanopillar disks that are of interest in our MFM studies.

Figure 5.8a and 5.8b show MFM images of the sample type 15PP-A for 500 nm and 1200 nm diameter disks, respectively. The samples were ac-demagnetized with a maximum in-plane field of 1 T followed by the application of a 3 T out-of-plane field, prior to imaging. The continuous film underneath the pillars was observed to have a maze-like domain pattern as expected due to PMA in these samples. The i-DMI at the CoFeB/Pt interface together with PMA leads to stabilization of Néel skyrmions in 500

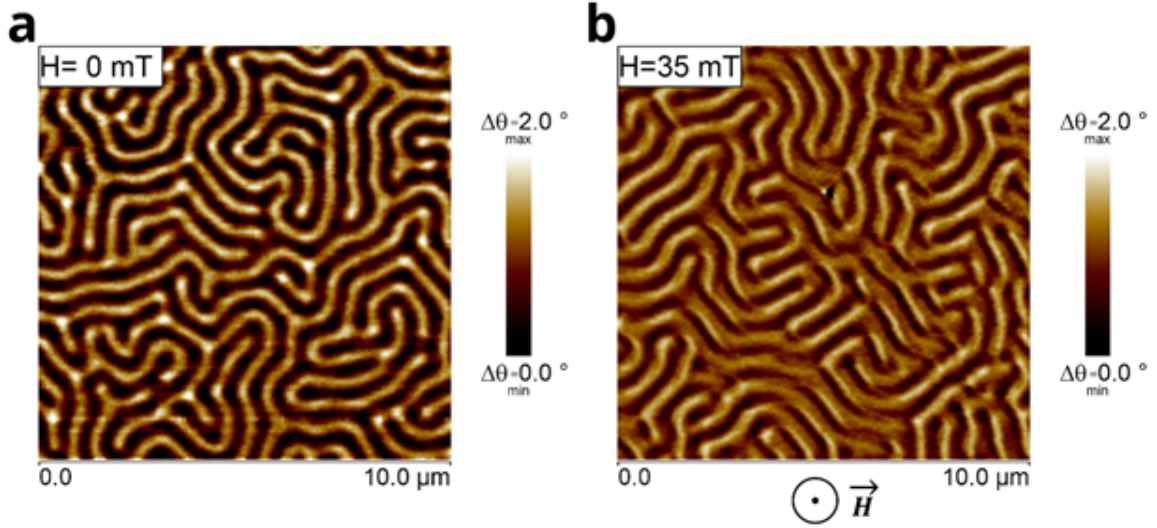


Figure 5.9. MFM images of sample 60C after in-plane AC demagnetization with a maximum field of 1 T a) with no external field b) under 35 mT external perpendicular to plane magnetic field in the indicated direction.

nm disks as shown in Figure 5.8a and horse-shoe domain patterns in 1200 nm disks of Figure 5.8b.

MFM images in Figure 5.8c and Figure 5.8d were obtained on 15FP-AI type samples having in plane anisotropy (IPA) after AC demagnetization process with a maximum in-plane field of 1 T and a subsequent 3 T out-of-plane magnetic field application. 1200 nm disks of Figure 5.8d show a multi-domain pattern including stripe-like domains reminiscent of a spider web configuration [23]. On the other hand, 300 nm disks display stable exotic magnetic configurations that appear as dots or extended dots as seen in Figure 5.8c. It is rather difficult to identify the nature of the magnetic ordering in this case since there are multiple possible magnetic structures such as Néel skyrmions or magnetic vortices that show similar contrast in an MFM image.

One way to diagnose the type of ordering is to analyze the characteristic behavior under the effect of an external magnetic field [23]. The possibility of having Néel skyrmions is eliminated by the fact that these samples (15FP-AI) have in-plane anisotropy and under 15 mT perpendicular-to-plane field they expand as predicted [61] shown in Figure 5.9. The other two candidates, namely circular vortices and radial vor-

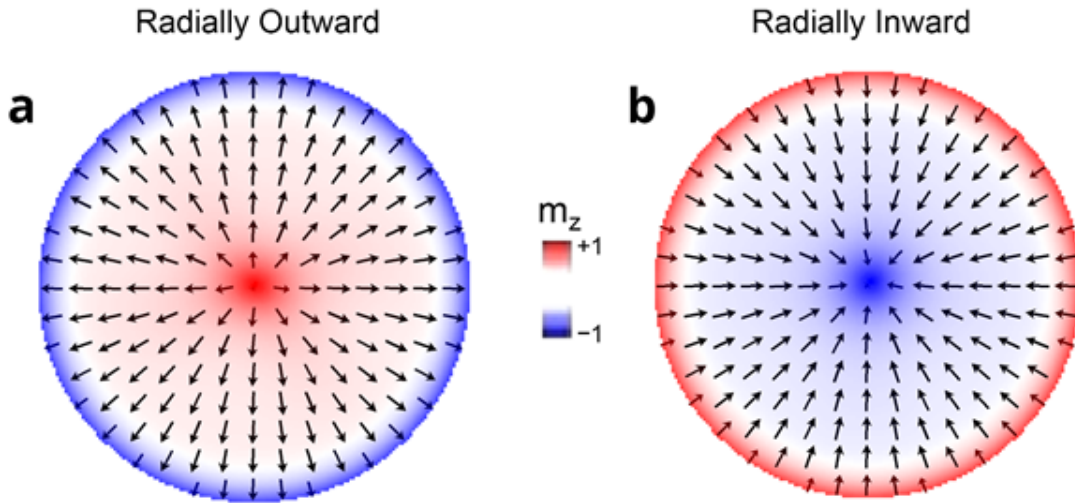


Figure 5.10. Micromagnetic simulation results obtained by using the experimental parameters indicate radially a) outward b) inward radial vortices.

tices, both of which are stable in samples with in-plane anisotropy can luckily be easily distinguished by their response to external magnetic field. If they are circular vortices, they are expected to move in a direction perpendicular to the field whereas the recently predicted radial vortices are expected to move parallel or antiparallel to the applied field depending on the radial chirality coupled with core polarity (In Figure 5.10 radially inward - core into the plane for the former or radially outward - core out of plane for the latter [23]).

Results of our external field dependent response analysis are summarized in Figure 5.11. The MFM data belong to 300 nm diameter disks that went through two different magnetic field conditioning procedures. Figure 5.11a shows the zero external field configuration of the array after an in-plane AC demagnetization process of 1 T maximum field and a subsequent 3 T out-of-plane field application. Majority of the disks display the dot and extended dot structures. Due to the finite diameter of 50 nm for the low moment magnetic tip used in this imaging, the minimum feature size that can be resolved is limited to 50 nm. Therefore, the dot sizes we observed in the range of 50 to 100 nm merely imply an upper bound of 100 nm dot diameter. Figure 5.11b shows the same disks imaged under an inplane magnetic field of 10 mT along the direction indicated in the figure. The response to the external field is highlighted

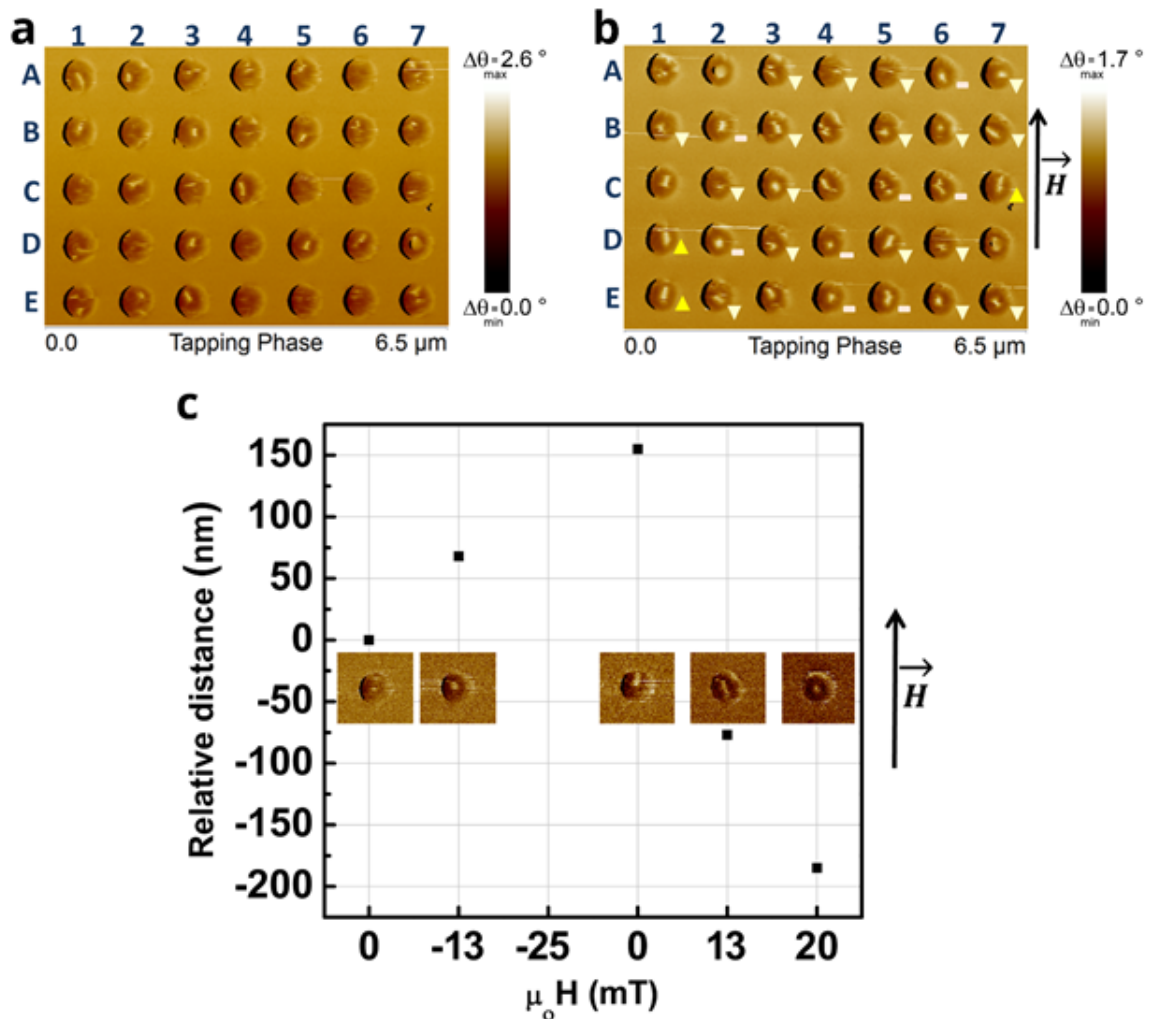


Figure 5.11. MFM images of 300 nm diameter disks sample type 15FP-AI under different conditions. a-b) 3 T out-of-plane field and c) -4 T out-of-plane field, both following an AC demagnetization process with a maximum 1 T in-plane field. The response to the external field is highlighted such that an upward or downward motion is indicated by triangles, appearance of the dots in disks after field application is denoted by a – sign. c) Motion under different in-plane magnetic fields. Relative displacement versus applied in-plane field

such that an upward or downward motion (parallel or antiparallel to the field direction) is indicated by triangles, appearance of the dots in disks after field application is denoted by a  $-$  sign. 23 % of the disks showed no clearly resolvable features in Figure 5.11a but revealed dots when the field was applied in Figure 5.11b; e.g. the disk A6. One plausible explanation is that the diameters of the dots are much smaller than the resolution of the MFM tip and seem to be visible under the application of an external magnetic field. The striking behavior in Figure 5.11b was that 49 % of the dots moved downward, opposite to the external field whereas 9 % moved upward along the field direction. This motion was either in the form of the dot relocating such as in disk E6 or extending in the vertical direction as in B3 and C7, the latter possibly due to pinning [61] effects which also explains how for example in disk A6 a dot becomes resolvable after the field application. For the remaining 19% of the dots, the behavior was not clear. Figure 5.7 used for the analysis of a larger array including 90 nanopillar disks. Figure 5.7a-b, shows a bigger array of disks (90 disks for better statistics) that went through the same field conditioning described in Figure 5.11a-b (3 T out-of-plane field following an AC demagnetization process with a maximum 1 T in-plane field) including the same array of disks labeled with rows A-E in Figure 5.11. In Figure 5.7b, as compared to Figure 5.7a, 36% of the dots moved downward whereas 3% moved upward and 22 % of the dots appeared in the disk under in-plane external magnetic field of 10 mT. For the remaining 39% of the dots, the behavior is not clear. It is evident from this experiment that majority of the dot-like structures move either parallel or anti-parallel to the direction of the field. These results support the idea that the observed magnetic features are radial vortices.

Figure 5.11c shows the observed behavior of a radial vortex in response to an in-plane field. Due to difficulties in keeping the magnetic tip magnetization stable at in-plane fields greater than 20 mT, all the in-plane field dependent measurements were done for fields below 20 mT. However, in order to confirm the change of behavior with changing polarity we focused on one device and performed measurements at zero field, -13 mT, zero field after -25 mT application, +13 mT and +20 mT. The relative displacement of the core is positive for negative fields and negative for positive fields. The core displacement is observed to be larger for larger applied fields and also polarity

dependent as expected.

We observed a variety of magnetic structures in nano-disks made of alternating layers of [Pt(5)/Co<sub>20</sub>Fe<sub>60</sub>B<sub>20</sub>(1)/Ti(1)] with i-DMI at the interface of the heavy metal Pt and the magnetic Co<sub>20</sub>Fe<sub>60</sub>B<sub>20</sub> layer. Previous studies report an i-DMI parameter of  $\sim 1$  mJ/m<sup>2</sup> for Pt/ Co<sub>40</sub>Fe<sub>40</sub>B<sub>20</sub> interface [57], [62] and  $\sim 2$  mJ/m<sup>2</sup> for Ir/Co/Pt heterostructure that has two heavy metal layers [51] having opposite i-DMI signs to prevent the cancellation in repeated structure. From BLS analysis we found that [Pt(5)/Co<sub>20</sub>Fe<sub>60</sub>B<sub>20</sub>(1)/Ti(1)] multilayer stacks are characterized by a quite large D parameter of  $\sim 1.5$  mJ/m<sup>2</sup>, even if they contain only one heavy metal layer. This is due to the presence of a thin Ti spacer layer which successfully avoids the degradation of i-DMI from symmetric Pt electrodes. Moreover, BLS measurements suggest that the i-DMI strength in the CoFeB/Pt interface is affected by the CoFeB composition. More specifically, we have shown that i-DMI together with dipolar field in these multilayers stabilizes the radial vortex structure for in-plane<sup>24</sup> anisotropy and Néel skyrmions for perpendicular [63] to plane anisotropy.

The magnetic characteristics of the repeated stacks are sensitive to the number of repeats as well as manufacturing conditions. XRD measurements suggest the presence of oxygen in Ti interlayers. Further x-ray photoelectron spectroscopy (XPS) studies confirmed partial oxidation of Ti interlayers resulting in predominantly TiO such that the oxide to metal ratio increases with increasing substrate temperature during long hours of deposition example Figure 5.7,5.12 and Table 5.1). Therefore, sample 60C, with higher final substrate temperature of 60°C compared to that of sample 15C (20°C), has improved interface quality due to decreasing lattice mismatch from 16% to 6% between Ti and Pt which induces a strong Pt <111> orientation and favors strong PMA. Consequently, samples 15C and 60C both have PMA yet due to more oxidation in Ti layers of the latter, PMA is observed to be enhanced.

While PMA is expected to be weaker in sample 15C-AI as well, the post-production treatment of annealing at 170°C for 45 minutes and ion-irradiation during milling for 2 hours further weakens PMA and switches the easy axis to in plane. A similar effect

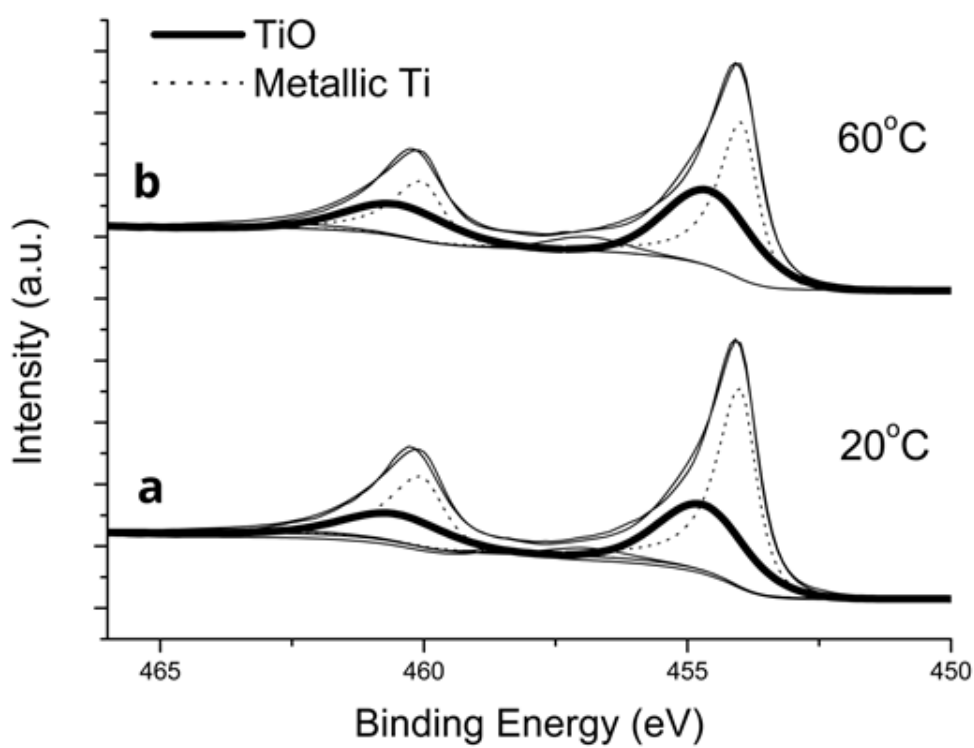


Figure 5.12. Overlaid XPS spectra of continuous Ti films, deposited at a) 20°C and b) 60°C. Dotted and bold lines correspond to Ti 2p peaks of metallic titanium and titanium monoxide, respectively.

was observed previously [64] with ion irradiation for the case of Co/Pt. Ion irradiation was reported to cause lattice distortion resulting in an increase in lattice mismatch favoring in-plane anisotropy.

In sample 15PP-A which displays PMA, magnetic structures like Néel skyrmions and horse-shoes appear in the disks with 500 and 1200 nm, respectively. Whereas the in-plane anisotropy in sample 15FP-AI leads to the observation of dot-like features with core radii 50-100 nm in MFM for disks of 300-500 nm diameter. Majority of these dot-like structures responded to in-plane external magnetic field by propagating along the field axis either parallel or anti-parallel to the field direction. Our results are in-line with the predictions of reference [23] which indicate the nucleation of radial vortices at the interface of Pt/CoFeB in structures with in-plane anisotropy.

The magnetic structures revealed here were nucleated with an external magnetic field treatment but did not require a dc bias-field to be stabilized afterwards which was found to be necessary in some earlier studies [51, 65]. Other skyrmion nucleation techniques include the application of external magnetic field pulses [22] or injection of current pulses through a constriction [20, 66]. Usually, demonstrated skyrmions are in a single ultra-thin magnetic layer with a few exceptions [51, 63].

The Pt/CoFeB/Ti multilayer whose magnetic anisotropy can be tuned with number of repeats and post-production treatments, provides a unique experimental workbench to study the spectrum of micro-magnetic configurations from Néel skyrmions, horse-shoes, spider-web like domains to radial vortices thanks to interfacial DMI and dipolar field. These extraordinary micromagnetic configurations can potentially find applications in magnetic memory, logic and sensor technologies. The radial vortex state which has been stabilized at room temperature for the first time in this work paves the way to unique applications such as particle trapping/detrapping in addition to nonuniform magnetization memories with efficient switching, where the magnetic layer that accommodates the radial vortex can act as a source of spin-polarized current with radial polarization.

## 6. ELECTRORESISTANCE AND EXCHANGE BIAS MANIPULATION BY CURRENT IN ANTIFERROMAGNETS

Antiferromagnets have become an attraction point for their functional component in spin transport devices [67]. Recently it has been discovered that antiferromagnetic order, prepared via field cooling below the Neel temperature, can be susceptible to spin orbit torques (SOT) originating from a heavy metal underlayer [68]. Furthermore, a (100) oriented antiferromagnetic metal IrMn has been shown to generate substantial self-torque due to a large spin Hall angle [69].

Exchange bias forming at the interface of ferromagnet/antiferromagnet bilayers results in a shift in the hysteresis loop. In 1956, Meiklejohn and Bean showed that the loop shift was equivalent to the assumption of a unidirectional anisotropy energy [32, 70, 71]. The stability of the antiferromagnet is crucial for the stability of exchange bias and hence the functioning of the device [70, 72].

More than a couple of decades studies focusing on FM-AFM exchange couples has become popular thanks to the effective bias,  $H_E$ , on a FM thin induced by the interfacial exchange with an AFM film provides broad application spectra for information storage industry. IrMn<sub>3</sub> is an antiferromagnet which has a large exchange bias, anisotropy coming from its L<sub>12</sub> ordered phase with a cubic symmetry [73] and thermal stability, is commonly used in the industry. In this study, we focus on ultrathin (100) oriented IrMn<sub>3</sub> due to its extraordinary response to the applied current such as electroresistance and exchange bias manipulation by pure spin current.

### 6.1. Magnetic Characterization of (100) Oriented IrMn<sub>3</sub> Thin Film

Magnetic characterization of the thin film was done by SQUID (Quantum Design), shown in Figure 6.1, as a function of the thickness of IrMn<sub>3</sub> layer. Blocking

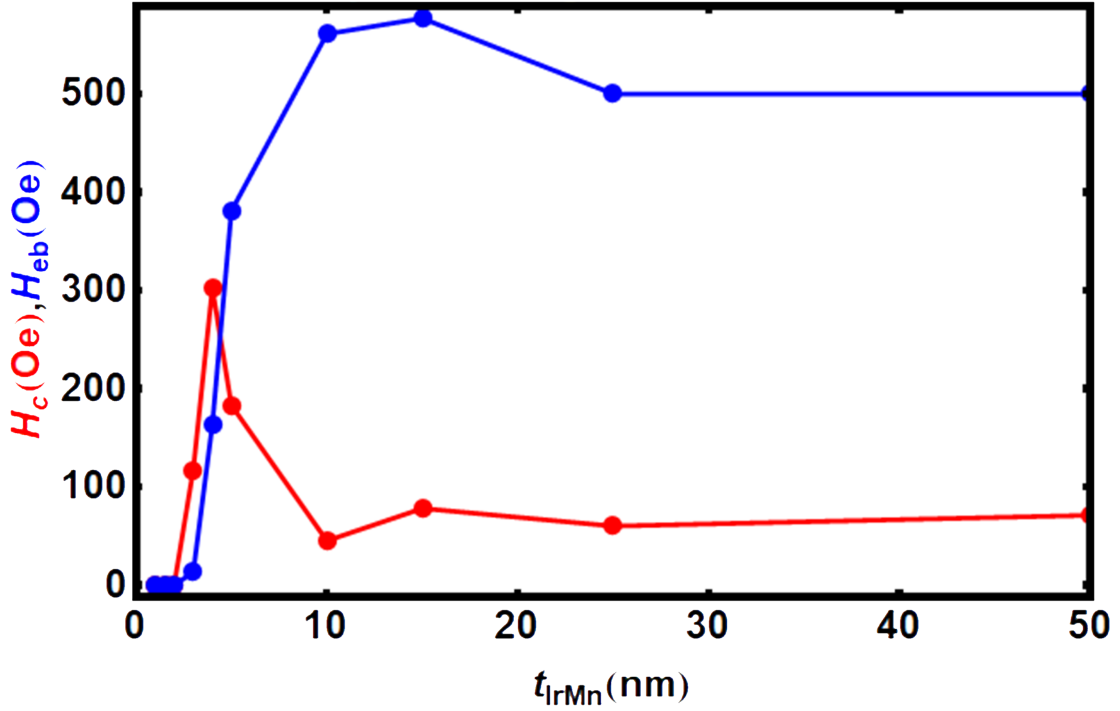


Figure 6.1. Coercivity(red), Exchange bias (blue) vs IrMn<sub>3</sub> thickness at 10 K

temperature of IrMn<sub>3</sub>, coercive field enhancement and variation of exchange bias magnitude were examined for the stack of Si (100)/ SiO<sub>x</sub> (300nm) / Pt (5nm) / NiFe (3nm) / Cu (15 nm) / NiFe (3 nm) / IrMn<sub>3</sub> (t) / Pt (5nm). We determined that 3 nm IrMn<sub>3</sub> layer was the minimum thickness in terms of having AF magnetic properties close to room temperature and high exchange bias field. Field cooling was done from 350 K to 10 K, for two different directions, parallel and perpendicular to the current direction.

For ultrathin layer of antiferromagnet, like 1, 1.5, 2, 3 nm samples, magnetization vs field measurement was conducted at 10 K, 200 K and 300 K, Figure 6.2, 6.3, 6.4, 6.5, hence we figured out where is the blocking temperature of the stack since above the blocking temperature exchange bias is zero.

## 6.2. Structural Characterization of (100) Oriented IrMn<sub>3</sub> Thin Film

We used MgO/[IrMn<sub>3</sub>(3nm)/Py(2 nm)]/Ti(2nm) multilayer for electrical measurement as well as material characterization. We grew the sample on (100) oriented

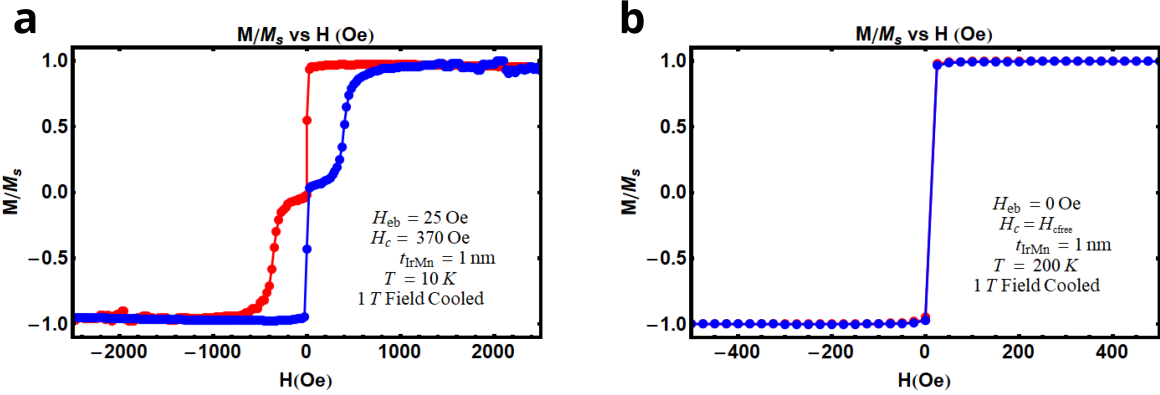


Figure 6.2. Magnetization vs field measurements at a) 10 K and b) 200 K for 1 nm  $\text{IrMn}_3$

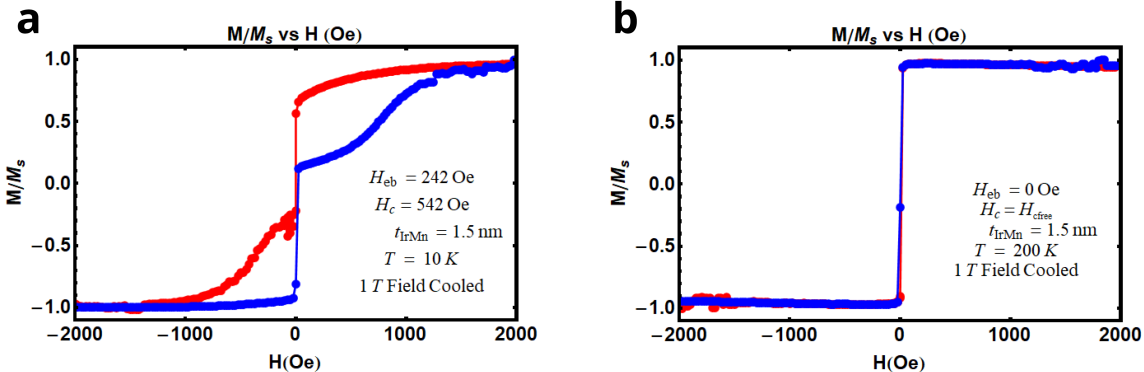


Figure 6.3. Magnetization vs field measurements at a) 10 K and b) 200 K for 1.5 nm  $\text{IrMn}_3$

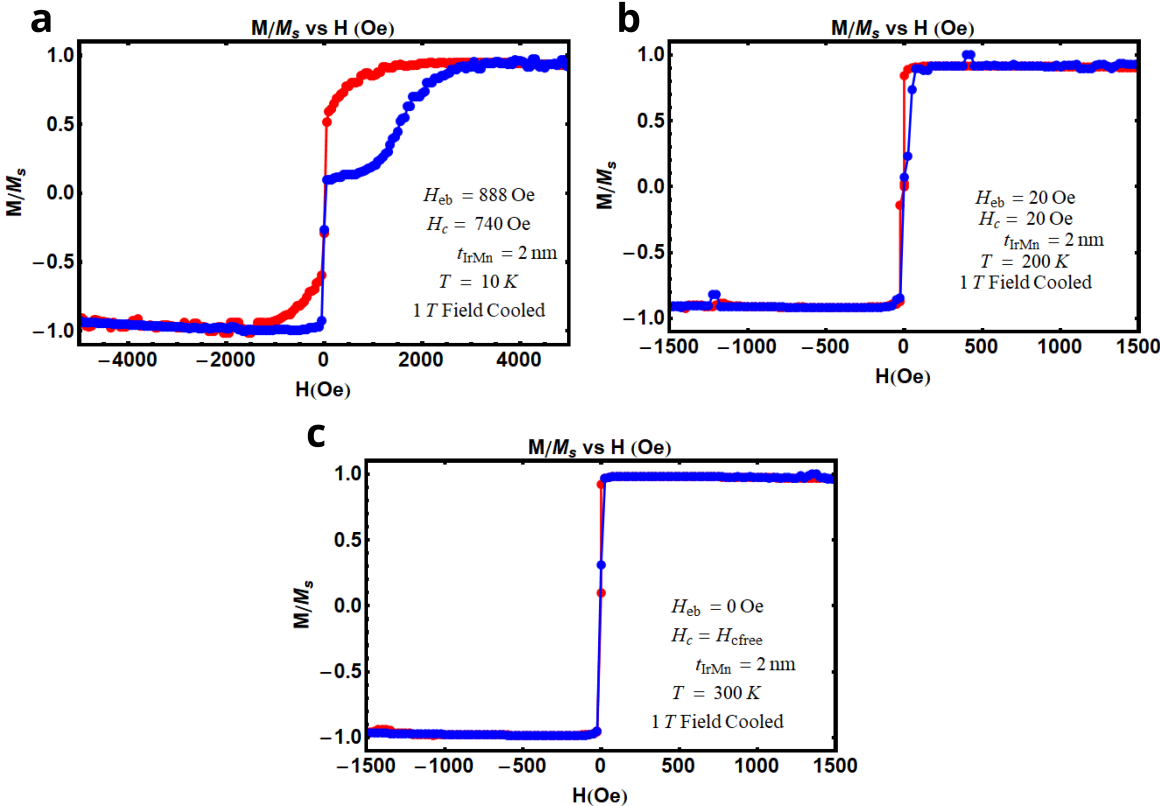


Figure 6.4. Magnetization vs field measurements at a) 10 K, b) 200 K and c) 300 K for 2 nm IrMn<sub>3</sub>

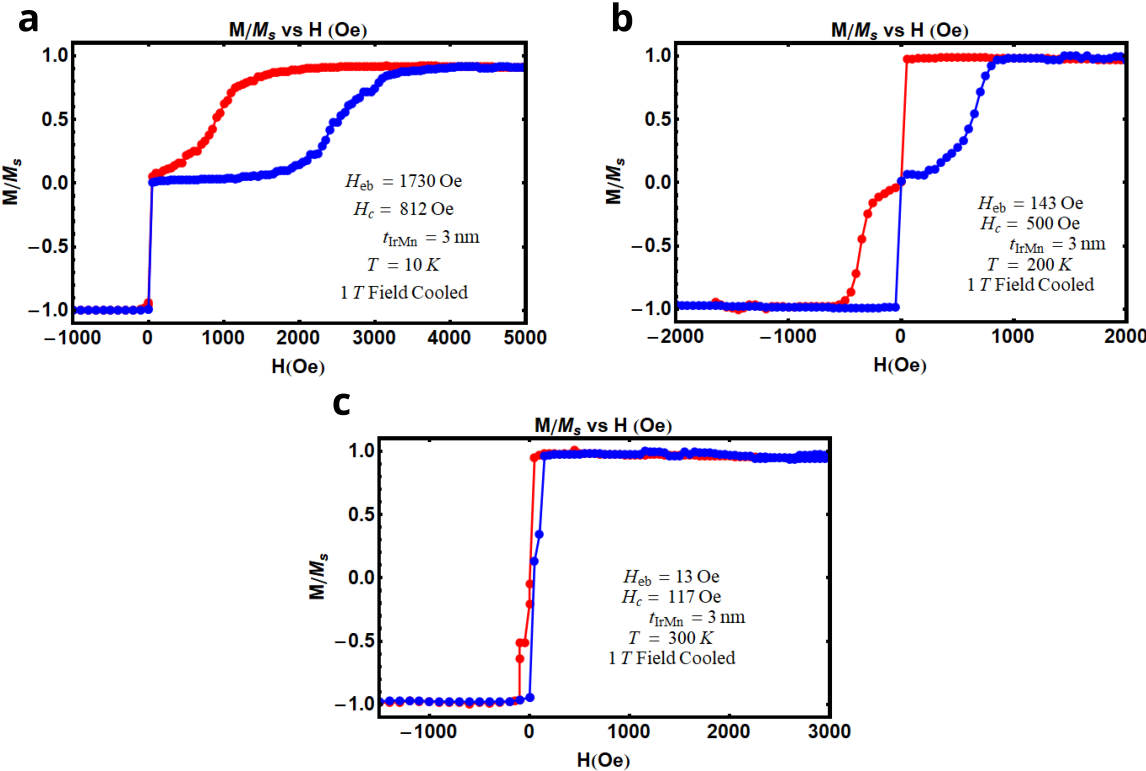


Figure 6.5. Magnetization vs field measurements at a) 10 K, b) 200 K and c) 300 K for 3 nm  $\text{IrMn}_3$

MgO substrate with the DC magnetron sputter system in 3 mTorr Ar pressure. Pre-bake was done at 825°C for 1 hour before starting Ir<sub>18</sub>Mn<sub>82</sub> deposition. We followed the procedure explained by Zhang et. al. [69] in order to grow (100) oriented IrMn<sub>3</sub> which gives the highest spin Hall angle among all the crystal orientations.

We decreased the temperature to 550°C then 3 nm IrMn<sub>3</sub> thin film growth process was started and needed 2 nm Ni<sub>20</sub>Fe<sub>80</sub> layer for forming exchange bias was coated at the room temperature. 2 nm Ti layer used as a capping layer.

Crystal structure of the MgO/IrMn<sub>3</sub> (3 nm)/Pt (2 nm)/Ti (3 nm) was performed by X-Ray diffraction (XRD) technique, peak location can be seen in Figure 6.6 and observed peak locations are consistent with literature [69]. Furthermore determination of the chemical composition of the samples was obtained by X-Ray photoelectron spectroscopy (XPS) technique. We started to mill from top to bottom layer and a few layers later we corrected for the relative sputter yields. Composition in the bulk of the material was found to be 3 for Ir and Mn ratio, as shown in Figure 6.7.

Also we performed tunneling electron microscopy measurement to prove crystal ordering was formed along (100) crystal orientation as shown in Figure 6.8.

### 6.3. Exchange Bias Manipulation by Spin Orbit Torque

We showed the SOT effects on the antiferromagnetic ordering of 3nm thick (100) oriented IrMn<sub>3</sub> thin films deposited on heated MgO (100) substrates. The IrMn<sub>3</sub> layer is overcoated with a 2 nm Ni<sub>20</sub>Fe<sub>80</sub> layer followed by patterning into a Hall bar. Upon cooling from 350 K below the Neel temperature of the IrMn<sub>3</sub> layer (300 K) with an external field of 1 T applied perpendicular to the bar, anisotropic magnetoresistance measurements of Ni<sub>20</sub>Fe<sub>80</sub> samples were performed. We can see that there is no field cooling direction dependence to form up exchange bias in system, as shown in Figure 6.10, As shown in Figure 6.9, the exchange bias was successfully manipulated by the SOT.

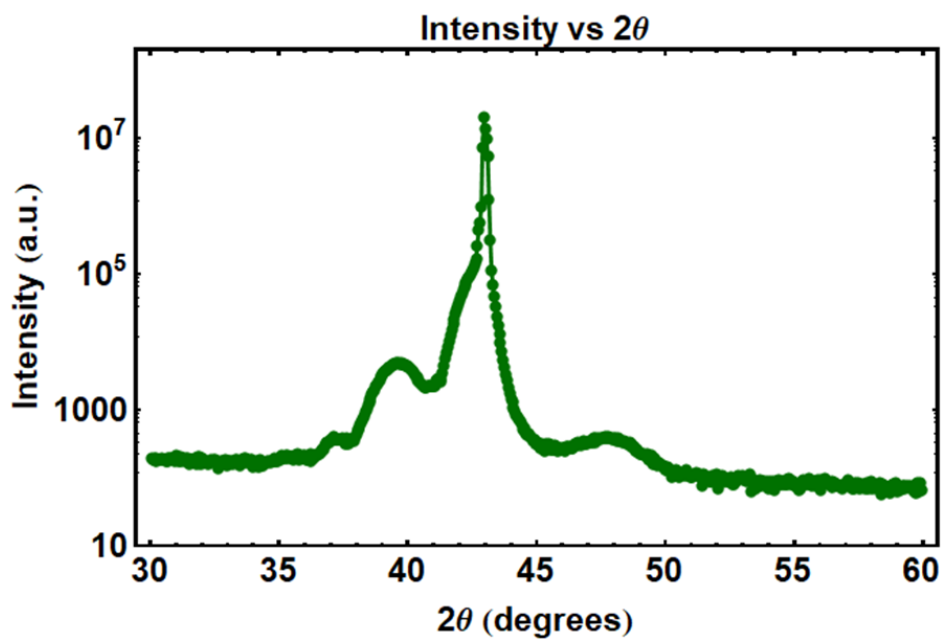


Figure 6.6. X-Ray diffraction measurement of MgO/IrMn<sub>3</sub>(3 nm)/Pt(2 nm)/Ti (3 nm)

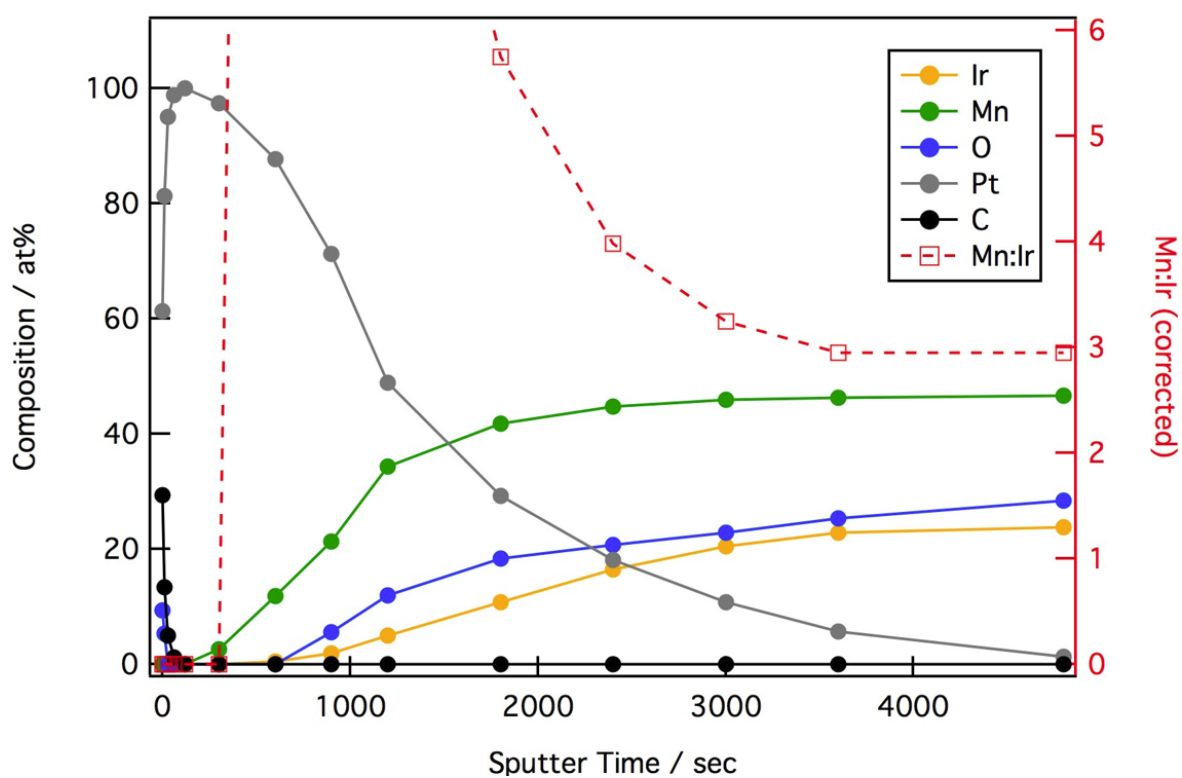


Figure 6.7. X-Ray photoelectron spectroscopy of MgO/IrMn<sub>3</sub>(3 nm)/Pt(2 nm) /Ti(3 nm)

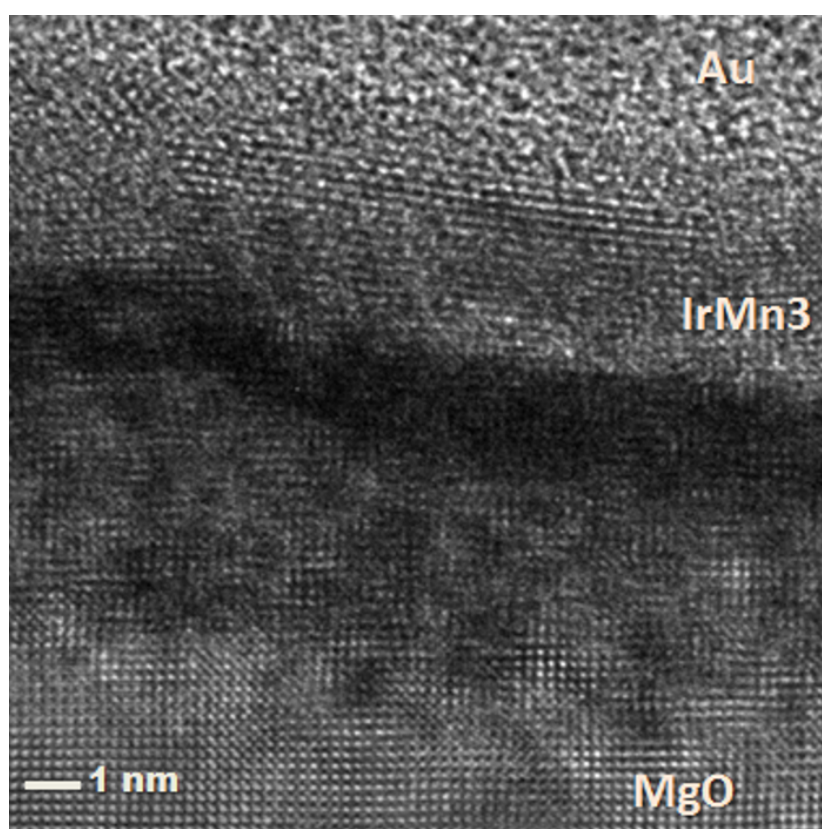


Figure 6.8. Transmission electron microscopy (TEM) of MgO/IrMn<sub>3</sub>(3 nm)/ Au(200 nm)

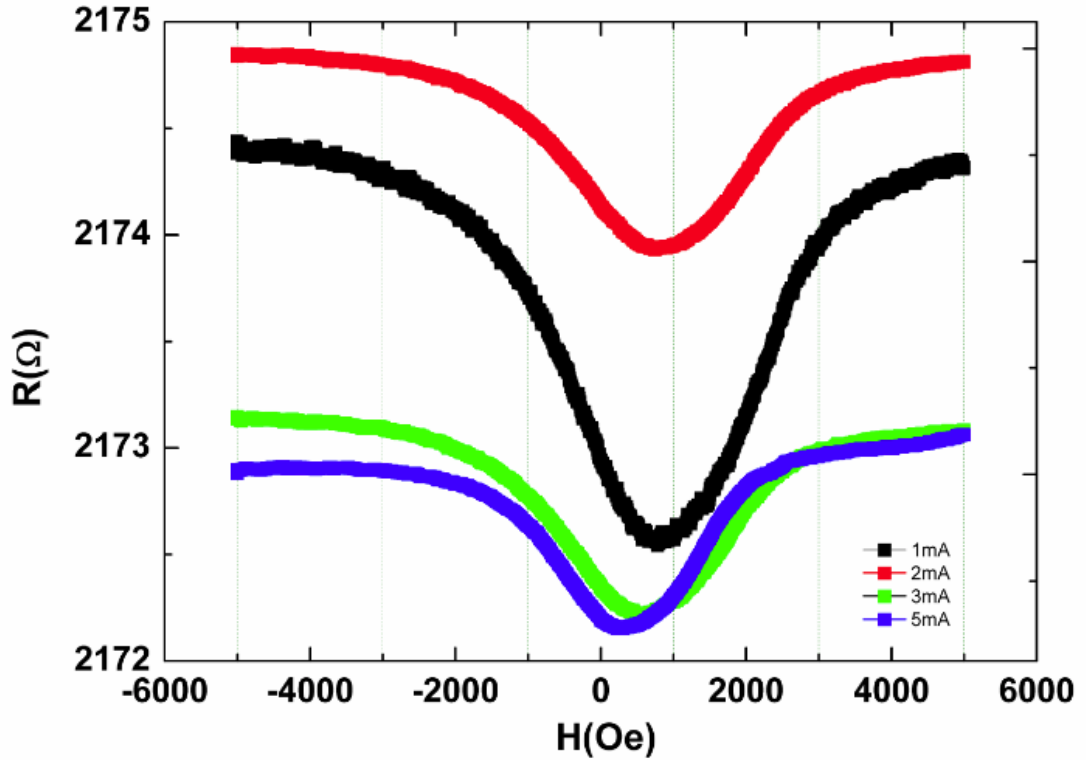


Figure 6.9. Resistance vs Magnetic Field for 1 mA (black), 2 mA (red), 3 mA (green), 5 mA (blue) applied current for the sample MgO/IrMn<sub>3</sub>(3 nm)/Py(2 nm)/Ti(2 nm).

In Figure 6.9, we showed that manipulation of the exchange bias has been achieved by spin orbit torque induced spin orbit coupling. As a conventional method exchange bias is measured by hysteresis loop shift but we can understand this shift with anisotropic magnetoresistance measurement as well. We gradually increased the applied current value as 1, 2, 3 and 5 mA, loop shifted to the left. There are two possible explanations for this loop shift, one of them is current assisted joule heating and the other one is spin orbit torque acting on the interface of permalloy and IrMn<sub>3</sub> layers. To understand which mechanism was dominant, exchange field vs current, resistance versus current and resistance versus temperature measurements were implemented, as shown Figures 6.10, 6.11 ,6.12, respectively.

Exchange bias field,  $H_{ex}$ , is reduced to zero at 10 mA.  $H_{ex}$  vs temperature measurement shows that  $H_{ex}$  is not even zero at 300 K (13 Oe). So one would need significant heating to see this effect. Resistance vs current data shows that resistance

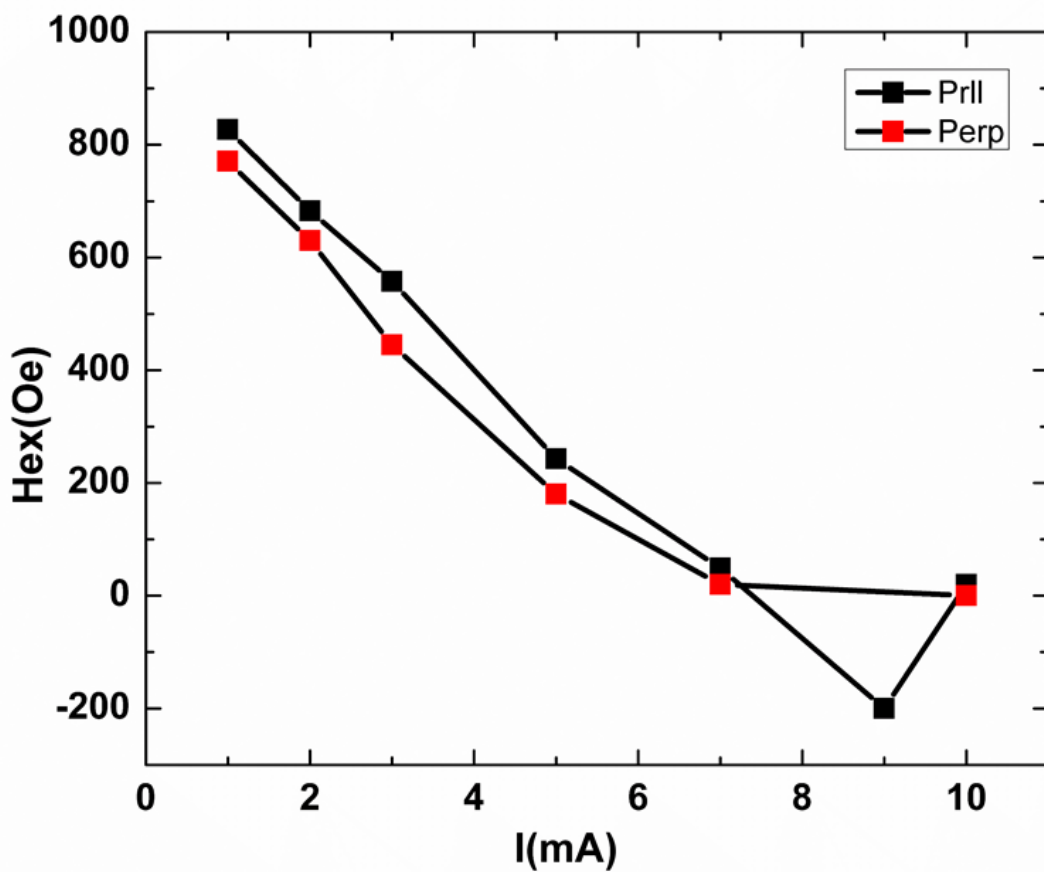


Figure 6.10. Exchange bias field vs current (parallel current direction o the field cooling direction (black), perpendicular current direction to the field cooling direction (red) of MgO/IrMn<sub>3</sub>(3nm)/Py(2 nm)/Ti(2nm)

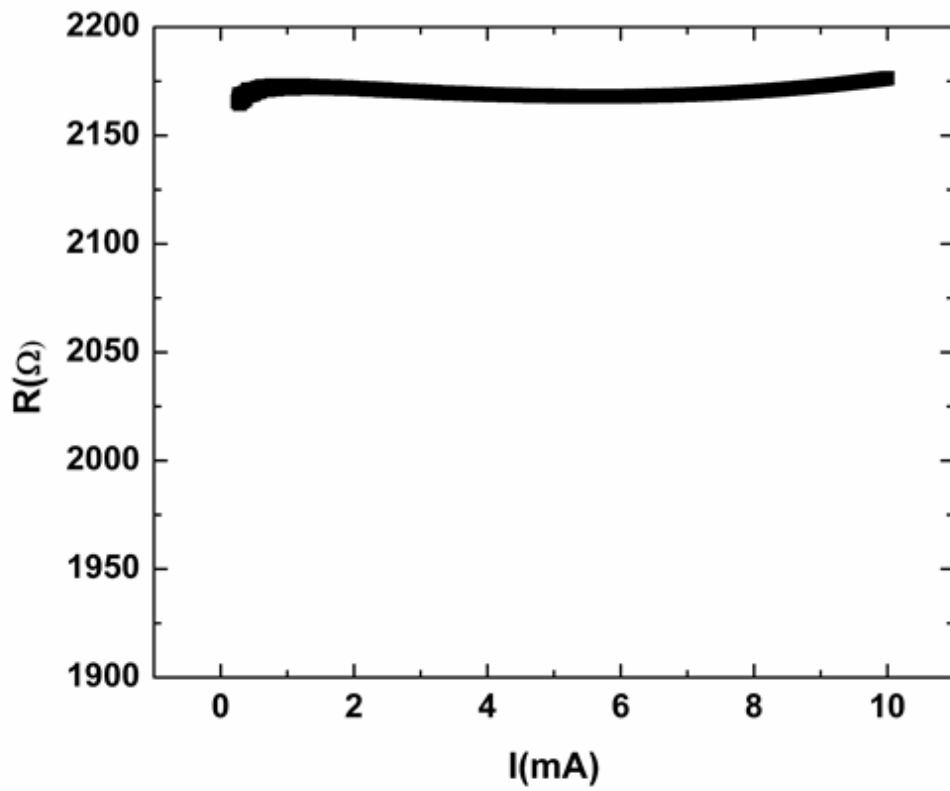


Figure 6.11. Resistance vs Current of MgO/IrMn<sub>3</sub>(3nm)/Py(2 nm)/Ti(2nm)

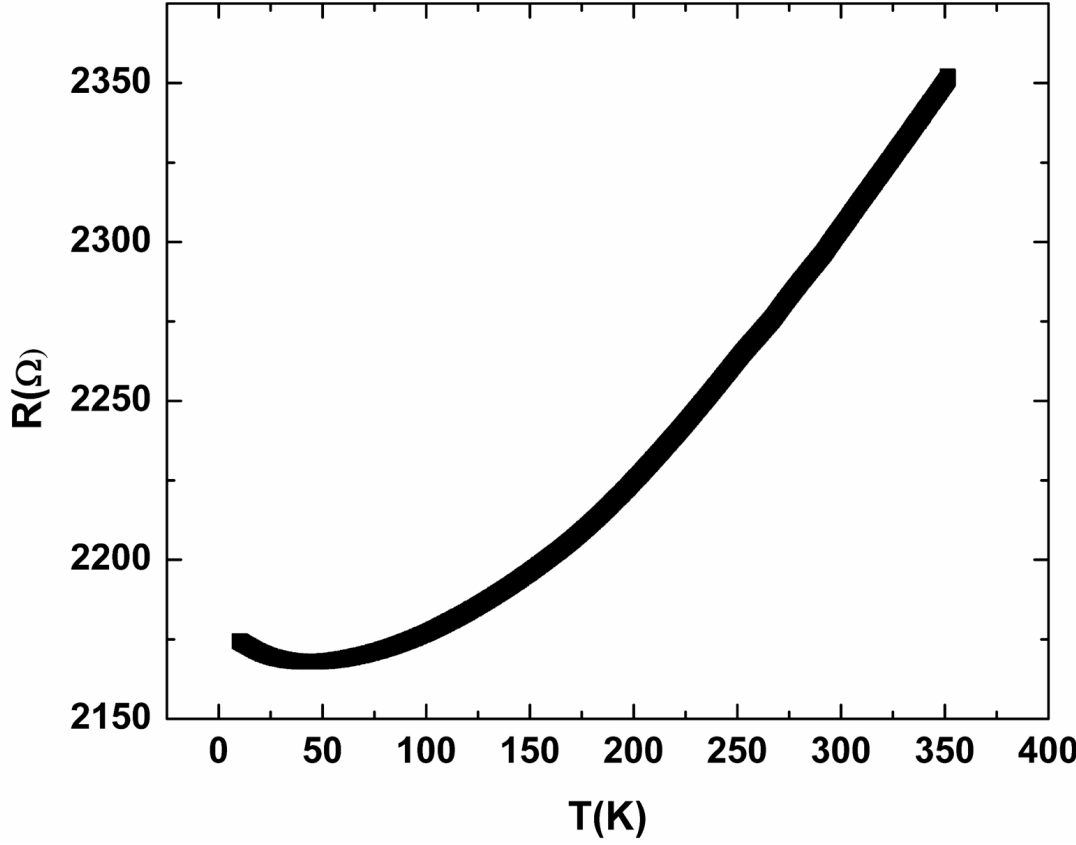


Figure 6.12. Resistance vs Temperature of MgO/IrMn<sub>3</sub>(3nm)/Py(2 nm)/Ti(2nm)

change with current is negligibly small whereas resistance vs temperature data shows that for a temperature change around 300 K causes a 200 ohm change in resistance. Therefore, we conclude that the effect that we observe can not be accounted for by Joule heating mechanism. So it must be due to spin orbit torque.

Furthermore, the manipulation of the exchange bias in system is possible with applied current for the sample MgO/IrMn<sub>3</sub>(3nm)/Py(2 nm)/Ti(2nm) as shown in Figure 6.9.

#### 6.4. Electroresistance in Antiferromagnet

We started with the Si/SiO<sub>2</sub>/Ti(5Å)/Pt(10 nm)/IrMn<sub>3</sub>(3nm)/Ti(3 nm) sample but we realized that 10 nm Pt was too thick to observe spin orbit torque effect. Resistance vs temperature measurement result was shown in Figure 6.13. Then we decreased the thickness of Pt layer to enhance current density that was flowing through IrMn<sub>3</sub> layer, we observed a drastic change in resistance vs temperature measurement shown in Figure 6.14 where resistance decreased with increasing temperature.

We tried to measure the change in resistance with respect to the applied current. Before starting measurement, field cooling ( $H_C$ ) was done under three different cooling directions as shown in Figure 6.17 with a 1 T external field. For Si/SiO<sub>2</sub>/Ti(5Å)/Pt(10 nm)/IrMn<sub>3</sub>(3nm)/Ti(3 nm), no resistance drop was observed for negative and positive applied current. Since big portion of current density passed through Pt layer instead of IrMn because there is an order of magnitude difference in resistivities [74], SOT was not dominant in the process. Then we decreased the thickness of Pt layer from 10 nm to 2 nm. Hence we were able to observe resistance variation for the sample Si/SiO<sub>2</sub>/Ti(5Å)/Pt(2 nm)/IrMn<sub>3</sub>(3nm)/Ti(3 nm). We observed a resistance drop for all field cooling directions at the level of 20 ohm.

It is recently reported that (100) oriented IrMn<sub>3</sub> has a huge spin hall angle,  $\theta_{SH}=0.35$  [69]. We wanted to observe the effect self torque of IrMn<sub>3</sub>, coming from its high spin orbit coupling, as a resistance change in Hall bar device. So, we observed

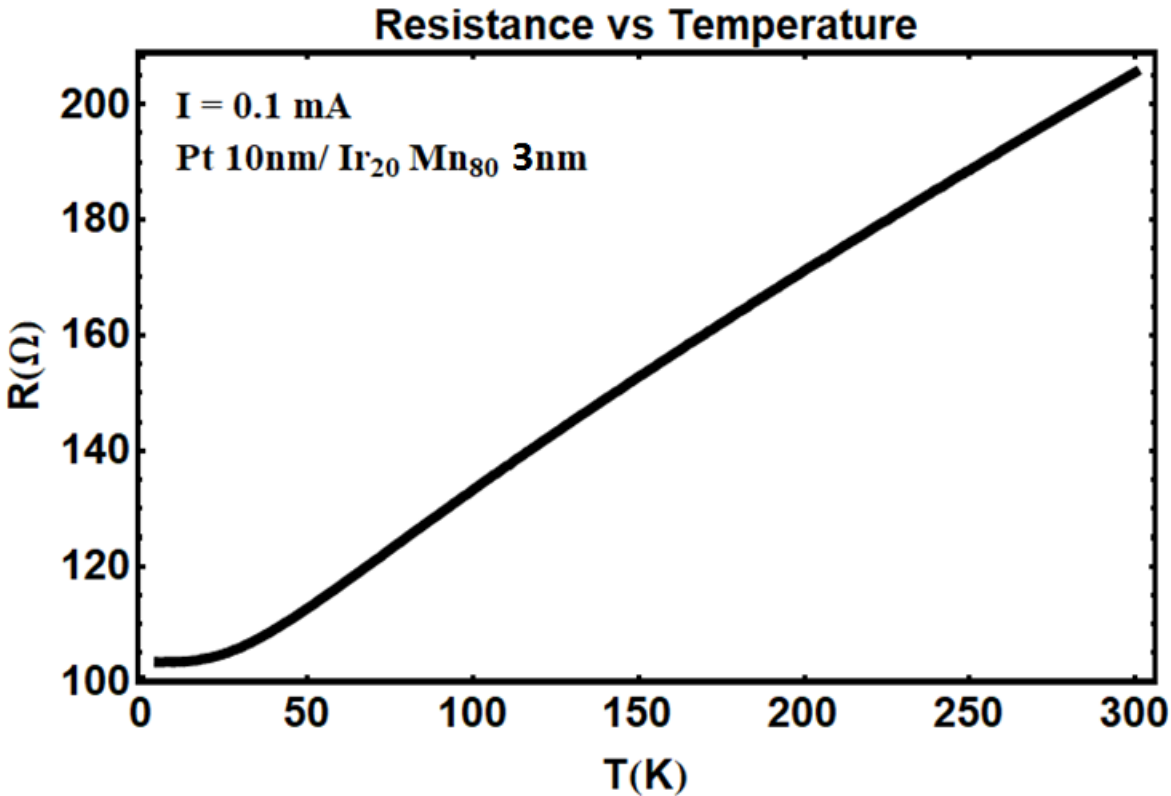


Figure 6.13. Resistance vs Temperature of Si/SiO<sub>2</sub>/Ti(5Å)/Pt(10 nm)/IrMn<sub>3</sub>(3 nm)/Ti(3 nm)

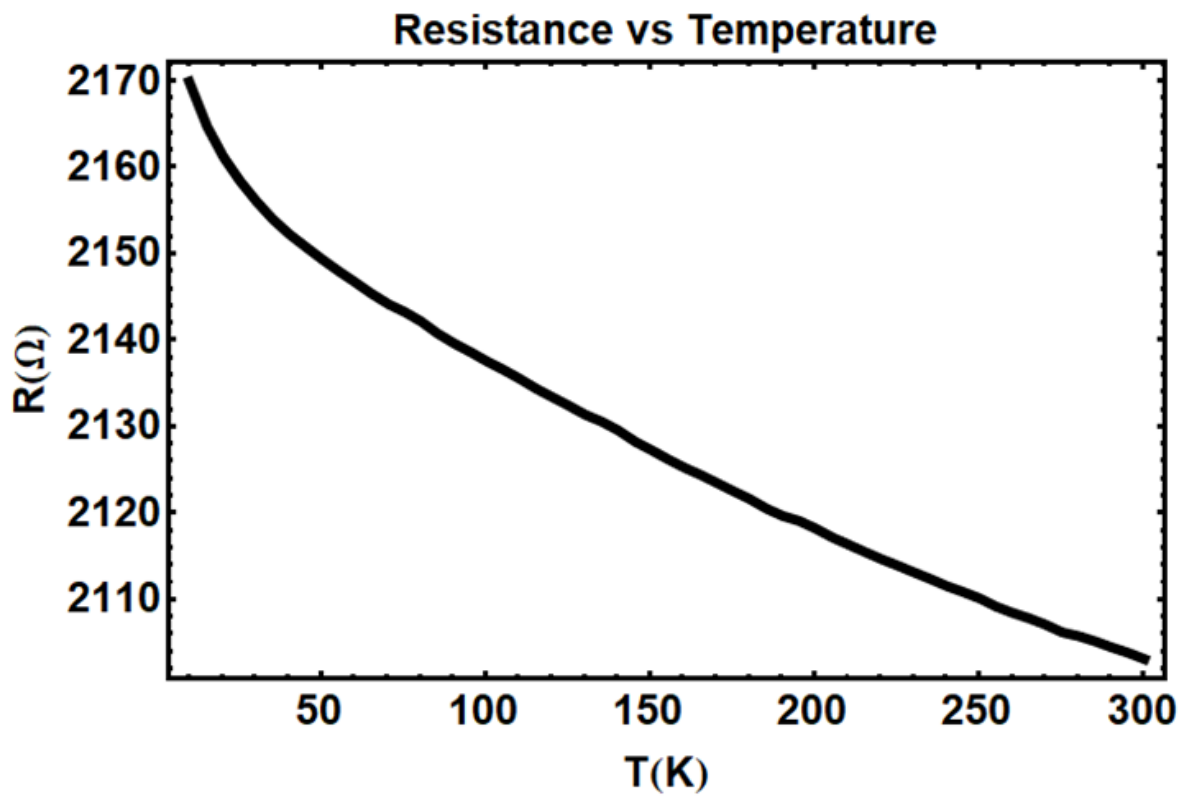


Figure 6.14. Resistance vs Temperature of Si/SiO<sub>2</sub>/Ti(5Å)/Pt(2 nm)/IrMn<sub>3</sub>(3 nm)/Ti(3 nm)

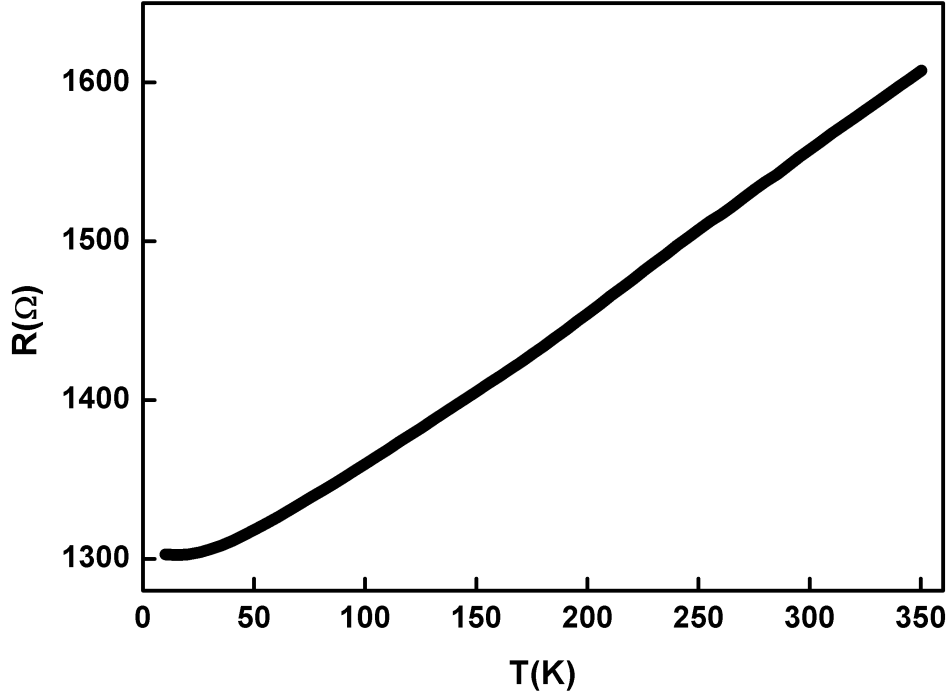


Figure 6.15. Resistance vs Temperature of MgO/IrMn<sub>3</sub>(3nm)/Pt(2 nm)/Ti(3 nm)

more variation in resistance for sample MgO/IrMn<sub>3</sub>(3nm)/Pt(2 nm)/Ti(3 nm) than sample Si/SiO<sub>2</sub>/Ti(5Å)/Pt(2 nm)/IrMn<sub>3</sub>(3nm)/Ti(3 nm) with the applied current on Hall bar device. We observed resistance drop for all field cooling directions at the level of 30 ohm for MgO/IrMn<sub>3</sub>(3nm)/Pt(2 nm)/Ti(3 nm).

Also we tried to understand the effect of field cooling value on resistance variation for the sample MgO/IrMn<sub>3</sub>(3nm)/Pt(2 nm)/Ti(3 nm). We changed the applied field as 3T, 7T shown in Figure 6.20 and Figure 6.21. We showed there was no correlation between the resistance variation and field cooling value. For three cases, we observed resistance drop for all field cooling directions at the level of 30 ohm for MgO/IrMn<sub>3</sub>(3nm)/Pt(2 nm)/Ti(3 nm). We decided to change the heavy metal of stack to enhance the ultimate spin orbit torque which plays an important role on exchange bias manipulation. Then we used W instead of Pt layer because beta phase W also have a relatively large spin hall angle [75, 76]. We applied current negative and positive direction up to 10 mA then we observed huge resistance drop around 1450 ohm as

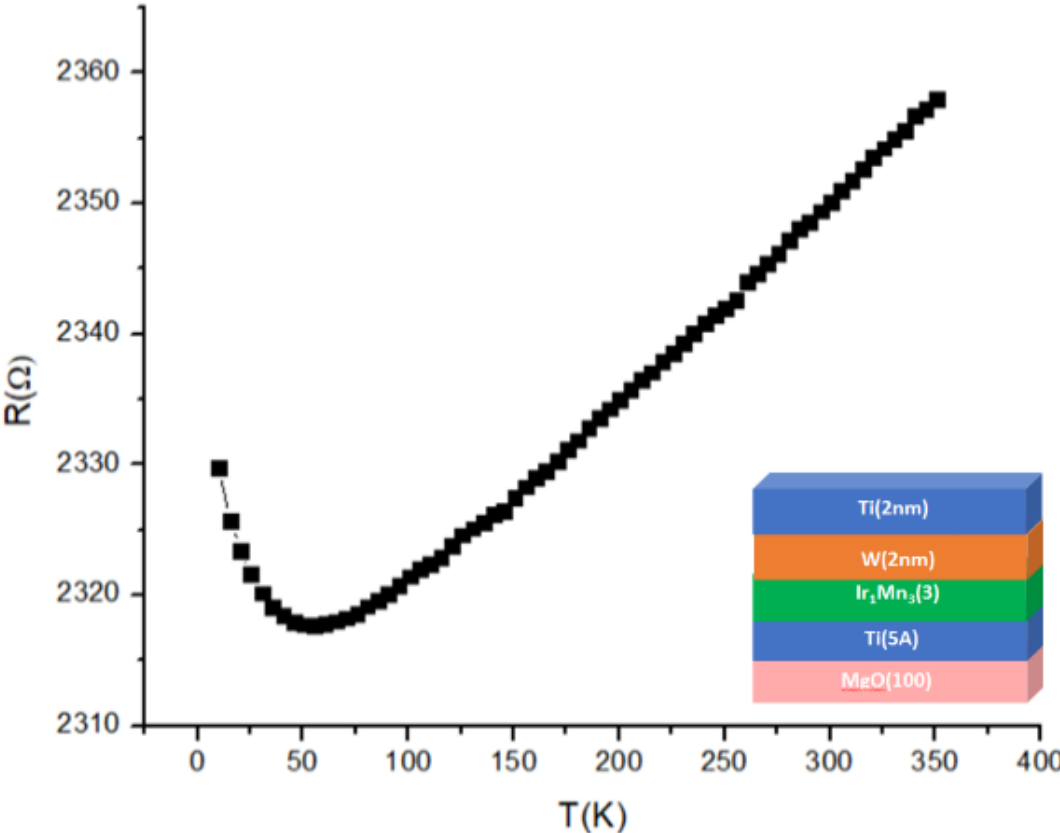


Figure 6.16. Resistance vs Temperature of MgO/IrMn<sub>3</sub>(3 nm)/W(2 nm)/Ti(3 nm)

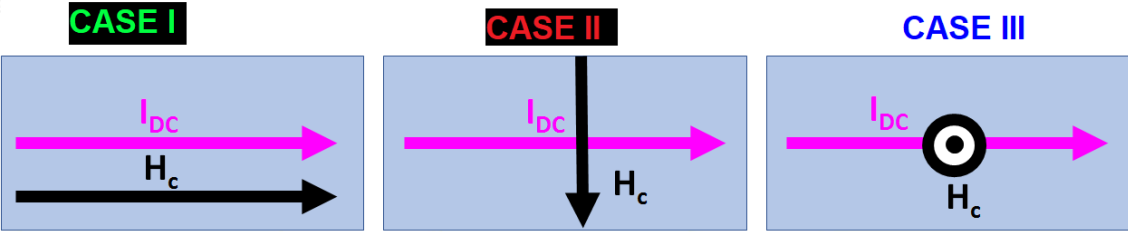


Figure 6.17. Field cooling ( $H_c$ ) and applied current ( $I_{DC}$ ) directions, 1 T external field applied in one of the above three directions.

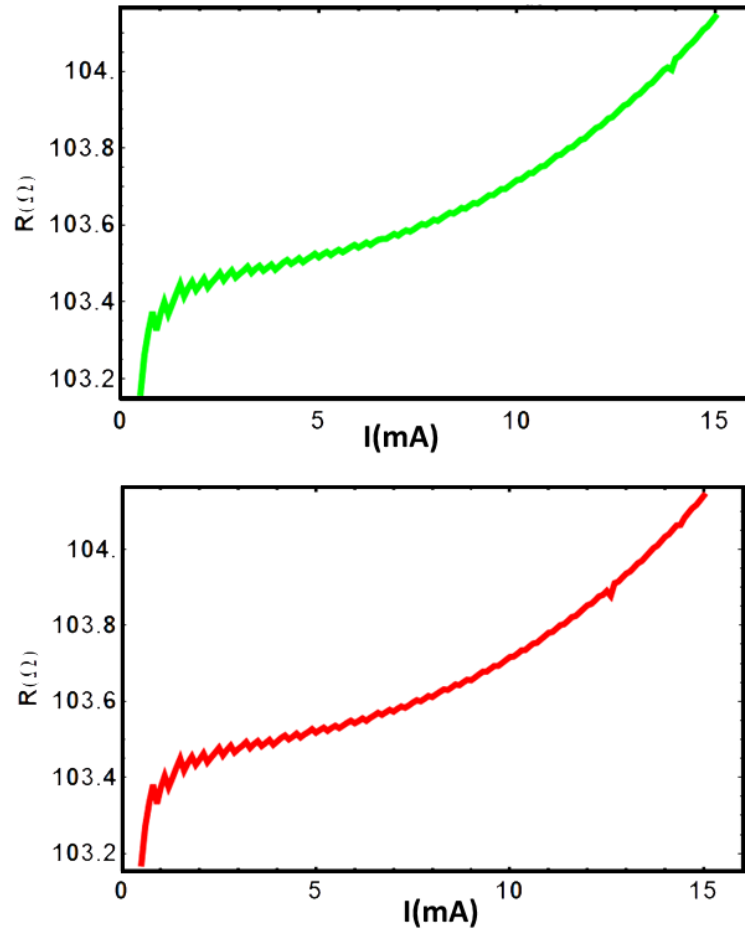


Figure 6.18.  $R$  vs  $I_{DC}$  measurements for Si/SiO<sub>2</sub>/Ti (5 Å)/Pt (10 nm)/IrMn<sub>3</sub> (3 nm)/Ti (3 nm) at 10 K with zero external field. (Green curve shows parallel field cooling, red curve belongs to perpendicular field cooling.)

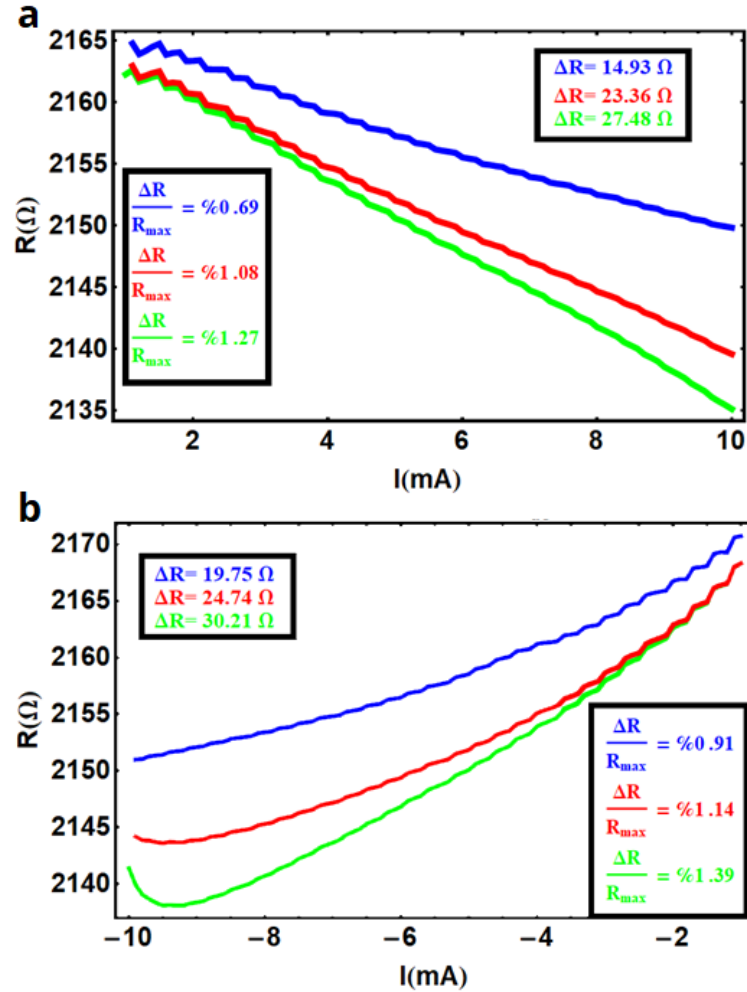


Figure 6.19.  $R$  vs  $I_{DC}$  for a) positive and b) negative current measurements for Si/SiO<sub>2</sub>/Ti(5Å)/Pt (2nm)/IrMn<sub>3</sub> (3 nm)/Ti (3 nm) at 10 K with zero external field. (Green, red and blue curves show parallel, perpendicular and out of plane field cooling directions respectively.)

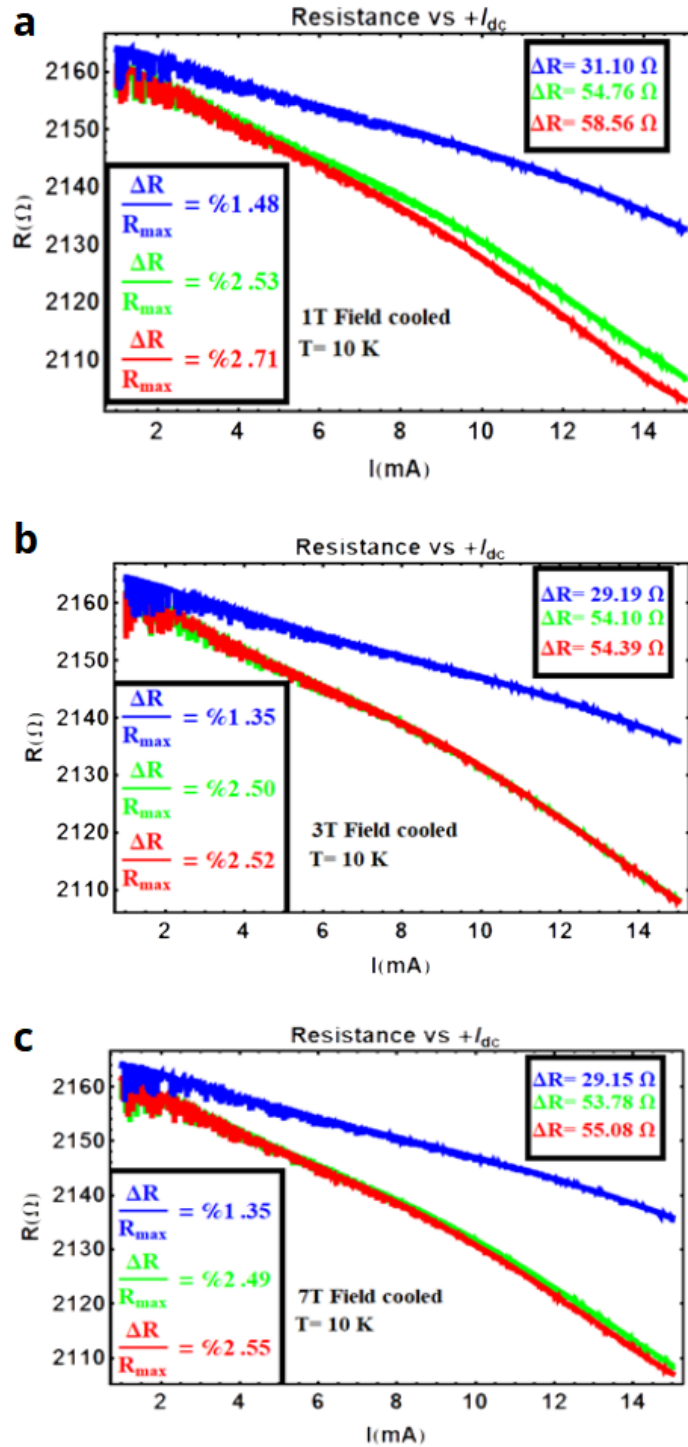


Figure 6.20.  $R$  vs  $I_{DC}$  for positive current measurements for MgO/IrMn<sub>3</sub> (3 nm)/Pt (2 nm)/Ti (3 nm) at 10 K with zero external field. (Green, red and blue curves show parallel, perpendicular and out of plane field cooling directions respectively for a) 1 T, b) 3 T and c) 7 T field cooling magnetic field value.)

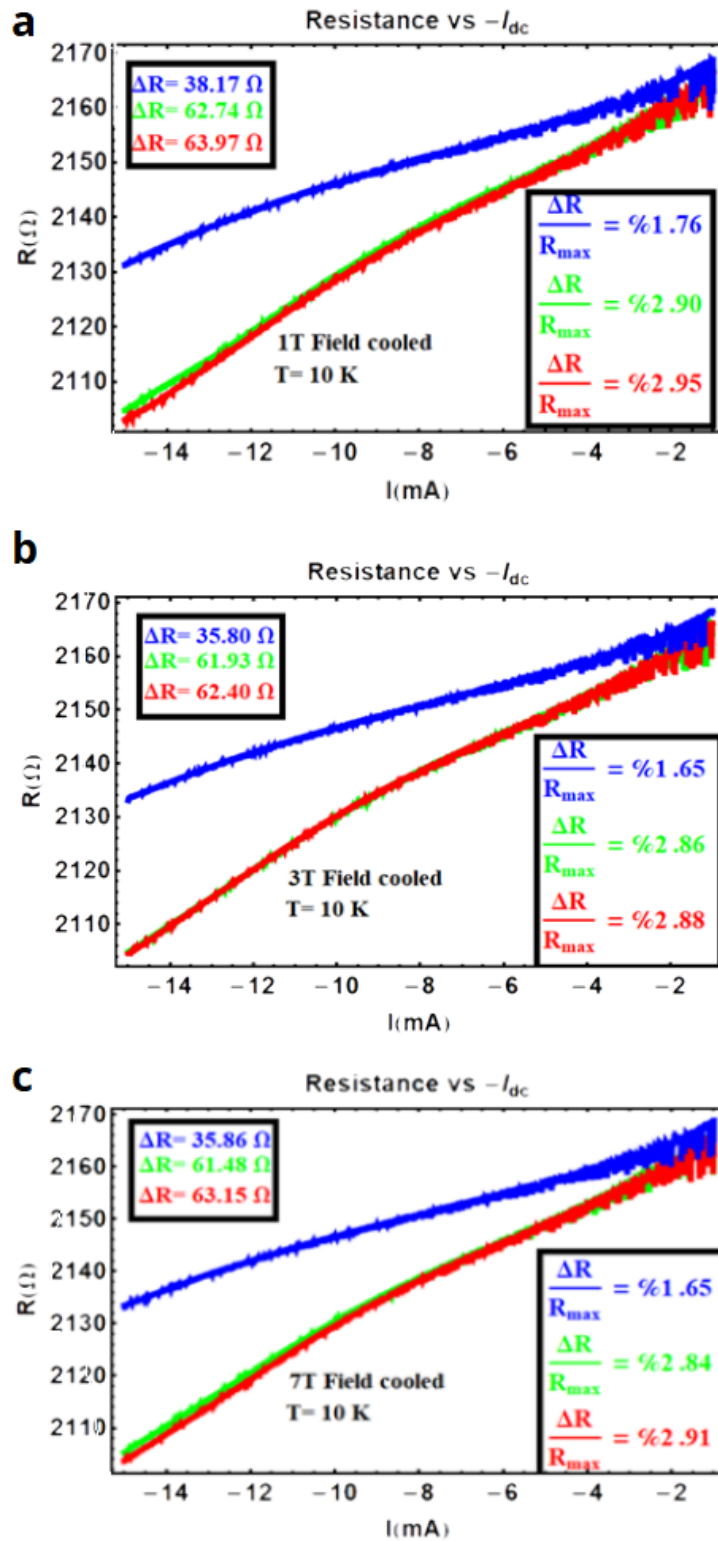


Figure 6.21.  $R$  vs  $I_{DC}$  for negative current measurements for MgO/IrMn<sub>3</sub>(3 nm)/Pt(2nm)/Ti(3nm) at 10 K with zero external field. (Green, red and blue curves show parallel, perpendicular and out of plane field cooling directions respectively for a) 1 T, b) 3 T and c) 7 T field cooling magnetic field value.)

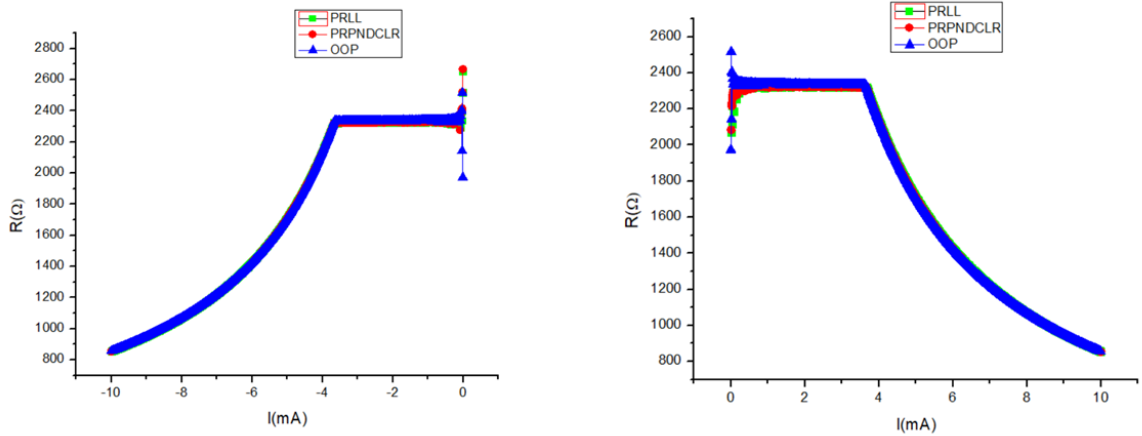


Figure 6.22.  $R$  vs  $I_{DC}$  (positive left, negative current right) measurements for  $\text{MgO}/\text{IrMn}_3(3\text{nm})/\text{W}(2\text{ nm})/\text{Ti}(3\text{ nm})$  at 10 K with zero external field. black and red curves show parallel, perpendicular and out of plane field cooling directions respectively, for 1 T field cooling magnetic value.)

shown in Figure 6.22, and also resistance vs temperature graph shown in Figure 6.12.

This spin orbit torque induced resistance variation was around 65%, to enhance resistance variation we decided to use 5 repeats of  $[\text{IrMn}_3(3\text{nm})/\text{W}(2\text{ nm})]$  multistack. During deposition temperature was  $580^\circ\text{C}$  only for the first layer of  $\text{IrMn}_3$  hence that was the only (100) oriented layer. The other layers were grown at room temperature so ultimately film had polycrystalline crystal structure. However we have observed very large resistance drop around 1200 ohm with the applied current as shown in Figure 6.23.

As a summary, we achieved the manipulation of exchange bias at the interface  $\text{IrMn}_3/\text{Py}$  of by self torque (100) oriented  $\text{IrMn}_3$ . Also giant resistance variation due to spin orbit coupling effect was observed for samples  $\text{IrMn}_3(3\text{nm})/\text{W}(2\text{ nm})$  and 5 repeats of  $[\text{IrMn}_3(3\text{nm})/\text{W}(2\text{ nm})]$  multistack.

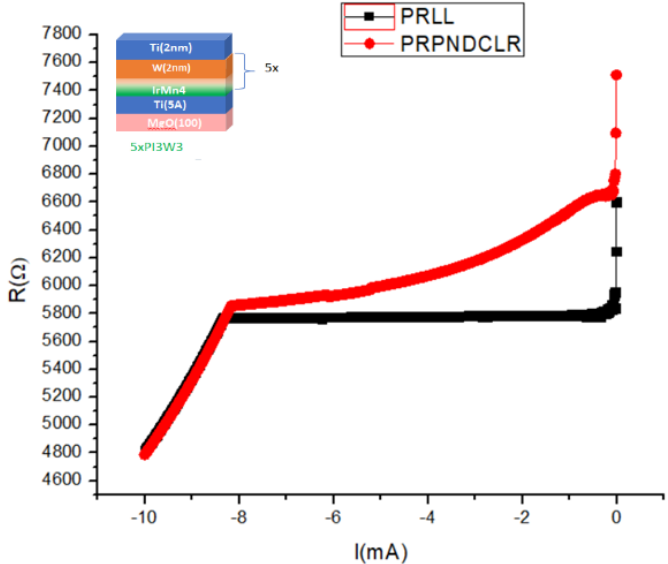


Figure 6.23.  $R$  vs  $I_{DC}$  ( positive left, negative current right ) measurements for  $MgO/5x[IrMn_3(3nm)/W(2 nm)]/Ti(3 nm)$  at 10 K with zero external field. (Green, red and blue curves show parallel, perpendicular field cooling directions respectively, for 1 T field cooling magnetic value.)

## 7. CONCLUSION

In this thesis, we have talked about experiments which were conducted through three different geometries. First geometry was an astroid shaped Py nanomagnet defined on Si/SiO<sub>x</sub> substrate fabricated with e-beam lithography and photolithography. Patterned nanomagnets have a variety of applications from nanoscale memory devices to on-chip nano-oscillators, detectors, magnetic sensors. Because they display a variety of features like AMR, high frequency oscillations of magnetic structures, spin waves etc. By adjusting the size and shape of our nanomagnet we can make a specific micro-magnetic configuration energetically favorable. In this geometry, micro magnetic configurations arise from the interplay between different energy terms like magnetostatic energy, exchange energy, Zeeman energy etc. At the end, the antivortex nanomagnetic configuration which has minimum energy is favoured.

AC demagnetized astroid shaped nanomagnet allows the nucleation of the antivortex. We observed the magnetic configurations under magnetic force microscopy and examined the interactions of the micro-magnetic antivortex configuration with magnetic field and electric current. Our aim was to move the position of the antivortex continuously, creating a high frequency motion, a nanosecond periodical motion which will eventually give an RF signal in the range of 100 MHz all the way to a couple of GHz.

In literature there are many studies focusing on vortex but there is a gap for antivortex so we investigated the stability of magnetic antivortices. Magnetic imaging with MFM and anisotropic magnetoresistance measurements proved that nucleation, observation and annihilation of antivortex micromagnetic configuration in astroid shaped nanomagnets were successfully achieved. Manipulation of antivortex motion by interaction with applied magnetic field was also accomplished. Several contact designs have been tried and different electrical setups have been constructed for room temperature and low temperature measurements under magnetic field.

We have worked with different device geometries to eliminate the high sample resistance, around  $900 \Omega$ , which prevented us from obtaining a detectable AMR signal. To make sure that the signal we receive from the device is coming from only the antivortex, we removed the top and bottom current paths in the astroid shape. After determining the final device and contact geometry, device resistance was around  $53 \Omega$  level at room temperature. By means of resistance vs field measurements, nucleation and annihilation conditions of the antivortex were figured out.

Detailed studies of the stability of antivortices presented in Chapter 3 showed that we have seen stable antivortex at zero field in parallel case. When the applied current was flown parallel to the field direction, antivortex nucleation and annihilation were detected. When the current was flown perpendicular to the field direction, there were some steps that may stem from defects or there can be nucleated antivortex or vortex-antivortex pairs. Simulations are in progress by our Italian collaborators to clarify the measurement.

Our second geometry was Pt/CoFeB/Ti multilayer nanopillar device grown on Si/SiO<sub>x</sub> substrate fabricated with e-beam lithography. In Chapter 4, we have studied the nucleation and observation of several magnetic configurations such as Néel skyrmions, horseshoes and radial vortices by magnetic force microscopy. Also the evolution of radial vortices from Néel skyrmions is achieved in Pt/CoFeB/Ti multilayer nanopillar device.

The configurations observed in the nanopillar device appearing in the presence of interfacial Dzyaloshinskii-Moriya Interaction (i-DMI), have potential applications in emerging spintronic technologies such as race-track magnetic memory, spin logic, radio frequency nano-oscillators and sensors. The foreseeable advantages of these configurations over conventional micro-magnetic structures are their small size, topological stability and easy spin-torque driven manipulation with much lower threshold current densities giving way to improved storage capacity, and faster operation with efficient use of energy.

The magnetic structures revealed here were nucleated with an external magnetic field treatment but did not require a dc bias-field to be stabilized afterwards which was found to be necessary in some earlier studies. Other skyrmion nucleation techniques include the application of external magnetic field pulses or injection of current pulses through a constriction.

We changed the repeat of multistack by means of milling technique resulting in the minimization of total energy of the system. Furthermore it is found that lattice mismatch is decreased and crystal structure is improved by enhanced oxidation. So the easy axis of the multistack switched from perpendicular to inplane allowing us to observe stable radial vortex. The Pt/CoFeB/Ti multilayer whose magnetic anisotropy could be tuned with number of repeats and post-production treatments, provides a unique experimental workbench to study a spectrum of micro-magnetic configurations.

Lastly in Chapter 6, we worked on Hall bar geometry made of IrMn<sub>3</sub> constructed on MgO substrate (by a procedure originally developed by Weifeng Zhang).

We achieved the exchange bias manipulation and electroresistance effect on (100) oriented IrMn<sub>3</sub> which is an antiferromagnet with three-fold symmetry resulting in a large positive spin Hall angle. Also giant resistance variation due to spin orbit coupling effect was observed for samples IrMn<sub>3</sub>(3nm)/W(2 nm) and 5 repeats of [IrMn<sub>3</sub>(3 nm)/W (2 nm)] multistack.

We demonstrated the magnetic, structural and morphological characterization of materials to understand the microscopic origins of the magnetic behaviour of the devices by techniques such as vibrating sample magnetometer, x-ray diffraction, x-ray photo electron spectroscopy, atomic force microscopy and magnetic force microscopy in Chapter 2.

We used DC magnetron sputtering system for deposition and ion milling of thin films. Using bow tie design, electrical properties of materials were characterized and their resistivity values are found.

By means of the dicer wafer is divided into the pieces and glued to resistivity option puck. A LEMO cable was designed to conduct low temperature measurement in PPMS. Also magnetic characterization of the materials are studied by Vibrating Sample Magnetometer (VSM) and SQUID magnetometer. Magnetic moment versus magnetic field measurements and exchange bias observation at the interface of IrMn/NiFe thin films are examined. Structural characterisation is done to understand the composition and crystal orientation of the samples that were especially used for Chapter 6.

We described the fabrication processes for nanopillar and Hall bar devices starting from the preparation of chips, followed by patterning with photolithography and electron beam lithography in Chapter 3.

For future work, we are planning to study dynamic properties of magnetic antivortices, formed in a special geometry called astroid. We want to detect gyration frequency of antivortex which is expected to be around GHz frequency level. This will provide novel spintronic application such as detectors, sensors and oscillators. Also we will create an array of nanopillars containing radial vortices to have a spin torque nano-oscillator. For this purpose we started to fabricate the 3 terminal device which can be found in the appendix. Additionally with this geometry, dynamics of the spin valve structure can be detected with much less current density by means of nano contact.

All in all, this thesis provides a perspective for future investigations on spintronics and antiferromagnetic spintronics.

## REFERENCES

1. Makarov, A., *Modeling of Emerging Resistive Switching Based Memory Cells*, Ph.D. Thesis, TU Wien, 3 2014.
2. Jungwirth, T., X. Marti, P. Wadley and J. Wunderlich, “Antiferromagnetic spintronics”, *Nature nanotechnology*, Vol. 11, No. 3, p. 231, 2016.
3. “Bruker Dimension Edge”, <https://www.bruker.com/products/surface-and-dimensional-analysis/atomic-force-microscopes/dimension-edge/overview.html>.
4. “MESP-HM”, <https://www.brukerafmprobes.com/p-3311-mesp-hm.aspx>.
5. Eaton, P. and K. Batziou, *Artifacts and Practical Issues in Atomic Force Microscopy*, pp. 3–28, Springer New York, New York, NY, 2019.
6. <http://www.nanophys.kth.se/nanophys/facilities/nfl/afm/fast-scan/bruker-help/and Apps/Troubleshooting/AFM Image Quality.htm>.
7. Ragusa, C., M. Carpentieri, F. Celegato, P. Tiberto, E. Enrico, L. Boarino and G. Finocchio, “Magnonics crystal composed by magnetic antivortices confined in antidots”, *IEEE Transactions on Magnetics*, Vol. 47, No. 10, pp. 2498–2501, 2011.
8. Zhu, Y., Z. Zhang, B. Ma and Q. Jin, “Thermal stability of CoFeB/Pt multilayers with perpendicular magnetic anisotropy”, *Journal of Applied Physics*, Vol. 111, No. 7, p. 07C106, 2012.
9. Barman, A. and J. Sinha, *Spin dynamics and damping in ferromagnetic thin films and nanostructures*, Vol. 1, Springer, 2018.
10. Tserkovnyak, Y., A. Brataas and G. E. W. Bauer, “Spin pumping and magneti-

- zation dynamics in metallic multilayers”, *Phys. Rev. B*, Vol. 66, p. 224403, Dec 2002, <https://link.aps.org/doi/10.1103/PhysRevB.66.224403>.
11. Kamionka, T., M. Martens, K. W. Chou, M. Curcic, A. Drews, G. Schütz, T. Tyliczszak, H. Stoll, B. Van Waeyenberge and G. Meier, “Magnetic antivortex-core reversal by circular-rotational spin currents”, *Physical review letters*, Vol. 105, No. 13, p. 137204, 2010.
  12. Hoffmann, A. and S. D. Bader, “Opportunities at the Frontiers of Spintronics”, *Phys. Rev. Applied*, Vol. 4, p. 047001, Oct 2015, <https://link.aps.org/doi/10.1103/PhysRevApplied.4.047001>.
  13. Griffiths, J., “Anomalous high-frequency resistance of ferromagnetic metals”, *Nature*, Vol. 158, No. 4019, p. 670, 1946.
  14. Chien, C.-L., F. Q. Zhu and J.-G. Zhu, “Patterned nanomagnets”, *Physics today*, Vol. 60, No. 6, p. 40, 2007.
  15. Haldar, A. and K. S. Buchanan, “Magnetic antivortex formation in pound-key-like nanostructures”, *Applied Physics Letters*, Vol. 102, No. 11, p. 112401, 2013.
  16. Shigeto, K., T. Okuno, K. Mibu, T. Shinjo and T. Ono, “Magnetic force microscopy observation of antivortex core with perpendicular magnetization in patterned thin film of permalloy”, *Applied Physics Letters*, Vol. 80, No. 22, pp. 4190–4192, 2002.
  17. Schulz, T., R. Ritz, A. Bauer, M. Halder, M. Wagner, C. Franz, C. Pfleiderer, K. Everschor, M. Garst and A. Rosch, “Emergent electrodynamics of skyrmions in a chiral magnet”, *Nature Physics*, Vol. 8, No. 4, p. 301, 2012.
  18. Yu, X., N. Kanazawa, W. Zhang, T. Nagai, T. Hara, K. Kimoto, Y. Matsui, Y. Onose and Y. Tokura, “Skyrmion flow near room temperature in an ultralow current density”, *Nature communications*, Vol. 3, p. 988, 2012.

19. Yu, X., Y. Onose, N. Kanazawa, J. Park, J. Han, Y. Matsui, N. Nagaosa and Y. Tokura, “Real-space observation of a two-dimensional skyrmion crystal”, *Nature*, Vol. 465, No. 7300, p. 901, 2010.
20. Jiang, W., W. Zhang, G. Yu, M. B. Jungfleisch, P. Upadhyaya, H. Somyali, J. E. Pearson, Y. Tserkovnyak, K. L. Wang, O. Heinonen *et al.*, “Mobile Néel skyrmions at room temperature: status and future”, *AIP Advances*, Vol. 6, No. 5, p. 055602, 2016.
21. Karakas, V., A. Gokce, A. T. Habiboglu, S. Arpaci, K. Ozbozduman, I. Cinar, C. Yanik, R. Tomasello, S. Tacchi, G. Siracusano *et al.*, “Observation of magnetic radial vortex nucleation in a multilayer stack with tunable anisotropy”, *Scientific reports*, Vol. 8, No. 1, p. 7180, 2018.
22. Woo, S., K. Litzius, B. Krüger, M.-Y. Im, L. Caretta, K. Richter, M. Mann, A. Krone, R. M. Reeve, M. Weigand *et al.*, “Observation of room-temperature magnetic skyrmions and their current-driven dynamics in ultrathin metallic ferromagnets”, *Nature materials*, Vol. 15, No. 5, p. 501, 2016.
23. Siracusano, G., R. Tomasello, A. Giordano, V. Puliafito, B. Azzerboni, O. Ozatay, M. Carpentieri and G. Finocchio, “Magnetic radial vortex stabilization and efficient manipulation driven by the Dzyaloshinskii-Moriya interaction and spin-transfer torque”, *Physical review letters*, Vol. 117, No. 8, p. 087204, 2016.
24. Slonczewski, J. C., “Current-driven excitation of magnetic multilayers”, *Journal of Magnetism and Magnetic Materials*, Vol. 159, No. 1-2, pp. L1–L7, 1996.
25. Berger, L., “Emission of spin waves by a magnetic multilayer traversed by a current”, *Physical Review B*, Vol. 54, No. 13, p. 9353, 1996.
26. D'yakonov, M. and V. Perel, “Possibility of orienting electron spins with current”, *Soviet Journal of Experimental and Theoretical Physics Letters*, Vol. 13, p. 467, 1971.

27. Finocchio, G., O. Ozatay, L. Torres, R. Buhrman, D. Ralph and B. Azzarboni, “Spin-torque-induced rotational dynamics of a magnetic vortex dipole”, *Physical Review B*, Vol. 78, No. 17, p. 174408, 2008.
28. Finocchio, G., V. Pribiag, L. Torres, R. Buhrman and B. Azzarboni, “Spin-torque driven magnetic vortex self-oscillations in perpendicular magnetic fields”, *Applied Physics Letters*, Vol. 96, No. 10, p. 102508, 2010.
29. Mistral, Q., M. van Kampen, G. Hrkac, J.-V. Kim, T. Devolder, P. Crozat, C. Chappert, L. Lagae and T. Schrefl, “Current-driven vortex oscillations in metallic nanocontacts”, *Physical review letters*, Vol. 100, No. 25, p. 257201, 2008.
30. Ruotolo, A., V. Cros, B. Georges, A. Dussaux, J. Grollier, C. Deranlot, R. Guillemet, K. Bouzehouane, S. Fusil and A. Fert, “Phase-locking of magnetic vortices mediated by antivortices”, *Nature nanotechnology*, Vol. 4, No. 8, p. 528, 2009.
31. Spaldin, N. A., *Magnetic materials: fundamentals and applications*, Cambridge University Press, 2010.
32. Meiklejohn, W. H. and C. P. Bean, “New magnetic anisotropy”, *Physical Review*, Vol. 105, No. 3, p. 904, 1957.
33. Devasahayam, A., P. Sides and M. Kryder, “Magnetic, temperature, and corrosion properties of the NiFe/IrMn exchange couple”, *Journal of applied physics*, Vol. 83, No. 11, pp. 7216–7218, 1998.
34. Nogués, J. and I. K. Schuller, “Exchange bias”, *Journal of Magnetism and Magnetic Materials*, Vol. 192, No. 2, pp. 203–232, 1999.
35. Lombard, L., E. Gapihan, R. Sousa, Y. Dahmane, Y. Conraux, C. Portemont, C. Ducruet, C. Papusoi, I. Prejbeanu, J. Nozières *et al.*, “IrMn and FeMn blocking temperature dependence on heating pulse width”, *Journal of Applied Physics*, Vol.

- 107, No. 9, p. 09D728, 2010.
36. Franssila, S., *Introduction to microfabrication*, John Wiley and Sons, 2010.
  37. “What is XPS?”, <http://xpssimplified.com/whatisxps.php>.
  38. Tan, E., *X-Ray Photoelectron Spectroscopy Studies of Aluminium Oxide Thin Films*, Ph.D. Thesis, 2006.
  39. Naumkin, A., A. Kraut-Vass, S. Gaarenstroom and C. Powell, “NIST X-ray Photoelectron Spectroscopy (XPS) Database, Version 3.5”, <http://srdata.nist.gov/xps/default.aspx>.
  40. Jones, J. E., “On the determination of molecular fields.—I. From the variation of the viscosity of a gas with temperature”, *Proceedings of the Royal Society of London. Series A, Containing Papers of a Mathematical and Physical Character*, Vol. 106, No. 738, pp. 441–462, 1924.
  41. Martin, Y. and H. K. Wickramasinghe, “Magnetic imaging by “force microscopy” with 1000 Å resolution”, *Applied Physics Letters*, Vol. 50, No. 20, pp. 1455–1457, 1987.
  42. Tomaszewski, P., “Jan Czochralski and his method”, *Institute of Low Temperature & Structural Research, PAS and ATUT Publishing House, Wroclaw-Kcynia*, 2003.
  43. Parker, N. W., A. D. Brodie and J. H. McCoy, “High-throughput NGL electron-beam direct-write lithography system”, *Emerging Lithographic Technologies IV*, Vol. 3997, pp. 713–720, International Society for Optics and Photonics, 2000.
  44. Thomson, W., “XIX. On the electro-dynamic qualities of metals:—Effects of magnetization on the electric conductivity of nickel and of iron”, *Proceedings of the Royal Society of London*, , No. 8, pp. 546–550, 1857.
  45. You, L., O. Lee, D. Bhowmik, D. Labanowski, J. Hong, J. Bokor and S. Salahud-

- din, “Switching of perpendicularly polarized nanomagnets with spin orbit torque without an external magnetic field by engineering a tilted anisotropy”, *Proceedings of the National Academy of Sciences*, Vol. 112, No. 33, pp. 10310–10315, 2015.
46. Romming, N., A. Kubetzka, C. Hanneken, K. von Bergmann and R. Wiesendanger, “Field-dependent size and shape of single magnetic skyrmions”, *Physical review letters*, Vol. 114, No. 17, p. 177203, 2015.
47. Marrows, C. H., “An inside view of magnetic skyrmions”, *Physics*, Vol. 8, p. 40, 2015.
48. Finocchio, G., F. Büttner, R. Tomasello, M. Carpentieri and M. Kläui, “Magnetic skyrmions: from fundamental to applications”, *Journal of Physics D: Applied Physics*, Vol. 49, No. 42, p. 423001, 2016.
49. Fert, A., V. Cros and J. Sampaio, “Skyrmions on the track”, *Nature nanotechnology*, Vol. 8, No. 3, p. 152, 2013.
50. Heinze, S., K. Von Bergmann, M. Menzel, J. Brede, A. Kubetzka, R. Wiesendanger, G. Bihlmayer and S. Blügel, “Spontaneous atomic-scale magnetic skyrmion lattice in two dimensions”, *Nature Physics*, Vol. 7, No. 9, p. 713, 2011.
51. Moreau-Luchaire, C., C. Moutafis, N. Reyren, J. Sampaio, C. Vaz, N. Van Horne, K. Bouzehouane, K. Garcia, C. Deranlot, P. Warnicke *et al.*, “Additive interfacial chiral interaction in multilayers for stabilization of small individual skyrmions at room temperature”, *Nature nanotechnology*, Vol. 11, No. 5, p. 444, 2016.
52. Romming, N., C. Hanneken, M. Menzel, J. E. Bickel, B. Wolter, K. von Bergmann, A. Kubetzka and R. Wiesendanger, “Writing and deleting single magnetic skyrmions”, *Science*, Vol. 341, No. 6146, pp. 636–639, 2013.
53. Nagaosa, N. and Y. Tokura, “Topological properties and dynamics of magnetic skyrmions”, *Nature nanotechnology*, Vol. 8, No. 12, p. 899, 2013.

54. Büttner, F., C. Moutafis, M. Schneider, B. Krüger, C. Günther, J. Geilhufe, C. v. K. Schmising, J. Mohanty, B. Pfau, S. Schaffert *et al.*, “Dynamics and inertia of skyrmionic spin structures”, *Nature Physics*, Vol. 11, No. 3, p. 225, 2015.
55. Mühlbauer, S., B. Binz, F. Jonietz, C. Pfleiderer, A. Rosch, A. Neubauer, R. Georgii and P. Böni, “Skyrmion lattice in a chiral magnet”, *Science*, Vol. 323, No. 5916, pp. 915–919, 2009.
56. Tacchi, S., R. Troncoso, M. Ahlberg, G. Gubbiotti, M. Madami, J. Åkerman and P. Landeros, “Interfacial Dzyaloshinskii-Moriya interaction in Pt/CoFeB films: effect of the heavy-metal thickness”, *Physical review letters*, Vol. 118, No. 14, p. 147201, 2017.
57. Di, K., V. L. Zhang, H. S. Lim, S. C. Ng, M. H. Kuok, X. Qiu and H. Yang, “Asymmetric spin-wave dispersion due to Dzyaloshinskii-Moriya interaction in an ultrathin Pt/CoFeB film”, *Applied Physics Letters*, Vol. 106, No. 5, p. 052403, 2015.
58. Hrabec, A., N. Porter, A. Wells, M. Benitez, G. Burnell, S. McVitie, D. McGruther, T. Moore and C. Marrows, “Measuring and tailoring the Dzyaloshinskii-Moriya interaction in perpendicularly magnetized thin films”, *Physical Review B*, Vol. 90, No. 2, p. 020402, 2014.
59. Miyake, S., *Novel Materials Processing by Advanced Electromagnetic Energy Sources: Proceedings of the International Symposium on Novel Materials Processing by Advanced Electromagnetic Energy Sources (MAPEES'04)*, Elsevier, 2005.
60. Authors, C. and editors of the volumes III/17G-41D, “Titanium oxide (TiO<sub>2</sub>): crystal structure, lattice parameters and related parameters of rutile”, *Non-Tetrahedrally Bonded Binary Compounds II*, pp. 1–5, 2000.
61. Boulle, O., J. Vogel, H. Yang, S. Pizzini, D. de Souza Chaves, A. Locatelli, T. O. Menteş, A. Sala, L. D. Buda-Prejbeanu, O. Klein *et al.*, “Room-temperature chiral

- magnetic skyrmions in ultrathin magnetic nanostructures”, *Nature nanotechnology*, Vol. 11, No. 5, p. 449, 2016.
62. Belmeguenai, M., J.-P. Adam, Y. Roussigné, S. Eimer, T. Devolder, J.-V. Kim, S. M. Cherif, A. Stashkevich and A. Thiaville, “Interfacial Dzyaloshinskii-Moriya interaction in perpendicularly magnetized Pt/Co/AlO<sub>x</sub> ultrathin films measured by Brillouin light spectroscopy”, *Physical Review B*, Vol. 91, No. 18, p. 180405, 2015.
63. Pollard, S. D., J. A. Garlow, J. Yu, Z. Wang, Y. Zhu and H. Yang, “Observation of stable Néel skyrmions in cobalt/palladium multilayers with Lorentz transmission electron microscopy”, *Nature communications*, Vol. 8, p. 14761, 2017.
64. Sakamaki, M., K. Amemiya, M. Liedke, J. Fassbender, P. Mazalski, I. Sveklo and A. Maziewski, “Perpendicular magnetic anisotropy in a Pt/Co/Pt ultrathin film arising from a lattice distortion induced by ion irradiation”, *Physical Review B*, Vol. 86, No. 2, p. 024418, 2012.
65. Yu, G., P. Upadhyaya, X. Li, W. Li, S. K. Kim, Y. Fan, K. L. Wong, Y. Tserkovnyak, P. K. Amiri and K. L. Wang, “Room-temperature creation and spin-orbit torque manipulation of skyrmions in thin films with engineered asymmetry”, *Nano letters*, Vol. 16, No. 3, pp. 1981–1988, 2016.
66. Jiang, W., P. Upadhyaya, W. Zhang, G. Yu, M. B. Jungfleisch, F. Y. Fradin, J. E. Pearson, Y. Tserkovnyak, K. L. Wang, O. Heinonen *et al.*, “Blowing magnetic skyrmion bubbles”, *Science*, Vol. 349, No. 6245, pp. 283–286, 2015.
67. Železný, J., P. Wadley, K. Olejník, A. Hoffmann and H. Ohno, “Spin transport and spin torque in antiferromagnetic devices”, *Nature Physics*, Vol. 14, No. 3, p. 220, 2018.
68. Han, J., Y. Wang, F. Pan and C. Song, “Spin-Hall-Effect-Assisted Electroresistance in Antiferromagnets via  $10^5$  A/cm<sup>2</sup> dc Current”, *Scientific reports*, Vol. 6, p.

31966, 2016.

69. Zhang, W., W. Han, S.-H. Yang, Y. Sun, Y. Zhang, B. Yan and S. S. Parkin, “Giant facet-dependent spin-orbit torque and spin Hall conductivity in the triangular antiferromagnet IrMn<sub>3</sub>”, *Science Advances*, Vol. 2, No. 9, p. e1600759, 2016.
70. Miltényi, P., M. Gierlings, J. Keller, B. Beschoten, G. Güntherodt, U. Nowak and K.-D. Usadel, “Diluted antiferromagnets in exchange bias: Proof of the domain state model”, *Physical Review Letters*, Vol. 84, No. 18, p. 4224, 2000.
71. Meiklejohn, W. H. and C. P. Bean, “New magnetic anisotropy”, *Physical review*, Vol. 102, No. 5, p. 1413, 1956.
72. Nowak, U., A. Misra and K.-D. Usadel, “Modeling exchange bias microscopically”, *Journal of Magnetism and Magnetic Materials*, Vol. 240, No. 1-3, pp. 243–247, 2002.
73. Ali, M., C. Marrows and B. Hickey, “Controlled enhancement or suppression of exchange biasing using impurity  $\delta$  layers”, *Physical Review B*, Vol. 77, No. 13, p. 134401, 2008.
74. Moriyama, T., M. Nagata, K. Tanaka, K. Kim, H. Almasi, W. Wang and T. Ono, “Spin-transfer-torque through antiferromagnetic IrMn”, *arXiv preprint arXiv:1411.4100*, 2014.
75. Mondal, S., S. Choudhury, N. Jha, A. Ganguly, J. Sinha and A. Barman, “All-optical detection of the spin Hall angle in W/CoFeB/SiO<sub>2</sub> heterostructures with varying thickness of the tungsten layer”, *Physical Review B*, Vol. 96, No. 5, p. 054414, 2017.
76. Pai, C.-F., L. Liu, Y. Li, H.-W. Tseng, D. C. Ralph and R. A. Buhrman, “Spin transfer torque devices utilizing the giant spin Hall effect of tungsten”, *Applied Physics Letters*, Vol. 101, No. 12, p. 122404, 2012.

77. Kohn, A., A. Kovács, R. Fan, G. McIntyre, R. Ward and J. Goff, “The antiferromagnetic structures of IrMn<sub>3</sub> and their influence on exchange-bias”, *Scientific reports*, Vol. 3, p. 2412, 2013.
78. Wu, D., G. Yu, C.-T. Chen, S. A. Razavi, Q. Shao, X. Li, B. Zhao, K. L. Wong, C. He, Z. Zhang *et al.*, “Spin-orbit torques in perpendicularly magnetized Ir<sub>22</sub>Mn<sub>78</sub>/Co<sub>20</sub>Fe<sub>60</sub>B<sub>20</sub>/MgO multilayer”, *Applied Physics Letters*, Vol. 109, No. 22, p. 222401, 2016.
79. Liu, L., *Manipulation of Magnetic Moment Using the Spin Current from Magnetic and Non-Magnetic Materials*, Ph.D. Thesis, Cornell University, 2012.

## APPENDIX A: 3 Terminal Device

In order to study the manipulation of the antiferromagnet layer by spin orbit torque of (100) oriented IrMn<sub>3</sub> which has three-fold symmetry [77] resulting in a large positive spin Hall angle [78], we designed the three terminal device, shown in Figure A.1. Basically it is a spin valve structure containing free and fixed 3 nm Ni<sub>20</sub>Fe<sub>80</sub> layers, separated by a non-magnetic 15 nm Cu spacer layer. IrMn<sub>3</sub> has been used as the antiferromagnet creating the exchange bias and fixing the adjacent ferromagnet. Pt is used as the heavy metal generating a pure spin current due to its spin Hall angle. Along with IrMn<sub>3</sub>, we expect the generated torque to add up and switch the magnetization of free layer by pure spin current. Additionally with this geometry, dynamics of the spin valve structure can be observed with much less current density by means of nano contact.

Device fabrication started with the calibration of deposition and ion milling rates shown in Table A.1 and Table A.2.

Following the calibration, we grew the multistack Au(100)/NiFe(3)/Cu(15)/NiFe(3)/IrMn<sub>3</sub>(t)/Ru(5) on Si/SiO<sub>x</sub> substrate, to grow (100) oriented IrMn<sub>3</sub> we switched to MgO substrate. We added 5 nm Ru capping layer on top of the multistack, because we used chemical etching instead of standard carbon deposition and etching technique during the fabrication of this device. We coat trilayer omnicoat/PMMA/HSQ resist combination that provide to get 1x1 μm<sup>2</sup> top contact region. If there is not Ru layer below omnicoat, the lift off process does not work and omnicoat does not stick well onto Pt or Ta [79] so the whole resist will peel off during development after e-beam lithography.

After the deposition, we started patterning by coating the sample with Shipley 1813 photoresist at 4000 rpm and baking it at 115°C for 1 minute. Green layers shown in Figure A.2 were patterned with laser writer using the following parameters:

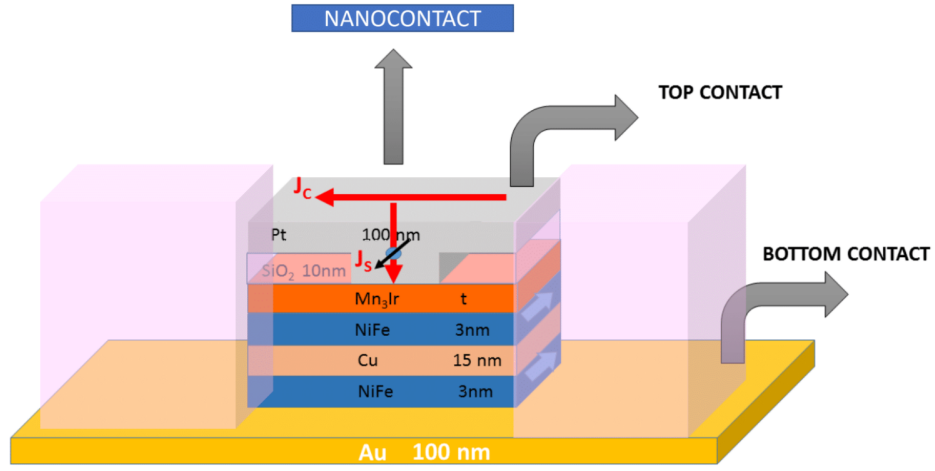


Figure A.1. Schematic drawing of three terminal device

Table A.1. Deposition rates of the three terminal device materials

Target	Pressure (mTorr)	Power (Watt)	Sputter Rate (Å/sec)
Ti	2	100	$0.343 \pm 0.01$
W	2	30	$0.211 \pm 0.01$
Ru	2	30	$0.319 \pm 0.01$
Pt	2	30	$0.314 \pm 0.01$
Au	2	80	$1.907 \pm 0.01$
Cu	2	30	$0.464 \pm 0.01$
IrMn	2	30	$0.242 \pm 0.01$
NiFe	2	30	$0.225 \pm 0.01$

Table A.2. Ion milling rates of the three terminal device materials

Target	Pressure (mTorr)	Beam Voltage (V)	Accelerator Voltage (V)	Beam Current (mA)	Ion Milling Etch Rate (Å/sec)
Ti	2	150	30	6	$0.177 \pm 0.01$
W	2	150	30	6	$0.162 \pm 0.01$
Pt	2	150	30	6	$0.255 \pm 0.01$
Au	2	150	30	6	$0.261 \pm 0.01$
Cu	2	150	30	6	$0.174 \pm 0.03$
IrMn	2	150	30	6	$0.151 \pm 0.01$
NiFe	2	150	30	6	$0.186 \pm 0.01$

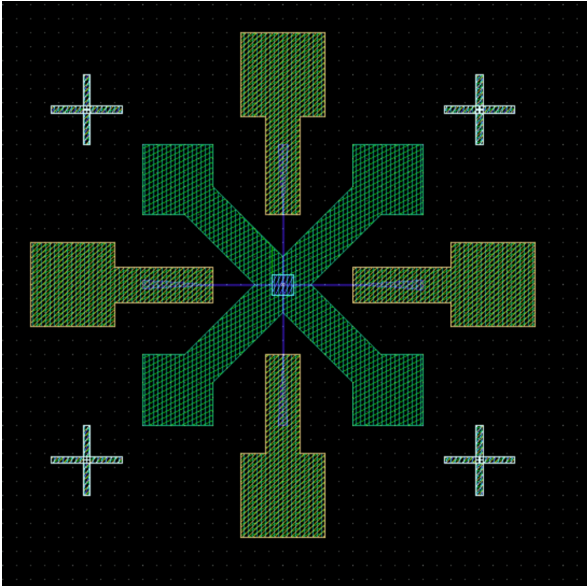


Figure A.2. Layout Editor drawing of three terminal device design

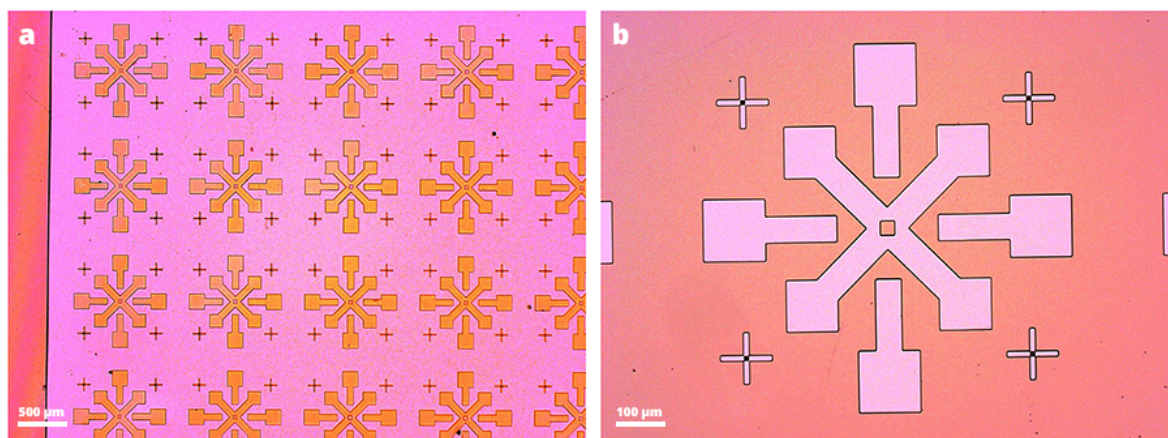


Figure A.3. Optical microscopy images of the three terminal device after the developing omnicoat/PMMA/HSQ resist combination, a) magnified 5 times, b) magnified 20 times.

- Filter: 3%
- D step: 4
- Position speed: 5
- Lens: 3
- Gain: 14.5
- Center to X Y enabled
- Plane enabled
- Interferometer enabled

Then the sample was developed with CD 26 for 1 minute after the UV light exposure. Descum was performed at 170 mTorr  $O_2$  pressure, 50 watt power, 24 sccm  $O_2$  flow rate for 30 seconds with MARCH CS-1701 Reactive Ion Plasma Etcher. The optical microscopy image of the sample after descum is shown in Figure A.3. Later the sample was sputtered 5 nm Ti and 100 nm Au and lift off was done with acetone and isopropanol as shown in Figure A.4. Then the sample was coated with the same photoresist and put into the laser writer to isolate the device with the same photolithography parameters. The optical microscopy image of the sample after develop is shown in Figure A.5. After developing, the sample was milled till  $SiO_x$  layer.

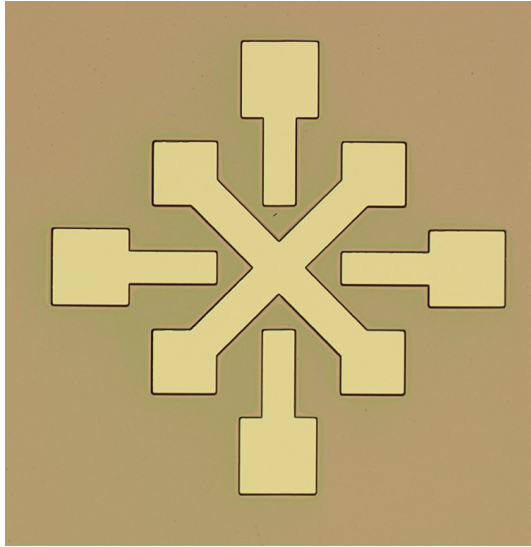


Figure A.4. Optical microscopy image of the sample after Au deposition and lift off

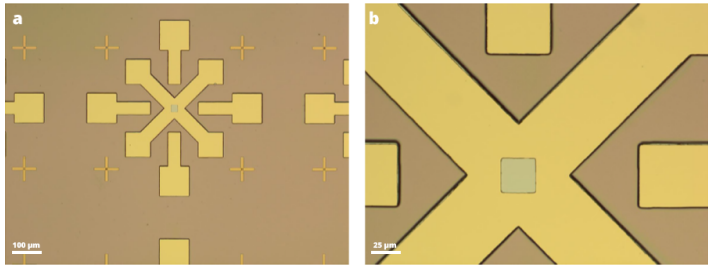


Figure A.5. Optical microscopy images after isolating the device, a) magnified 20 times, b) magnified 50 times.



Figure A.6. Optical microscopy image after defining 30x30  $\mu\text{m}$  device area

When we finished the sample isolation process, 30x30  $\mu\text{m}^2$  device area was defined with aligned photolithography as shown in Figure A.6. Next step for the three terminal device is defining the 1x1  $\mu\text{m}^2$  pillar by aligned e-beam lithography. For this purpose, the sample was first coated with omnicoat at 1000 rpm, spun twice for 45 seconds and baked at 170°C for 1 minute, resulting in approximately 30 nm thickness. Secondly, it was coated with PMMA A2 495 at 4000 rpm for 45 seconds and baked at 170°C for 15 minutes that results in approximately 50 nm thickness. Lastly, the sample was coated with HSQ XR1541006 at 3000 rpm for 45 seconds and baked at 170°C for 2 minutes, resulting in approximately 100 nm thickness. For the exposure of the sample, we performed dose test between 1000 and 10000  $\mu\text{C}/\text{cm}^2$ . The sample was then exposed with 2000  $\mu\text{C}/\text{cm}^2$  and developed with 1:3 MIBK/ISO solution for 45 seconds. PMMA and omnicoat were etched by O<sub>2</sub> plasma at 100 Watt and 24 sccm flow rate for 2 minutes.

After plasma etch, the sample was ion milled until IrMn layer and then 30 nm MgO was deposited by e-beam evaporation. Following MgO deposition, lift off was performed by soaking the sample in PG Remover for 24 hours at 90°C and sonication. Optical microscopy images of the device are shown in Figure A.7.

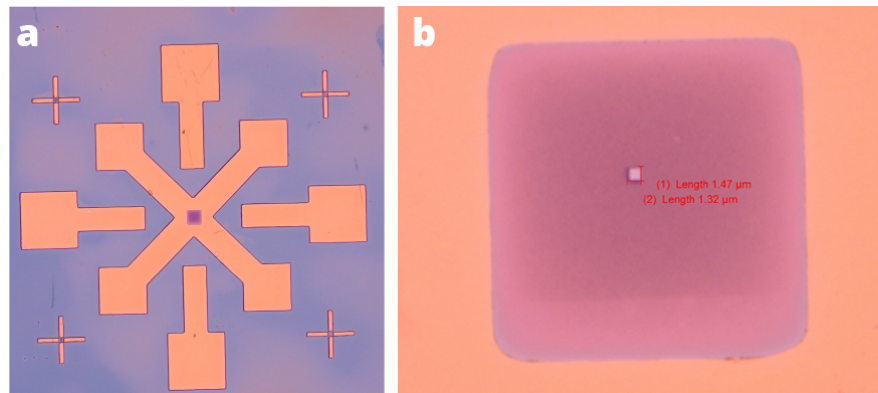


Figure A.7. Optical microscopy image after MgO deposition and lift off

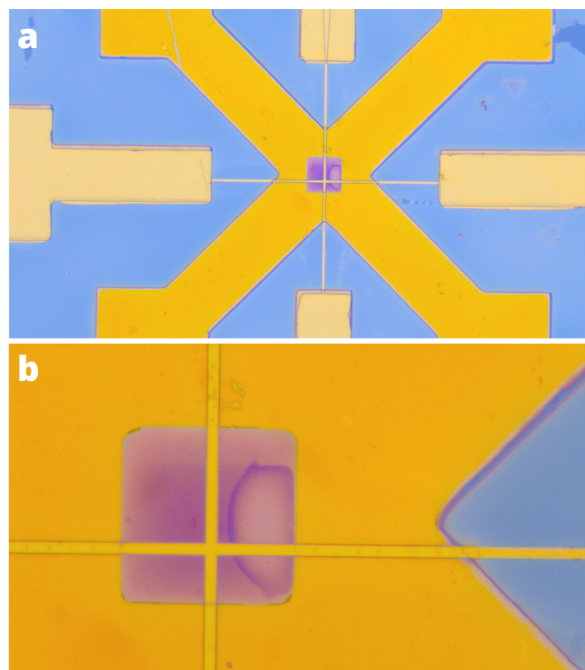


Figure A.8. The final state of the three terminal device

The last step in the fabrication of the three terminal device was the formation of the top contact. Patterning was done by aligned e-beam lithography where we coated the sample with PMMA C2 495 at 1000 rpm for 45 seconds and baked at 170°C for 5 minutes. Then the sample was exposed with 100  $\mu\text{C}/\text{cm}^2$  and developed. Finally, the sample was deposited 5 nm Ti and 100 nm Au, as shown in Figure A.8.